rijksuniversiteit
groningen

Structural and electrical characterization of phase-change memory line cells

Proefschrift

ter verkrijging van de graad van doctor aan de
Rijksuniversiteit Groningen
op gezag van de
rector magnificus prof. dr. E. Sterken
en volgens besluit van het College voor Promoties.

De openbare verdediging zal plaatsvinden op

vrijdag 11 april 2014 om 14:30 uur

door

Jasper Leonard Martin Oosthoek

geboren op 25 december 1982
te Everdingen

Promotor
Prof. dr. ir. B.J. Kooi

Beoordelingscommissie
Prof. dr. M. Wuttig
Prof. dr. J. Schmitz
Prof. dr. T. Banerjee

Structural and electrical characterization of phase-change memory line cells

Jasper L.M. Oosthoek

Voor Bob, Trudi en Jelmer

Zernike Institute PhD thesis series 2014-08
ISSN: 1570-1530
ISBN: 978-94-91909-08-5 (printed)
ISBN: 978-90-367-6969-3 (electronic)

university of groningen / faculty of mathematics and natural sciences / zernike institute for advanced materials

The work described in this thesis was performed at the Zernike Institute for Advanced Materials of the Rijks*universiteit* Groningen.

The research was carried out under project number MC3.05241 in the framework of the Strategic Research program of the Materials innovation institute M2i. (www.m2i.nl)

Contents

Chapter 1

Introduction

1.1 Abstract

This chapter describes the basic concepts of phase-change materials (PCMs) and how they are incorporated in existing and future memory devices. A brief history is given from the first switching of PCMs by Ovshinsky [71] to the present day rewritable optical disks which are based on PCMs. Although the market for rewritable optical disks has strongly declined, new applications are emerging in the field of solid state memory devices that are likely to replace the currently popular flash memory in the near future. Various concepts for these electrical devices and their remaining challenges are described. At the end of this chapter an overview of this thesis is given.

1.2 Introduction

Phase-change materials (PCMs) are alloys that are characterized by their striking ability to exist in two (or more) distinct phases at room temperature, i.e. the crystalline and the amorphous phase. The name can be confused with phase-change materials used for heat storage or heat release. Here the name applied to a different class of materials which by heating and cooling, it is possible to switch between these two phases which are stable at room temperature [71, 78, 85]. The phase a PCM is in can be directly used to carry nonvolatile information in a computer memory. This principle and a computer memory developed (and produced for R&D purposes) by NXP has been the basis of this thesis.

In the amorphous phase the atoms are (from long-range order point of view) arranged at random positions, resembling the atom distribution of ordinary glass, which is generally based on SiO_2. Amorphous PCMs are optically transparent and have a high electrical resistivity, but not as high as glass. Ordinary glass has a *glass transition temperature*, or glass temperature, of typically 700 °C. When heated above this temperature it becomes soft and malleable, but brittle when cooled below. Like glass, PCMs also have a glass temperature, but it is typically about 150 °C. Amorphous

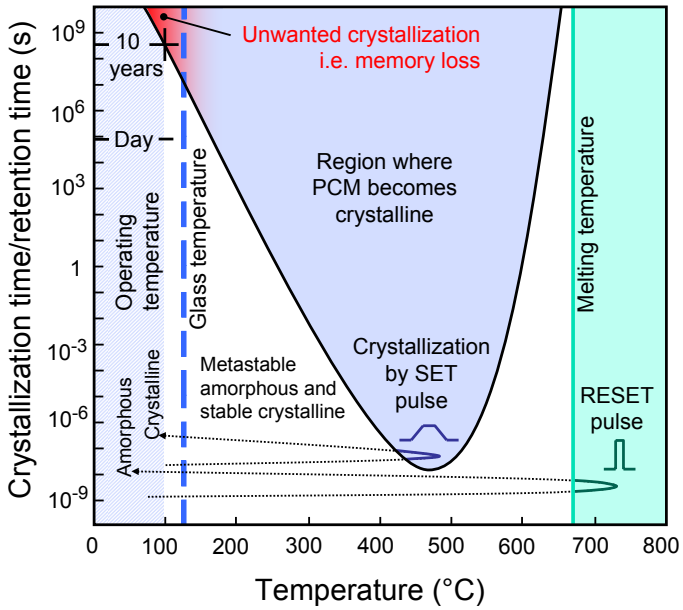

Figure 1.1: *The required time to crystallize an amorphous bit in a typical phase-change material is shown as a function of temperature. Note the seventeen orders of magnitude decrease in crystallization time when the temperature is increased from about 100 °C to the peak temperature at 470 °C. This illustrates the exceptional kinetic properties of phase-change materials. The retention time refers to unwanted spontaneous crystallization at operating temperatures (e.g. 10 years at 100 °C).*

PCMs on the other hand are inherently unstable above the glass temperature, and below the melting temperature (typically around 600 °C), the atoms will spontaneously arrange themselves to their natural low energy form where the atoms are arranged in regular patterns. This is the crystalline phase which, at temperatures below the glass temperature, can exist along with the amorphous phase for extended periods. The crystalline phase has metal-like properties which translate into a lower electrical resistivity of several orders of magnitude and higher optical reflectivity when compared to the amorphous phase.

Crystallization occurs spontaneously within a period of time which is temperature-dependent and when the PCM is cooled it retains its crystalline form. Figure 1.1 shows the time for crystallization to take place of an amorphous PCM as a function of temperature. To bring the crystalline PCM to the amorphous state it has to be molten. Normally, in metal alloys, when the temperature is lowered following melting, the material solidifies, leading to a new crystal structure. However in PCMs when the temperature is lowered so fast that the time spent between the melting temperature and glass temperature regime is adequately short then the material becomes a

melt-quenched solid. This maximum cooling time is in the range of milli-second to as low as the nano-second depending on PCM composition. In fact, some metals alloys can be brought to an amorphous phase, too, although very high cooling rates are needed, which is known as metallic glass [95]. Unlike PCMs, (melt-quenched) amorphous metal alloys do not show the strikingly large differences in both the optical and electrical properties from their crystalline form. The same holds for ionic glasses like based on SiO_2 and ordinary semiconductors like Si and Ge. Therefore PCM offers large advantages over those materials in terms of practical applications as storing information in a computer memory. Even though the amorphous phase of PCM is still inherently unstable below the glass temperature, the material cannot return to the favorable crystalline phase due to the low mobility of the atoms at these lower temperatures. The atoms are in fact 'frozen' into a higher energy state. When crystallization is slow, the longer allowed cooling time makes it easier to switch from the crystalline to the amorphous phase. However, switching from the amorphous phase to the crystalline phase will also take longer, which effectively slows down switching rates and increase energy consumption. For most memories, switching sufficiently fast to the amorphous phase can be achieved easily. Therefore it seems desirable to make the crystallization time as short as possible. But this has an undesired outcome: Faster crystallization generally leads to a shorter memory retention time, which is the time an amorphous state is stable at the highest operating temperature of the memory (which for consumer applications is defined as 10 years at 80-90 °C). PCMs typically show that the glass temperature is not sharply defined and crystallization can take place very slowly at temperatures below and relatively close to it. Although it would take several years to crystallize, such a memory retention time is still a very normal requirement of a computer memory. Therefore, for a memory to function properly a PCM is required which has material properties that are a fine balance between conflicting requirements.

1.3 History

Ovshinsky first reported electrical switching between the two phases of PCMs in 1968 [71]. His devices were thin films of PCM that could be switched by the heat supplied by an electrical pulse. He understood the possibilities for data storage from exploiting the two phases to carry information [85]. Feinleib et al. first demonstrated optical switching of PCMs using laser pulses in 1971 [14]. In 1978 the first prototype of a 1024 bit memory was built by Burroughs Corporation [91]. Although the research of PCMs had a very promising start the high power consumption related to the slow crystallizations times in the millisecond and microsecond range [96] prevented any product to reach the market. For a decade the research was largely abandoned. However, this changed with the discovery of fast switching alloys by Yamada et al. which was reported in 1987 [101]. These alloys allowed for the first commercial application of a 500 MB PCR optical disk by Panasonic in 1990, and later the CD-RW in 1997, DVD-RW in 1999 and the Blu-ray disk in 2003. In optical discs, PCMs can be switched reversibly at least more than ten thousand times between amorphous and

crystalline phase (Fig. 1.2). The large difference in optical reflectivity between the two phases makes it possible to read the state of the written amorphous or crystalline mark [99]. A fast high energy laser pulse transforms the crystalline mark into an amorphous state by melt-quenching. The crystalline state can be re-obtained via a longer lower energy pulse that heats the cell optimally below the melting temperature, where the mobility of the atoms becomes high, allowing crystallization. This can also be done fast (<100 ns), but not as fast as melt-quenching that is possible in picoseconds. The information is read by an even lower intensity laser, the same way a normal optical disc is read.

1.4 Electrical memories

The combination of ultra-fast crystallization kinetics with large changes between the optical properties led to great success of rewritable optical discs in the mid '90s. However, the two phases of PCMs exhibit large changes in both optical *and* electrical properties. The advances of optical memories prompted the research on an electrical memory based on PCMs known as Phase-change random-access-memory (PRAM or PCRAM). In PRAMs, the PCMs are formed into miniature resistors that are part of a computer memory chip. In PRAMs the PCM is completely encapsulated and cannot be switched optically. The resistors are switched between the phases by the heat generated by electrical pulses instead of optical pulses. In PRAM the state is read by the amount of current passing through a resistor (PRAM cell) instead of observing how much light is reflected.

Around the turn of the century, PRAM was still in early development, while Flash memory had become the primary choice of non-volatile electrical memory, finding widespread consumer usage in e.g. USB sticks and later on insmart phones and tablet computers. Flash memory is based on storing electric charge in an electrode surrounded by an insulator (silicon oxide). It was predicted that Flash memory would not meet the demands of future memory because further miniaturization would lead to very high local electric fields [2, 4]. This apparent future limitation of Flash memory was seen as an opportunity for PCMs. PRAM does not have the predicted problems with miniaturization that Flash has. Around 2004 there was consensus in research groups that optical memories based on PCMs do not meet the demands for future applications. Therefore the research on PCMs changed focus from optical memory to electrical memory, taking it back to the original idea by Ovshinsky.

Several different device topologies have been proposed that are all based on the same principle of how PCMs work (see Fig. 1.3). An electrical pulse heats a PRAM memory cell by Joule heating. This can be done either directly, by passing a current through a small amount of PCM, or indirectly where most of the heat is supplied to a heater connected next to the cell. Figure 1.3 shows an Ovonic PRAM cell which is switched by indirect heating. In an Ovonic cell the current flows vertically with respect to the wafer and through both the heater and the PCM. During melt-quenching the current density is highest close to the heater which leads to a mushroom shaped amorphous mark. The vertical geometry allows for a very high memory density [12].

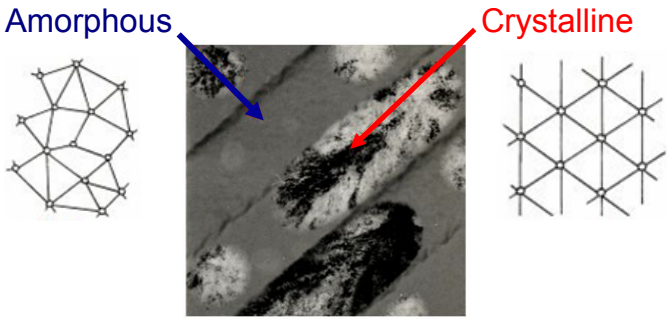

Figure 1.2: *A TEM image of a DVD track in an optical disk based on a phase-change material: Crystalline marks are written by a laser in an amorphous layer of PCM. Image adapted from website of Plasmon Storage Technologies.*

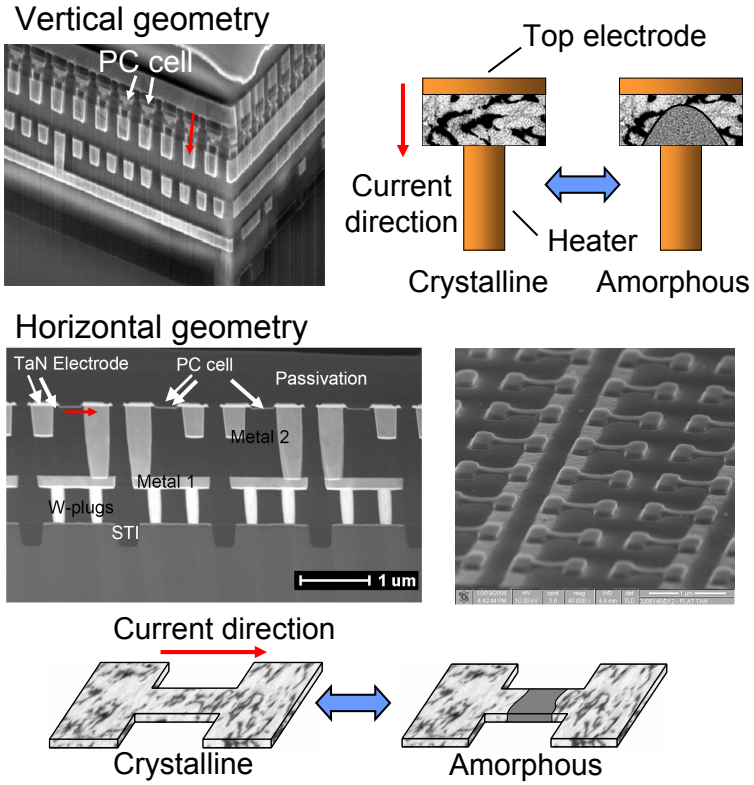

Figure 1.3: *Two different geometry types of PRAM are prevalent, the vertical geometry (image adapted from [37]) and the horizontal geometry (images courtesy of NXP). Although both geometries exist in several variants, the largest difference is the direction the switching current flows with respect to the silicon wafer.*

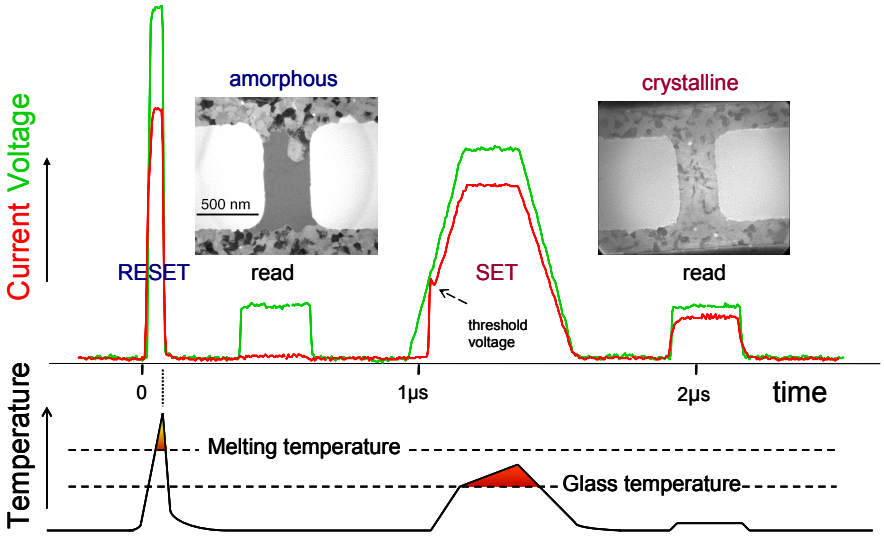

Figure 1.4: *Typical electrical switching cycle of a PRAM cell. A short (50 ns) high energy RESET pulse transforms the cell from the crystalline via melt-quenching into the amorphous phase. A longer (300 ns) lower energy SET pulse transforms the cell from the amorphous into the crystalline phase. Note the important role played by threshold switching allowing at low voltage a transition (breakdown) from a highly insulative to a conductive state in the amorphous phase-change material. In the lower panel the corresponding temperatures are illustrated schematically. Two TEM images indicate the structure of the cell in the amorphous and crystalline state (i.e. with and without amorphous mark).*

Another concept was proposed by NXP (at the time Philips Semiconductors) where the direction of current flow is horizontal with respect to the silicon wafer ([52] and Fig. 1.4). This line-cell concept has the benefit that the switching current and related power consumption can be limited by the thickness of the deposited layer of PCM. This can be controlled much easier in the nanometer range than the lithographic dimensions. In Ovonic PRAM memory, the PRAM cells can be made smaller by applying sub-lithographic processes. However, this may be not cost effective [12, 58].

Figure 1.4 is an example to illustrate how a PRAM cell is switched between the two states. The PRAM cell shown is a line-cell produced by NXP and this particular type was used in this thesis. It is a single memory cell which was especially designed only for testing purposes. In the structure, there is a constriction (known as a dog bone shape) where the current density is highest and where the heat from the electrical pulse can be dissipated. First a short (50 ns) but relatively high voltage electrical pulse melts the line. This is called the RESET pulse and is used to bring the cell to the amorphous state. Figure 1.4 shows a RESET pulse taken from an actual measurement (see Chapter 6). At the end of the pulse the voltage drops from the maximum value to zero in 4 ns. Because the material surrounding the cell is still at room temperature the cell is able to cool fast to a temperature below the glass temperature and it will be

melt-quenched into the amorphous state. To read the state of the cell, a second low voltage pulse is applied and the current flowing through the cell is measured. It can be observed in Fig. 1.4 that a low current flows during the read pulse, even though a relatively high current, with respect to the pulse voltage, flowed during the previous RESET pulse. The low current confirmed that after the RESET pulse the cell was switched from a low electrical resistance to a high resistance state. Subsequently, a lower voltage and longer (300 ns) pulse brings the cell temperature above the glass temperature and below the melting temperature. The longer pulse width of this so-called SET pulse allows the cell to have sufficient time to crystallize. After the SET pulse a second read pulse confirms that the cell is in a low resistance state. It can be clearly observed in Fig. 1.4 that a considerable amount of current flows compared to the first read pulse. During the beginning of the SET pulse the current suddenly increases when the voltage increases above the threshold voltage [71, 78]. At this point the cell switches from a high resistance to a low resistance state. This is called threshold switching and was actually the first phenomenon observed by Ovshinsky [71] and is not to be confused with crystallization. After the threshold event the cell will be able to carry a high current because of the increased density of free charge carriers even at voltages below this threshold voltage [79]. If this current is maintained long enough only then crystal growth is able to occur in the cell. The occurrence of threshold switching is a crucial property for the operation of a PRAM cell and is further studied in Chapter 6. Without threshold switching, very high voltages, not compatible with computer memories, would be required to supply enough heat to crystallize the amorphous cell.

1.5 Requirements of phase-change materials

The description above indicated that phase-change materials have to fulfill a number of complicated and sometimes contradictory requirements. This means that meeting some requirements will have a negative effect on other requirements. This will be addressed below [99, 92, 55, 52]. The first three requirements deal with crystallization kinetics and Fig. 1.5 shows why these properties can affect each other.

1. Low crystallization rate, i.e. high thermal stability of amorphous marks, at the highest operational temperature. The operating temperature is the ambient temperature of the memory itself, not to be confused with the elevated temperature at which the individual cells are switched. This requirement corresponds to a data retention time of approximately 10 years at 100 °C. In the operating temperature regime, the data retention time will always be shorter at higher temperatures as the crystallization rate increases with increasing temperature. Therefore the maximum operating temperature is used (see Fig. 1.5, Chapter 4 and 5).

2. High crystallization rates at elevated temperatures, e.g. 450 °C., allowing erasure of amorphous marks within 100 ns. This is conflicting with requirement (1) as high crystallization rates at elevated temperatures can lead to short memory

retention times at operating temperature. This can be observed in Fig. 1.5 as merely shifting the curve to the left will have an adverse effect on requirement (1).

3. Low melting temperature (typically 600 °C), enabling easy amorphization by melt-quenching. This significantly limits the power consumption of the memory, because the melting step requires most power. Figure 1.5 shows that a lower melting temperature translates into the in the right part of the curve shifting to the left. However, the left part of the curve is not allowed to shift to the left because of requirement (1). Therefore, several material properties such as the activation energy of crystallization have to increase too to allow for lowering of the melting temperature.

4. A large number of times a PRAM cell can be switched (cycled) between the amorphous and crystalline phases. Cyclability of for instance $>10^6$ switching cycles, without affecting the cell properties in a negative way, allows a good endurance of the memory. For instance, cell cycling will lead to decomposition of the PCM which in our case (Chapter 6) lowered the memory retention times and eventually lead to failure of the cell.

5. Sufficiently large electrical/optical contrast between the amorphous and crystalline phases. This requirement relates to the readability of memory as low contrast makes it harder to read the state of written information. Low contrast between the phases may be more time consuming or may require additional circuitry to read the state of a memory which will affect performance and/or cost.

Currently known and applied PCMs have been found by trial and error. Alloys containing high Sb and/or Te concentrations turn out to exhibit best the required phase-change characteristics [55, 85]. However, to obtain other desired properties, addition of one or more elements, mostly Ge but also In, Ag and/or Ga are required. As in traditional semiconductors, introducing these additional elements is called doping. However, doping of traditional semiconductors can be seen as intentionally introducing impurities into a single crystal lattice. Therefore, concentrations of dopants are in the ppm range to keep long range order. In PCMs however, doping concentrations are in the percentage range which resembles more an alloy. Doping is particularly important to stabilize the amorphous phase sufficiently at low temperatures (i.e. increase memory retention). Ge-Sb-Te alloys have become prototypical for PCMs [85]. Efforts have been undertaken to increase our understanding of PCMs in a way that an optimal composition for certain applications can be predicted [99, 92, 55, 29, 100]. However, the most optimal composition of dopants to supplement the properties of PCMs with regard to the aforementioned requirements has not yet been established.

Figure 1.6) is the ternary Ge-Sb-Te phase diagram where three compositional regions show alloys with suitable phase-change properties. In fact, the alloys that are exploited commercially originate from these three different regions in the phase diagram. The first region, most widely studied and applied commercially, is located on and near the GeTe-Sb_2Te_3 tie-line. $Ge_2Sb_2Te_5$, commonly known as GST-225, is

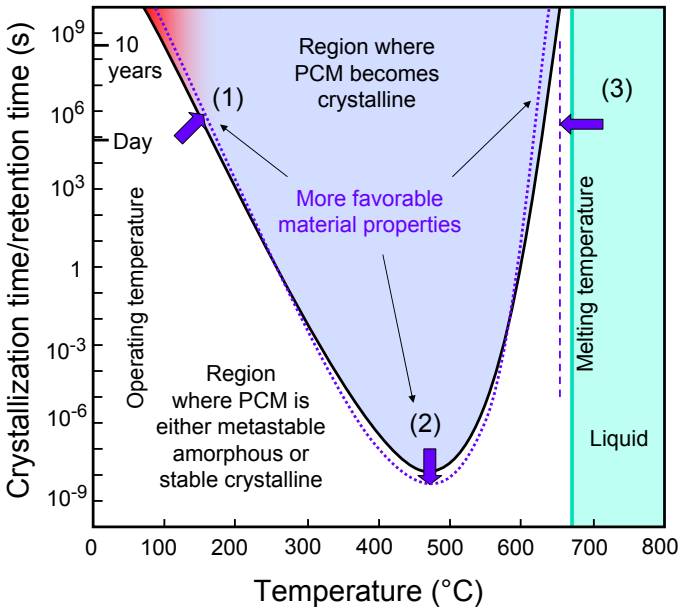

Figure 1.5: *The required time to crystallize an amorphous bit in a typical phase-change material is shown as a function of temperature. The black line shows the crystallization properties of a typical PCM and the blue dotted line shows a PCM with more desired properties (see main text). Requirement (1) will lead to a better memory retention, (2) will lead to faster switching to the crystalline state and (3) lowers the temperature of switching to the amorphous state.*

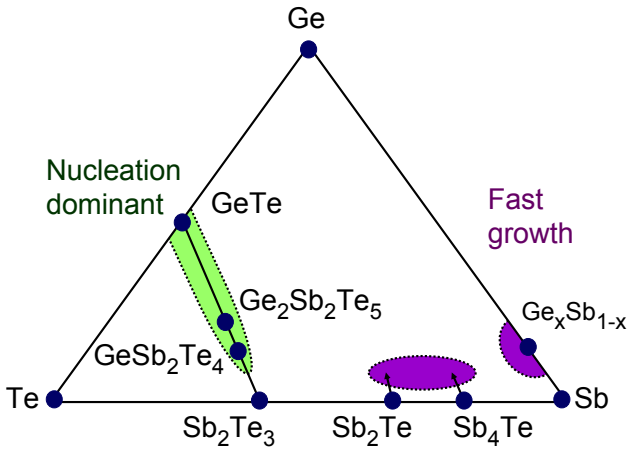

Figure 1.6: *Ge-Sb-Te ternary phase diagram showing by the color-shaded areas the three compositional regions in which materials with suitable PCM properties are found. Adapted from Ref. [55].*

of particular importance. This region corresponds to so-called nucleation-dominant materials (NDMs). These materials show very fast and high density crystal nucleation leading to crystal sizes typically less than a few tens of nanometers. The second region contains 'doped Sb_xTe alloys where x is typically in the range of 2 to 4 and where doping concentrations are about 8 atomic percent. Although Fig. 1.6 only shows Ge [55], also Ge+In [77], or Ag+In. (AIST) are used [59]. As can be seen in Fig. 1.6, the pure Sb_xTe alloys are not inside the region as doping is essential for obtaining the desired material properties, most importantly lowering crystallization rate at external operating temperatures. The third region contains doped Sb alloys. As Sb and Te are next to each other in the periodic table, their atomic sizes are just slightly different which will cause mutual frustration. In the absence of Te, a higher doping concentration of $\approx$ 15 atomic percent of Ge is required to sufficiently stabilize the amorphous phase at low temperatures.

The alloys of the second and third regions are so-called fast-growth materials (FGMs). They show low nucleation rates, but ultra-fast growth, typically leading to micron-sized crystals. Fast crystal nucleation is not required for PCMs, because in actual applications the amorphous mark is generally surrounded by crystalline material that enables fast re-growth (without nucleation) into the amorphous mark. Figure 3.2 illustrates the difference between fast growth and nucleation dominant behavior. Although the material is of the same fast growth type, oxidation of one sample has caused the material to behave more like a NDM leading to a higher nucleation rate without significantly affecting the crystallization rate. Particularly with the continuous down-scaling of memory sizes, all PCMs increasingly shift towards FG behavior [8]. Within the research field on PCMs it is not uncommon that the results for NDMs are considered representative for all PCMs, but then the significant differences between NDMs and FGMs are neglected. The PRAM line cells studied throughout this thesis contain a Ge+In doped Sb_xTe alloy and thus corresponds to the second region in Fig. 1.6 and can thus be classified as an FGM.

1.6 Main objective of this thesis

This project was initiated and has been carried out in close collaboration with NXP (formerly Philips Semiconductors) in Eindhoven. As already mentioned, a new PRAM concept that offered many advantages was proposed by NXP in 2005 [52]. Still, several fundamental questions had to be answered before a technological breakthrough could be achieved and this new concept could be transformed into a reliable prototype memory with clear market potential. For instance, a retention of 10 years at 80 °C could not be guaranteed. After about 10^6 SET/RESET cycles it was no longer possible to switch the cell to the amorphous state. After about 10^8 cycles, the cell stayed in a highly resistive state (dead). Clearly, a better understanding of the switching dynamics on the single cell level was required before a reliable prototype memory could be successfully engineered. The objective of this PhD project was to contribute to this understanding, particularly by improving knowledge of the nanostructure-property relationship. The properties of cells can be characterized very

well by electrical measurements. However, nanostructure information is not easily retrieved for the same cells, because they are completely embedded obscuring any direct microscopy imaging for instance with scanning or transmission electron microscopy. The main aim of the present project was to add nanostructure TEM information to the electrical behaviour of single line cells. The final goal was to image an operating PRAM cell in the TEM, i.e. where the cell can be switched by nano-second electrical pulses and can be electrically characterized, while it is in the TEM where it can be imaged at nano-meter scale. These goals have been accompanied by many challenges which are described in this thesis.

1.7 Outline of this thesis

The chapters in this thesis can be read independently and therefore it is possible that some information can appear twice, especially in the introductions to the chapters. Chapter 2 gives background information on the experimental techniques and methods used for obtaining the results presented in following chapters. Chapter 3 presents results on the crystallization process, particularly on the crystal growth rate and its dependence on temperature, in doped SbTe phase-change thin films. *In situ* heating in a transmission electron microscope (TEM) was employed to study the crystallization process in detail. A new procedure has been developed for automatic growth rate determination from a time series of TEM images. Particularly problems with the complex contrast in TEM images were solved in order to make the procedure run successfully. Exactly the same alloy as studied in these blanket films in Chapter 3 were used in PRAM line cells which were studied for obtaining the results presented in Chapter 4 to Chapter 10.

In Chapter 4 a comparison is made between data retention of these line cells as based on (i) electrical measurements of line cells, (ii) crystal growth rate measured in an actual PRAM cell in the TEM and (iii) crystal growth rate measured with TEM in the blanket films. The most important conclusion is that crystal growth in the as-deposited blanket films is significantly slower than in melt-quenched amorphous structure present in the PRAM line cells. Slower growth at these low temperatures corresponds to a better data retention, but the present work demonstrates that the as-deposited amorphous structure cannot be used to predict data retention of the melt-quenched amorphous structure.

In Chapter 5 two methods of obtaining the memory retention time are studied. In the first method called isothermal crystallization, the time it takes for cells to crystallize is measured at various temperatures which are kept fixed in time. The crystallization times found follow an Arrhenius dependence from which the memory retention at lower temperatures can be extrapolated. The second method called isochronal crystallization involves crystallizing cells at different heating rates which will result in a different crystallization temperature for each heating rate. By employing Kissinger analysis [40] the equivalent (isothermal) Arrhenius temperature dependence can be calculated. These two methods were found to give equal physical results and are interchangeable, a feature that is exploited in Chapter 6. Moreover, Chapter 5 shows that

line cells based on identical phase-change material can still behave very differently when the cells are produced (and the PCM is packed) in a different way.

Apart from data retention another important property of a (nonvolatile) memory is its endurance, i.e. how many cycles the memory can be switched between its two distinct states (without too much degradation of the properties of one of the states). In Chapter 6, detailed results on the evolution of the line cell memory characteristics during cycling are presented. We measured the resistances, resistance drift, threshold voltage, threshold-voltage drift, crystallization temperature, and activation energy for crystallization during cycling. The these properties have been obtained simultaneously for a single cell with excellent reproducibility when repeating for several cells. Important conclusions about the initialization phase, usable life and the end of life of the line cells have been drawn.

An important property of PRAM is that the resistance associated with the amorphous phase shows temporal drift. Due to this drift it is very difficult for PRAM to become a multilevel memory (i.e. where single memory cells can obtain more than two states). When feasible, multilevel memory properties would enormously favor commercialization of the PRAM concept. In Chapter 7 results are presented of a detailed electrical study on drift, acceleration of drift at higher temperatures and influence of drift on the determination of the activation energy for conduction in the amorphous semiconductor phase of PRAM line cells. The observed increase in the amorphous resistance as a function of annealing history (for various frozen-in drift levels) has been modeled and well-reproduced using a trap limited band transport model.

PRAM cells have been studied extensively using electrical characterization and rather limited by detailed structure characterization, for instance using TEM. The combination of these two characterization techniques is addressed in Chapter 8. Particularly for improving the reliability of PRAM such combined studies can be considered indispensable. In Chapter 8 TEM images are shown for PRAM line cells prepared after series of voltage pulses with increasing magnitude were applied, leading to the first minimum sized amorphous mark, maximum amorphous resistance and over-programming, respectively. Furthermore, the crucial effect of electromigration limiting the endurance (cyclability) of the cells is demonstrated.

The line cells described in Chapter 8 could not be switched or electrically characterized after TEM specimen preparation. Therefore, an important objective was to prepare TEM specimen of PRAM cells that could still be switched or electrically characterized, preferably fully inside the TEM. This preparation is explained in detail in Chapter 9. Interesting results could be obtained for one such electrically switchable TEM sample.

Instead of TEM also scanning electron microscopy (SEM) can be used for in situ electrical switching and characterization of PRAM cells, with the advantages that (i) in SEM much more space is available around the sample than in TEM and (ii) in SEM the region of interest (the phase-change line cell) has to be in a certain depth range below the surface of the passivation layer, whereas in TEM it is required to be covered by a thin foil with a thickness not more than a few hundred nanometers. Chapter 10 presents results on developing an in situ probe station for line cells in an SEM and on the finally obtained images using charge collection microscopy (CCM).

Chapter 2

Experimental

2.1 PRAM cells

The PRAM cells used throughout the project are line cells made by NXP. The cells were produced on silicon wafers at two different locations. Electron beam (e-beam) lithography was used for the PRAM cells from Eindhoven. Very small geometries can be obtained using this technique without requiring a state-of-the-art wafer fabrication laboratory. The cells from Eindhoven were available in length ranging from 100 nm to 600 nm. On the other hand, the PRAM cells from the IMEC in Leuven were produced by optical lithography. These cells are larger than the cells produced by e-beam lithography and ranged in length between 400 nm to 2 µm. However, the single cells were produced alongside 1 Mbit memories on the same wafer (see 2.10(a)). The PCM used for the single cells was therefore identical to the material used for the memories. The single cells allowed for a better understanding of the material properties and electrical characteristics of the PCM used for the larger memory structures that were not examined during this project.

A PRAM line cell is basically an electrical resistor made from PCM. During cell production the PCM is deposited in the amorphous phase on top of pre-patterned electrodes (see Fig. 2.1). It is patterned by lithography into a so-called dog bone shape. This shape has a constriction in the middle where the current density is largest. This is the part of the PCM that will be switched between the phases. After patterning a passivation layer (SiO_2 and Si_3N_4) is applied on top of the cell. This process occurs at 400 °C which crystallizes the PCM. Therefore, the cells start out in the low resistance state. The wider sides of line cell, known as flaps, are connected to bond pads on top of the passivation layer. The line cell is sandwiched between passivation layers for protection and is electrically accessible through bond pads. A connection between equipment and the bond pads is made either by probe needles or a permanent connection can be made by a wire bonding (see Section 10).

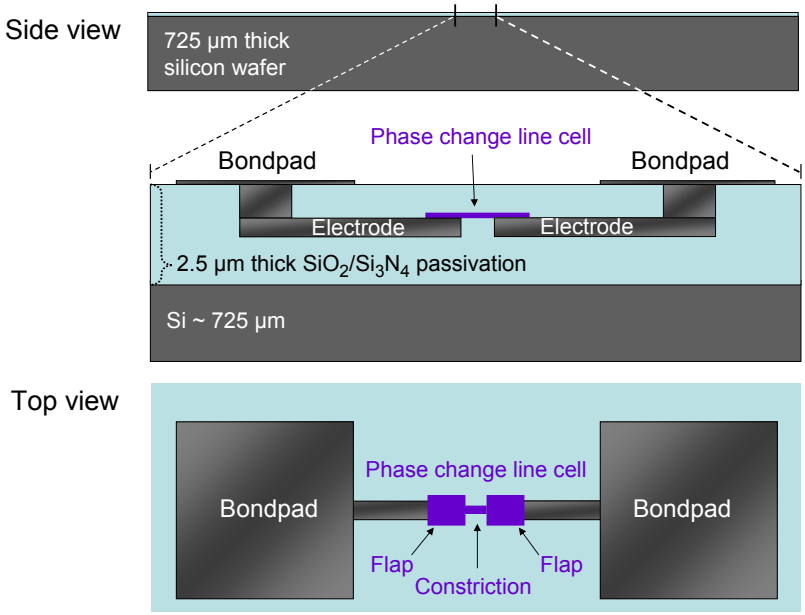

Figure 2.1: *PRAM line cells are produced by optical or e-beam lithography on silicon wafers. This is a schematic representation of how the cells are encapsulated in a passivation layer. The line cell has constriction in the middle where the current density is largest. Each side of this so-called dog bone shape is electrically connected to a bond pad. These particular cells were especially designed for testing purposes.*

2.2 Electrical characterization setup

The electrical characterization setup contains all the components to switch PRAM cells; perform electrical measurements and change the cell temperature. It contains the following components:

1. A probe system and manipulators to establish an electrical connection to the bond pads of the PRAM cells.
2. A pulse generator to switch the cells.
3. A storage oscilloscope to read the voltage and the resulting current supplied to the cell during switching.
4. A source meter to measure the electrical resistance.
5. A temperature controller and hot plate to change the cell temperature while performing electrical measurements.

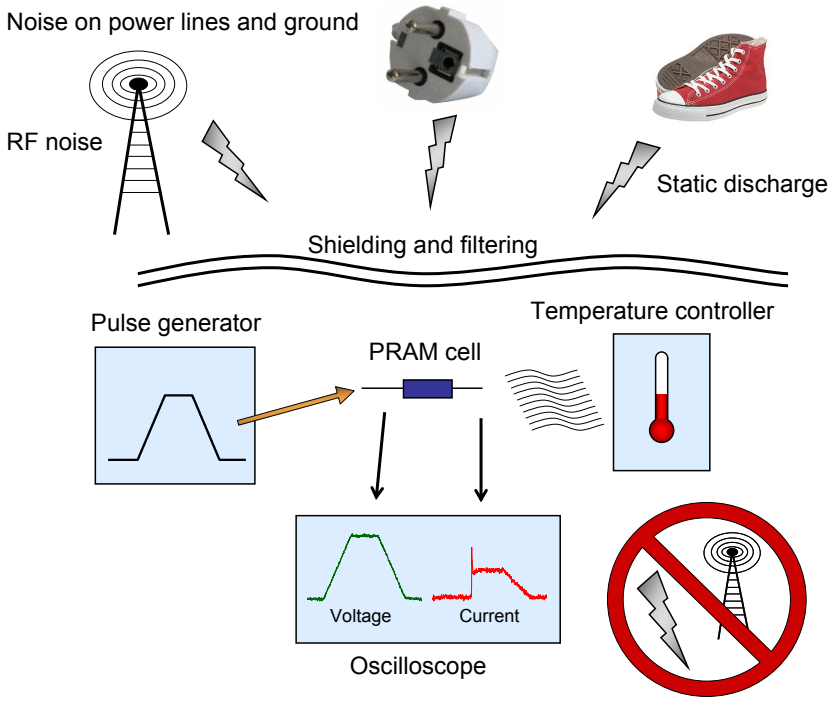

Figure 2.2: *Three types of noise were taken into account when designing the electrical characterization setup: RF noise, noise on the power line and ground and static discharge.*

2.2.1 Filtering noise and spurious pulses

Considerable time and effort was put into avoiding noise from entering the setup (see Fig. 2.2). In the beginning of the project many unexplained glitches occurred that switched or even damaged the cells (Fig. 2.3). Because filtering noise has been such an integral part of the design of the setup it is discussed before the individual components of the setup are described in detail. Three different contributors where identified that produce noise and glitches.

1. RF noise is created by components such as electrical motors and switching power supplies and is picked up by loops in the signal or ground cables. RF noise was suppressed by breaking ground loops with inductive filters and by double shielding cables. These steps have the additional benefit of increasing the signal to noise ratio of resistance measurements. Although RF noise is an important factor to consider, from hindsight this was not the most important contributor of glitches *i.e.* 'spontaneous' switching of the PRAM cell.

2. Any high current surges from equipment in the vicinity of the setup that is switched on or off creates voltage spikes on the power line or earth ground (Section 10.3.4). A direct connection between the earth ground to the signal ground of the measurement system was part of the design of the oscilloscope. Spikes can be passed on through the oscilloscope to the signal ground and to the signal wire by capacitive coupling. Disconnecting the earth ground from the oscilloscope is not an option as it would have been unsafe. Instead, commercially available line filters especially designed for this purpose were installed to filter the mains power supply and earth ground. Although similar filters are already present in the equipment they generally only filter the 50 Hz power line from spikes *not* the earth ground. The filters are based on an inductor and capacitor network and produce a high impedance path for high frequency glitches. Each component was given a separate filter after which the unexplained glitches have not been experienced again.

3. It is common knowledge that static electricity is picked up by the human body on days with low humidity. Electric discharge creates high voltage spikes which can travel to the cell and still have more than enough energy to switch the cells. Static discharge was simply avoided by wearing an anti-static belt connected to the ground by a resistor. The resistor slowly discharges the static energy instead of by a spark. When this strap is not worn the cells were sometimes switched when a metal part of the setup is merely touched by hand. This happened even if no spark was felt.

Figure 2.3 shows two examples of glitches that occurred. Prior to the glitch, the increase of the resistance in time follow a well established power law [78]. Here, the glitch is of importance, however the power law behavior will be discussed in Chapter 5 and the following chapters. The measurement was performed before the line filters to the equipment were installed. The blue and the red data are a measurement of the resistance of a PRAM as a function of time after the RESET pulse. The blue data was measured first, however the cell spontaneously crystallized during the measurement. This can be observed by the resistance decreasing more than two orders of magnitude. This spontaneous and unwanted effect was attributed to a voltage spike picked up by the setup. Subsequently, the cell was RESET again and the red data shows the resistance measured directly after the RESET pulse. The overlap shows that the cell was brought to a very similar electrical state. During this measurement another even more powerful voltage spike (glitch) occurred that supplied more energy to the cell than original RESET pulse. This can be observed by the higher resistance which is related an increased amorphous mark.

2.2.2 Electrical connection to the PRAM cells

During the project the emphasis has been on in depth characterization of single PRAM cells. Therefore a relatively compact and simple *probe station* was built (see Fig. 2.4). The probe station creates a mechanical connection between the wafer and a probe needle system. A wafer part containing PRAM cells is placed on a ceramic hot plate

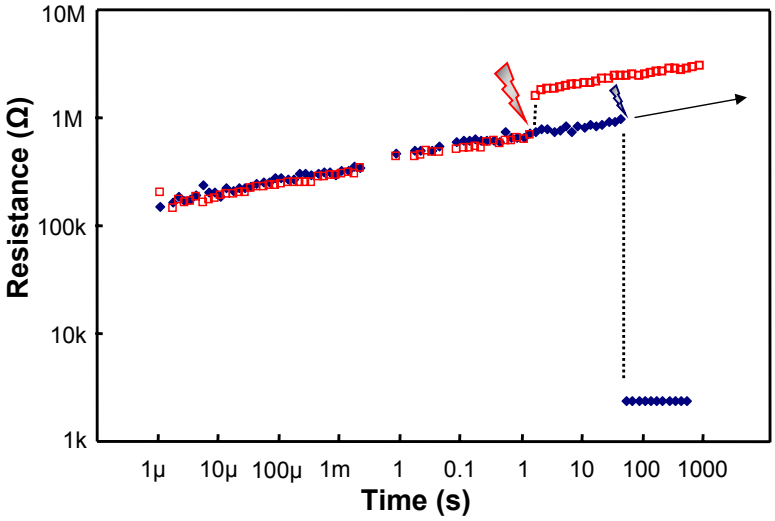

Figure 2.3: *A PRAM line cell was brought to the amorphous state and the resistance was measured as a function of time. During both measurements a glitch occurred which either led to crystallization of the amorphous mark (blue data) or to an increased size of the amorphous mark (red data).*

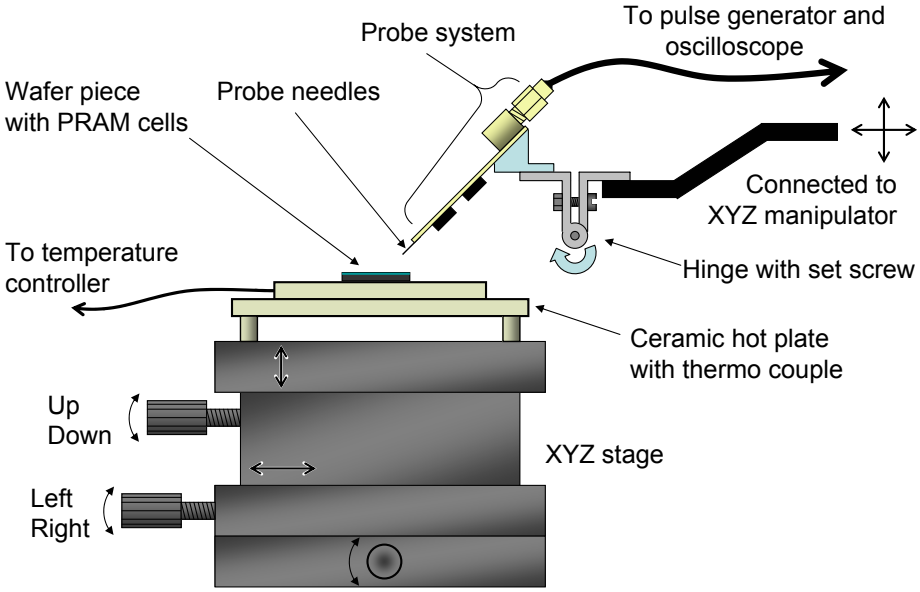

Figure 2.4: *Contact to the cell was made by a custom built probe station. Both the wafer piece containing the PRAM cells and probe needle system can be manipulated in three dimensions.*

mounted on an XYZ stage. Electrical contact is made, to one cell at the time, by a probe needle system mounted to an XYZ manipulator.

When the temperature of the hot plate is raised (Section 2.2.6) the thermal expansion of the stage pushes the sample upwards. This will cause the probe needles to move sideways and even off the bond pads. To minimize this effect a hot plate made from ceramic material was mounted on stilts. The stilts raise the hot plate from the metal XYZ stage. This avoids heating and thermal expansion of the metal parts of the stage. Furthermore, a spring loaded hinge, not present in the factory design, was constructed to allow the manipulator to flex upwards. The axis of rotation was designed to be at the same height of the sample. This minimizes lateral movement of the probe needles when the probe system flexes upwards. Still, contact problems remained an experimental difficulty when the temperature is changed, especially in annealing experiments where the temperature was cycled for up to twenty times between 3 °C and 125 °C (Chapter 7).

2.2.3 Switch cells with a pulse generator

Several pulse generators were tested before a decision was made. The type of pulse generation that is normally used is only able to produce two different pulse shapes at the same time. A Keithley 3402-F pulse generator was tested for a week. It has similar specifications as an Agilent 81110A which was present in the setup from NXP at IMEC. The tested Keithley 3402-F appeared to have a few issues: the delay time between the trigger pulse and actual pulse was not constant. Therefore when the trigger pulse was used to trigger the oscilloscope the pulse would not appear at the same location. Furthermore, the pulse edges were sometimes distorted after the settings where changed. But most importantly, the unit appeared to output glitches in the µs range when the settings were changed. These glitches were more than adequate to switch and even damage the PRAM cells. However, these pulse generators can only generate two different pulse shapes at the same time. A completely different type of pulse generator was found to be much more versatile and did not have the issues of the Keithley 3402-F. A Tektronix AFG3102 arbitrary function generator (AFG) was tested for a week and subsequently ordered for this project. An AFG is basically a digital analog converter (DAC) that can operate at $1{\cdot}10^9$ samples per second (1 GS/s). The fastest leading and falling edges that can be obtained are 4 ns which is more than adequate for a RESET pulse (i.e. the pulse needed to switch the cell to the amorphous state). The unit did not output any glitches when the voltage range was set from -5.0 volts to 5.0 volts.

2.2.4 The storage oscilloscope

An Agilent storage oscilloscope was especially ordered for this project. It has a 300 MHz band width with a 4 GS/s resolution. Figure 2.5 is a simplified diagram of the setup that highlights the interaction of the computer with the AFG, a PRAM cell and a computer. The AFG has the advantage of being able to output any pulse shape imaginable. Labview code was written to 'draw' and combine SET, RESET and read

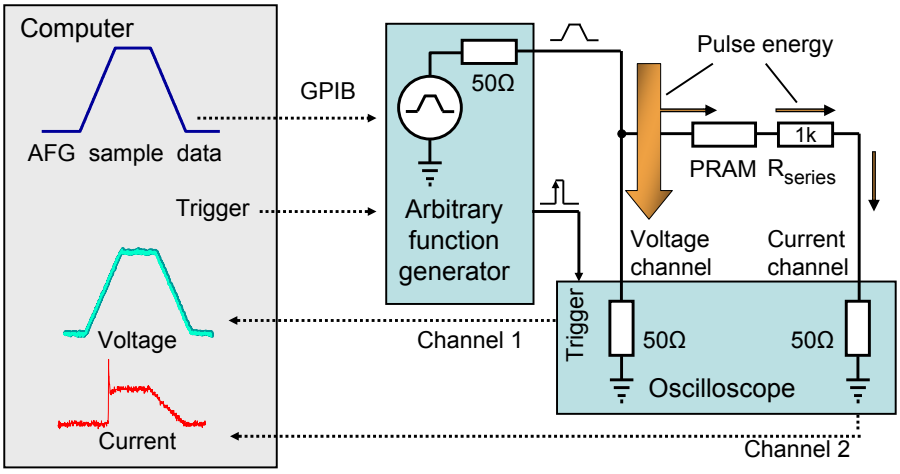

Figure 2.5: *The procedure of switching a cell: the computer first programs and then triggers the AFG. The AFG outputs a pulse that switches the cell. The voltage of the pulse and the related cell current are read by a storage oscilloscope. The computer reads and analyses the pulses from the oscilloscope.*

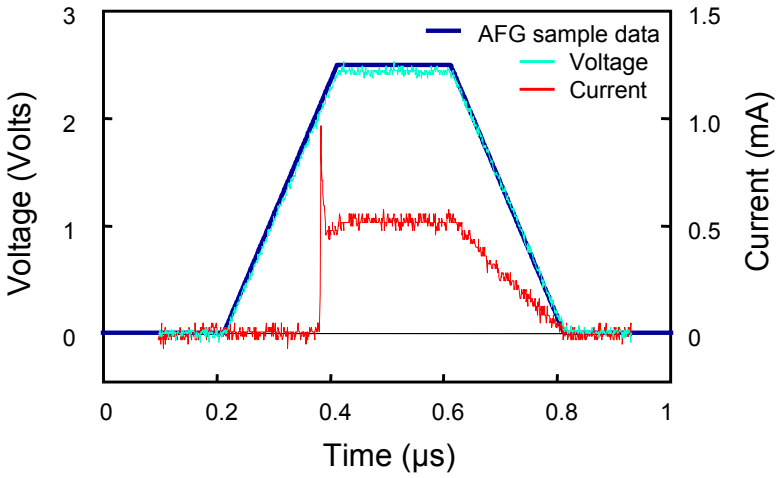

Figure 2.6: *Oscilloscope trace showing the excellent reproducibility between the desired SET pulse (dark blue curve) and the measured pulse supplied to the cell (emerald curve). The red curve represents the cell current and can be viewed as the response of the cell to the applied voltage.*

pulses. The trigger output pulse of the unit always starts at exactly the same time interval before the start of each pulse. Therefore the oscilloscope trace can be directly coupled to the programmed pulses. This makes analysis of the oscilloscope traces very easy. For instance, a RESET - read - SET - READ pattern was programmed to cycle the cell once or up to a million times (see Fig. 6.2). As long as the internal memory of the oscilloscope allowed, each separate pulse could then be retrieved. The analysis of whether the cells switched became a software programming issue. These pulse patterns would not have been possible if a traditional pulse generator was used.

The computer first programs the AFG with sample data created in a Labview program and then sends a trigger command to the AFG through the GPIB cable. The AFG simultaneously outputs the desired pulse along with a trigger pulse. The oscilloscope uses the trigger pulse to commence acquisition. The oscilloscope signal is therefore always synchronizes with the trigger pulse of the AFG, not with the much slower trigger command of the computer. The pulse travels through a coaxial cable to the oscilloscope. In fact, almost all pulse energy from the output of the AFG is dissipated inside the oscilloscope across the internal 50 Ω of the oscilloscope (big arrow). The 50 Ω resistor in the AFG and oscilloscope are necessary to avoid reflections that lead to distorted pulses. Only a small portion of the pulse energy (current) is able to travel through the higher resistance PRAM cell and series resistor which 1 kΩ at its lowest. The series resistor and cell are connected in series between the 'pulse line' (big arrow) and another cable leading to channel 2 of the oscilloscope which is also terminated by a 50 Ω resistor. This geometry generates a small voltage across the 50 Ω resistor of channel two of the oscilloscope proportional to the current through the cell. Although this voltage drop itself is negligible the signal is used as the cell current signal.

Figure 2.6 shows the combination of sample data used for programming the AFG and the resulting voltage and current signals acquired by the oscilloscope. The dark blue line represents the sample data (voltage) that was sent to the AFG while the emerald line is the voltage received by the oscilloscope. Note the excellent reproducibility between the desired pulse and the obtained result. This measurement flexibility has been fully exploited with complicated cycle measurements and measurements of the amorphous resistance from a micro second after RESET (Fig. 2.3).

2.2.5 The source meter

A Keithley 2601 source meter unit (SMU) was used throughout this project. The SMU has two operating modes that could be used: pulse mode and constant voltage mode. In the beginning of the project it was noticed that the resistance measured with a positive and negative voltage was not always equal. This had been attributed to a voltage offset in the system. Therefore all resistance measurements where performed in pulse mode at 0.1 volts followed by a second measurement with -0.1 volts. The average of these two measurements was taken. Figure 2.7 shows how the SMU is incorporated in the setup. An RF relay, operated by the digital output of the SMU, switches the cell between channel 2 of the oscilloscope and the source meter. When the RF relay is latched as shown the SMU is connected to allow for a measurement of

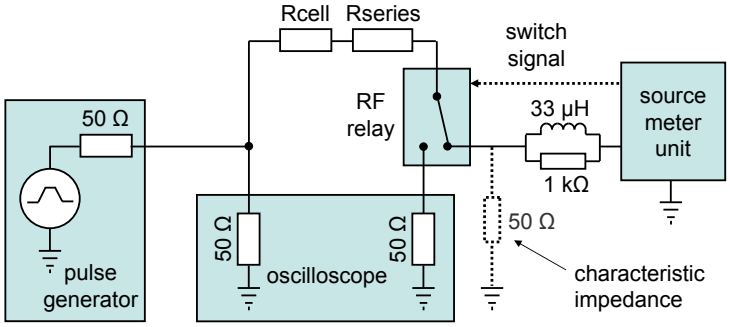

Figure 2.7: *Schematic representation of the electrical characterization setup. The inductor and 1 kΩ resistor are a compromise to filter as much noise as possible without having an influence on the resistance measurement.*

current from which the resistance is calculated. The cell resistance is always measured along with the series resistance and both the 50 Ω output of the AFG and the 50 Ω input of the oscilloscope in parallel. Therefore it has to made sure that the AFG does not output any pulses as these would influence the resistance measurement. Furthermore, a 33 µH inductor is connected in series to the output of the source meter. This inductor acts as a high impedance path for glitches and prevents them from entering the measurement system through the output of the source meter. The DC resistance of the inductor is below 1 Ω and does not influence (adds series resistance to) the measured DC resistance. However, a 1 kΩ resistor in *parallel* to the inductor was required to avoid the output of the source meter from oscillating as it is not designed to measure an inductive load. Although this 1 kΩ is able to leak noise into the measurements system at frequencies above 300 MHz it is attenuated by the 50 kΩ characteristic impedance of the cable. When the RF relay is switched to the channel 2 of the oscilloscope the setup becomes equal to Fig. 2.5.

2.2.6 Temperature controller

When the project started an already available Eurotherm 2216E temperature controller was implemented. The controller was connected to a solid state relay that switched a variable autotransformer on or off. The autotransformer was set to 70 volts and was connected to a heating coil in the ceramic hotplate described earlier in this section. Although this setup was able to regulate the temperature it was found that as soon as the temperature controller was turned on the PRAM cells stopped working. The problem appeared to be the fly back effect of switching the autotransformer on and off. The autotransformer has an inductance of several henries. Switching off the current will generate a high voltage spike which is the natural response of an inductor. This spike travelled through the heating wire of the ceramic hotplate. The probe needles are capacitively coupled to the heating wire because of stray capacitance. An other explanation is that the spike generates RF noise which

was then picked up by the needle system shown in Fig. 2.8. To avoid this spike altogether a similar model temperature controller was ordered with a linear output. This linear output could be connected to a linear power supply which acted as a DC amplifier. The new system allowed for much more accurate control of the temperature without the noise.

2.2.7 Probe system

The first probe system was based on the electrical setup of NXP at IMEC in Leuven. This system employed two DC-probes with a resistor soldered to one of the needles. Although this system was initially adopted its use was found to be problematic. Figure 2.8 shows how the two probe system is used. Both probes are connected by an XYZ manipulator located on either side (not shown). The probes are landed on the bond pads with the help of a microscope. Although the probe needles are intended for accurate current measurements it was found that they also could be used in this setup.

To transmit high frequency pulses without distortion, reflections need to be avoided. This was solved by running an accompanied ground signal line from the one probe to the other (Fig. 2.8). However, when the ground wire was made small, the two probes became mechanically connected. When one probe is moved the other probe also tends to move in the same direction. A larger less rigid wire solves this but will lead to distortion of the pulses. Furthermore a large ground wire will present a big inductive loop (Fig. 2.8) that works as an antennae picking up unwanted RF noise.

The problem of the inductive loop was solved by incorporating the ground connection between the probes into the design. The ground was connected by a small spring on the leftmost probe that needed to be landed on a pad on the left probe (Fig. 2.9). However, this created even more problems with manipulating the probes as the two probed needed to be connected firmly.

Finally the two probe system was completely abandoned and a dedicated single probe was ordered that connects to both bond pads at the same time. This solves the problem of the ground loops (Fig. 2.8) and allows for a very sturdy mechanical connection to the cell. A design was made for a dual probe system with built in RF reed relays (not to be confused with the much larger RF relay shown in Fig. 2.7). The probe needle system had space for three reed relays (Meder CRF05). All three reed relays are connected in series to the cell. Two of the relays are connected in parallel with either a 2.2 kΩ or a 330 kΩ resistor. By selectively opening the relays the probe system can switch between series resistances of 1.0 kΩ, 3.2 kΩ, 331 kΩ, 333 kΩ or disconnect the cell from one side.

The choice between 1.0 kΩ and 3.2 kΩ (1.0 kΩ and 2.2 kΩ in series) was added to be able to program different cell geometries: to bring a 700×340 nm^2 cell to the SET state the 1.0 kΩ was required. However, the much smaller 400×180 nm^2 cell required the 3.2 kΩ series resistor for proper SET operation. The 333 kΩ option was originally added to be able to (threshold) switch PRAM cells without crystallizing (i.e. repeat the experiments of Pirovano et al. [78]). However, due to currents associated to the ubiquitous stray capacitance of the probe system this was not possible.

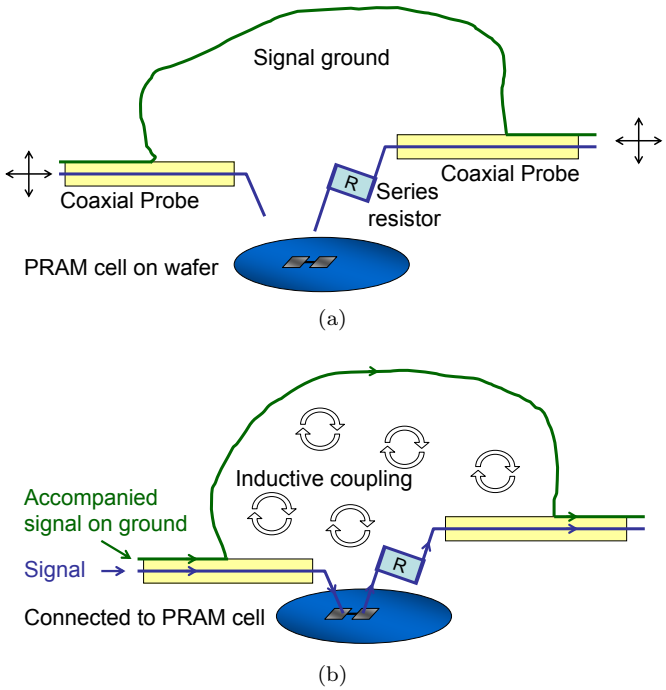

Figure 2.8: *The first probe system was based on two DC probes. One of the probes has a series resistor soldered to the output. A large signal ground wire creates an inductive loop and is able to damage the cells.*

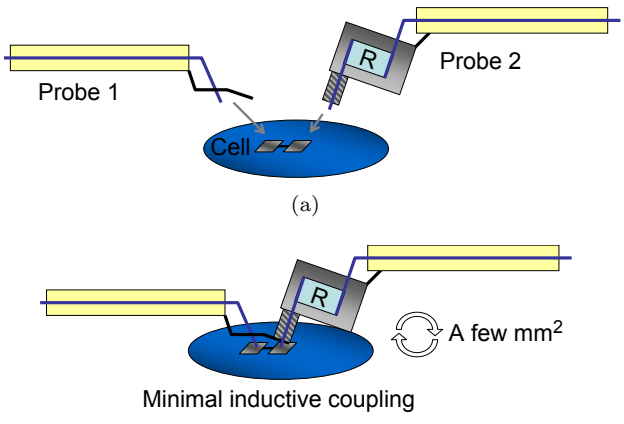

Figure 2.9: *The probe needle system was modified to avoid ground loops. The ground wire was connected when the probes were in contact with the cell.*

A dedicated switch box was designed and constructed to latch the relays without damage to the cells. Because the coil of the relay is capacitively coupled to the signal wire (the reed contact) it was feared that voltage spikes and glitches would travel to the signal wire and influence the cell.

The switch box is connected to the digital output of the source meter but has its own power supply (Fig. 2.10(b)). It is powered by an *old fashioned* transformer and a linear voltage regulator. Although much more advanced switching mode power supplies are available these are known to introduce high frequency noise to the system. The power in the switch box is first fed through an LC low pass filter to remove any possible high frequency noise from the power line or picked up by the cables. The ground of the switch box is connected by a capacitor to the signal ground of the probe system (parts shown by the green lines). This shorts high frequency noise on the coil to the signal ground which could otherwise travel to the signal wire by the 0.7 pF stray capacitance. The 100 pF capacitor shorts noise across the coil as the inductance of the coil allows high frequency noise to appear on the drive wire (black line). The digital output of the source meter is connected to an opto-coupler to break ground loops. The output of an opto-coupler drives a circuit that supplies the current to the coil. It also acts as a low pass filter for the switch pulses i.e. to remove the high frequency component.

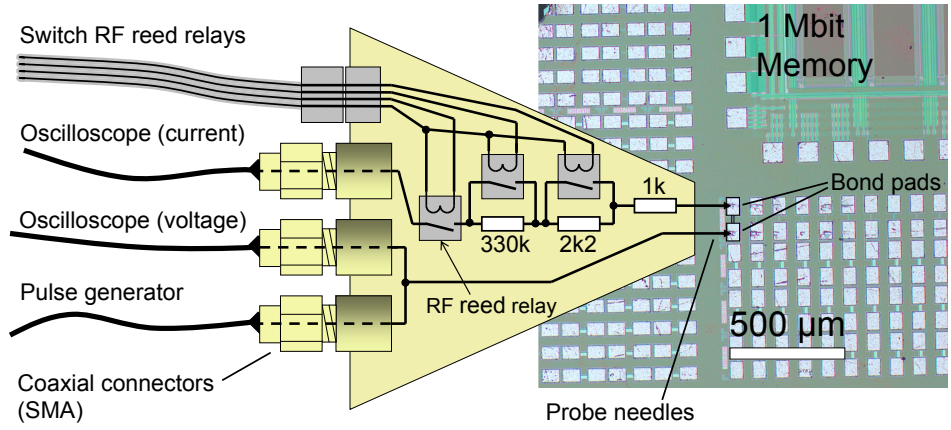

(a)

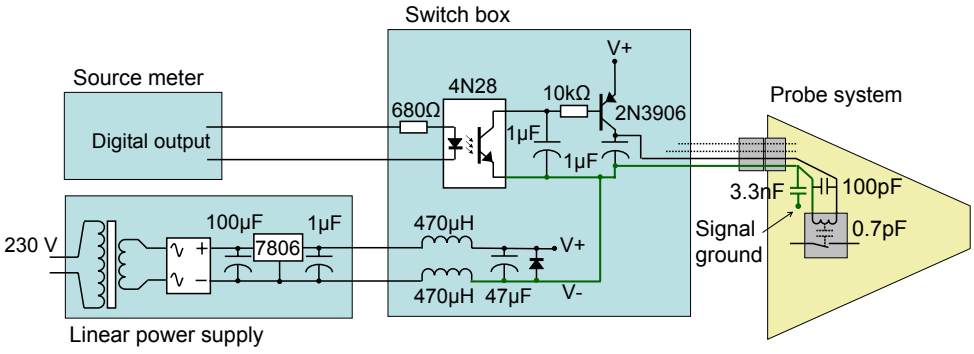

(b)

Figure 2.10: ***(a)*** *Schematic representation of the probe system connected to the bond pads of a PRAM cell. The bond pads shown are from an actual PRAM wafer.* ***(b)*** *The switch box designed for switching the RF relays. An opto-coupler and an LC-filter was used for filtering noise. Furthermore, a single 3.3 nF capacitor and a 100 pF capacitor for each reed relay was added to the probe needle system to filter any noise to the cells.*

Chapter 3

Crystallization studies of doped SbTe phase-change thin films

3.1 Abstract

A computer controlled procedure is outlined here that first determines the position of the amorphous-crystalline interface in an image. Subsequently, from a time series of these images the velocity of the crystal growth front is quantified. The procedure presented here can be useful for a wide range of applications and we apply the new approach to determine growth rates in a so-called fast-growth type phase-change material. The growth rate (without nucleation) of this material is of interest for comparison with identical material used in phase-change random access memory (PRAM) cells.

Crystal-growth rates in the amorphous phase-change layers have been measured at various temperatures using *in situ* heating in a transmission electron microscope. Doped SbTe films (20 nm thick) were deposited on silicon nitride membranes and samples with and without without silicon oxide capping layer were studied. The activation energy for growth was found to be 3.0 eV. The samples without capping layer exhibit a nucleation rate that is an order of magnitude higher than the samples with a silicon oxide capping layer. This difference can be attributed to the partial

Published as:
J.L.M. Oosthoek, B.J. Kooi, J.T.M. De Hosson, R.A.M. Wolters, D.J.Gravesteijn, and K. Attenborough,
Microsc. Microanal. **16**, 291 (2010).

oxidation of the phase-change layer in air. However, the growth rates of the samples with and without capping are quite comparable.

3.2 Introduction

A quantitative analysis of growth phenomena in a series of images is of importance for a wide range of fundamentally oriented and application driven studies. For example crystal growth in amorphous films is the rate-limiting step in rewritable data storage based on phase-change materials [99]. These materials have been successfully applied in rewritable optical recording based on the well-known CD, DVD [89] and Blu-Ray Disk [18] formats. Currently, phase-change materials are extensively tested as the storage element in nonvolatile solid-state electrical memory generally called phase-change random access memory (PRAM). PRAM is one of the most promising candidates to replace Flash memory in the near future [3, 10, 11, 21, 50, 52].

Flash memory is nowadays the technology for nonvolatile memory applications. Even though Flash memory exceeded the expectations that were foreseen in the past, it is expected that further down-scaling is no longer possible [21, 52]. PRAM on the other hand is scalable using the next generations of lithography, requires less lithographic steps, has a higher (over)writing speed and uses less program energy [3, 10, 11, 21, 50, 52].

PRAM is based on a large, i.e. typically three orders of magnitude, difference in electrical resistivity between the amorphous and crystalline phase. A nano-sized resistor made from phase-change material is brought to the amorphous state by a short high energy RESET pulse. During the pulse the material melts. Because the material cools rapidly after the pulse, it is quenched into the high resistance amorphous state. A longer and lower energy SET pulse, still in the sub micro second range, heats the resistor to a temperature above the glass transition temperature but below the melting temperature. During this pulse crystals nucleate and grow until the cell is fully crystallized to a low resistance state. The amorphous state is metastable and therefore undesired spontaneous crystal growth and nucleation can occur at any temperature (below the melting temperature). However, because these processes are thermally activated only the high operating temperatures (typically above 80 °C) limit memory retention times (i.e. how long the amorphous state is stable at a certain temperature). The process of memory retention and cell degradation upon cycling in phase-change line-cells is not yet fully understood [52]. In this chapter the crystallization of blanket-films is being investigated as viable comparison with (the retention behavior of) the identical material employed in these line cells.

Generally, the process of crystallization can be separated into two different physical phenomena: nucleation and growth [88, 106]. The phase-change material studied here is a so-called fast-growth type material. Probably more appropriate would be to call it a slow-nucleation type material. However, in many applications nucleation is not required or even undesirable and therefore these materials can be exploited in high-speed and high-density storage applications such as Blu-ray rewritable disks [6, 19, 20, 38, 51, 70], where the amorphous marks are relatively small. Also the PRAM

cells already have a crystalline area at the boundary of the amorphous mark from which crystallization can progress. Therefore, when PRAM cells are produced from a fast-growth material the crystallization in this material can be fast and in principle only depends on growth (nucleation does not occur) [52, 60].

Although this study is based on phase-change blanket layers, the crystal growth rate (i.e. without nucleation) of this material is of interest for a comparison with (the retention behavior of) identical material and layer thickness used in PRAM cells of the line-cell geometry [9, 16]. A new procedure and algorithm are presented in this study that provide direct measurements of the pure crystal growth rate without having problems associated with variable growth directions, variable boundary shapes or new nucleation events.

In the past we have extensively employed *in situ* heating in a TEM to determine the crystal growth rates (and to a lesser extent nucleation rates) in various types of phase-change materials [42, 44, 74]. The growth rates were obtained from a sequence of TEM images recorded at constant temperature as a function of crystallization time. In order to derive these growth rates, the positions of the crystallization fronts in such a sequence were determined visually. This weak point of visual judgment has been removed in our present analysis, and all analysis is automated. Therefore, the present work presents a major improvement with respect to earlier published results of the crystal growth analysis in phase change thin films [33, 42, 44, 64, 74, 76, 81, 88]. Moreover, the procedures we present here are of importance for a wide range of applications, where the growth rate has to be analyzed quantitatively from a series of images.

3.3 Materials and methods

Fast-growth doped SbTe thin films with a thickness of 20 nm were deposited using DC magnetron sputtering on commercially available 25 nm thick silicon nitride TEM windows. On top of each phase-change film a 20 nm or 50 nm thick silicon oxide layer was deposited by RF magnetron sputtering. Such an oxide layer is essential for protective purposes as we will show below, but also allows a closer comparison with the line cells where the phase change line is surrounded by the identical oxide. For comparison also phase-change films without oxide capping layer have been investigated.

Samples were isothermally annealed at 160 °C, 165 °C, 170 °C and 175 °C by *in situ* heating in a Transmission Electron Microscope (JEOL 2010F operating at 200 kV). The highest temperature is limited by the requirement that crystal nucleation should not occur during heating, but only after stabilization at the desired annealing temperature. The lowest temperature is limited by the nucleation time, which has to be sufficiently small (within hours) for a practical measurement. TEM images were taken at regular intervals after nucleation had taken place. For each temperature a complete series typically consisting of 30 images was taken. Figure 3.1 shows a selection of images from one series.

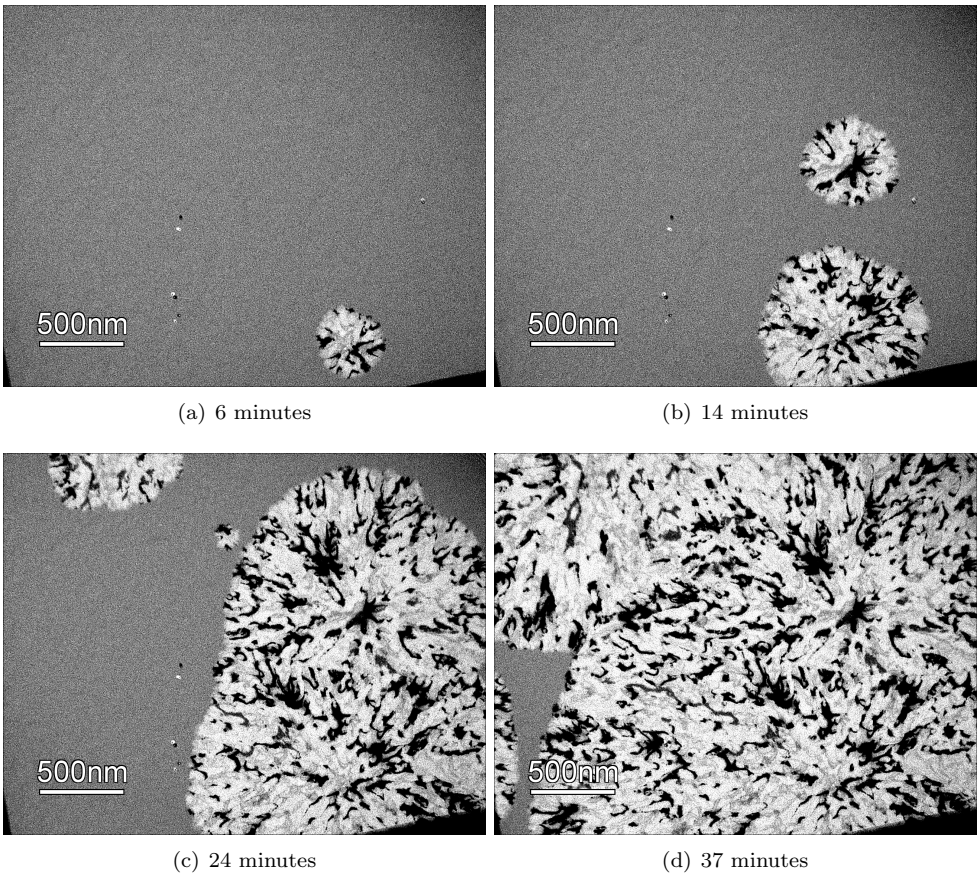

(a) 6 minutes (b) 14 minutes

(c) 24 minutes (d) 37 minutes

Figure 3.1: *Plan view bright-field TEM images of a 20 nm thick, initially amorphous doped SbTe phase change film (between 25 nm Silicon nitride and 50 nm silicon oxide layers) taken 6, 14, 24 and 37 minutes after reaching 165 °C.*

The temperature of the TEM sample holder was accurately controlled with a Gatan model 901 SmartSet Hot Stage Controller. It employs a PID controller which allows accurate control of the temperature within ± 0.5 °C. A desired final temperature can be reached with a fast ramp rate without overshoot. The temperature of the area that is imaged within the TEM is generally lower than the temperature of the furnace in the holder. This is because the sample consists of a very thin sheet surrounded by a vacuum. All the thermal energy has to be conducted through the sheet itself. Therefore all measurements were performed on an area nearest to the edge of the silicon nitride window (i.e. as close as possible to the thick Si wafer). This can be seen in Fig. 3.1(a) where the silicon substrate shows up as dark corners (bottom left and right). Moreover the edge of the window could be used to correct for image drift during heating caused by thermal expansion of the TEM sample holder.

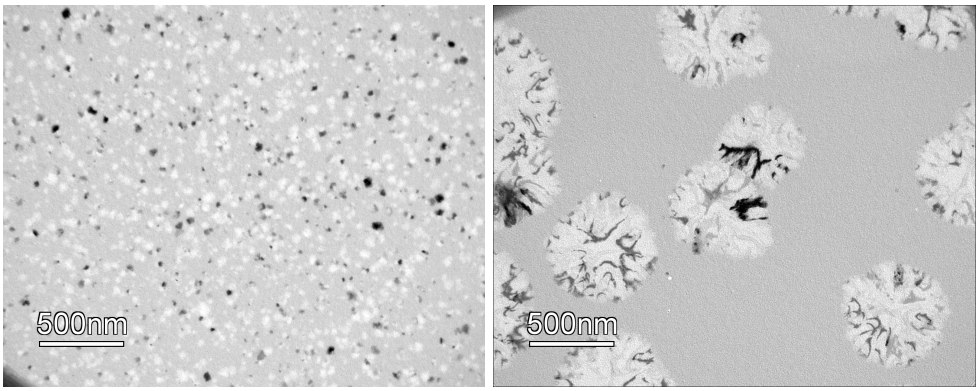

(a) (b)

Figure 3.2: *Plan view bright-field TEM images of 20 nm thick doped SbTe phase change films partially crystallized at 160 °C.* ***a.*** *Phase-change film without capping layer.* ***b.*** *Phase-change film capped with 50 nm thick silicon oxide. Note the much higher nucleation density in case the capping layer is absent.*

3.4 Results and discussion

Typical examples of TEM images recorded during the *in situ* heating at 165 °C are shown in Fig. 3.1. Crystals can be observed readily, because they are imaged both clearly brighter and darker than the surrounding amorphous phase. This black and white contrast of the crystals is peculiar and it is caused by the transrotational nature of the crystal structure [41, 42]. Previous crystallization studies on similar fast growth materials were performed without a capping layer [42, 43]. During crystallization the phase-change material shrinks slightly because of the difference in density between the amorphous and the crystalline phase. The amorphous layers of the samples have a free surface where bending can occur [42]. The combined action of densification with movement of the crystallization front results in bending of the crystal lattice planes. These crystals tend to have a regular (often three fold symmetrical) bending shape. The amorphous phase-change layer in the present study is sandwiched between a silicon oxide and silicon nitride layer. A free surface is therefore absent. Bending in this situation is constrained and it explains the more random black and white contrast associated with the transrotational crystal structure.

The importance of the silicon oxide capping layer is shown in Fig. 3.2, where Figures 3.2(a) and 3.2(b) show phase-change films, partially crystallized at 160 °C, with and without capping layer, respectively. The annealing experiment/crystallization took place about two weeks after deposition and keeping the samples in air. The crystallization of the phase change film without capping proceeds much faster, because of the shorter incubation times for nucleation and a much higher nucleation rate and thus nucleation density (as the growth rate is not strongly influenced). Partial (surface) oxidation of the phase change film can be held responsible for the increased

nucleation rate and the reduction in crystallization temperature. Similar results we observed for $Ge_2Sb_2Te_5$ films [43].

Although TEM images represent two-dimensional projections of a three-dimensional structure, the present analysis can be purely 2D, because the crystallites to be analyzed have sizes that are much larger than the 20 nm thickness of the phase-change film. In order to determine the crystal growth rate(s) at a certain temperature it is first required to quantify the position of the interface between the amorphous and crystalline phase. The procedure to do this is explained in the next section.

3.4.1 Image filtering: detecting the amorphous-crystalline interface

Figure 3.1 illustrates that geometrical information can only be used at an early stage of crystallization. Crystals nucleate at random locations and merge with one another to form odd crystal shapes with no well-defined centers or radii and where after merging the crystal boundaries cannot be detected anymore. Still, the movement of the crystal boundary with time is a direct measurement of the growth rate. To quantify this movement, the location of the amorphous-crystalline interface has to be obtained from the image.

Figure 3.3(a) shows the histograms (number of pixels with a certain grey level versus the grey level) pertaining to the amorphous and crystalline phases present in an image. The amorphous phase is represented by a bell-shaped peak (red solid line), whereas the crystalline phase corresponds to a histogram that extends its pixel levels over a much larger range including the one for the amorphous phase (blue dashed line). Therefore regions in the crystalline area exist with the same pixel level as found in the amorphous phase. Also the image has a considerable amount of noise. A simple threshold operation to separate the two phases apparently does not work. As a solution, a seven step filter procedure was designed that turns out to yield excellent results in producing the exact position of the crystal-growth front. The seven steps are summarized in the following:

1. The crystalline phase consists of areas being both brighter and darker than the amorphous phase; see Fig. 3.4(a) showing a part of an original (as-recorded) image. Therefore, the bright and dark grey level values have to be unified: in this step all amorphous regions become dark and all crystalline regions become bright. This is done by taking for each pixel the absolute value with respect to the average amorphous pixel value. The average pixel value of the amorphous area is obtained from the original image. This is simply done by selecting an area that is known to be amorphous and determining the grey value associated with the peak maximum in the histogram of the amorphous phase (from Fig. 3.3(a) a value of 925 was obtained). When the settings of the TEM are not changed during a single measurement this value stays constant for all images in the series and does not have to be obtained for each image separately. The bright and dark grey levels are turned into a bright "color". The grey levels of the amorphous phase are turned into a dark "color". The resulting image is shown in Fig. 3.4(b) and the resulting histograms for the amorphous and

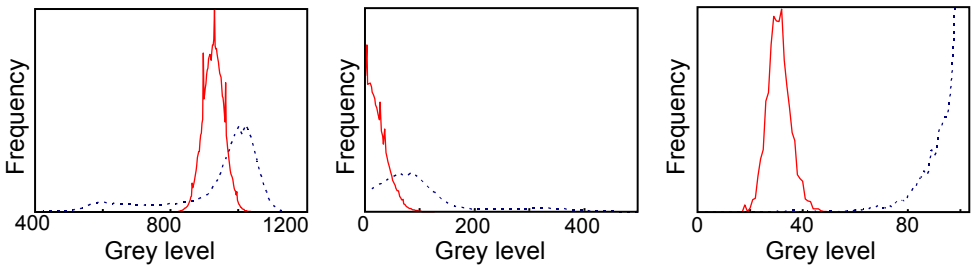

(a) (b) (c)

Figure 3.3: *Each figure shows a histogram of the amorphous phase (solid red line) and crystalline phase (dashed blue line).* ***a.*** *Original image. The two histograms overlap.* ***b.*** *After filter step 1 (see main article text for details). The two histograms still overlap considerably. The crystalline phase has a few isolated bright spots which are removed in step 2 (not shown).* ***c.*** *After filter step 3: the MLV filter has led to a complete separation of the two histograms.*

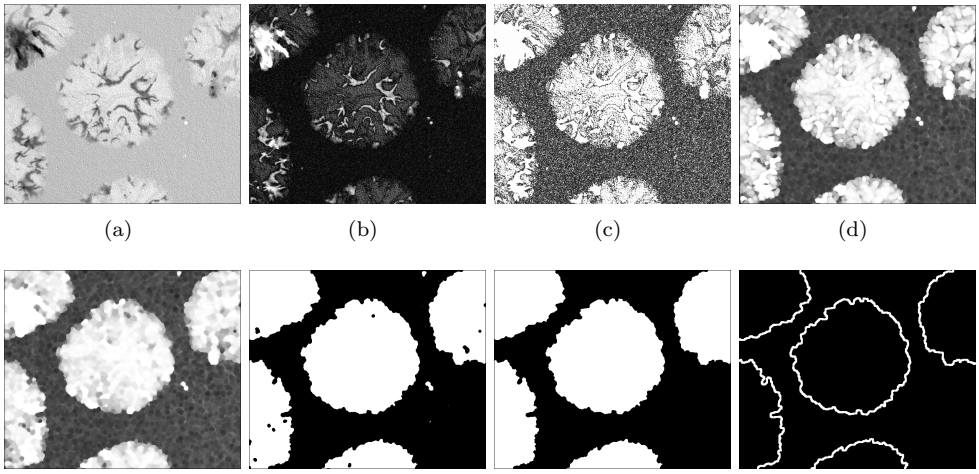

(a) (b) (c) (d)

(e) (f) (g) (h)

Figure 3.4: *Series of images that show the evolution of the filter process.* ***a.*** *Subsection of an original image before filtering.* ***b.*** *to* ***h.*** *Images after the filter steps 1 to 7 (explained in detail in the main text of this article), respectively.*

crystalline phases after this "contrast-flip" operation are shown in Fig. 3.3(b) again as a solid line and a dashed line, respectively. Although this "contrast-flip" operation largely normalizes the original bright and dark areas of the crystalline phase into bright areas, it will also create dark(er) "ribbons" at the transition between these black and a white areas in the original image. An important step is thus to remove these ribbons later; see step 4.

2. There is still unnecessary contrast in the crystalline phase after step 1. Very bright spots can be seen in Fig. 3.4(b) where a dark (almost black) spot was in the original image. The crystalline phase is made more uniform by setting a maximum pixel value. A value is chosen that is just above the highest value of the amorphous phase (in this case a value of 100). Pixels that exceed 100 will be set to 100. The resulting image is shown in Fig. 3.4(c). Although the crystalline phase is more or less uniform considerable noise is still present.

3. Applying a threshold operation after step 2 will result in a very poor quality image and therefore image noise has to be reduced. This is done with the so-called *Mean of Least Variance filter* (MLV filter) which was published by Schulze and Pearce [90]. The MLV filter enhances the image quality by smoothing homogeneous regions without blurring the edges; see Fig. 3.4(d). After application of the MLV filter the histogram shows that the crystalline phase and amorphous phase now have their own well separated peak; see Fig. 3.3(c). The structuring element used in the MLV filter [90] was circular with a typical diameter of 8 pixels.

4. Still dark regions (the ribbons, see step 1) exist in the crystalline phase where in the original image a dark area and a bright area met. These regions are further reduced by a morphological *close* operation (subsequent *dilation* and *erode* operation) which are operations in Matlab. The same structuring element that was used for the MLV operation was also used for the close operation. The resulting image Fig. 3.4(e) a large contrast exists between the amorphous and crystalline phase.

5. After step 4 a standard *threshold* operation outputs a 1 for each pixel value above a certain chosen threshold and a 0 for each value equal or below.

6. The resulting binary (black and white) image Fig. 3.4(f) still has a few isolated spots. These spots are caused by noise, imperfections in the sample or spots associated with the CCD camera. At this stage an operation *removes spots* that are smaller than a certain amount of pixels. The resulting image is shown in Fig. 3.4(g).

7. A final operation creates a growth front image. This operation outputs a white pixel at a location where a white pixel is next to a black pixel and a black pixel anywhere else. Such an image has a line where the black and white areas in the previous image meet. See the image shown in Fig. 3.4(h), where the line is made thicker for clarity.

3.4.2 Image processing: quantifying the growth speed

A complete time series of TEM images is converted into binary growth front images with the procedure delineated in the previous section. The pixel values of each growth-front image are multiplied with the value of the time (in seconds) that the image was taken. Only the growth front (line) has this time value and the rest of the image is

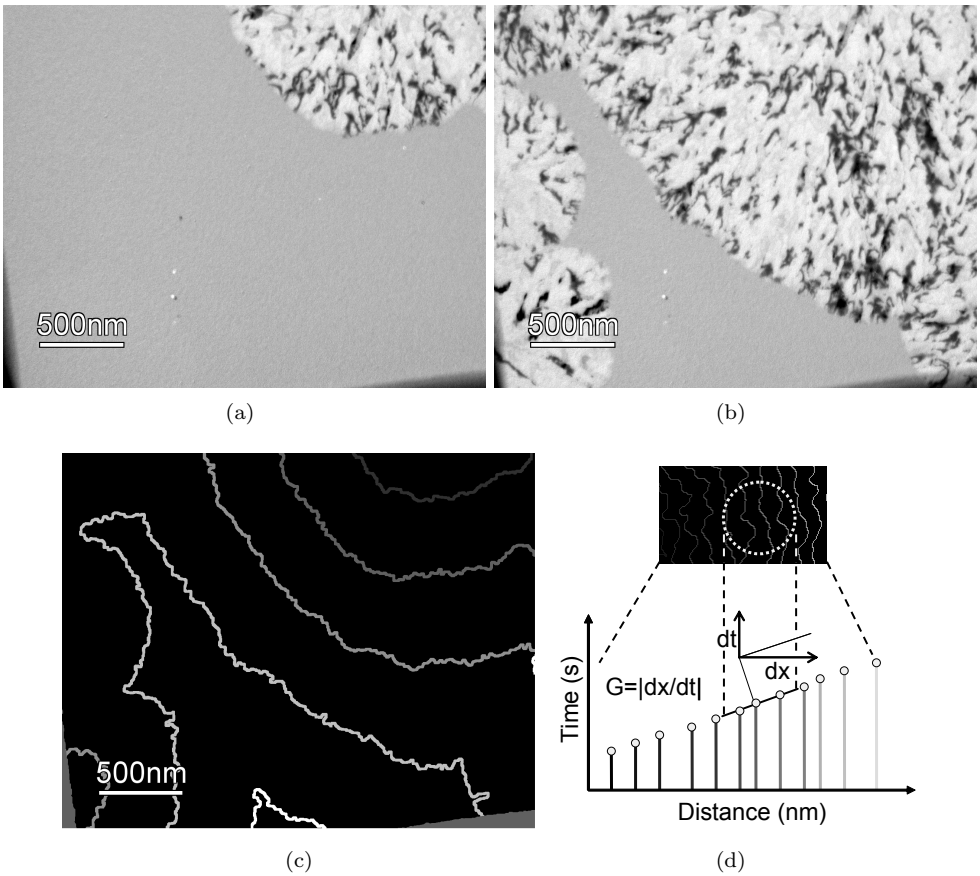

(a) (b)

(c) (d)

Figure 3.5: *Determination of growth rate from a series of TEM images. A sample was annealed at 170 °C and an image was taken every 30 seconds.*
a. *TEM image taken 8.5 minutes after reaching 170 °C.*
b. *TEM image taken exactly 10 minutes after (a)*
c. *Figure showing the growth fronts of the series for 5 minute intervals (where each minute a TEM image was recorded). The lines are made thicker for visibility.*
d. *Schematic representation of the determination of the growth rate from the growth fronts. At each position a surface is fit to the grey (non-zero) points that are on a growth front and are located within a circle centered at that position. From the spatial components (a and b) of the surface ($ax+by+t=c$) the growth rate is calculated: $G(nm/s) = \Delta D(nm/pixel)/\sqrt{a^2+b^2}$.*

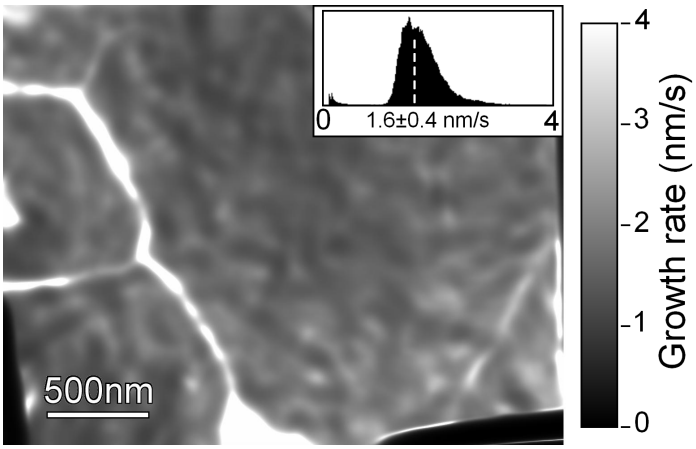

Figure 3.6: *From the complete set of TEM images the growth rate is calculated for each position. The inset shows a histogram of the value of the growth rate. A growth rate of 1.6 ± 0.4 nm/s was obtained (based on FWHM).*

equal to zero. Then, all these images in the series are summed to create a single final image that contains all essential information for determination of the crystal growth rate. In this single "growth front - time" image each growth front is represented as a line with a pixel value equal to the time (in seconds) that the image was taken. This is shown schematically in Figures 3.5(a) - 3.5(c), where for reasons of visibility only a small selection of the total number of TEM images was taken to create larger steps in time (see Fig. 3.5(c)). The brighter the line the later in time the original image was taken. At each position in the time image a statistically averaged value of the slope is found by fitting a surface to that position and all points around it with a distance less than or equal to r pixels (see Fig. 3.5(d)). Only the pixels that are on a growth front are used for the fit, the black pixels (value of zero) are omitted. This last point is important for obtaining accurate results. The radius r is chosen such that the circle contains several growth boundaries. The spatial components a and b of the fitted surface $ax + by + t = c$ have the units time per pixel and represent the inverse growth rate and direction. The average growth rate $G(\mathrm{nm/s})$ is obtained from the spatial components a and b and has the value: $G = \Delta D/\sqrt{a^2 + b^2}$ Where ΔD is the physical size in nm of a pixel. The final result presenting the growth rate is shown in Fig. 3.5(d).

Our procedure is very useful to determine the evolution of growth rate with time or crystal size (or growth-front curvature). However, our analysis shows that the crystal growth rate in our present phase-change system does not depend on time and therefore the grey level in Fig. 3.6 is relatively uniform (except for the boundaries where the growing crystals coalesce, because there a singularity occurs in the computer controlled determination of the growth rate).

Many traditional methods for quantifying the kinetics of phase transformations rely on the determination of the total transformed volume or area fraction as a func-

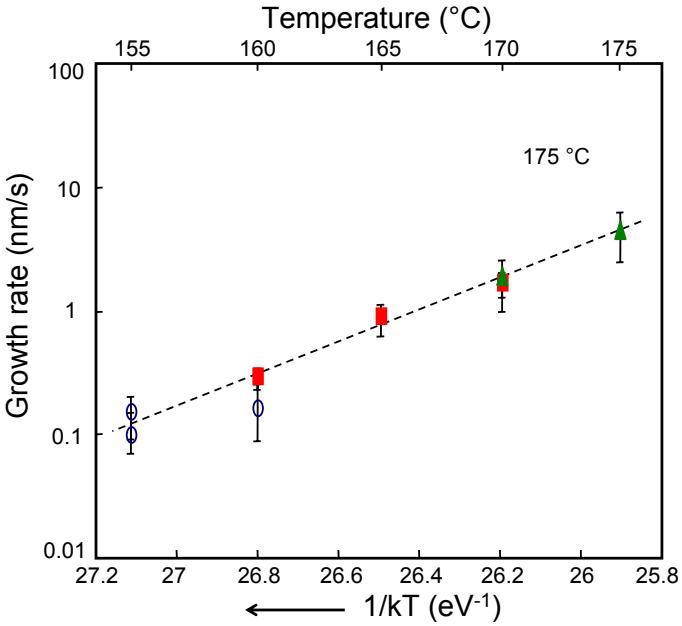

Figure 3.7: *Arrhenius plot showing the growth rate of the samples with silicon oxide capping layer (green triangles: 20 nm, red squares: 50 nm) and without (blue circles) capping layer. The dashed line is a fit to the triangular and square data points only. Extrapolation to 155 °C shows that growth rate of the samples without capping layer is the same as the growth rate of the samples with capping layer.*

tion of time. If the area fraction is based on an image where the boundary between the two phases has to be assessed, the detected boundary can be found at an offset from the location of the actual boundary. This offset will depend on the applied filter method and sensitivity. The higher the ratio between boundary length and surface area (the smaller the crystals) the larger the error due to an offset will be. The total transformed area will therefore depend on the size of the crystallite and the filter method and its evolution and is thus susceptible for having a relatively large systematic error.

The method proposed here is only sensitive to the movement of the boundary. A fixed offset that is shared by two boundaries will not show up in the time image because it is based on the slope (derivative). Also, the method proposed here allows for a spatial and time dependent measurement of the growth rate. Even a non-linear growth rate (time dependent growth rate) can in principle be quantified. This makes the procedures delineated in the chapter of importance for a wide range of applications analyzing an evolution rate in a series of images. Particularly applications where one entity is growing at the expense of another entity and where the grey levels in the image of the two one entities are (partially) overlapping.

3.4.3 Growth rate as a function of temperature

Samples with an oxide capping layer were annealed *in situ* in the TEM at 160 °C, 165 °C, 170 °C and 175 °C. For each data point a new sample was used. The closed red data points represent samples with a 50 nm silicon oxide capping layer and for the closed green data points the capping layer was 20 nm. After nucleation had occurred a series of images was recorded at constant time intervals until the area was crystallized. It was found that only the area that had been irradiated by the electron beam was completely crystallized. Crystals did appear in the area outside the irradiated area but these were smaller. These results indicate that the electron beam of the TEM increases the nucleation rate (decreases incubation time for nucleation) and maybe also increases the growth rate. The average growth rate of the oxide capped samples, as obtained from the images with the procedures described in the previous two sections, is show versus the reciprocal temperature in Fig. 3.7 (closed red and green squares). No difference in growth was found between the samples capped with 20 nm and 50 nm silicon oxide. Assuming an Arrhenius type dependence of the growth rate on temperature, an activation energy of 3.0 ± 0.1 eV is determined from fitting the data.

Samples without capping layer were also annealed *in situ* in the TEM at 155 °C and 160 °C. The growth rates measured for these samples at these temperatures are shown in Fig. 3.7 as open blue circles. These samples had been kept in air for two weeks prior to the measurements. The amount of nuclei per unit area counted after complete crystallization of the imaged area was at least an order of magnitude larger than the amount found in the previous cases with oxide capping layer (cf. Fig. 3.2). Apparently exposing the phase-change film to air greatly increases the nucleation rate. This can be attributed to partial oxidation of the phase-change layer which apparently forms starting points for nucleation and thus lowers the activation energy barrier required for nucleation.

Because of the large amount of nuclei present in the samples without oxide capping layer, the distance a crystalline mark can grow before it meets another mark is much smaller. This also makes the measurement of the growth rate more susceptible to drift of the image. These variations of the location of the crystalline mark will not influence the average of the growth rate because the crystals grow outwards in all directions. Still, the error bar of the growth rate of these samples is definitely larger (open circles). However, the present results still clearly show that despite the large differences in the nucleation rate, the growth rate of the samples with and without oxide capping layer are nearly the same. To confirm the influence of the electron beam on the growth rate a measurement at a (2.5×) higher magnification was performed, i.e. irradiation occurs with a (6.25×) higher current density. This measurement was performed on a sample without oxide capping layer at 155 °C on an area that was not previously exposed to the electron beam, but the sample itself was already annealed for 30 min. at 155 °C. The region that was not irradiated was still largely amorphous with only a few nuclei. In this second measurement nucleation had thus been taken place without the presence of the electron beam. The average growth rate is slightly (but in principle not significantly) larger than average growth rate

of the previous measurement that had been nucleated in presence of the electron beam. This result seems to indicate that the growth rate is not strongly increased by electron irradiation and that the previously mentioned difference between overall crystallization rate can largely be attributed to an increased nucleation rate in the electron beam exposed area. However, we also observed that the growth rate in previously thermally annealed areas is slightly but significantly lower than in areas that are during thermal annealing from the beginning also continuously irradiated by the electron beam. Therefore, the increased growth rate due to an increased electron beam current density was compensated by a decreased growth rate due to a previous thermal anneal (without electron beam exposure) .

3.5 Conclusions

An image filter procedure (algorithm) has been presented in this study that allows the discrimination (threshold) between two entities (e.g. phases) where the grey levels in the image of one entity are overlapping with the ones of the other entity. Subsequently, an image processing procedure has been presented that allows the determination of the evolution rate in a series of images, where one entity is growing at the expense of another entity. This procedure directly quantifies the pure growth rate without being affected by factors like varying growth directions, varying boundary shapes during growth or new nucleation events. The procedures were particularly developed to analyze the crystal growth rate in initially amorphous phase-change thin films. The growth rates were obtained from a sequence of TEM images recorded at constant temperature as a function of crystallization time. The present work presents a major improvement with respect to results published earlier on crystal growth rates in phase-change films, were the position of the growth front was based on visual judgment.

To exemplify details of the procedure blanket doped SbTe films (20 nm thick) deposited on silicon nitride membranes and capped with 20 nm or 50 nm silicon oxide were isothermally heated inside a TEM. The activation energy for pure growth was found to be 3.0 eV (assuming an Arrhenius type dependence of growth rate on temperature). It was found that the samples without any capping layer had an order of magnitude higher nucleation rate than the samples with silicon oxide capping layer. This difference can be attributed to the partial oxidation of the phase-change layer in air. However, interestingly the growth rates of the samples with and without capping layers were comparable.

Chapter 4

Memory retention of PRAM line cells

4.1 Abstract

Crystal growth rates in FIB processed phase-change random access memory (PRAM) line cell were measured at various temperatures using in-situ heating in a transmission electron microscope. The results were compared to the crystal growth rates and activation energy of amorphous fast growth phase-change layers of identical composition as the PRAM cells presented in Chapter 3. The activation energy related to the retention times and crystal growth rate of the PRAM line cells as measured by in-situ heating and electrical characterization in a probe station was found to be 2.7 eV. This value is comparable to the activation energy for growth in the blanket films as measured by in-situ TEM which was found to be 3.0 eV. More interestingly the equivalent retention times calculated for the blanket layers are much higher than the retention times observed for the PRAM line cells; a shift of about 25 °C occurs.

4.2 Introduction

The amorphous phase is meta-stable by nature: over time the cell returns to the crystalline phase (SET state) by spontaneous crystal growth and nucleation of the

---

Adapted from:
J. Oosthoek, B. J. Kooi, J.T.M. De Hosson, D. Gravesteijn, K. Attenborough, R. Wolters, and M. Verheijen, "Crystallization studies of doped SbTe phase-change thin films and PRAM line cells: Growth rate determination by automated TEM image analysis,"
Proc. E/PCOS Symp. p. 140 (2009).

phase-change material. This is by all means an undesirable effect and is related to the data retention time, i.e. the time it takes for cell in the RESET state to return to the SET state at a certain temperature. These processes, like most phase transformations, are thermally activated, because the underlying physical phenomena such as atomic jump frequencies, viscosity, diffusion, nucleation and growth are thermally activated. [80] This thermal activation is generally considered to be of Arrhenius type which allows for extrapolation of measurements of data retention at elevated temperatures to the (much lower) maximum operating temperature of a memory.

In this chapter a comparison of the data retention at elevated temperatures was made between phase-change blanket layers (see Chapter 3) and PRAM line cells. This type of analysis is important, as a lot of research in the field of phase-change materials (PCMs) is performed on as-deposited films and considered representative for PCMs in memory applications. However, blanket films are only confined in one nano-scale dimension (thickness), whereas PCMs in PRAM are confined in three nano-scale dimensions. Moreover, in applications the amorphous phase is obtained by melt-quenching and the corresponding structure differs from the one of the as-deposited amorphous phase in blanket films. In the present chapter research is performed to determine whether these factors influence data retention.

Phase-change blanket films and PRAM line cells were annealed in a transmission electron microscope (TEM). During annealing a series of images was taken at constant time intervals. The procedure and algorithm outlined in Section 3.4 was used and provided a direct measurement of the pure crystal growth rate without having problems associated with variable growth directions, variable boundary shapes or new nucleation events. Based on the growth rates measured on the basis of these TEM images equivalent data retention times were determined which were then compared to direct electrical measurements of data retention times in PRAM line cells performed with a probe station.

4.3 Experimental

PRAM cells with a length of 700 nm and a width of 300 nm were brought to the amorphous state in the electrical characterization setup (Section 2.2). The temperature was raised with the heating stage and kept constant. The time it takes for crystal growth fronts to meet, i.e. allowing a conductive crystalline path through the cell, is known as the retention time. Generally, the resistance dropped rapidly from around 100 kΩ) to below 10 kΩ) indicating that a conductive path was formed (see Fig. 4.2(b)). The cell was assumed to be crystallized when the resistance dropped below 10 kΩ). Although this value is arbitrary, the sharp drop in resistance meant that the results are insensitive to the exact value chosen and that it accurately determines when crystallization occurs. After the cell is crystallized it can be brought to the amorphous state again and the annealing experiment is repeated at a different temperature. From TEM evidence (Fig. 4.1 and 4.2) the size of the amorphous mark can be estimated and the retention time can be directly related to the growth rate of the blanket layers.

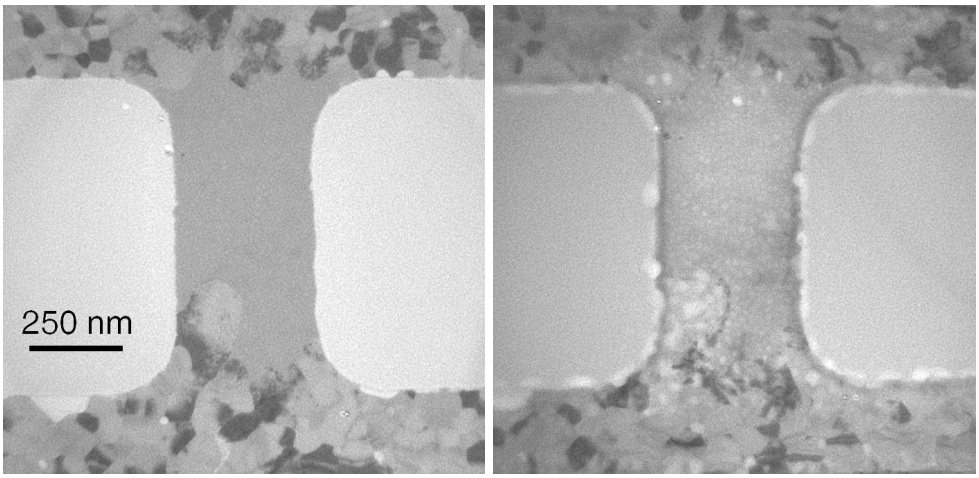

(a) (b)

Figure 4.1: ***(a)*** *TEM image of a PRAM line cell before annealing in presence of the electron beam.* ***(b)*** *Voids were introduced because of exposure to the electron beam, even though the cell was not crystallized/annealed during the exposure.*

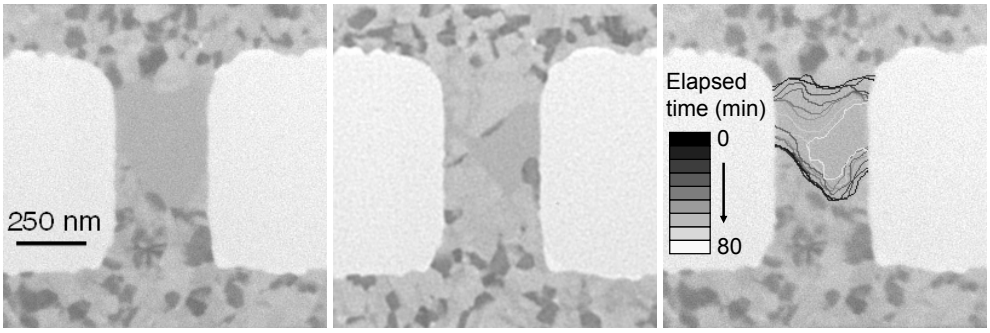

(a) (b) (c)

Figure 4.2: ***(a)*** *TEM image of a (new) PRAM line cell before annealing. The cell was not completely brought to the RESET state.* ***(b)*** *image taken after eight 10 minutes anneal steps at 129 °C. Because of electron beam damage the cell could only be imaged at room temperature.* ***(c)*** *The crystal fronts after each subsequent anneal step were superimposed on the image of Fig. 4.1(a).*

A PRAM cell in the RESET state was prepared for TEM by NXP using two main steps: a mechanical polishing step followed by cutting and lift out of a thin lamella using a focused ion beam system (FIB). In brief: the polishing step is used to create a cross-sectional surface close to the feature of interest. Subsequently, FIB trenches are ion milled in the cross section such that a lamella with dimensions of about 50 mm long, 10 mm wide and 6 mm deep with respect to the original surface is produced. This lamella is then lifted out and attached to a dedicated Mo grid giving more flexibility for subsequent precise (finally low, 100 pA current) FIB milling under various orientations to remove the substrate and covering nitride layer. Thus, a plan-view sample typically 300 nm thick containing the 15 nm PC layer sandwiched in oxide remains. In order to avoid charging and damaging of the vulnerable memory cell special precautions were necessary: Initially after cross section polishing and prior to FIB processing a thin Pt layer was deposited in a sputter coater and later also Pt strips were deposited on special locations of the lamella after lift out inside the FIB. In addition, layers that would become electrically isolated during the FIB milling procedure were first connected using conductive Pt lines to the larger Pt strip covering the sample, in order to avoid electrostatic discharges in the sample during the milling procedure. This step proved to be vital in order to keep the PRAM cells intact and in their programmed state during the FIB sample preparation procedure.

4.4 Results and Discussion

4.4.1 PRAM line cell

A PRAM test cell of size 700×380 nm^2 was brought to the amorphous RESET state in an electrical characterization setup similar to the one described in Section 2.2. The cells are produced on silicon wafers and are embedded in between several layers of silicon oxide and silicon nitride that are deposited on top of the wafer. The cell was prepared for TEM imaging by a focused ion beam setup (FIB). To prevent damage to the cell, a layer of several hundred nano-meters of SiO_2 was still surrounding the cell. This rather thick oxide layer (for TEM purposes) results in much less contrast between the crystalline and amorphous phase in the PRAM line cell compared to the blanket layers. Also, electrons from the electron beam have a much higher probability to be inelastically scattered and absorbed in the oxide. Therefore, particularly at higher (annealing) temperatures, it is most likely that the electron beam damages the sample. An example of beam damage (before and after exposure) can be seen in Fig. 4.1, respectively. In order to avoid damage as much as possible, the cell was only imaged at room temperature with a relatively defocused beam (requiring long exposure times).

A TEM image of a cell before annealing is shown in Fig. 4.2(a). The cell was not fully amorphous. Figure 4.2(b) shows the same cell but after 8 subsequent anneal steps at 129 °C in the TEM with the beam switched off. After 10 minutes of annealing the TEM holder was brought back to room temperature and an image was taken. The progression of the crystal front can be seen in figure Fig. 4.2(c) where each line represents the crystal boundary after an anneal step.

4.4.2 Comparing retention of blanket layers with PRAM cells

A 700×300 nm^2 size line cell was cycled in a probe station for at least 100 RESET+SET cycles. This step avoids any starting up effects. It was RESET at room temperature and left to drift for 1000 seconds. The resistance follows a well established power law $R_t = R_0 \cdot (t/t_0)^{\alpha}$ [78]. The amorphous resistance at 1.00 second after RESET was $R_0 = 3.8 \pm 0.5$ MΩ and a drift coefficient $\alpha = 0.077 \pm 0.002$ was found. The cell was brought to the anneal temperature and the resistance was monitored until it crystallized (cell resistance dropped below 10 kΩ). The actual crystallization is a very sharp transition as can be seen in Fig. 4.3(a). The retention time is the interval between the moment the measurement temperature was reached to the crystallization event. The retention time versus the temperature is presented as an Arrhenius plot in Fig. 4.3(b). From the data the retention time at 80 °C could be extrapolated which is 10 years. An activation energy of 2.7 eV was found for growth. The retention time of the PRAM cell prepared for TEM has been added to Fig. 4.3(b) (red square). The retention time was calculated from the growth rate obtained from the series of TEM images; cf. Fig. 4.2(c). Although more quantitative data is needed the value obtained is very comparable to the ones of the PRAM cell in the probe station, but deviates strongly from the ones of the blanket layers.

From the growth rate of the blanket layers an equivalent retention time for a 700 nm cell was calculated by assuming a uniform growth of the two crystal boundaries to the center of the cell. The retention time is the time it takes for the crystal to grow half the length of the cell (from either side till they meet in the center). The result is shown Fig. 4.3(b) by the green points. In case of pure crystal growth (without nucleation) the activation energy of the retention time can be assumed to be identical (apart from a minus sign) to the activation energy of growth.

Interestingly, the equivalent retention time of the blanket layers is significantly higher than the retention time of the PRAM cells (both the cell crystallized in the TEM as the cell crystallized in the probe station). A shift of about 25 °C occurs. This difference can be attributed to the fact that the PRAM cells have already been cycled, at least once as the CMOS processing crystallizes the cells. Therefore they are (always) melt-quenched by a RESET pulse. The blanket films on the other hand are as-deposited and are crystallized for the first time. Since the results of the retention times of the PRAM line cells measured using the probe station and the TEM are very similar it can be concluded that the observed difference between blanket films and PRAM line cells is not caused by TEM growth measurements versus electrical characterization in a probe station.

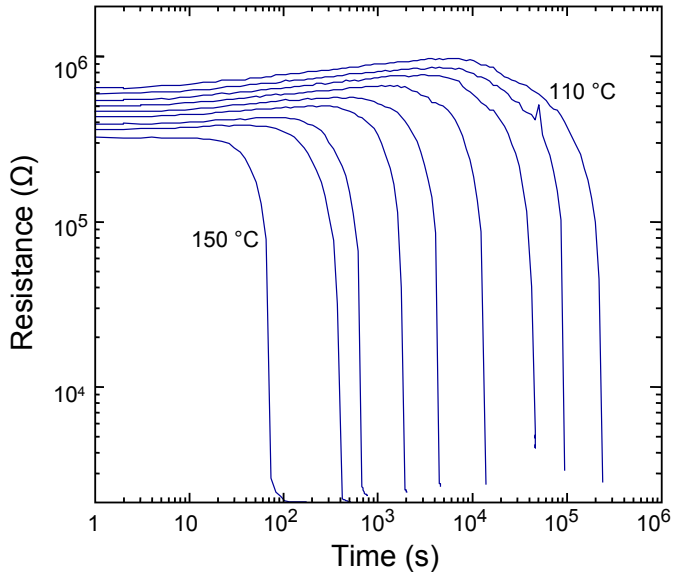

(a)

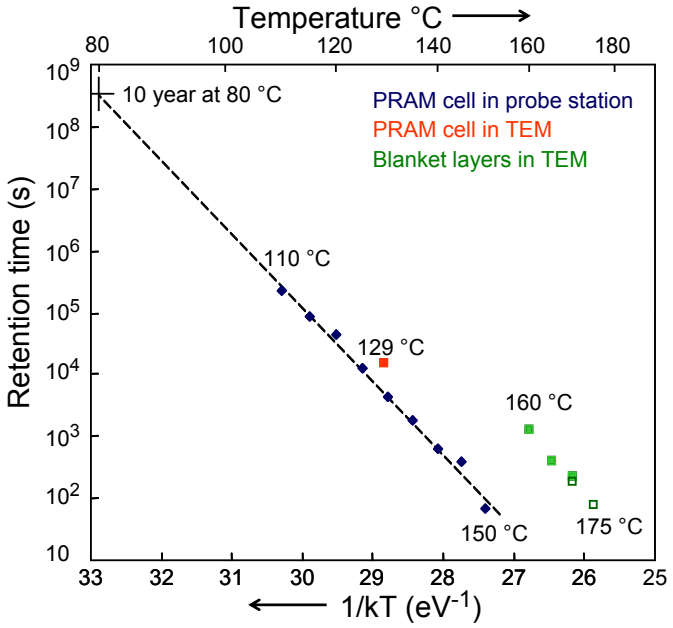

(b)

Figure 4.3: ***(a)*** *A 700×300 nm² PRAM line cell was brought to the amorphous state by a 50 ns RESET pulse (at room temperature). It was crystallized at 110 °C and the resistance was measured until the cell crystallized. This sequence was repeated for 115 °C, 120 °C etc. up to 150 °C.* ***(b)*** *The measured crystallization time versus the temperature is shown in an Arrhenius plot along with the equivalent retention time of the PRAM cell (Fig. 4.2(c)) and blanket layers crystallized in the TEM and the blanket (Section 3.4.3).*

4.5 Conclusions

The retention time of a PRAM line cell was obtained in a probe station for various temperatures in the range of 110 °C to 150 °C. From the data a retention time of 10 years at 80 °C was extrapolated. Assuming an Arrhenius type dependence, an activation energy of 2.7 eV was obtained. An equivalent retention time was calculated from the growth rate of the blanket films that were presented in Section 3.4.3 that had been crystallized in the TEM. This equivalent retention time was much higher than the retention time of PRAM cells measured in the probe station. This difference has to be attributed to the fact that the amorphous layer of the blanket films were as-deposited and the PRAM cell was melt-quenched (created by RESET pulse). This conclusion is corroborated by the observation that the retention time measured for a PRAM cell by in-situ heating in a TEM is similar to the ones measured in a probe station.

Chapter 5

Memory retention of PRAM: isothermal versus isochronal heating

5.1 Abstract

Doped SbTe phase change (PRAM) line cells produced by e-beam lithography were cycled for at least 100 million times. The memory retention of the PRAM cell was measured both isothermally and isochronally which showed excellent agreement. An activation energy for growth of 1.7 eV was found (after 100 million cycles) for both measurements. Similar isothermal and isochronal measurements were performed on PRAM cells produced by optical lithography which yielded activation energies of 3.0 eV and 3.3 eV, respectively. Our results show that the same phase-change material can show large differences in retention behavior depending on the way the cells are produced.

5.2 Introduction

Currently, in many applications so-called fast-growth type phase-change materials are employed, where the crystallization process only depends on growth and not

---

Adapted from:
J.L.M. Oosthoek, B.J. Kooi, K. Attenborough, F.A.M. Hurkx, and D.J. Gravesteijn, "Memory retention of doped SbTe phase change line cells measured isothermally and isochronally" *Mater. Res. Soc. Symp. Proc.* G14-04-H07-04 (2010).

on nucleation. One such an application is in PRAM line cells [52]. As the crystal grows from the already present crystal boundary the growth process is in principle one-dimensional. Because the crystal growth rate in PRAM line cells is not easily obtained, the retention time, i.e. stability of the amorphous mark at a fixed temperature, is measured instead. The retention time is generally inversely proportional to the growth rate.

Instead of this isothermal analysis, more convenient and popular is to perform isochronal measurements, i.e. measuring the stability of the amorphous mark with various heating rates, kept constant in time, where the temperature at which the cell crystallizes is the parameter being measured. *Only* in the 1D-growth case of the line cells, an exact relation can be derived between the retention times of the cells measured isothermally and isochronally. The activation energy can then be determined from the data by using a (first-order) approximate method known as Kissinger analysis [40]. Accurate memory retention measurements are slow, because the most significant data points are closest to operating temperatures and retention times, for example 10 years at 80°C. In contrast to isothermal measurements, isochronal measurements have the advantage that an upper limit of how long a measurement is going to take is better known a-priori.

In this chapter results are shown on cyclability, amorphous resistance drift and data retention of PRAM line cells and in particular it is demonstrated that the retention behavior as measured isochronally with the Kissinger method excellently agrees with retention behavior measured isothermally.

5.3 Theory

We start with the assumption (which can be validated experimentally) that the growth rate G follows an Arrhenius dependence:

$$G_T = G_\infty \cdot e^{-E_g/kT} \tag{5.1}$$

Then, in order to determine the activation energy, e.g. for crystal growth, the most straight-forward and accurate procedure is to determine the growth rate at various temperatures, and then to plot the logarithm of growth rate versus the reciprocal (absolute) temperature (T). The slope from a linear fit to the data is then equal to the activation energy (E_g) divided by Boltzmanns constant (k). In PRAM line cells crystal growth occurs at both amorphous-crystalline boundaries (see Chapter 4). For a line cell with an amorphous mark having a length of $2L$, the retention time τ can therefore be taken directly from Eq. 5.1 as:

$$\tau = L/G_\infty = \tau_\infty \cdot e^{E_g/kT} \tag{5.2}$$

(with $\tau_\infty = L/G_\infty$)

The activation energy for growth can be directly obtained from retention times. Then, in order to derive the isochronal case, the Arrhenius equation is integrated assuming a constant increase of temperature as a function of time: $T = \phi \cdot t$ i.e. with a constant ramp rate ϕ. The lower temperature, where the integration starts is not critical,

because only the temperatures close to the crystallization temperature (T_c) have a relevant influence on the integral. The distance dL a crystal grows at a certain time dt will be $dL = G_T \cdot dt = (G_T/\phi) \cdot dT$. The length L a crystal boundary has grown at a given temperature with a given ramp rate will thus be:

$$L = \int \frac{G_\infty}{\phi} exp\left(\frac{-E_g}{kT}\right) dT \tag{5.3}$$

The solution of this integral, running from 0 to T_c, can be represented as an infinite power series:

$$L = \frac{-G_\infty}{\phi} exp\left(\frac{-E_g}{kT_c}\right) \cdot \sum_{i=1}^{\infty} i! T_c (T_c k/ - E_g)^i \tag{5.4}$$

From the first-order approximation the usual Kissinger equation can be derived:

$$L = \frac{G_\infty}{\phi} exp\left(\frac{-E_g}{kT_c}\right) \cdot T_c^2 k/E_g \Rightarrow ln(\phi/T_c^2) = ln(kG_\infty/LE_g) - E_g/kT_c \tag{5.5}$$

By plotting $ln(\phi/T_c^2)$ versus $1/kT_c$ the slope clearly yields the value $-E_g$ which is the original Arrhenius activation energy. The intercept of $ln(\phi/T_c^2)$ versus $1/kT_c$ yields $ln(kG_\infty/LE_g)$. The Arrhenius pre-factor $\tau_\infty = L/G_\infty$ is taken from the intercept using the value of E_g from the slope. The Kissinger analysis can be extended to higher order (or more) approximations. For three orders, the activation energy E_g is obtained from the slope of $ln(\phi/(T_c^2 - 2kT_c^3/E_g + 6k^2T_c^4/E_g^2)$ versus $1/kT_c$. The fact that E_g is obtained from data points that already contain E_g is solved iteratively. The pre-factor is found similarly. It is important to notice that the Kissinger analysis *requires* that retention follows the Arrhenius behavior. If an Arrhenius type temperature dependence behavior does not occur then the Kissinger analysis does not have a physical relevance.

5.4 Experimental

5.4.1 Cyclability

Doped SbTe line cells with dimension 225×50×20 nm^3 were produced by e-beam lithography; details can be found in [28]. A cell was cycled with a series of RESET/SET pulses (see Fig. 5.1). It was shown that 100 million cycles were possible before the cell becomes stuck in the SET state; see Fig. 5.1. Typically, during the first few hundred cycles the cell does not show a constant behavior. This initialization phase can be related to residual effects from cell production: e.g. initial stresses and trapped argon atoms from sputter-deposition. The usable life span ranges over 10 millions cycles during which the resistance difference between the crystalline and amorphous state is at least 3 orders of magnitude. The end of life is characterized by a large drop in amorphous resistance until, after further cycling, the cell becomes stuck

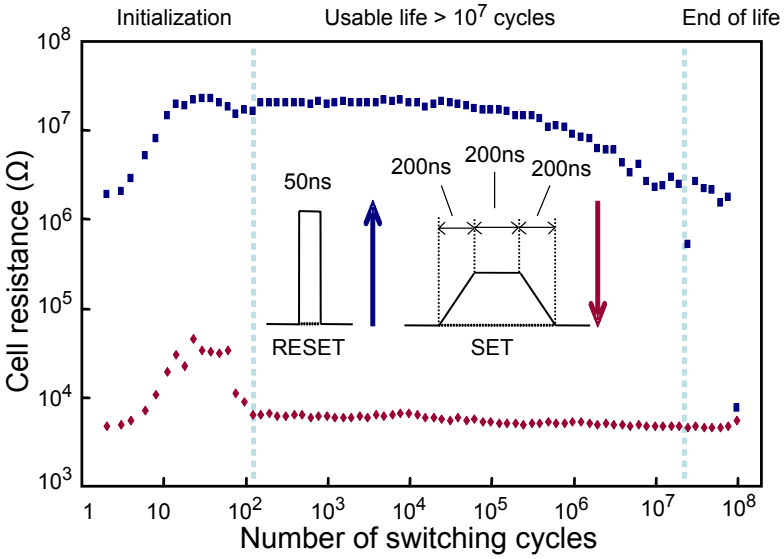

Figure 5.1: *A phase change line cell was cycled (RESET/SET) for 100 million times. RESET pulses of 1.1 mA, 50 ns pulse width with 4 ns edges and a SET pulses of 500 µA, 200 ns pulse width with 200 ns edges were used.*

in the SET state. The cell can still be brought to the RESET state but the magnitude of the switching current has to be increased. The resistance of the crystalline state also drops slightly. Although this drop is small compared to the drop in amorphous resistance, it is significant and may be related to changes in atomic (de)composition of the programmable region.

5.4.2 Resistance drift

After cycling a 100 million times, the PRAM line cell was brought to the RESET state with a 50ns/1.1mA pulse at a temperature of 25.0±0.1 °C. The resistance was measured for 1000 seconds with a source meter (at 100 mV) starting directly after the RESET pulse. Results are shown in the inset of Fig. 5.2(a). The resistance drift as a function of time follows a well known power law $R = R_1 \cdot t^{\alpha}$ where R_1 is the resistance at one second after RESET and α is a power law exponent [78]; see the inset in Fig. 5.2(a). A value of $(50\pm5)\cdot10^{-3}$ was found for α, which is comparable to a value of 0.06 found earlier [78]. After this drift period either an isothermal or isochronal retention experiment was started. The temperature was measured with a thermocouple located very close to the cell and kept stable with a PID controller connected to a linear power supply and heating filament. After the cell was crystallized during the experiment it was brought back to 25.0 °C and the whole sequence of RESET, drift was repeated and a new isothermal or isochronal retention experiment was started.

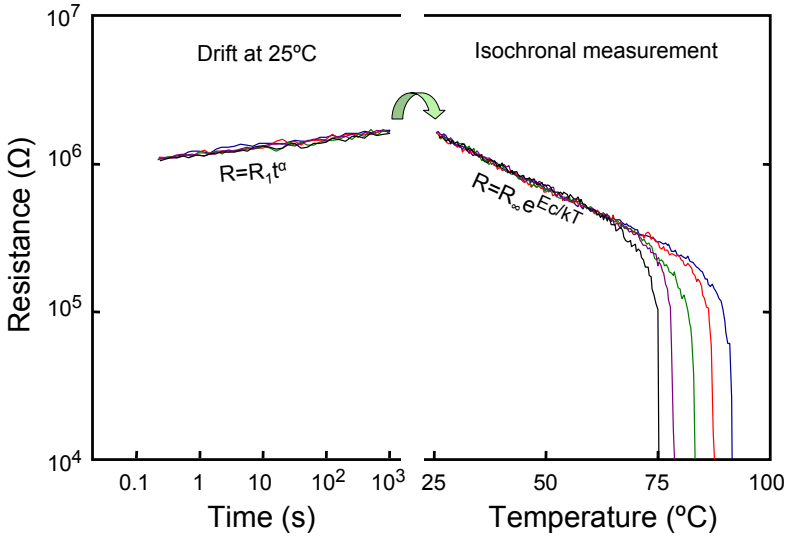

(a)

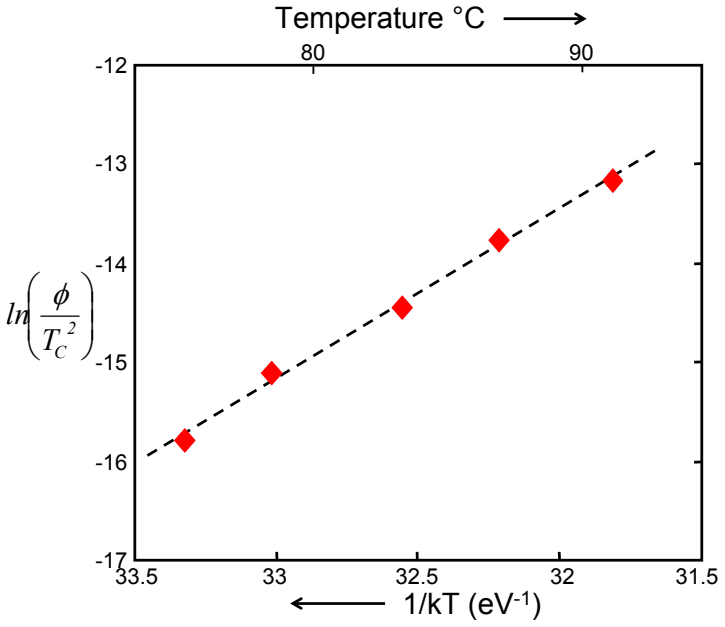

(b)

Figure 5.2: *For each isochronal measurement (see text), the cell is first drifted for 10^3 seconds to avoid influence of drift on the temperature measurement. The temperature is increased with a constant ramp rate and the resistance is measured until the cell is crystallized. The crystallization temperatures from* ***(a)*** *are shown in a Kissinger plot in* ***(b)****. The resistance drift in* ***(a)*** *was reproduced for each measurement proving that the cell returned to the same state for all isochronal measurements.*

5.4.3 Isochronal retention

The temperature is raised with a constant ramp rate ϕ (in $^\circ C/minute$) until the cell crystallizes; see Fig. 5.2(a). As the temperature is raised the resistance drops steadily. This initial drop in resistance, which is not dependent on the ramp rate (see Fig. 5.2(a)), cannot be attributed to crystal growth but to the natural temperature dependence of the amorphous low field resistance (R_T) which follows the Arrhenius equation $R_T = R_\infty \cdot e^{E_c/kT}$ where R_∞ is a pre-factor and E_c is the activation energy for conduction. The value of E_c is generally half the value of the band gap [78]. A value of 0.29±0.01 eV was found here, which is comparable to values found in the literature [78] even though a different material and cell geometry was used. The natural strong dependence of the cell resistance on temperature was conveniently used to verify that there is no (ramp rate dependent) thermal lag between the cell and the measured temperature for the ramp rates that were used.

Crystallization occurs when the resistance starts to deviate from this temperature dependent thermally activated resistance. The crystallization temperature (T_c) is taken at the point with the maximum drop in resistance (on a logarithmic scale). This is the moment when the crystalline boundaries (of the amorphous mark) meet and a continuous crystalline conductive path is formed (see Section 9.3. The crystallization temperatures are shown in a Kissinger plot depicted in Fig. 5.2(b). From the data an (equivalent Arrhenius) activation energy for crystal growth is found of 1.7 eV and a pre-factor of $6.4{\cdot}10^{-23}$ s (shown in Fig. 5.3(b) as a red line).

5.4.4 Isothermal retention

The temperature was raised to a certain temperature and the resistance was measured until the cell resistance dropped below 10 kΩ. The time between the moment that the temperature was reached and the time that showed (within a time step) the largest drop in resistance (on a logarithmic scale) is taken as the value of the retention time. The transition generally occurs very fast; see Fig. 5.3(a). This can be explained by a gradual growth from the crystal boundaries that suddenly meet at this point, possibly assisted by the voltage of resistance measurement. Retention times were measured ranging over almost five orders of magnitude; see Fig. 5.3(b).

The data clearly show that an Arrhenius type retention behavior is met over the whole range. Also, the Arrhenius retention that was calculated from the Kissinger data (red line in Fig. 5.3(b)) shows excellent consistency with the actual Arrhenius data, considering the error margins in the data, this difference of 3 °C is not significant and demonstrating that for these cells the two measurement techniques are interchangeable. Activation energies for growth of 1.7 eV were found for both isothermal and isochronal measurements. Although the data are very consistent, the retention behavior does not meet the requirements from industry.

The measurement was repeated on 700×300×20 nm^3 PRAM cells of the same composition but produced by a different fabrication method including optical lithography; details can be found in [9]. For instance, with optical lithography a hard mask was used, whereas with e-beam lithography the soft resist was not removed from the PCM surface. For the cells produced with optical lithography, activation energies for

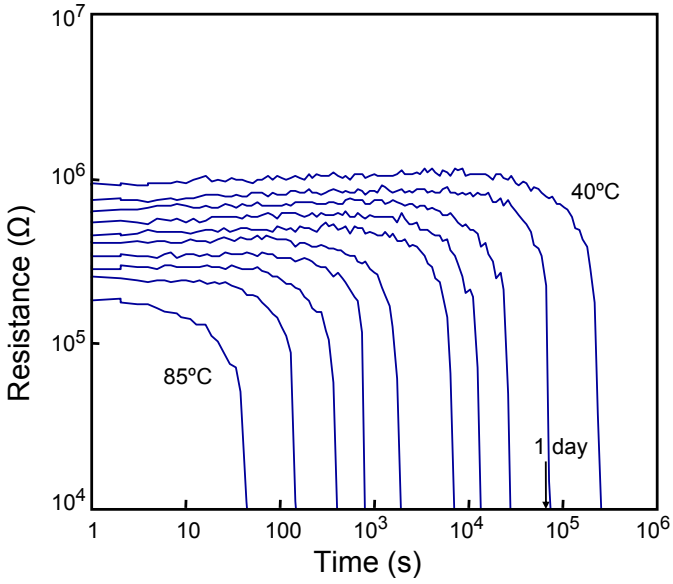

(a)

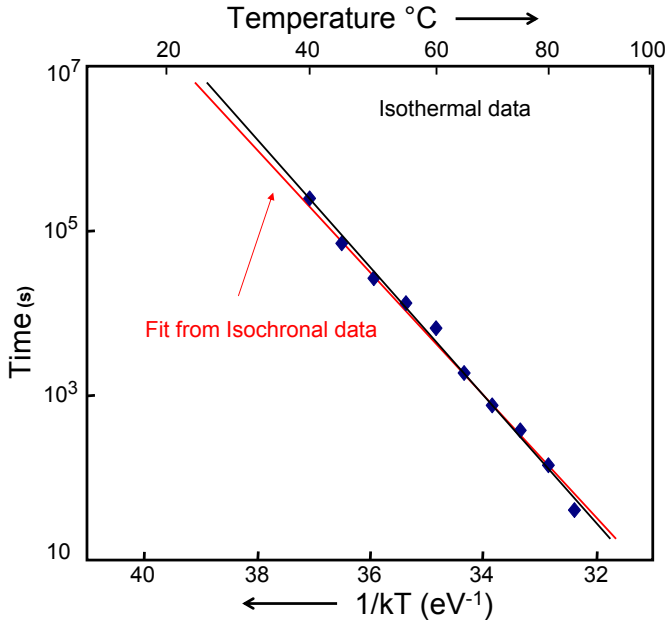

(b)

Figure 5.3: *After a RESET pulse and drift period (see text), the resistance is measured until the cell is crystallized. The memory retention data of* ***(a)*** *is shown in an Arrhenius plot in* ***(b)****. The red line in* ***(b)*** *is a fit from equivalent Arrhenius activation energy and pre-factor obtained from the isochronal measurement shown in Fig. 5.2(b). It is shown that the isothermal and isochronal data are in excellent agreement.*

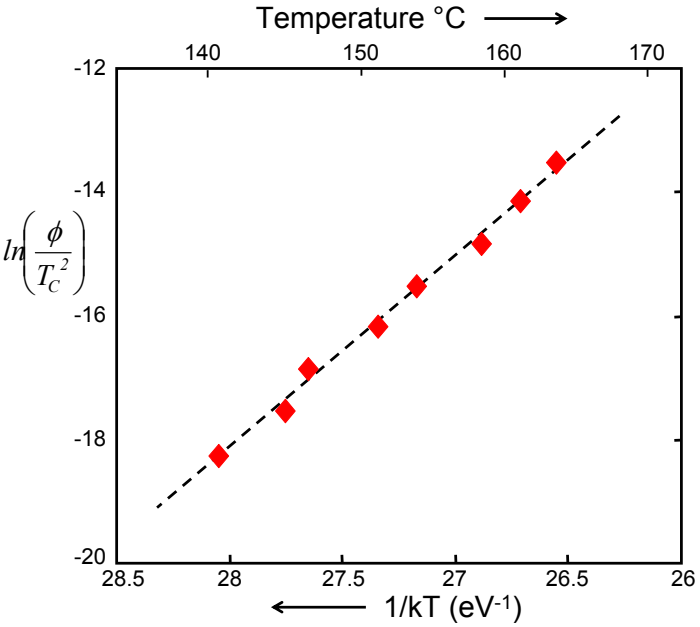

Figure 5.4: *The memory retention of a PRAM cell produced by optical lithography is measured isochronically. An activation energy of 3.3 eV was obtained.*

growth of 3.0 eV and 3.3 eV were found for isothermal (see Fig. 5.5(a)) and isochronal measurements respectively, which are consistent within measurement limits (see Fig. 5.5). These values are in excellent agreement with earlier measurements on phase-change blanket films of identical composition and layer thickness (see Section 3.4). Small differences in activation energy lead to larger differences in the (extrapolated) retention at operating temperatures. The isothermal measurements indicate memory retention of 10 years at 89 °C, isochronal indicates 10 years at 92 °C.

Interesting large differences are found between the retention behavior obtained for the cells produced by e-beam or optical lithography. For the e-beam cells, we have proof that the memory retention degrades with cycling: The crystallization temperature (measured with a ramp rate of 30 °C/minute) decreases from 122 °C to 92 °C during the 10^8 cycles (see Fig. 6.10). Also, the activation energy decreases with cycling from 2.2 ± 0.2 eV to 1.7 ± 0.2 eV. Furthermore, it is expected that the e-beam cells which have a smaller geometry will have a slightly lower memory retention. Although cell cycling and geometry influences memory retention they cannot explain the large differences between cells produced by e-beam and optical lithography on its own. These results demonstrate that the same phase change material can exhibit large differences in properties such as crystallization temperature and activation energy depending on the way it is packed and processed in the device.

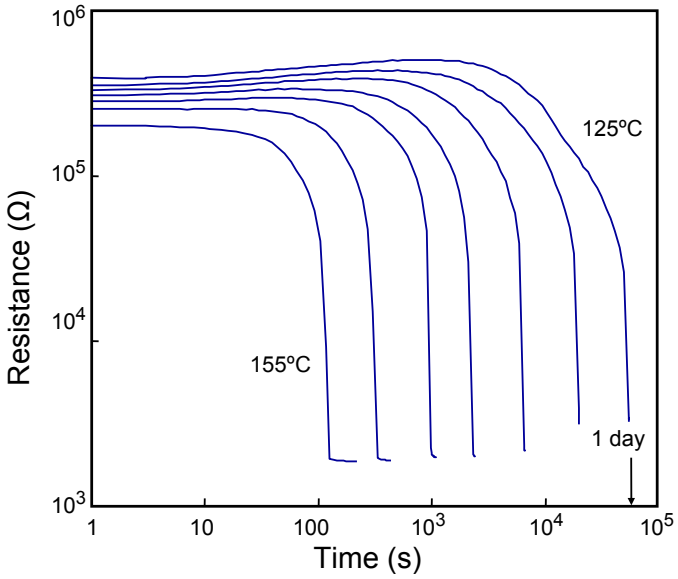

(a)

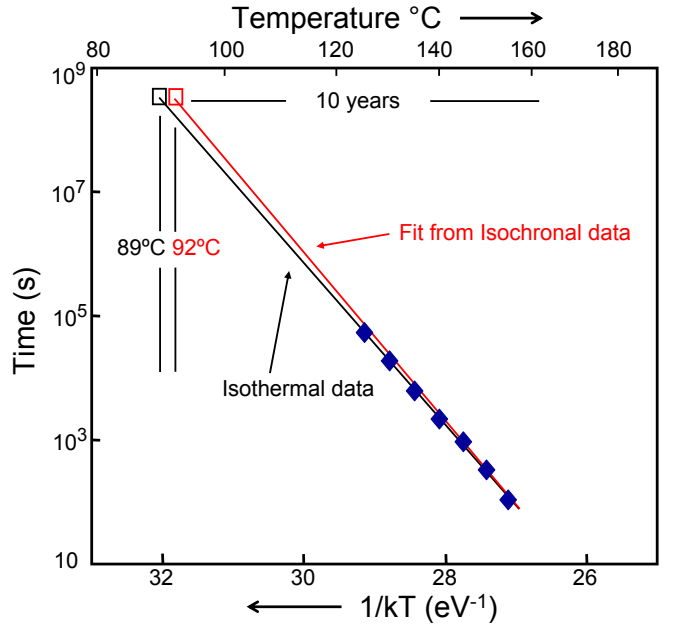

(b)

Figure 5.5: *(a) Shows an isothermal crystallization experiment performed on a PRAM cell produced by optical lithography.* ***(b)*** *Is a comparison between the data shown in* ***(a)*** *and the isochronal measurement shown in Fig. 5.4 which are in excellent agreement.*

5.5 Conclusions

Doped SbTe PRAM line cells with dimensions $225 \times 50 \times 20$ nm^3 produced by e-beam lithography could be SET/RESET for at least 100 million cycles. The memory retention of the PRAM cell was measured both isothermally and isochronally, which gave the same activation energies for growth, 1.7 eV. The isothermal and isochronal retention measurements were repeated on PRAM cells produced by optical lithography and activation energies of 3.0 eV and 3.3 eV were found, respectively. Although the isothermal and isochronal retention measurements were again very similar, they strongly deviate from what we found for the cells produced by e-beam lithography. This deviation mainly originates from the different ways the cells are produced as well as, for the cells produced by e-beam lithography, reliability of the deposition system which could have led to variations in composition across the wafer. Cell cycling and geometry explained for a smaller part the differences that were found.

Chapter 6

Evolution of cell properties during cycling

6.1 Abstract

Doped SbTe phase change (PRAM) line cells produced by e-beam lithography were cycled 100 million times. During cell cycling the evolution of many cell properties were monitored, in particular the crystalline and amorphous resistance, amorphous resistance drift exponent, time-dependent threshold voltage, threshold voltage as a function of RESET pulse height, crystallization temperature, and activation energy of crystal growth. The power of the present approach is that all these properties were measured simultaneously during the life of single cells. The evolution of the cell properties can be summarized by (i) an initialization phase characterized by settle-in effect of the material surrounding the programmable region, (ii) a usable life phase where initially the cell properties remain fairly constant until after $\approx 5 \cdot 10^5$ cycles decomposition of the programmed region caused degradation of the cell properties, and (iii) finally an end of life phase where the cell is stuck in the SET state after typically 10^8 cycles. Although generally the threshold voltage is directly related to the amorphous resistance it was found that during cycling this relation is not constant but evolved as well. Instead, the crystallization temperature could be linked to the threshold voltage throughout the complete life cycle of the cell which could lead to new insights to the nature of the threshold event.

Published as:
J.L.M. Oosthoek, K. Attenborough, G.A.M. Hurkx, F.J. Jedema, D.J. Gravesteijn, and B.J. Kooi, *J. Appl. Phys.* **110**, 11 (2011).

6.2 Introduction

Phase change random access memory (PRAM) is considered to be one of the most promising candidates for future non-volatile memories [84]. Its application ranges from mass data storage to embedded memories in, for instance, smart cards and automotive integrated circuits. For the embedded memories the so-called line-cell geometry was proposed by NXP [52]. Line-cells typically have a larger foot print compared to vertical cells (Ovonic universal memory, OUM) [15] and are thus less suitable for mass data storage. However for embedded memory applications this is compensated by the minimum impact on a standard CMOS process: only three additional lithographic steps are necessary. Furthermore, due to the planar geometry the programming current scales with the phase change layer thickness and line width, rather than with the minimum lithography feature size only. Although sub-lithographic features are possible [27] and will most likely be mandatory for mass data storage applications, the easy processability and reduction of energy consumption with layer thickness make line-cells an ideal candidate for low-cost applications where less memory density is not critical. PRAM exploits the large (three to four orders of magnitude) difference in electrical resistance of the amorphous and crystalline states of phase-change materials, which are renowned for their extremely fast crystallization kinetics at high temperatures and stability at operating temperatures [84]. A fast, high-energy pulse transforms the crystalline cell into an amorphous state by melt-quenching. The crystalline state can be recovered by applying a longer low-energy pulse that heats the cell, optimally below the melting temperature. The higher mobility of the atoms allows crystallization of the amorphous region during the pulse. This can also be performed fast, within 100 ns, but not as fast as melt-quenching that can in principle be performed with sub-picoseconds pulses [68, 93].

The amorphous phase displays peculiar properties such as threshold switching [71] and temporal drift of the resistance and threshold voltage of the amorphous phase [78, 23, 35] that are critical for the PRAM behavior. The threshold event by itself does not crystallize the cell and has been explained in literature by either an electrical switching phenomenon [78, 23] related to trap kinetics and electron recombination or to the creation of crystalline filaments [35, 36]. In the absence of crystal growth and nucleation, which is predominant at elevated temperatures, the amorphous resistance continuously increases (drift) as a function of time even at room temperature. This is ideal for a memory based on two distinct stable states since (in the absence of crystallization) the read window improves in time. However for multilevel memory applications based on programming the cell to different amorphous states [104, 67] within the continuum of three to four orders of magnitude this creates the possibility that one state drifts into the resistance window of the next state. The temporal drift of the threshold voltage, which also corresponds to a continuous increase with time [78, 23, 35], can complicate the operation of PRAM. Therefore it is imperative that the maximum expected value does not exceed the operation voltage of the memory.

Accurate knowledge and understanding of these phenomena and the critical properties of non-volatile memories, including data retention (archive stability), program settings (voltages and currents needed to switch between the two or multilevel states

of the memory) and cyclability (endurance), are essential for the PRAM technology. Line cell endurance is currently limited to one hundred million cycles (see Fig. 5.1). Within this limit all the other properties of the memory should ideally be independent of the cycle number. In this work we show detailed results on the evolution of memory cell characteristics during cycling. We measured the resistances, resistance drift, threshold voltage, threshold-voltage drift, crystallization temperature, and activation energy for crystallization during cycling. The uniqueness and novelty of the present work is that all these properties have been obtained simultaneously for a single cell with excellent reproducibility when repeating for several cells. Generally the evolution of a single property, like the threshold voltage, with cell cycling is measured [78]. This enables us, to determine more accurately the interdependences of several parameters.

Here, we demonstrate the usefulness of this approach by showing that during cycling the threshold voltage and crystallization temperature of the phase-change material both decrease and follow a remarkable similar evolution. Generally, it is assumed and also demonstrated [78] that the threshold voltage and the amorphous phase resistance are linked in a rigid way. We show that in our measurements the amorphous resistance is not the dominating factor for predicting the threshold voltage. We relate the decrease in threshold voltage and crystallization temperature as cycling progresses to decomposition of the phase-change material. Finally the cell becomes stuck in the (crystalline) SET state after typically 10 to 100 million cycles.

6.3 Experimental

Phase change line cells of dimension $15\times75\times225$ nm^3 were produced by e-beam lithography (see TEM image in Fig. 6.1). The devices were fabricated on (100) Si wafers with a 500 nm grown thermal oxide layer. First, TiW bottom electrodes are deposited and patterned by standard optical lithography. Subsequently an oxide layer is deposited and the surface is planarized by a chemical mechanical polishing (CMP) step. After CMP, the TiW electrodes were cleaned by an in situ sputter etch after which a 15 nm doped SbTe phase change layer was sputter deposited at room temperature. Single line cells are then patterned by e-beam lithography and Ar plasma etching, using a *Hydrogen Silsesquioxane* (HSQ) hard mask and then passivated by oxide. More processing details can be found elsewhere [28].

Wafer pieces containing cells are mounted on a ceramic plate with built-in heating filament and thermocouple allowing for a fast and accurate control of the cell temperature. The temperature is controlled with a PID controller and a controllable DC power supply connected to the heating filament. The temperature is kept stable to ±0.1 °C.

The total measurement setup is schematically depicted in Section 2.2. Contact to the cell was made by a custom built dual probe needle system with a 3.2 kΩ series resistor connected close to the needle. This series resistor limits the SET current after the threshold event and simulates the selection transistor in a memory. A Tektronix AFG3102 arbitrary function generator was used as a pulse generator which can produce any combination (and shape) of SET, RESET and read pulses with

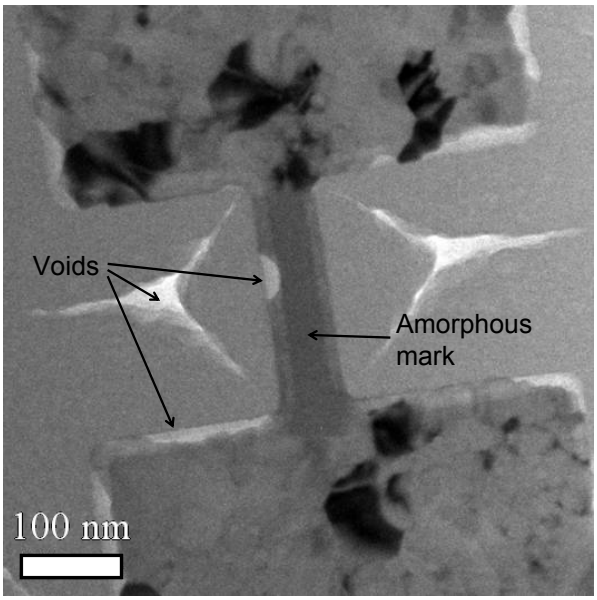

Figure 6.1: *Plan-view TEM image of an FIB processed line cell with dimensions $15\times50\times250$ nm^3 showing the RESET state with a large amorphous mark. Except for the slightly different dimensions this cell is identical to the cells characterized in this study.*

pulse edges down to 4 ns. Pulse voltage and currents were monitored by an Agilent DSO6052A digital storage oscilloscope which also provides 50 Ω termination. The cell resistance was measured accurately with a Keithley 2601 source meter. An RF switch selects between the current channel of the oscilloscope and the source meter Fig. 2.7.

A complete switching cycle consists either of a single RESET (see Fig. 6.2(a)) and SET pulse (see Fig. 6.2(b)), where the cell resistance is measured with the source meter after both the RESET and the SET pulse, or a single RESET-read-SET-read pulse sequence (see Fig. 6.2(c)), where a complete cycle is performed with a single programmed pulse from the arbitrary function generator which can be repeated up to a million times.

6.3.1 Accurate RESET/ SET cycle

After a single RESET pulse (Fig. 6.2(a)) the resistance is measured for 10 seconds as a function of time with exponentially increasing intervals after the RESET event (Fig. 6.4). It is a well known fact that the amorphous resistance exhibits a time dependence [78]. It increases (drifts) in time and follows a well established power law $R_t = R_0 \cdot (t/t_0)^\alpha$ where R_0 is the resistance at $t_0 = 1$ second after RESET and α is an empirical power law coefficient [78]. From the resistance measurements both R_0

and α were obtained. After the 10 seconds drift the arbitrary function generator is reprogrammed and a single SET pulse (Fig. 6.2(b)) crystallizes the cell. The SET pulse has long (200 ns) leading and trailing edges. The long leading edge allows for a measurement of threshold voltage. The current increases suddenly during the threshold event (faster than the measurement limit of our equipment). The 200 ns trailing edge avoids large capacitive currents related to the $\approx$ pF stray capacitance of the probe system. As the temperature of the cell during the SET pulse is close to (but below) the melting temperature, a capacitive current from a sharp edge (in the mA range) can lead to parasitic RESET [22]. In a real memory application these leading and trailing edges are not necessary because capacitive currents of the selection transistor are orders of magnitude smaller [22].

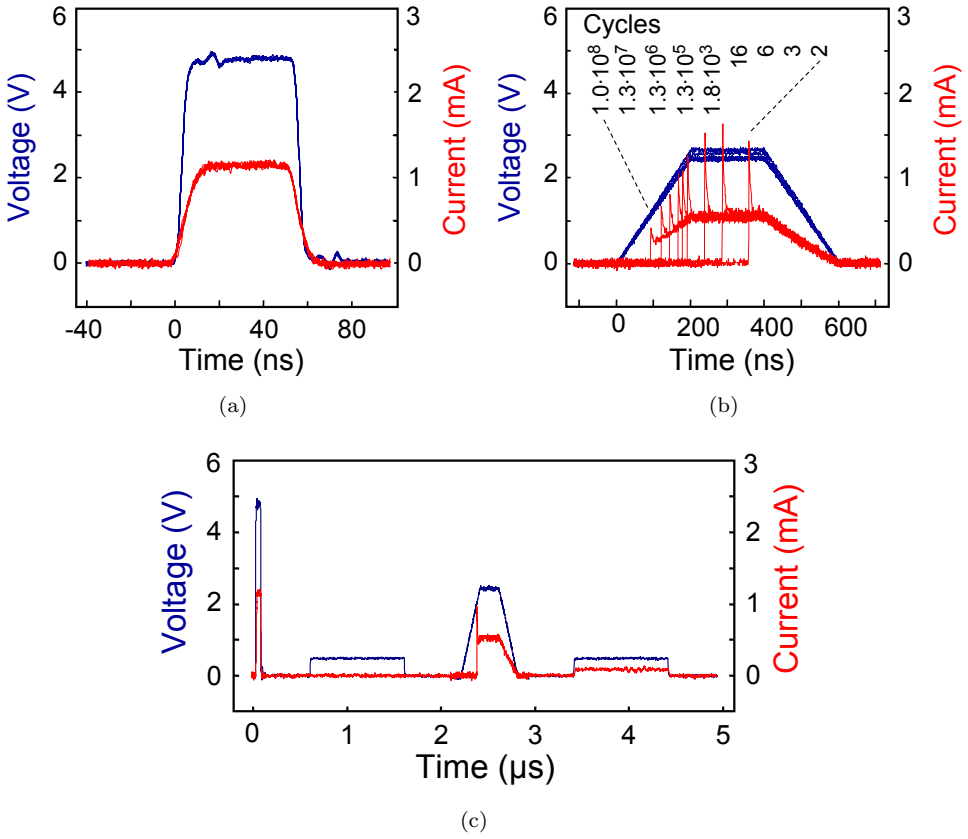

Figure 6.2: ***(a)*** *Oscilloscope traces of nine single RESET pulses taken every decade of cycling showing no evolution in the programming current,* ***(b)*** *nine single SET pulses taken throughout cycling, and* ***(c)*** *a fast cycle. The latter consists of four separate oscilloscope traces (one for each pulse) from the same measurement. The apparent lower noise of the read pulses arises from averaging performed by the oscilloscope when acquiring traces longer than 250 ns.*

6.3.2 Fast RESET/ SET cycle

The previous accurate single cycle is only practical for tens or maybe hundreds of cycles as the resistance measurement with the source meter and the switching of the RF relay take considerable time. To cycle the cell millions of times a pulse pattern was programmed into the arbitrary function generator consisting of a RESET read SET read pattern (shown in Fig. 6.2(c)). The (1 µs) read pulses validated that the cells were actually switched. Ten data points were collected for each decade of cycling Fig. 6.3. For each of the data points up to ten fast cycles were recorded for validation of switching. The read pulses allowed for a resistance (V/I) measurement directly after the RESET and SET pulse. The upper measurement limit of the resistance obtained with the 0.5 V read pulses was $\approx$ 50 kΩ which is sufficient to distinguish between the amorphous and crystalline state.

6.3.3 Isochronal crystallization

The cycle experiment was periodically interrupted to perform one or more isochronal crystallization measurements. The cell is made amorphous with a single RESET pulse. The resistance is measured for 1000 seconds to allow the cell to drift. The temperature is then increased with a constant ramp rate and the resistance is measured at constant temperature intervals until the cell is crystallized (i.e. when the resistance drops below 10 kΩ). The temperature is returned to 25.0 °C by passive cooling.

The activation energy for crystal growth was obtained from isochronal crystallization measurements with varying ramp rates (ranging from 1 K/minute to 60 K/minute) employing the so-called Kissinger analysis [40]. Between each thermal measurement 10 fast cycles, with identical pulse settings as the general cycling experiment, were performed to bring the cell back to the same state as after cycling (named hereafter by *imprint removal cycle*). The imprint removal cycle between the temperature ramps are applied to ensure that the cell had the same value of R_0 and α for each temperature measurement i.e. to avoid variations in the retention parameters due to partial crystallization after the isochronal measurement.

6.3.4 Threshold voltage measurement

Apart from the threshold voltage measurement performed automatically during the general cycle experiment a separate more elaborate measurement of the threshold voltage was performed at various cycle numbers. The threshold voltage was measured as a function of delay time: Short delay times ranging between 2.3 µs and 43 µs were obtained by programming a RESET - read - SET - read pattern into the arbitrary function generator. Longer delay times were obtained from a single RESET and SET pulse from $\approx$ 5 seconds to 1000 seconds after the RESET pulse.

Also, the threshold voltage as a function of the RESET pulse height was measured: After a RESET pulse, varying in pulse height, the resistance is measured for 100 s. The cell is then switched back to the crystalline state with a SET pulse from which the threshold voltage is obtained. Between each single threshold voltage measurement an imprint removal cycle was applied.

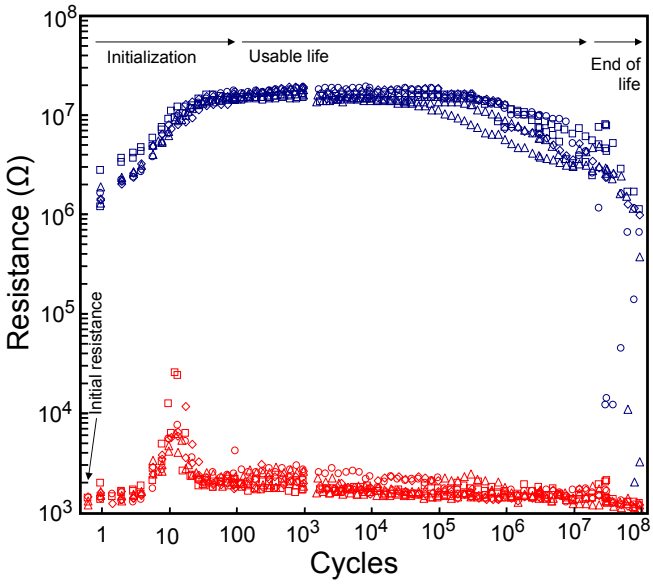

Figure 6.3: *A set of complete switching cycles of seven 15×75×225 nm³ line cells. The resistances shown are measured with the source meter after either a single RESET or SET pulse. The amorphous resistance R_0 is always obtained from the time dependent measurement.*

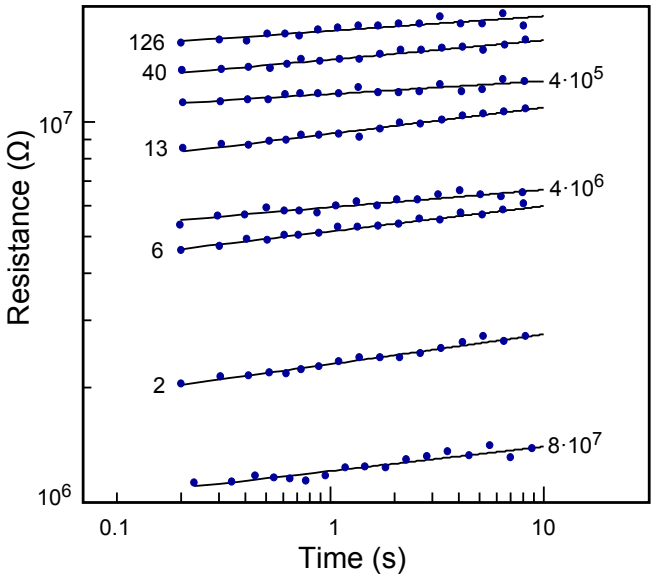

Figure 6.4: *A selection of resistance measurements as a function of time (and power law fit) performed at various cycle numbers from which the amorphous resistance R_0 and a were calculated.*

6.4 Results

6.4.1 RESET/SET resistance

The life cycle of the line cells analyzed for the used program settings are shown in Fig. 6.3, demonstrating that the cells can be switched 10 to 100 million times. The life cycle consists of an initialization phase and a usable life phase until the cell becomes stuck in the SET state (see Fig. 6.3).

During the initialization phase the amorphous resistance R_0 increases about an order of magnitude from the first to about one hundred cycles. This is accompanied by a measured drop of the drift coefficient α from 0.075 ± 0.007 to 0.04 ± 0.01 during the first 100 cycles (see Fig. 6.5). A strong increase of the SET resistance from about 1.3 kΩ to 10 kΩ followed by a decrease to about 2 kΩ was observed during the initialization phase (Fig. 6.3). The usable life phase is characterized by quite stable cell parameters up to about $3.3 \cdot 10^5$ followed by a strong drop in amorphous resistance on a log scale of cycling. Although the amorphous resistance drops significantly the cell can still be switched. Finally the cell can only be brought to the amorphous state by applying a larger magnitude RESET pulse which is recognized here as the end of life phase.

6.4.2 Threshold voltage

6.4.3 Accurate RESET/ SET cycle

The measured threshold voltage as a function of the number of switching cycles is shown in Fig. 6.6. After about 100 cycles the threshold voltage dropped considerably. Figure 6.2(a) shows that during the initialization phase the threshold event occurred during the flat part of the SET pulse shortening the crystallization time. This shorter crystallization time could in fact simply explain the higher SET resistances during this phase as partial crystallization. But successive SET pulses were applied after the threshold event when the SET resistance exceeded 10 kΩ to fully crystallize the cell. However these pulses did not lead to a lower resistance, i.e. did not fully crystallize the amorphous mark.

An important observation is that the current during the RESET pulse was not related to the crystalline resistance prior to the pulse. Figure 6.2(a) shows that the oscilloscope traces from the nine RESET pulses taken at fixed intervals during cycling overlap considerably. The fact that the pulse voltage traces overlap is trivial but this is not the case for the pulse current traces. Although the crystalline resistance continuously decreases from about 2 kΩ to 1 kΩ during the life time, the RESET current was 1.1 mA throughout. This translates to an invariable cell resistance of 1.2 kΩ during melting which was the same for each cell presented in Fig. 6.3.

During the usable life phase the threshold voltage is nearly constant up to around 10^5 cycles and then starts to decrease significantly. Figure 6.6 also nicely demonstrates that the threshold voltage observed during the SET pulse is dependent on how much time passed after the RESET pulse. The longer the time after the RESET pulse the higher the threshold voltage. This holds for each individual line cell, but does

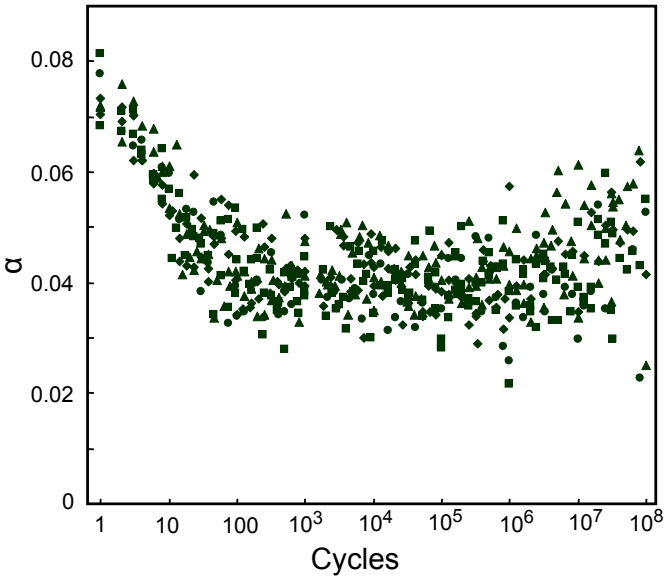

Figure 6.5: *Drift exponent a measured for the amorphous resistance as a function of the number of switching cycles for the seven cells.*

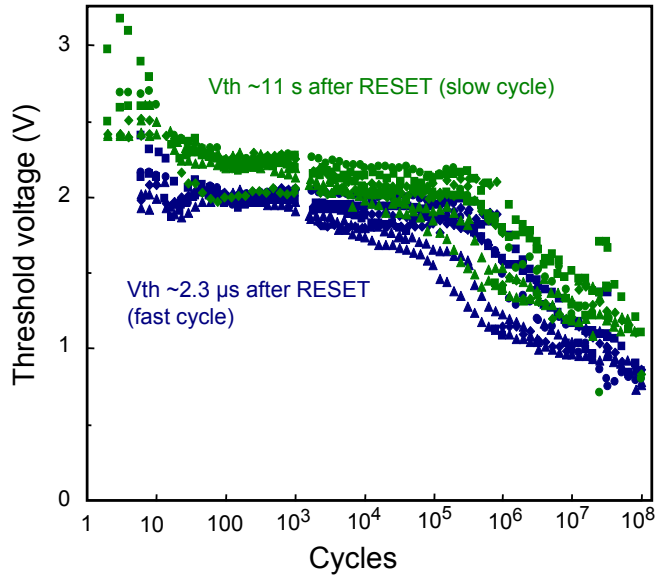

Figure 6.6: *Threshold voltage as a function of cell cycling measured at 2.3±0.1 µs and ≈11 seconds. The uncertainty of the 2.3 µs measurements arises from the fact that the threshold voltage is measured with a 200 ns leading edge: Higher threshold voltages therefore will always have a slightly longer delay time and vice versa. The uncertainty of the measurement at 11 s arises mainly from the reprogramming time of the arbitrary function generator which takes ≈1 second (which is added to the 10 seconds resistance drift time).*

not hold beyond 10^5 cycles when comparing the different cells. This gives Fig. 6.6 a somewhat chaotic appearance beyond 10^5 cycles. However, also in Fig. 6.3 it is observed that some cells show a more rapid decrease in amorphous resistance with cycling than others. Therefore it is interesting to correlate the threshold voltage with the amorphous resistance for the (seven) line cells during their life. The result is shown in Fig. 6.7. The various phases during the life of the line cells can be readily discerned. In the initialization phase the amorphous resistance clearly increases and the threshold voltage slightly decreases. During the usable life phase, the threshold voltage and amorphous resistance drop until finally the cell is stuck in the SET state. An interesting observation is that the data are not chaotic anymore beyond 10^5 cycles. For all cells the threshold voltage 2.3 µs and 11 seconds after the RESET pulse are now well separated. The threshold voltage and amorphous resistance show a dependence that appears to consist of two linear regimes (Fig. 6.7). This observation can be explained by two separate processes taking place during the evolution (degradation) of properties induced by cycling.

To gain more understanding on the evolution and behavior of the threshold voltage a more elaborate measurement was performed twice per decade of cycling from 10^3 cycles on. This measurement could not be performed earlier during cycling due to the amount of cycles required for the measurement. Also, as the material properties change quite significantly during the initial 100 cycles such a measurement would generate artifacts caused by the change of properties during the measurement.

Figure 6.8(a) shows the time dependence of the threshold voltage after the RESET pulse. The threshold voltage was either measured with a single RESET-read-SET-read pulse or by a single RESET and SET pulse with altered delay time. The total time scale spans nine orders of magnitude. Figure 6.8(a) shows that the threshold voltage as a function of time after RESET can be properly fitted with a power law (solid lines) similar to the resistance drift: [78]

$$V_T = V_{T0} + \Delta V_T (t/t_0)^{\nu} \tag{6.1}$$

This power law was proposed by Ielmini et al. [23] and is based on a linear dependence between the threshold voltage and amorphous resistance [78, 23]:

$$V_T = V_{T0} + \gamma \cdot R \tag{6.2}$$

where γ is a fitting parameter. A natural consequence of Eq. 6.1 is that the coefficient of resistance drift and threshold drift necessarily must have the same value. Therefore the threshold drift coefficient ν was set equal to the resistance drift coefficient α, obtained from the resistance drift measurements prior to the threshold event, and the parameters V_{T0} and ΔV_T were fitted to the data (also $t_0 = 1$ second was used). The (left) inset of Fig. 6.8(a) shows that both ν and ΔV_T remained fairly constant during cycling: $(41 \pm 2)\cdot 10^{-3}$ and 0.40 ± 0.05 V respectively. However, V_{T0} dropped from 1.7 V to 0.8 V and follows the general evolution of the threshold voltage of Fig. 6.6. The biggest drop in ΔV_T occurred between $3.3\cdot 10^5$ and $3.3\cdot 10^6$ cycles. As the cell continued to be cycled to $3.3\cdot 10^7$ the value of ΔV_T continued to decrease until finally at $1.0\cdot 10^8$ cycles the cell was stuck in the SET state.

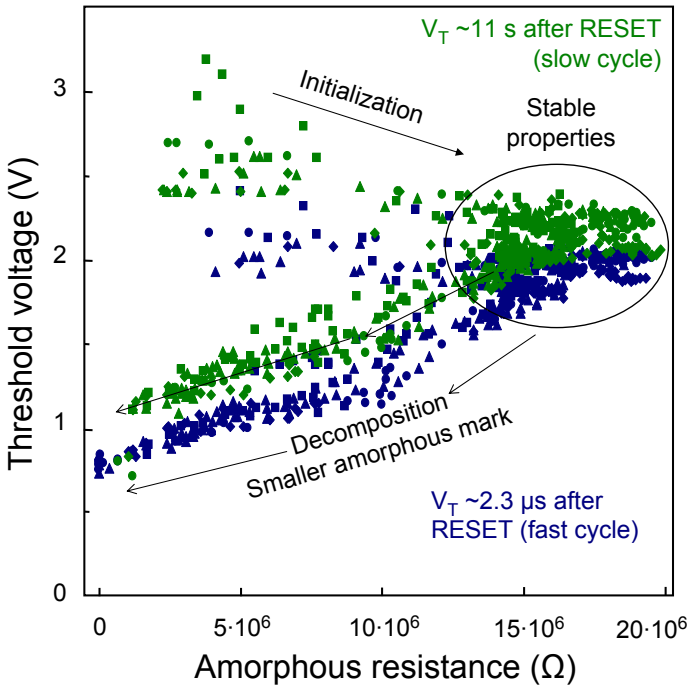

Figure 6.7: *The threshold voltage from the data of Fig. 6.6 is plotted versus the amorphous-phase resistance (at 1.0 s) from the data of Fig. 6.3. However for the slow cycles, the actual resistance during the SET pulse at which the threshold event takes place (≈11 seconds after RESET) will be 5% to 22% higher depending on the value of α. This difference is very small compared to the evolution the actual resistance values and does not change the observations. Furthermore, during the fast cycles the resistance cannot be measured this accurately and the amorphous resistance of the slow cycle following that particular fast cycle was used.*

Our data can also be fitted with the same degree of accuracy to a linear increase of the threshold voltage on a logarithmic time scale (dashed lines) explained by a theoretical model proposed by Karpov et al. [35]:

$$V_T = V_{T0}[1 + \nu \cdot ln(t/t_0)] \tag{6.3}$$

This model explains the increase of threshold voltage by a random double well potential of a meta-stable disordered atomic structure of a glass. Here the values of V_{T0} and the threshold drift coefficient ν are fitted to the data. The (right) inset in Fig. 6.8(a) clearly shows that both V_{T0} and ν evolve during cycling. V_{T0} which is the threshold voltage at $t_0 = 1$ s, clearly drops significantly which can be expected. However, to keep the slope of the linear fit on log time (fairly) constant ν has to increase by an equal amount. A direct consequence is that according to this model

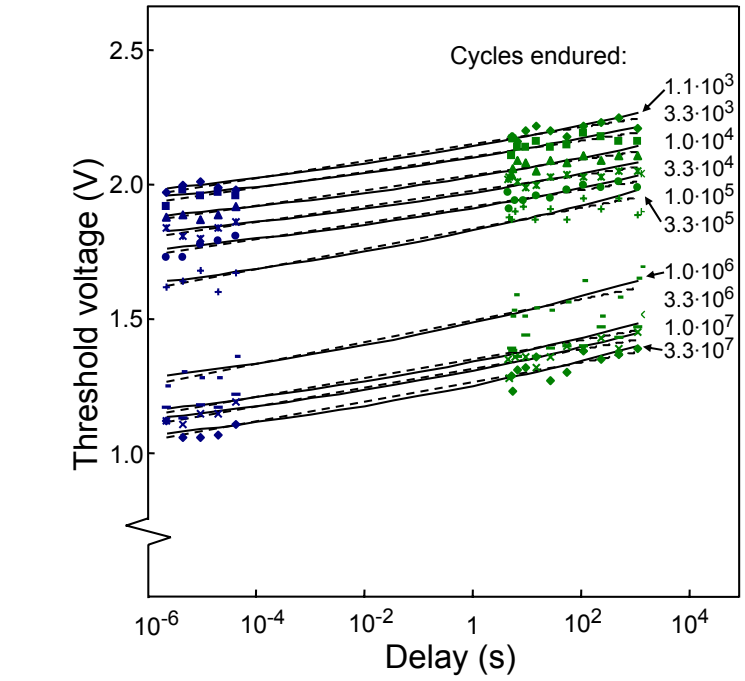

(a)

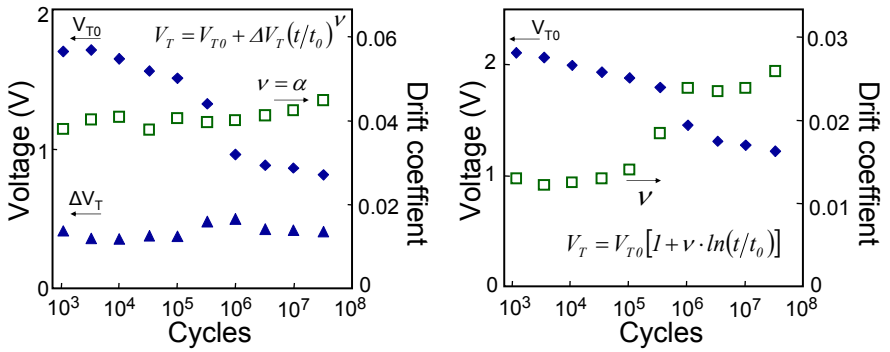

Figure 6.8: *The threshold voltage was measured as a function of time after RESET. The measurement was performed twice every decade of cycling from $1.1{\cdot}10^3$ to $3.3{\cdot}10^7$ cycles. The dotted lines are a fit based on a linear increase in log time [35], the solid line is a fit based on a power law [23].*

the resistance drift, which remains very constant during cycling, does not follow the evolution of the threshold drift coefficient which doubles.

Furthermore, unlike the amorphous resistance that depends directly on a power law, the threshold voltage dependence in both models has the additive constant V_{T0}. Due to this constant both the models of Ielmini and Karpov produce very similar results. We expect that a threshold voltage measurement as a function of delay time of at least eleven decades of time are required on cells with high values of α ($>$ 0.07) before the validity of either model can be proven on the basis of such a direct measurement. The fit based on the power law (solid line in Fig. 6.8(a)) is surprisingly similar to the fit based on a linear increase with log time. Therefore no preference between the models can be made on the basis of the accuracy of our data. However, the model of Ielmini (Eq. 6.1) predicts the evolution of only V_{T0} while the other fit parameter ΔV_T remains fairly constant. The model of Karpov (Eq. 6.3) on the other hand implies an evolution of two parameters namely V_{T0} and the threshold drift coefficient ν which we consider to be contradictory to the evolution of the resistance drift.

Threshold voltage and resistance as a function of pulse height

The amorphous resistance and threshold voltage were measured as a function of RESET pulse height ranging between 3.6 volts and 6 volts (see Fig. 6.9(a) and 6.9(b)). RESET pulses with pulse heights lower than 3.6 volts were applied, but were unable to bring the cell to the RESET state. This is interesting as it shows that these cells are immediately programmed to a state $> 10^6$ Ω without going into unstable lower resistance intermediate states. The limiting value of 6 volts was chosen to avoid damage to the cell. After each individual SET pulse an imprint removal cycle was applied to avoid influencing the next measurement.

During the first $3.3{\cdot}10^5$ cycles the cell behavior was very consistent (Fig. 6.9(a)). For pulse heights up to 4.5 volts the amorphous resistance increases slightly with pulse height and a decrease in amorphous resistance is observed for pulses larger than 4.5 volts. However, the threshold voltage continuously increases with the RESET pulse height leading to the slight, but significant and not yet reported, inverse relation between threshold voltage and amorphous resistance beyond 4.5 V. This inverse relation between the amorphous resistance and threshold voltage can be considered to be an over-programming artifact related to these cells.

Lacaita et al. [49] have observed a linear relation between the amorphous resistance and threshold voltage across a large range (more than an order of magnitude difference) in resistance values. The extrapolation of the threshold voltage to zero amorphous resistance gives the value of V_{T0} on which the model of Ielmini et al. [23] is based (Eq. 6.1 and 6.2). Therefore it would be interesting to correlate the evolution of V_{T0} obtained from the threshold voltage drift (Fig. 6.8(a) left inset) with values obtained from the threshold voltage (Fig. 6.9(b)) and amorphous resistance (Fig. 6.9(a)). The relation between the amorphous resistance and threshold voltage when varying the pulse height is not a simple linear dependence on these cells. Therefore it is impossible to obtain accurate values of V_{T0} from the data presented in Fig. 6.9(a)

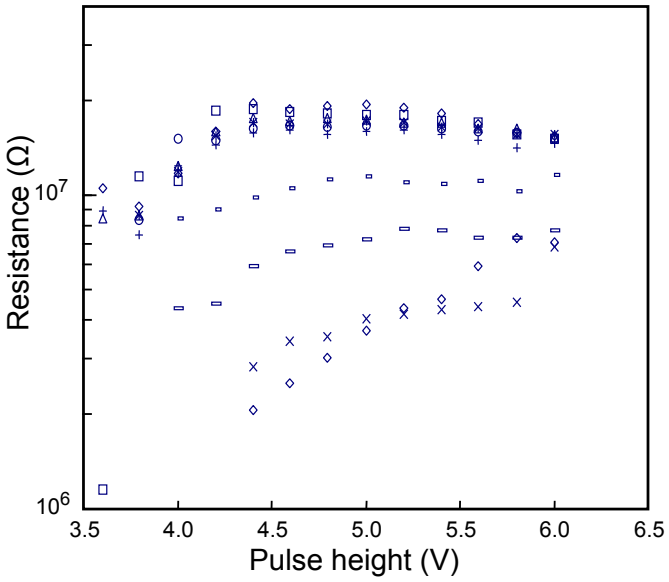

(a)

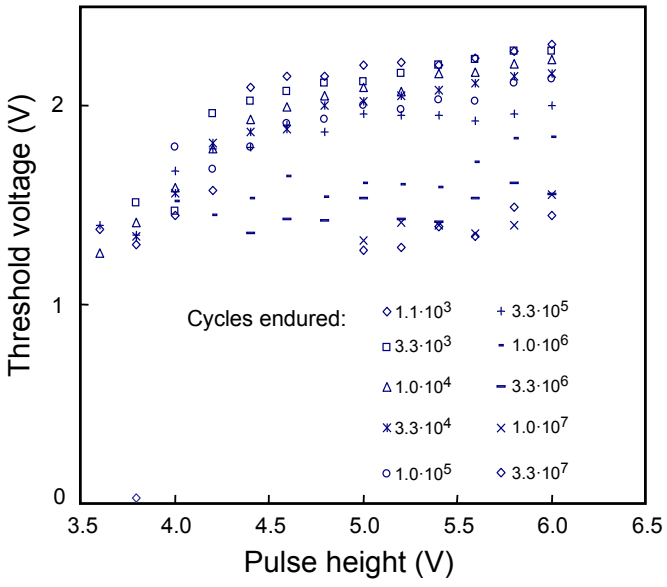

(b)

Figure 6.9: ***(a)*** *The amorphous resistance was measured for different pulse heights at different cycle numbers.* ***(b)*** *The threshold voltage was measured by applying a SET pulse after the amorphous resistance was monitored for 100 s, see Fig. 6.9(a). Some (low resistance) data points did not result in a threshold voltage measurement as the cell switched back while latching the RF relay or reprogramming the arbitrary function generator. This shows that the lower resistance states are inherently unstable and can be affected by very small spurious transients.*

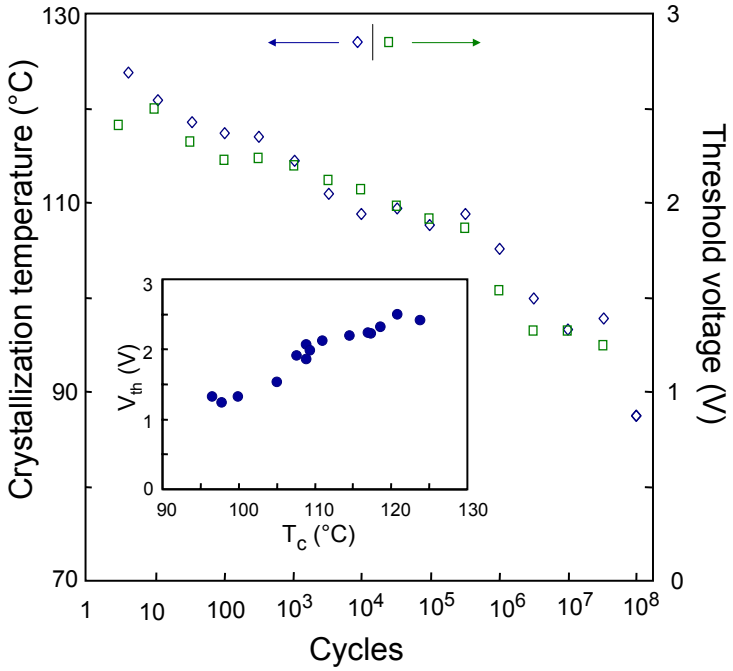

Figure 6.10: *The threshold voltage and the crystallization temperature at a fixed ramp rate (of 30 K/min) versus the number of switching cycles. The crystallization temperature was measured the cycle directly following the threshold voltage and therefore represents a different cycle number. Both the threshold voltage and the crystallization temperature show a strong correlation during cycling (see inset).*

and 6.9(b). Moreover, taking into account the varying material properties (within a single fit) it is fundamentally not meaningful to derive V_{T0} from the data. However, the data of Fig. 6.8(a) show that when keeping the programming parameters constant it is possible to obtain very reproducible results. The reason is that now the changes in material properties occur between the different fits in Fig. 6.8(a) and these changes are reflected in the varying V_{T0} values (Fig. 6.8(a) left inset). As the cell is cycled beyond $3.3{\cdot}10^5$ cycles, the threshold voltage and amorphous resistance both drop significantly and the peak in the amorphous resistance occurs at higher pulse heights. The resistance of the molten region (Fig. 6.2(a)) and thus the program energy does not change during cycling. Therefore the observations cannot be explained by assuming that a significantly smaller area is molten. The most viable explanation is partial re-growth of the molten region during quenching that leads to a lower resistance and threshold voltage which has also been observed in TEM. This explanation is further supported by the following. Some of the data points in Fig. 6.9(b) (after $3.3{\cdot}10^5$ cycles), corresponding to lowest resistance values in Fig. 6.9(a), are missing

as the cell crystallized spontaneously between the end of the resistance measurement and the application of the SET pulse. Switching the RF-relay and re-programming (through the GPIB port) of the arbitrary function generator leads to ubiquitous spurious pulses that can crystallize only the most sensitive states i.e. states with a very small amorphous mark.

6.4.4 Isochronal crystallization

The crystallization temperature was measured at regular intervals during cycling (see Fig. 6.10). It was found to continuously decrease during cycling from about 125 °C to 90 °C. This continuous decrease is quite unexpected as the amorphous resistance shows stable values at least in the range from 10^2 to 10^5 cycles (Fig. 6.3). In this range the crystallization temperature decreases at least 15 °C. Interestingly, the continuous decrease in crystallization temperature is correlated with a continuous decrease in the threshold voltage (Fig. 6.10). The crystallization temperature was also measured with ramp rates (ϕ) of 1, 2, 4, 8, 15, 30 and 60 K/minute (Fig. 6.11(a)). The upper inset of Fig. 6.11(a) shows the resistance-drift curves prior to the temperature ramp, which overlap for a time interval of more than three orders of magnitude. This proves that the cell could be returned to an identical state prior to each temperature measurement.

The activation energy of growth was obtained after the various numbers of cycles from Kissinger plots (figures not shown): The slope of $ln(\phi/T^2)$ versus T^{-1} gives the activation energy, which was proven for these cells to be the same as the activation energy obtained from isothermal measurements (see Chapter 5). The activation energy of growth was found to remain within 2.2 ± 0.2 eV during cycling (see Fig. 6.11(b)), i.e. no significant evolution with cycling was observed. This is in contrast with the crystallization temperature that shows a relatively dramatic evolution, i.e. decrease with cycling.

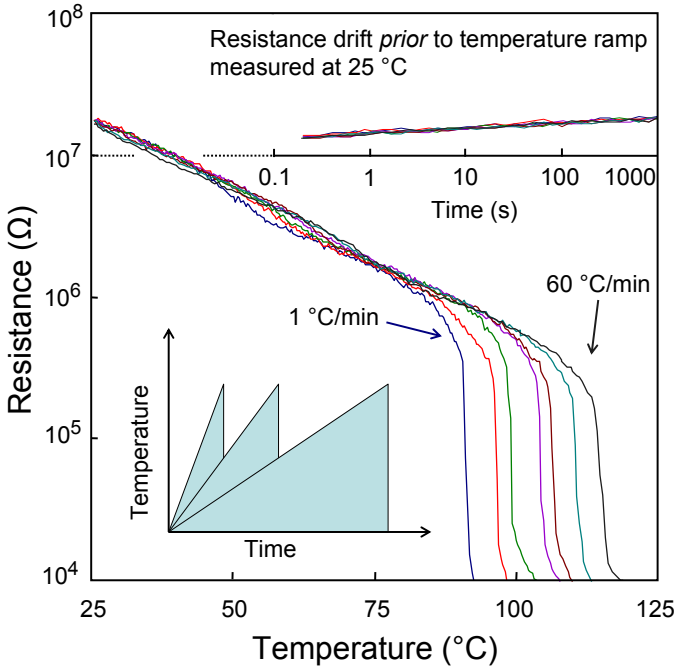

(a)

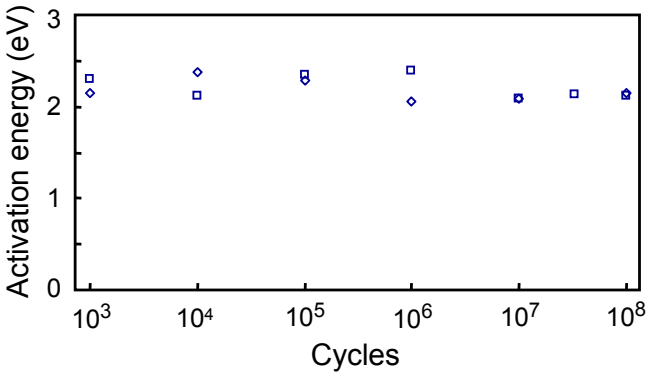

(b)

Figure 6.11: ***(a)*** *A cell was switched to the RESET state and drifted for 1000 seconds while the resistance was measured (upper inset). Immediately after the drift period the temperature was raised with a constant ramp rate until the cell crystallized. This was repeated for various ramp rates as schematically depicted in the lower inset (see article text for more details).* ***(b)*** *The activation energy for crystallization (E_C) vs the number of switching cycles. E_C was obtained from the crystallization temperature measured at different ramp rates using the Kissinger analysis. Unlike the crystallization temperature at a fixed ramp rate the activation energy did not show a significant evolution during cycling.*

6.5 Discussion

6.5.1 Initialization phase

It was shown in Fig. 6.3 that the amorphous cell resistance increases sharply during the first one hundred cycles. This increase is accompanied by a decrease of the resistance drift exponent α from 0.075 ± 0.007 to 0.04 ± 0.01. Generally, drift has been attributed to either the dynamics of intrinsic traps [78] or to stress release [63] of the programmed amorphous region of the phase-change material. With each RESET pulse the crystalline to amorphous phase change causes a volumetric expansion of the order of 6% [75, 98]. However, also the material surrounding the active phase-change material can respond to and accommodate the volumetric expansion. This accommodation will definitely also occur during the initialization phase and then will not be an effect that is reactivated (RESET) by each RESET pulse, but will be a continuous process like we observed during the first ≈ 100 cycles (see Fig. 6.3). The fact that we observed such strong initialization effects can be explained by a settle-in/compression of the surrounding (relatively) soft inorganic resist (HSQ) still present on top of these cells. TEM images have confirmed that after the initialization the line narrows at the location of the amorphous mark. As the relatively soft resist is compressed the molten region (with 15×75 nm^2 cross section perpendicular to the current direction) takes a more circular shape due to surface tension of the molten material. The total surface area of the cross section stays (roughly) the same as the current during melting does not change significantly.

Therefore after each RESET pulse stresses are generated that can subsequently relax in time and can thus be associated with the observed drift. This explanation is consistent with reported drift coefficients of capped and uncapped nanowires that show more drift and much higher values of α when the programmed region is more rigidly constrained [63]. It also explains why in the initialization phase the drift exponent decreases, because the programmed region becomes less constrained. It is important to note that also the increase in amorphous resistance during the first one hundred cycles is consistent with the larger volumetric freedom the active phase change region gets with accommodation of the soft resist. However this view contradicts the experimental evidence of Ref. [78] where resistance drift could be repeated with pulses of insufficient energy to either crystallize or melt the cell.

Therefore, a second explanation is provided that correlates with the experimental evidence presented in this study and of both Ref. [78] and [63]: The actual increase of the amorphous resistance as a function of time is predominantly related to annihilation of traps, in line with Ref. [78] (although stress release during drift is in principle possible). Stress release or accommodation occurs in the material surrounding the active region during the RESET pulse. The increased stress present at the initial cycles is stable after cooling and during drift. Compressive stress narrows the band gap of the amorphous state [78] that could lead to a stronger relation between the amorphous resistance and the number of traps i.e. changing the value of the drift coefficient. It is important to note that in both explanations the material surrounding the active region becomes compressed during the first 100 cycles leading to lower

compressive stress within the phase-change material. The only difference is whether the drift of the amorphous resistance is directly related to stress release [63] or that the amorphous resistance is a function of the number of traps [78] which is modified by stress.

Within the initialization phase the threshold voltage continuously decreases during cycling. This implies that an inverse relation holds between the threshold voltage and amorphous resistance in the initialization phase. This clearly implies that the increase in amorphous resistance cannot be attributed to merely an increase of the length of the amorphous region in the line cell, but must be related to the increased freedom to expand. The crystalline resistance shows a large increase followed by a decrease to a value still higher than the initial resistance. However, the resistance during melting (during the RESET pulse) and crystallization (during the SET pulse) do not evolve significantly. Various factors can play a role in this peculiar behavior of the crystalline resistance, but the following explanation appears most consistent: The initial increase in crystalline resistance is caused by increasing tension in the line as it crystallizes and shrinks, because the PC material in the line remains bonded to the surrounding material that expands (in response to the expansion of the amorphous phase). This is in agreement with the previous explanation for the increasing amorphous resistance and decreasing drift exponent. After a certain number of cycles, corresponding to the maximum in the crystalline resistance, the PC material in the line physically becomes separated from the surrounding material and the crystalline phase is able to relax and can adopt a lower resistance. This separation can be directly observed using TEM as a narrowing (and most likely a thickening) of the line at the location of the amorphous mark (see Chapter 8).

6.5.2 Usable life phase

The cell behavior during the first $3.3{\cdot}10^5$ cycles showed a very consistent behavior (Fig. 6.9(a)). For pulse heights up to 4.5 volts the amorphous resistance increases slightly with pulse height and a decrease in amorphous resistance is observed for pulses larger than 4.5 volts. This anomalous behavior is an over-programming artifact: The thermo-electric Thomson effect [9] that was observed on line cells of identical composition (but different processing conditions [9]) causes an asymmetrical thermal distribution in the line during programming. When applying more current than necessary and desirable for switching (over-programming), part of the amorphous mark will appear partly outside the line and into one flap of the dog bone shaped phase change material. TEM images have confirmed that this is indeed the case (see Fig. 8.3). The amorphous region present outside the line that was not programmed before can display initialization effect complicating the analysis.

It is important to note that the conduction mechanism at low carrier concentrations (ohmic region at low read voltages) is fundamentally different from the conduction mechanism at high carrier concentrations. The RESET (and also SET) pulse always leads to a large current density (typically $7{\cdot}10^{11}$ A/m^2 during the RESET pulse) and large electric fields ($\approx 10^7$ V/m) within the line cell. During the RESET pulse (and SET pulse), the atoms in the programmed region become mo-

bile [83, 34, 39, 65, 102, 103]. Atoms can be ionized and Sb^{3+} and Te^{2-} will move in opposite directions to the electric field. This movement particularly occurs in the molten region during the RESET pulse [102, 73].

A natural consequence of this ionization of mobile atoms is that electro-migration will take place during cycling and that the phase-change material will experience decomposition. Our observations show that the usable life phase of the line cell is characterized by a decrease of (i) the amorphous resistance (see Fig. 6.3), (ii) crystalline resistance (see Fig. 6.3), (iii) threshold voltage (see Fig. 6.10) and (iv) crystallization temperature (see Fig. 6.10). These observations are indeed consistently explained by decomposition of the programmed region caused by electro-migration. During the RESET pulses the ionized atoms move in different directions with respect to the electric field. This will lead to regions enriched in either Sb or Te. Starting from the homogeneous phase-change alloy the decomposed alloy will always lead to a lowering of the crystallization temperature. It will be more difficult to produce amorphous regions in the decomposed material since a part of the melt-quenched region is able to re-crystallize. Therefore, with smaller amorphous marks the amorphous resistance and threshold voltage will decrease [105].

Our measurements clearly indicate that the molten region during the RESET pulse is not affected by cycling; only quenching of this molten state into the amorphous state becomes increasingly difficult beyond $\approx 3.3{\cdot}10^5$ cycles. Finally amorphous marks cannot be produced (with the standard pulse settings) anymore beyond 10^7 or 10^8 cycles and the cell becomes stuck in the SET state (end of life). This is exactly what we observe and is thus consistently explained by electro-migration induced decomposition of the phase-change material. Only with increasing the magnitude of the RESET pulse an amorphous region can be created. The region that melts during the pulse needs to be much larger to accommodate recrystallization. However, then also decomposition is accelerated by the higher programming current.

Figure 6.9(a) shows that the RESET pulse height chosen for the majority of the cycles (Fig. 6.3) was at the maximum amorphous resistance up to $3.3{\cdot}10^5$ cycles where the line is fully amorphous. Afterwards, the decomposition started to become dominant and the shape of the amorphous resistance versus pulse height changed significantly (Fig. 6.9(a)). Instead of having a maximum, the amorphous resistance developed a long slope that is explained by partial re-crystallization after the RESET pulse. Decomposition fundamentally changes the amorphous structure and crystallization temperature. As the crystallization temperature decreases the cell will naturally spend more time above the crystallization temperature as it melt-quenches. Recrystallization will lead to a smaller amorphous mark that will be more sensitive to ubiquitous spurious pulses ('spontaneous' SET, see Section 6.4.3 and 6.9(b)). This is exactly what we observe.

6.5.3 Temperature and activation energy of crystallization

The activation energy of crystallization (Fig. 6.11(b)) did not evolve significantly during cycling, because it is quantified as 2.2 ± 0.2 eV independent of cycling. A strong relation between activation energy and the dielectric material surrounding the

phase change material was reported recently [30]. Different activation energies where reported for identical phase change material when either SiO_2 or ZnS:SiO_2 where applied as a top layer. Furthermore, line cells with identical composition but instead capped with a SiO_2 passivation layer yielded an activation energy of 3.3 eV (Fig. 5.4. Therefore the lack of evolution, within the error margin, of the activation energy measured here is an indication that the HSQ capping layer largely determines the activation energy. Phase change line cells of identical composition as presented in this study but capped with SiO_2 had been found to have a higher activation energy of 2.7 eV (Chapter 4) and 3.0 eV (Chapter 5). A decrease in activation energy from 2.4 eV to 1.75 eV was reported in literature for an increase in Sb content [105]. Although our measurement data were obtained for a much broader ramp-rate range than those of Ref. [105] we believe that isochronal measurement data are needed with a larger range before such a statement can actually be proven. Moreover, we measure in the line cells the combined effect of separate regions becoming enriched in either Te or Sb and therefore the measured activation energy is not directly related to a material with only an increased Sb content.

Figure 6.10 shows that during cycling the crystallization temperature (measured at a ramp rate of 30 K/minute) decreased continuously from 125 °C to 90 °C. This decrease in crystallization temperature is accompanied by a decrease in threshold voltage. Although a reduction in programmed volume (length of the amorphous mark) will lead to a lower crystallization temperature and threshold voltage, it cannot, on its own, explain the drop in both quantities over the complete life of the cells. A reduction of the amorphous mark length of three orders of magnitude would be required to explain the observed change in crystallization temperature which is not in accordance with the observed limited change in threshold voltage and amorphous resistance. However, it can be associated with part of the life cycle, in particular after $3.3{\cdot}10^5$ where re-crystallization of the amorphous region is believed to become apparent (Section 6.5.2). Our conclusion is that the threshold voltage and crystallization temperature are both closely related to the decomposition of the amorphous volume (see inset of Fig. 6.10). The decomposed material, with separate regions enriched in either Sb or Te, exhibits an overall lower crystallization temperature. As a consequence the amorphous-phase resistance and the threshold voltage also decrease. The threshold field, at which electrical breakdown occurs, is known to vary greatly among materials [52, 45]. Furthermore, the extrapolated threshold voltage at zero amorphous mark size is finite and also material dependent [23, 36, 49, 45]. The phenomenological threshold voltage is therefore related to both quantities and the length of the amorphous mark. A decrease of both the crystallization temperature and threshold voltage accompanied by a decrease of the amorphous resistivity of almost an order of magnitude was observed for increasing the Sb content in Sb_xTe_{1-x} alloys ($x \geq 0.64$) [105] which is consistent with our data.

The general view today is that the electrical breakdown during the threshold event is a purely electrical phenomenon [78, 45, 87]. However, Karpov et al. [36] have provided an alternative explanation that relates threshold switching to nucleation of conductive (cylindrical) crystalline filaments induced and stabilized by the electric field. Although the doped SbTe alloy used here (see Chapter 3). is a fast growth

material, with little chance of nucleation, the crystallization kinetics at sub-threshold field strength could be fundamentally different. For completeness, we put forward this alternative explanation for threshold switching, because it naturally explains our observation that the threshold voltage is directly related to the crystallization temperature.

6.6 Conclusions

This work presents an extensive study on phase change random access memory, and in particular the horizontal line cell geometry [52]. Many cell properties (i.e. the amorphous and crystalline resistances, amorphous resistance drift, threshold voltage, threshold-voltage drift, crystallization temperature, and activation energy for crystallization) were measured during cell cycling on the same cells and can therefore be directly related. Cells can be cycled typically 100 million times and show stable properties after an initialization phase of about 100 cycles up to about $5{\cdot}10^5$ cycles. Beyond this number of cycles the amorphous resistance, the threshold voltage and the crystallization temperature decrease significantly. This behavior is attributed to electromigration induced decomposition of the active phase-change material in the line cell.

Generally, it is assumed and also demonstrated that the threshold voltage (V_T) and the amorphous phase resistance (R_a) are linked in a rigid way. We show that in our measurements the R_a is not the dominating factor for predicting the threshold voltage V_T. By varying the magnitude of the RESET pulse the R_a shows a peak value while the threshold voltage V_T continuously increases leading to both a positive and negative dependence between R_a and V_T. Furthermore, the evolution of the threshold voltage can be linked to the evolution of the crystallization temperature. The crystallization temperature and threshold voltage appear to continuously decrease during cycling due to electromigration induced decomposition and follow a remarkably similar trend.

As the crystallization temperature drops, the molten region can partly re-crystallize as it is melt-quenched, i.e. more time is spent above the crystallization temperature leading to smaller amorphous mark, which starts to become apparent after $\approx 3.3{\cdot}10^5$ cycles. Finally the cell becomes stuck in the SET state after typically 10 to 100 million cycles. Although the material is still molten during the application of a RESET pulse this does not load to an amorphous melt-quenched state as the cell fully crystallizes directly after the pulse.

Chapter 7

Resistance drift and the activation energy of conduction

7.1 Abstract

Temporal drift of the amorphous resistance in Phase-change Random Access Memory is a temperature accelerated process. Increasing the temperature will speed up the drift process which is shown to affect measurements of the activation energy of conduction (E_A, slope of $log(R)$ versus $1/kT$). Doped SbTe phase change (PRAM) line cells were brought to the amorphous state and were subjected to annealing experiments. First it is shown that when the temperature is increased by a fixed rate the resistance does not follow a unique function of temperature but depends on the heating rate. This can be attributed to resistance drift taking place during the ramp. Upon cooling the drift process freezes and only then physically relevant, i.e. time independent, values for E_A can be obtained, because of the absence of additional drift. The observed increase in resistance as a function of annealing history (for various frozen-in drift levels) is modeled and well-reproduced using a trap limited band transport model. The model explains these observations by an increase of the temperature dependent band gap by about 47 meV due to drift at 418 K.

Published as:
J.L.M. Oosthoek, D. Krebs, M. Salinga, D.J. Gravesteijn, G.A.M. Hurkx, B.J. Kooi
J. Appl. Phys. **112**, 084506 (2012).

7.2 Introduction

Phase change random access memory (PRAM) is one of the most promising candidates for the next-generation of non-volatile memories [84]. A well-known and important phenomenon found in PRAM in general is that the amorphous resistance is not stable in time [78]. After a cell is brought to the amorphous state (e.g. by applying a RESET pulse), the resistance drifts (increases) as a function of time by a power law when kept at a constant temperature. Values for the power law exponent vary for different cell types (also meaning geometrically identical cells with the same phase-change material, but produced by different methods) typically between 0.04 and 0.1 (see Chapter 6 and [84, 78, 35, 63, 7, 23, 5]).

Resistance drift is not necessarily a problem for a memory based on two distinct stable states, since (in the absence of crystallization) the contrast between the states improves in time. However, multilevel memory applications are based on programming the cell to different amorphous states [104, 67] with resistances in the whole range of typically three orders of magnitude between the fully crystalline and maximally amorphous state. Here the resistance drift poses the danger of one state drifting into the resistance window of the next state. Furthermore, resistance drift is a temperature accelerated process [23, 26, 46]. Increasing the temperature will speed up the drift process. This process of drift qualitatively shows similar behavior at a large range of temperatures [26]. Therefore, when performing temperature dependent measurements on amorphous cell properties, the effect of drift has to be taken into account. One important parameter is the activation energy of conduction E_A [78, 72, 81] of the amorphous phase. In the simplest model of a single carrier semiconductor1 (p-type here [9]) E_A can be linked to the difference between the valence band and the Fermi energy level for hole conduction [78] and is about half the value of the band gap [78, 1]. E_A is commonly obtained directly from the slope of the (natural logarithm of the) resistance R as a function of temperature T (i.e. $log(R)$ versus $1/kT$ where k is Boltzmann constant) and thus provides information on the band gap of the amorphous phase. In literature an increase of E_A with drift was reported [78, 5, 46, 24, 25]. Two studies [78, 5] were based on direct measurements obtained from the resistance data. One of these studies [78] reported an increase of E_A from 0.22 eV as determined directly after RESET to 0.38 eV after annealing at 443 K. Another study [5] reported that the activation energy measured after annealing at a temperature of 363 K increased by 40 meV after subsequently annealing at 403 K. Furthermore, the increase in activation energy upon drift has been related to an increase in the optical band gap [46].

In order to measure the activation energy from resistance data, care must be taken to properly separate the effect of temporal drift from the regular negative temperature dependence [78, 5, 72]. In this paper it will become clear that the activation energy of conduction cannot be obtained from the slope of the resistance versus temperature data by directly heating the cell after RESET as has been done regularly in previous works. It will be shown that when drift occurs during the measurement, a lower value of the slope of $log(R)$ versus $1/kT$ will be found during heating. Therefore, any apparent increase of the slope with drift will appear to overshadow the actual

physically relevant increase of E_A. Furthermore it is shown that even in the absence of (additional) drift the temperature dependence of the band gap, and thus the activation energy, has to be taken into account.

7.3 Experimental

PRAM line cells with dimensions 700(±10)x340(±40)×20 nm^3 were produced by optical lithography; details can be found in [9]. The cells were switched with a Tektronix AFG3102 arbitrary function generator allowing for 50 ns RESET pulses with 3 ns edges. The cell resistance was measured with a Keithley 2600 source meter at 0.1 V. The cell temperature was accurately controlled with a PID controller and a linear power supply connected to a heating filament located close to the cell. Cooling was performed passively by switching off the power supply. To reach temperatures below room temperature (298 K) the stage is connected thermally to a liquid nitrogen reservoir by a ≈ 50 cm copper heat conductor.

7.4 Results

In a first experiment a PRAM line cell was switched to the amorphous state and the resistance was subsequently measured as a function of time (Fig. 7.1(a)). Note the excellent reproducibility when this measurement is repeated after various annealing histories. The resistance follows the well-established power law behavior [78] $R = R_0 \cdot (t/t_0)^\alpha$ with α=0.081. 1000 seconds after RESET the temperature was increased by a fixed ramp rate until the cell crystallized (resistance dropped below 10 kΩ). As the phase-change material is of a fast growth type the crystallization behavior is characterized by a sharp drop in resistance (see Fig. 4.3(a)) when two crystal growth fronts meet (see Fig. 4.2) Since this study mainly focuses on drift, the final crystallization is not shown in Fig. 7.1(b) to aid readability. After cooling back to 298 K the cell was fully crystallized by a SET pulse to crystallize any remaining amorphous regions. The experiment was performed for a wide range of ramp rates (15, 8, 4, 2, 1, 0.5 K/min). The resistance curves are plotted in Fig. 7.1(b) as a function of $1/kT$.

Figure 7.1(b) clearly shows that the measured amorphous resistance is not a unique function of the temperature. Although the resistance curves during the temperature ramp all start from the same point R_S at 298 K, the curves diverge as the temperature is increased. This is quantified in Fig. 7.1(a) where the slope of $log(R)$ versus $1/kT$ is calculated from the start of the ramp. The slope has been identified with the activation energy of conduction [78, 72, 81]. The obtained values of the slope at the start of the ramp range vary between 0.17 eV and 0.24 eV. It is considered to be highly unlikely that the band gap differs with a factor of 1.4 while the resistance and its drift measured only seconds before at 298 K was completely reproducible. Above 333 K the slopes of all curves are equal to about 0.17 eV. The resistance values of the slowest ramp at a given temperature remain a factor of two higher than the resistance values measured during the fastest ramp at the same temperature. This can be explained

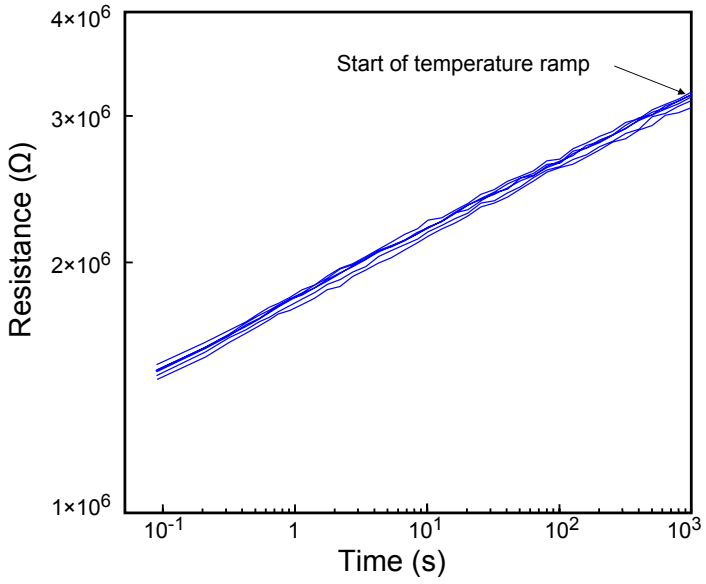

(a)

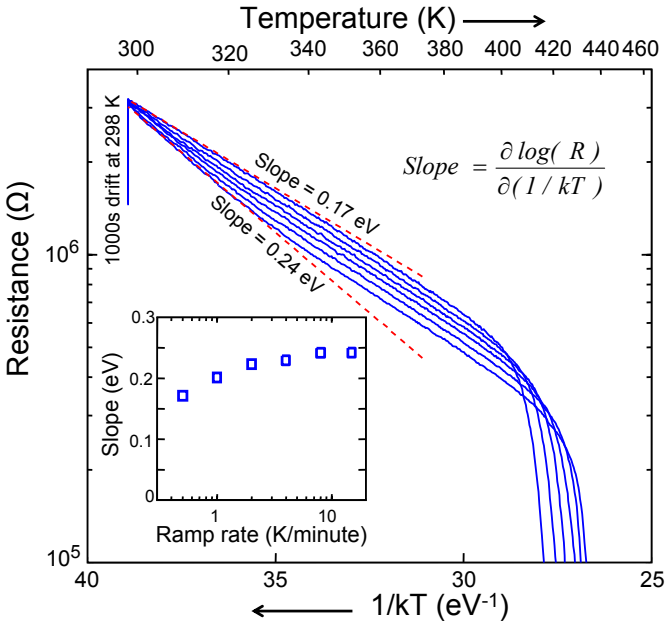

(b)

Figure 7.1: ***(a)*** *After RESET, the cell resistance was measured as a function of time for 1000 seconds.* ***(b)*** *1000 seconds after RESET the temperature was increased with a constant ramp rate until the cell crystallized. This was repeated for a wide range of ramp rates (15, 8, 4, 2, 1, 0.5 K/min). The x-axis has been reversed so the cell temperature increases to the right. The slope of the resistance versus* $1/kT$ *(obtained from the data below 333 K) depends on the ramp rate (see inset).*

by the lower ramp rates taking longer to reach a given temperature allowing for more drift and thus leading to a higher cell resistance. Clearly, the reversible temperature dependence and the irreversible drift are entangled in this measurement. In the following we will present data in which the two contributions to the resistance will be separated. The question is now which one, or if any, of the measurements of the slope can in fact be interpreted as physically relevant measurement of the activation energy of conduction. The answer is given below and would correspond to heating with the highest possible ramp rate (i.e. close to 0.24 eV), but it has to be emphasized that this is not a reliable procedure; a reliable method is outlined below.

Figure 7.2(a) shows the cell resistance as a function of temperature for a single temperature ramp (10 K/min) that was started at 1000 seconds after RESET (blue curve). Figure 7.2(b) shows the resistance as a function of time after RESET from the same measurement (also blue curve). A drift coefficient $\alpha = 0.08$ was obtained. This measurement (blue curve) serves as a reference measurement. After crystallization, the cell was RESET again and allowed to drift at 298 K for 1000 seconds. The cell is now subjected to a more complicated temperature-time profile (green curve in Fig. 7.2(a) and 7.2(b)). Instead of a continuous temperature ramp a series of interrupted ramps were applied (each with 10 K/minute). Each subsequent temperature ramp had a higher peak temperature and after each ramp the temperature was returned back to 298 K. The first ramp had a peak of 348 K. It can be observed in Fig. 7.2 that this interrupted curve overlaps with the previous uninterrupted curve up to this peak temperature. This shows the excellent reproducibility of the measurement, because up to this point the time and temperature profiles were exactly the same. The slope at the start of the ramp has a value of 0.24 eV and, as also observed in Fig. 7.1(b), the resistance curve shows evidence of drift as the temperature reaches 348 K shown by the slight increase of the resistance at the peak temperature. Directly after reaching 348 K the temperature was decreased back to 298 K. The slope of the descending temperature ramp equals 0.26 eV, notably different from the previous ascending ramp. Directly after the previous resistance measurement at 298 K, the temperature is brought back up to 348 K (Fig. 7.2(b)). Now the cell resistance follows exactly the same values of the previous descending curve except for the temperature just below the former peak temperature of 348 K (Fig. 7.2(b)). Clearly, the cell properties have not been changed during the ramp down followed by a ramp up. As the temperature is further increased close to 348 K and beyond, the $R(T)$ curve starts to resemble the uninterrupted (blue) curve. The same heating-cooling cycle is repeated with a next peak temperature of 398 K and in principle shows similar behavior as for the peak temperature of 348 K. The slope of 0.26 eV is roughly the same when descending from 398 K. The resistance, though, is at a higher absolute level than for the previous cooling curve after annealing only up to 348 K. During a final ramp to 423 K the cell is eventually crystallized. In summary, Fig. 7.2(a) shows that the resistance curve during each cooling ramp is reproduced during the directly following heating ramp. This is important, because it shows that a time-independent slope of $log(R)$ versus $1/kT$ can be obtained, which can be considered a physically relevant measure of E_A. As the ramp is increased beyond the previous maximum temperature, the resistance curve (green) resembles the one for the single

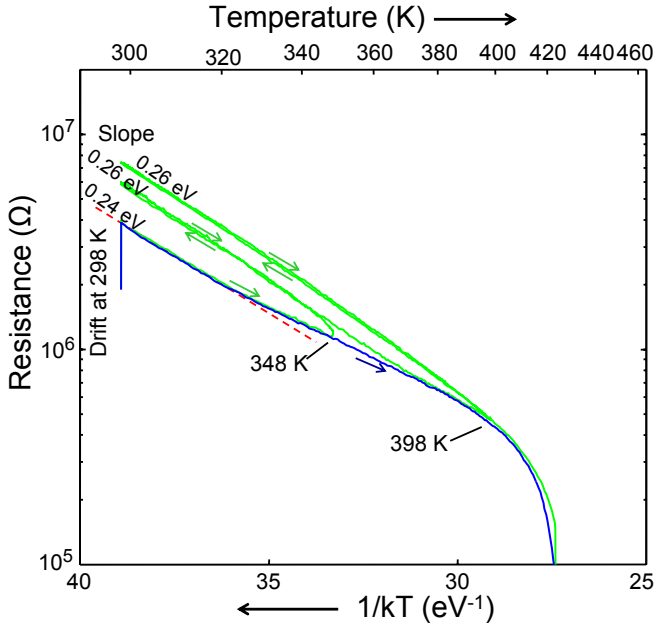

(a)

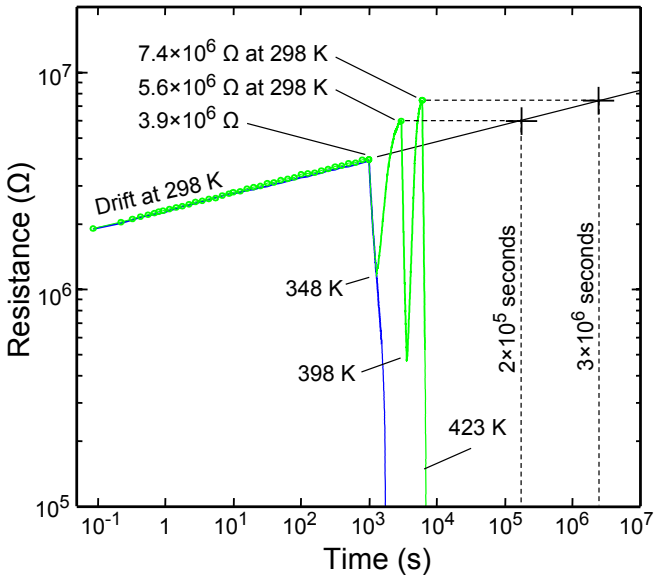

(b)

Figure 7.2: *Cell resistance as a function temperature* ***(a)*** *and time* ***(b)*** *for a PRAM line cell switched to the amorphous state at 298 K. The blue line shows the cell being crystallized by a single uninterrupted temperature ramp initiated 1000 seconds after RESET. At 298 K the cell was RESET again and a series of temperature ramps were applied with peaks at 348 K, 398 K and 423 K and each time cooling down to 298 K (green curves). The elevated temperatures experienced during the ramps accelerated the resistance drift compared to the drift at 298 K.*

uninterrupted ramp (blue) and we again enter a region where the slope becomes time dependent, because it is affected by additional drift. The cell resistance at a constant temperature increases in time by the well-established power law dependence [78]. Figure 7.2(b) shows that after each interrupted ramp the resistance at 298 K has been increased more than what would be expected from the extrapolated power law dependence (black line). Clearly, the temperature ramps accelerated the drift. The resistance at 298 K after a heating-cooling cycle with a peak at 348 K and 398 K were measured at $3.0{\cdot}10^3$ seconds and $6.1{\cdot}10^3$ seconds respectively after the RESET pulse (Fig. 7.2(b)). But the cell resistance at 298 K increased from $3.9{\cdot}10^6$ Ω just before the first cycle to $5.9{\cdot}10^6$ Ω after the first cycle and $7.4{\cdot}10^6$ Ω after the second cycle. Figure 7.2(b) indicates that these resistance values are the equivalent of a continuous uninterrupted drift at 298 K of $2{\cdot}10^5$ seconds (more than two days) and $3{\cdot}10^6$ seconds (five weeks), respectively. The heating-cooling cycle to 398 K thus increased the (equivalent) drift time by a factor of 500.

The values of E_A after the ramps to 348 K and 398 K remained rather constant even though the resistance at 298 K did increase due to drift by a factor of 1.5. The relation between the amorphous resistance at 298 K and E_A is further investigated with a more elaborate measurement. A PRAM cell was brought to the amorphous state and the resistance was measured at 298 K for 20 seconds. Figure 7.3(a) and 3c show the resistance as a function of temperature and time, respectively (blue curve). Figure 7.3c shows the first twenty seconds after RESET plotted on a double-logarithmic scale to show that the cell follows the power law for two orders of magnitude in time. A drift coefficient of $\alpha = 0.09$ was obtained. Then the temperature was increased with a 10 K/min ramp rate until the cell crystallized (blue line). Figure 7.3(a) shows that as the temperature increases, the resistance decreases first with a slope of 0.12 eV (to 303 K) and above 313 K with a slope of 0.19 eV. Next, the cell was RESET again at 298 K and after the cell drifted for twenty seconds the temperature was decreased to 276 K. As the temperature decreases, the resistance initially has a slope of 0.37 eV and below 290 K has a slope of 0.25 eV. As mentioned above, this apparent discrepancy can simply be explained by drift still occurring during both ramps leading to increased or decreased values for the slope depending on the ramp direction, i.e. either cooling or heating respectively. In the previous measurements (cf. Fig. 7.2), before any annealing cycle the device was allowed to drift at room temperature for 1000 seconds; sufficiently long that a subsequent decrease in temperature would not cause observable influence of drift on the resistance. However, since in this experiment only 20 seconds of drift were allowed prior to the temperature cycle, a reduction in temperature still shows initially a behavior influenced by drift, as can be observed from the first part of the green curve in Fig. 7.3(a) (i.e. the blue and green curves have clearly different initial slopes at 298 K). Subsequently, starting from 276 K a series of heating-cooling cycles with a peak at 298 K, 308 K, etc. were applied while the cell resistance was measured. Figure 7.3(a) shows the resistance as a function of temperature. The red data points in Fig. 7.3 correspond to the resistances at 298 K.

Due to the constant heat flow between the temperature stage and the liquid nitrogen reservoir and the heat capacitance of the copper heat conductor (not present during the measurements shown in Fig. 7.1 and 7.2 a small but significant discrepancy

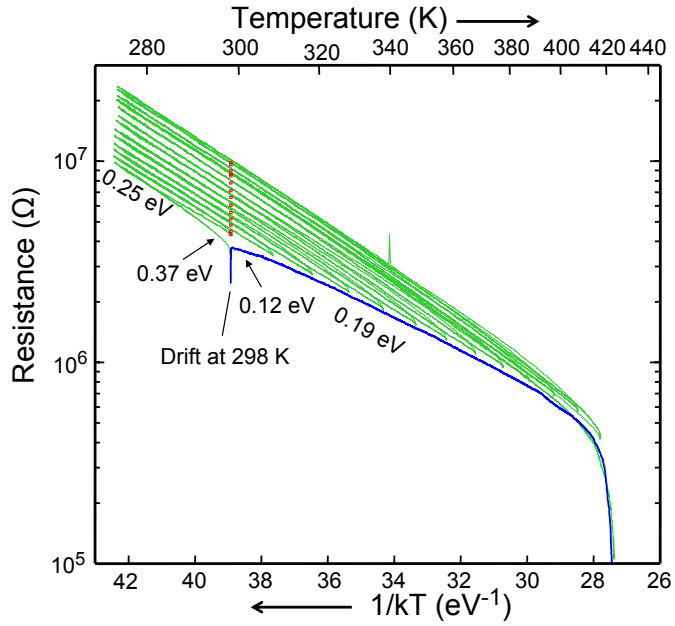

(a)

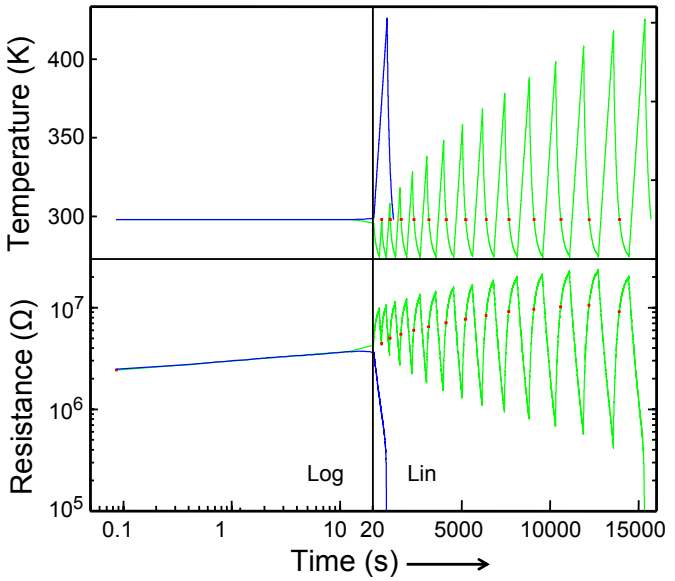

(b)

Figure 7.3: *Cell resistance as a function temperature* ***(a)*** *and time* ***(b)*** *for a PRAM line cell switched to the amorphous state at 298 K. The blue line shows the cell being crystallized by a single uninterrupted temperature ramp initiated 20 seconds after RESET. At 298 K the cell was RESET again and after 20 seconds the temperature was lowered to 276 K. A series of temperature ramps were applied with a peak at 298 K, 308 K etc. and each time cooling down to 276 K (green curves). The red dots indicate the resistance at 298 K obtained during the ramp after each peak.*

exists between the cell temperature and the measured temperature. The temperature shown in Fig. 7.3 was compensated for this effect by a thermal capacitive model on the basis of the evidence of Fig. 7.2 allowing for a maximum correction of 1 K. From Fig. 7.3(a), values of the activation energy were obtained from the (time-independent) slopes of the temperature curves. Each data point represent a measurement performed after the indicated peak anneal temperature in the temperature range below 298 K. The obtained activation energies are shown as a function of the previously experienced peak anneal temperature in Fig. 7.4 together with a fit to the data. Also, Fig. 7.4 shows the resistance measured at 298 K plotted as a function of the (previously experienced peak) anneal temperature. Figures 7.3 and 7.4 show that the resistance at 298 K as well as the activation energy increases slightly due to the application of the temperature ramps each time to a higher maximum temperature. The resistances measured at 298 K after annealing to the highest temperatures were probably due to partial crystallization. Along with the experimental results, simulated resistance and activation energy are plotted in Fig. 7.4 (red line). The applied model explaining the increase of R^* and E_A will be discussed in the following section.

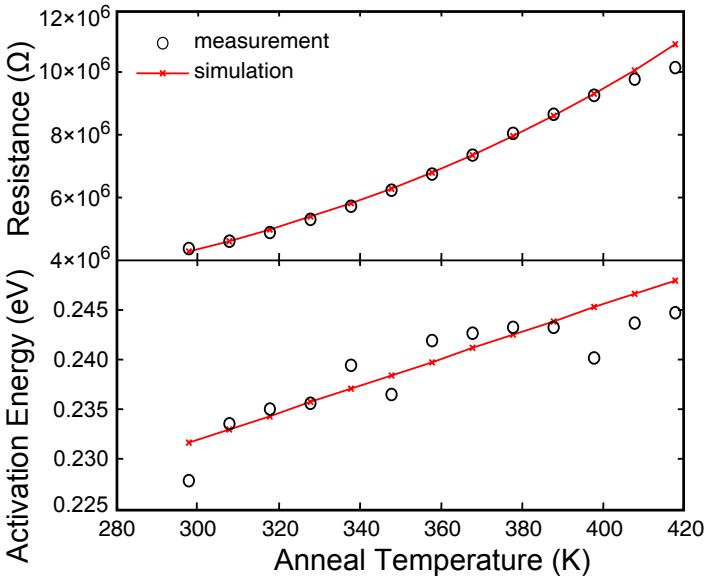

Figure 7.4: *Resistance measured at 298 K and activation energy E_A extracted from the cooling ramps in Fig. 7.3 below 298 K (black circles). The anneal temperature on the horizontal axis refers to the maximum temperature that has been reached prior to the measurement at and below 298 K, Both, resistance and activation energy at 298 K increase upon drift due to the temperature dependence of the activation energy. The simulation reproduces this behavior (red line).*

7.5 Discussion

Different physical interpretations of the nature of charge conduction and drift of the amorphous phase are proposed in literature [78, 35, 63, 5, 25]. Assuming that the electrical transport of phase change materials can be described with semiconductor behavior [78, 5, 72], the resistance can be written as:

$$R = R^* \cdot e^{\left(\frac{E_A}{kT}\right)} \tag{7.1}$$

The activation energy E_A, typically assumed to be a temperature-independent constant, is roughly half the optical band gap E_G [78]. Therefore it is commonly assumed, that the Fermi level E_F is pinned in the middle of the band gap. For hole transport electrons need to be activated from the band edge at $E_V = 0$ to above the Fermi level leaving holes behind and the activation energy can be written as:

$$E_A = E_F - E_V = \frac{E_G}{2} \tag{7.2}$$

Varshni found a general empirical law for the temperature dependence of the optical band gap in semiconductors with α, β and E_0 being empirical parameters [97].

$$E_G = E_0 - \frac{\alpha T^2}{T + \beta} \tag{7.3}$$

For various phase change materials it has been shown experimentally that they follow a simplified version of this law [56, 47].

$$E_G = E_0 - \xi T^2 \tag{7.4}$$

Typical values for E_0 and ξ for amorphous phase change materials like GeTe and $Ge_2Sb_2Te_5$ are about 0.9 eV and 1.3 eV/K2, respectively. Clearly, this temperature dependence needs to be taken into account when calculating resistances using Eq. 7.1 and Eq. 7.2. Furthermore, it has been shown that after accelerated drift by annealing, the band gap is increased [46, 13] while the shape of the temperature dependence is preserved [57]. In particular for GeTe an increase of the band gap upon annealing at 413 K by about 9% has been measured [57]. Based on these findings the temperature dependent resistance shown in Fig. 7.3(a) has been modeled using Eq. 7.1, Eq. 7.2, Eq. 7.4 and the parameters of Table 7.5. The parameters are chosen to reasonably fit the experimental data. E_0 is lower than for GeTe or $Ge_2Sb_2Te_5$ because the optical band gap of doped SbTe compounds are lower [69, 82]. The temperature dependence of the band gap ξ is assumed to be in the same range as for other phase change materials and the pre-exponential factor R^* is adjusted in order to account for the device geometry. The band gap increase is chosen to be just slightly higher than experimentally observed for GeTe.

Tabel 7.5: Parameters used in the simulation.

R^*	$1{\cdot}10^4\Omega$
E_0	0.39 eV
ξ	0.9 µeV/K^2
$E_0(T_a = 418\text{ K})/E_0(T_a = 298\text{ K})$	1+0.12
$\xi(T_a = 418\text{ K})/\xi(T_a = 298\text{ K})$	1-0.12

The temperature dependence of the band gap for annealing temperatures from 298 K to 418 K is shown in Fig. 7.5. The lowest (blue) curve corresponds to the temperature dependence right after RESET at 298 K. The highest (red) curve corresponds to the temperature dependence of the band gap after the device has drifted at 418 K (and thus has obtained a frozen-in drift state for temperatures lower than 418 K) leading to an assumed increase E_0 by 12% and an assumed decrease of ξ by 12%. Between the initial band gap after RESET and the maximum band gap increase, a linear increase of the band gap with annealing temperature is assumed as a first order approximation. The intermediate curves correspond to 10 K steps in the range between 298 K and 418 K, where it is assumed that the drift after each increase of 10 K leads to a change of the band gap parameters by 1%. This way, the band gap is increased while the shape of its temperature dependence is preserved after drift at the various annealing temperatures. As indicated, each curve in principle only holds for a temperature lower than its corresponding annealing temperature, because only then additional drift can be neglected.

Calculating the resistance using this temperature dependent band gap after different sequential annealing steps yields the resistances shown in the lower panels of Fig. 7.6. For comparison, the experimental data from Fig. 7.3 are plotted in the upper panels using identical x- and y-scales. As Fig. 7.6(a) shows, the absolute resistance as a function of temperature is matched correctly and also the increase of resistance can be explained quite accurately by an increase of the band gap by 12%. Not obvious in Fig. 7.6(a), Fig. 7.6(b) reveals that all curves deviate significantly from a strict Arrhenius behavior. This is a natural consequence of the temperature dependence of the band gap and, thus, activation energy. As shown in Fig. 7.5, around 298 K the temperature dependence is linear (to a first approximation) following roughly $E_G/2 = E_A = E_0 - \gamma T$. Inserting this into Eq. 7.1 yields:

$$R = R^* \cdot e^{\left(\frac{E_a}{kT}\right)} \approx R^* \cdot e^{\left(\frac{E_0 - \gamma T}{kT}\right)} = R^* \cdot e^{\left(\frac{-\gamma}{k}\right)} \cdot e^{\left(\frac{E_0}{kT}\right)} \tag{7.5}$$

Therefore, the temperature dependence of the activation energy around room temperature results in a decrease of the pre-exponential factor R^* by $exp(-\gamma/k)$. Furthermore, the slope of the Arrhenius plot shows an activation energy that is higher than the difference between $E_F - E_V$. In our case, the real activation energy for holes $E_F - E_V$ at room temperature equals $E_G/2 = 0.15$ eV (see Fig. 7.5) while the slope

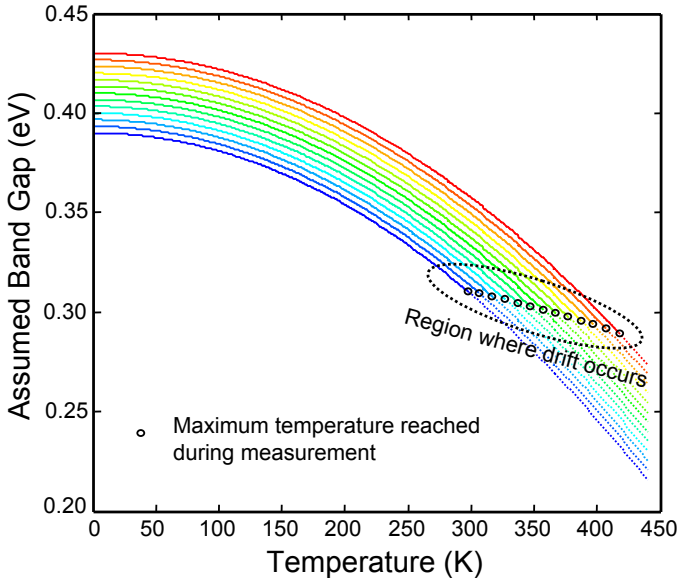

Figure 7.5: *The lowest (blue) curve corresponds to the temperature dependence right after RESET at 298 K. The highest (red) curve corresponds to the temperature dependence of the band gap after the device has drifted at 418 K leading to an assumed increase of the band gap by 12%. The intermediate curves correspond to 10 K steps in the interval 298 418 K.*

of the Arrhenius plot yields roughly 0.23 eV (Fig. 7.4). To keep the model simple the activation energy was assumed to be equal to half the band gap which is not necessarily the case. However, a natural consequence of the temperature dependence of the band gap is that the measured activation energy appears to be larger than the true activation energy. This is true regardless of the position of the Fermi level within the band gap. This explains also why phase change materials typically are p-type even though the measured activation energy is half the optical band gap suggesting that the Fermi level is as close to the conduction band edge as to the valence band edge. In reality, the Fermi level is pinned closer to the valence band edge and only because of the temperature dependence the activation energy appears to be larger. This demonstrates how dangerous it is to neglect the temperature dependence of the band gap for modeling electrical transport behavior as it is common practice.

Since the temperature dependence of the activation energy leads to a contribution in R^* as well as the measured activation energy (slope of the Arrhenius plot), the increase of E_G upon annealing leads to an increase in bothas well as E_A. The increase of those parameters upon annealing determined from the simulation is plotted alongside the experimental results as red lines in Fig. 7.4. The nice match demonstrates that the typical temperature dependence of the band gap explains the unexpected behavior naturally without any artificial assumptions.

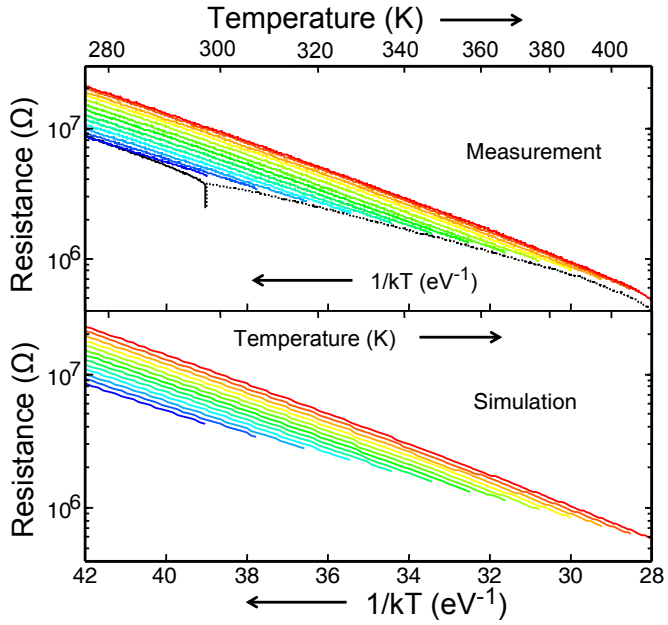

(a)

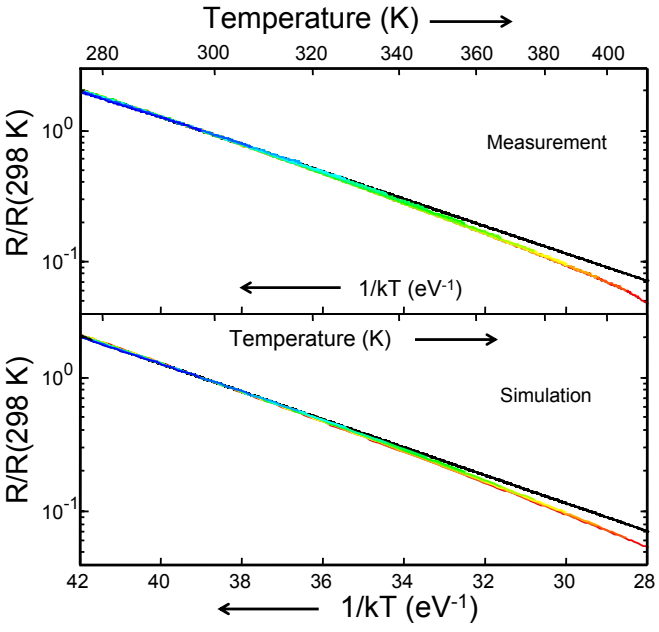

(b)

Figure 7.6: *Comparison of measurement and simulation of the absolute* ***(a)*** *and normalized* ***(b)*** *resistance of a device annealed to increasingly higher temperatures after RESET. The measurement data are identical to the once plotted in Fig. 7.3. The color code indicates the maximum annealing temperature the device was exposed to. The black lines in* ***(b)*** *are calculated from temperature independent activated behavior with an activation energy of* $E_A = 0.24$ *eV plotted for reference.*

7.6 Conclusions

When a phase-change memory cell is brought to the amorphous state and the temperature is increased by various fixed rates, the resistance is not a uniquely defined function of temperature (cf. Fig. 7.1(b)). In fact, resistance drift will occur during the temperature ramp, which will lead to a dependence of the resistance on the ramp rate. Lower ramp rates will allow more time for drift and lead to a higher resistance (R) at a specific temperature (T). In addition, by raising the cell temperature the effect of drift is accelerated. As drift progressively takes place during the measurement (i.e. temperature ramp) the activation energy for conduction (E_A) as based on the slope of R versus T is underestimated. Therefore, E_A cannot be obtained by increasing the temperature without properly taking resistance drift into account. In contrast, when the cell is cooled down, additional temporal drift does not occur at these lower temperatures and only then a time-independent slope of $log(R)$ versus $1/kT$ can be obtained, which can be considered a physically relevant measure of E_A. For doped SbTe, we showed that a ramp up to 413 K and cooling back to room temperature accelerates drift by a factor of 500 with respect to drift solely at room temperature. The activation energy of conduction and pre-exponential factor were measured as a function of annealing temperature (based on the time-independent slope of $log(R)$ versus $1/kT$ due the absence of additional drift below the annealing temperature). An increase of both parameters was observed and all the experimental results were reproduced excellently on the basis of a theoretical model that takes the temperature dependence of the optical band gap into account. According to our model the change of the optical band gap with changing temperature does not alter after various annealing temperatures from room temperature up to 418 K, but annealing increases the absolute value of the band gap by 47 meV. Still it has to be emphasized that the temperature dependence of the optical band gap has to be taken into account; neglecting it leads to a significant overestimation of the values derived for the optical band gap and pre-exponential factor.

7.7 Acknowledgements

M. Salinga acknowledges funding by DFG through the collaborative research centre SFB 917 Nanoswitches.

Chapter 8

Nanostructure-property relations for phase-change line cells

8.1 Abstract

Phase-change random access memory (PRAM) cells have been studied extensively using electrical characterization and rather limited by detailed structure characterization. The combination of these two characterization techniques has hardly been exploited and it is the focus of the present work. Particularly for improving the reliability of PRAM such combined studies can be considered indispensable. Here we show results for PRAM line cells after series of voltage pulses with increasing magnitude are applied, leading to the first minimum sized amorphous mark, maximum amorphous resistance and over-programming, respectively. Furthermore, the crucial effect of electromigration limiting the endurance (cyclability) of the cells is demonstrated.

8.2 Introduction

Phase-change random access memory (PRAM) technologies hold strong cards for replacing the currently popular Flash memory [84]. Even though Flash memory exceeds the expectations that were foreseen in the past, it is expected in the near

---

Published as:
B.J. Kooi, J.L.M. Oosthoek, M.A. Verheijen, M.Kaiser, F.J. Jedema, D.J. Gravesteijn,
Phys. Status Solidi **249**, 1972 (2012).

future that further downscaling is no longer possible [84, 21, 52]. PRAM on the other hand is scalable with the next generations of lithography, requires less lithographic steps, has a higher (over)writing speed, improved endurance (cyclability) and requires less program energy [84, 21, 52].

PRAM exploits the large (three to four orders of magnitude) difference in electrical resistance of the amorphous and crystalline states of phase-change materials, which are renowned for their extremely fast crystallization kinetics at relatively high temperatures (e.g. 400 °C) and amorphous phase stability at operating temperatures (e.g. up to 100 °C). A fast, high energy electrical (RESET) pulse transforms the crystalline cell into an amorphous state by melt-quenching. The crystalline state can be recovered by applying a longer low energy (SET) pulse that heats the cell optimally below the melting temperature. The higher mobility of the atoms allows crystallization of the amorphous region during the SET pulse. This can also be performed fast, within 100 ns, but not as fast as melt-quenching that can in principle be performed with sub picoseconds pulses [68].

Despite the large potential of PRAM still reliability issues have to be addressed, which require improved understanding of the relation between nanostructure and properties of actual PRAM cells. A very suitable technique for establishing this relation is Transmission Electron Microscopy (TEM). Ideally, the electrical switching and characterization are combined employing in situ TEM observations. Recent examples of this approach are provided in [61, 62, 54]. However, disadvantage of this approach is that locally the PRAM cell (i.e. the layers above and below the active phase-change medium) has to be thin in order to allow for TEM imaging. This reduced thickness clearly alters the thermal properties and thereby also the electrical properties of the PRAM cells, i.e. the cells in a memory will not behave the same as the in situ analysed cells. In order to avoid these effects we performed electrical characterization on real memory cells and brought these cells to certain well defined final states and then prepared (locally thinned) the cells such that they could be analysed by TEM. In this way we are able to establish and understand nanostructure property relations for actual memory cells.

Earlier TEM studies of PRAM cells concentrated on the most popular phase-change material $Ge_2Sb_2Te_5$ [61, 62, 54, 32], that can be typified as a nucleation dominant material [84]. In contrast, in this chapter we analyze a so-called fast-growth type material. Thermal erasure of an amorphous mark in this type of material does not depend on nucleation, but only on (re)growth from the crystalline rim. However, during electrically driven erasure, after threshold switching, crystalline filaments are expected to play a crucial role.

8.3 Experimental

Phase change line cells with designed dimensions $250\times50\times15$ nm^3 were produced by e-beam lithography. The details of device fabrication can be found in Section 6.3 and Ref. [28]. Before TEM samples were prepared, the line cells were electrically tested and characterized (Chapter 6) and brought to known specific final electrical

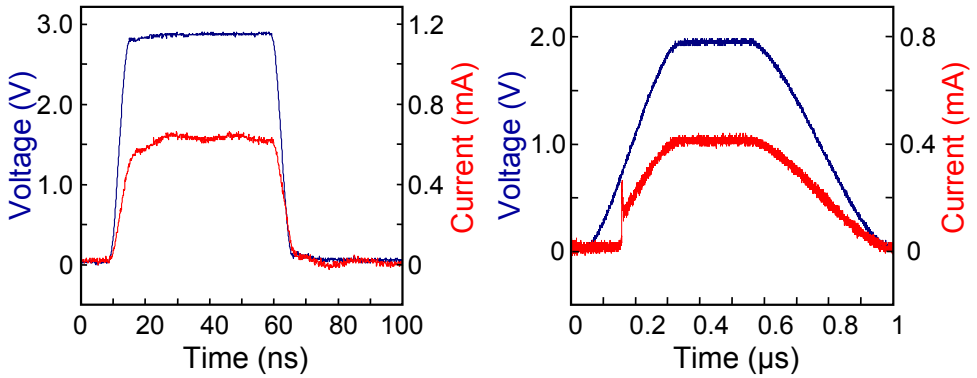

Figure 8.1: ***(a)*** *Example of 50 ns RESET pulse.* ***(b)*** *250 ns SET pulse (250 ns rising and 400 ns falling edges) including threshold event.*

states, i.e. a series of PCM modules differing in their programming history (number of SET/RESET cycles or RESET current used) have been analysed. Details on the programming history will be specified in Section 8.4 for each analysed cell individually. Duration of all RESET pulses was 50 ns and of the SET pulses was 250 ns, but with a 250 ns rising edge and a 400 ns falling edge. Example oscilloscope traces of used electrical pulses for (a) RESET (switching from crystalline to amorphous state), (b) SET (switching from amorphous to crystalline state) are shown in Fig. 8.1. TEM studies were performed using a TECNAI F30ST TEM operating at 300kV. Details about the TEM preparation process are found in Section 4.3.

8.4 Results and discussion

8.4.1 First amorphization

Although the phase-change material is amorphous after sputtering, it crystallizes during the bake out step of the HSQ hard mask [28]. Therefore, the phase-change material in the as-produced line cells is always fully crystalline, i.e. in the SET state. In order to switch to the RESET state an amorphous mark has to be introduced by melting the line by a voltage pulse. If the line is able to solidify sufficiently fast (in the order of nano-seconds) the molten region is quenched into the amorphous state. In order to find the minimum required voltage/current for the RESET pulse the pulse values are increased in relatively small incremental steps. A specific example for the line cells with designed dimensions 250×50×15 nm^3 is shown in Fig. 8.2, where Fig. 8.2(a) shows electrical results and Fig. 8.2(b) the corresponding TEM image after the final electrical pulse used. The TEM image shows that the actual dimensions of the line cell, 222×58×15 nm^3, differ from the designed ones. The electrical results show that we start melting the phase-change material for a voltage/current that is

in between 2.52 and 2.62 V or 0.560 and 0.576 mA, respectively. The initial SET resistance of the cell is 1.07 kΩ. A 3.3 kΩ series resistance is always present that functions as the transistor in an actual memory. Therefore the actual cell voltages are lower than the values given here. The minimum RESET resistance found after the 2.62 V/0.576 mA pulse used is 426 kΩ, i.e. an increase of about 400 times.

The location and size of the amorphous mark can be identified in the TEM image, where by tilting of the specimen in the TEM the contrast between the phases can be increased: Depending on tilt, crystals show relatively large variation in contrast (from light grey to black), whereas the amorphous mark does not show such changes. The approximate positions of the amorphous crystalline boundaries detected in this way are indicated in the inset of Fig. 8.2(b). The length of the amorphous mark is 38±7 nm. The amorphous mark has an hourglass shape. This shape cannot have been developed fully during the melt-quenching process, but indicates that before the RESET pulse was applied a kind of constriction (local reduced width) was present in the line. A higher current density will of course be present in such a constricted region during the electrical pulse which explains the position of the amorphous mark.

The reason for the presence of this type of constrictions is relatively straightforward. Initially the phase-change material film is deposited amorphous. Then during further processing high temperatures are reached (350-400 °C) and crystallites are formed. As the relatively soft photo resist is still present on top of phase-change material it can be compressed leaving space for variations in crystal structures. Since the phase-change material type can be classified as a so-called fast-growth material, i.e. with low nucleation rates, large crystals are formed. During formation of these large crystals in the small width of the line in a cell, the edges of the line change from straight to a more jagged pattern. On some locations the jagged patterns of both edges of the line then lead to constrictions. These results indicate that the relatively coarse grained nature of the phase-change material can promote constrictions, which after typically 10^6 cycles can cause failure as we will show in Section 8.4.4.

The minimum width in the constricted region as determined from the TEM image is 30±5 nm. With a thickness of 15 nm this means that the cross section area is 450 nm^2. The critical current density for melting is thus 576/450 = 1.3±0.1 A/nm^2). The energy required to melt the phase-change material in this cell is I^2R_t ≈18 pJ.

8.4.2 Increasing amorphous mark size

Figure 8.4 and 8.3 show results for the same type of line cell as depicted in Fig. 8.2 and described in the previous section, but now the RESET voltage/current is increased clearly beyond the critical value needed to initiate the minimum amorphous mark. The critical current for RESET is now 0.72 mA, clearly higher than the 0.57 mA found for the sample in Fig. 8.2. However, this largely scales with the cross section area, because the line in Fig. 8.3 is less constricted than in Fig. 8.2(b). The critical current density for RESET as derived from Fig. 8.4 is 720/585 = 1.23±0.05 A/mm^2 (similar to that found in the previous section). The energy required to melt the phase-change material is I^2R_t ≈36 pJ, twice as high as in the previous section. However, the resistance reached with this energy pulse is 2.0 MΩ, 4 to 5 times higher than in

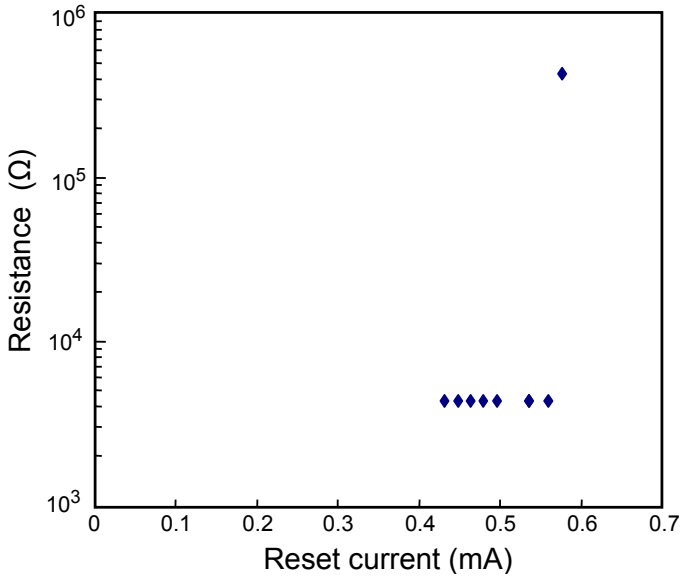

(a)

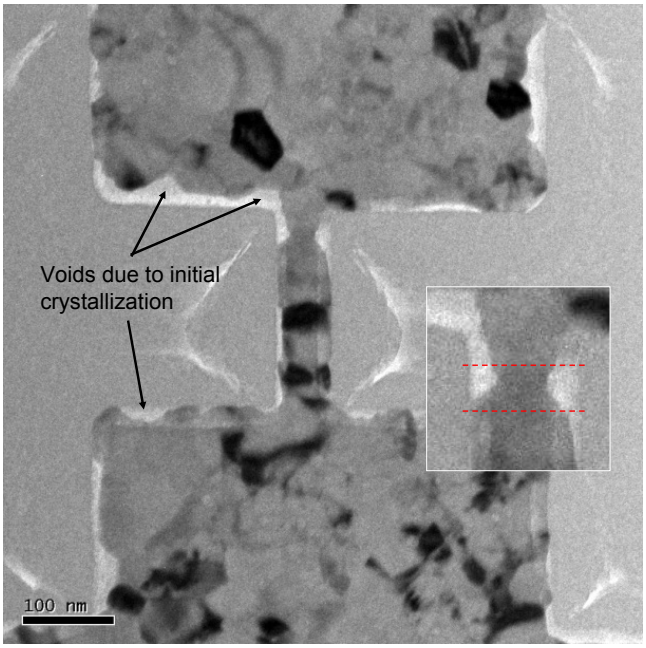

(b)

Figure 8.2: ***(a)*** *Resistance versus stepwise increase of RESET pulse voltage and current leading to first minimum sized amorphous mark.* ***(b)*** *Bright field TEM image indicating position and size of minimum amorphous mark.*

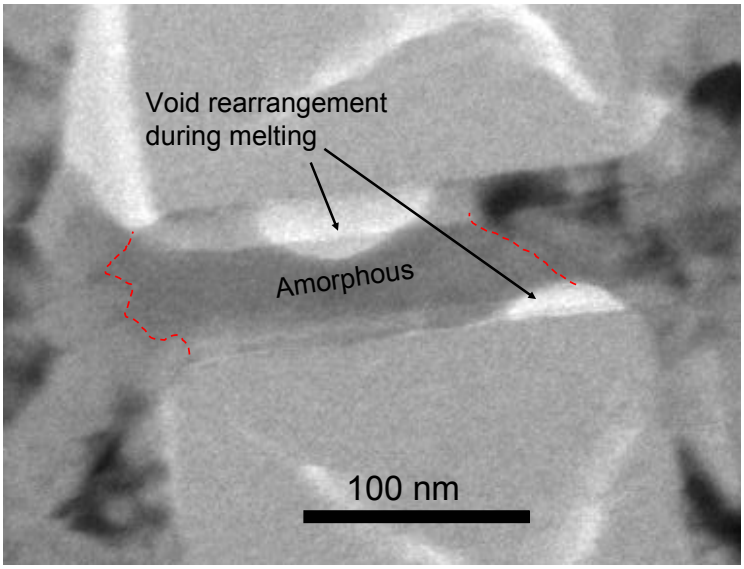

Figure 8.3: *TEM image indicating the amorphous mark after the RESET pulse with highest current shown in Fig. 8.4(a)*

the previous section and correspondingly the molten region and thus the amorphous mark is clearly larger than in the previous section. When increasing the current from 0.72 to 0.91 mA the length of the amorphous mark is increased to nearly the full length of the line, 200×10 nm and the resistance increased from 2.0 MΩ to 21.5 MΩ. So, note that the final amorphous resistance is 50 times higher for the line cell in Fig. 8.4 than the one in Fig. 8.2. The amorphous mark is only about a factor of 5 longer. This shows that there is not a direct relation between amorphous mark length and resistance of the line cell and apparently the resistivity of the amorphous material is changed an order of magnitude. Figure 8.4(a) shows that the final RESET resistance is thus four orders of magnitude higher than the SET resistance. This demonstrates the excellent contrast between the two states of the memory.

The evolution of measured threshold voltage with amorphous resistance is shown in Fig. 8.4(b). A linear relation holds between the two entities. For the amorphous mark shown in Fig. 8.3 it would be interesting to know the threshold voltage. Unfortunately, this knowledge is not available, because after the mark was produced the cell was directly prepared for TEM imaging and a SET pulse allowing determination of the threshold voltage was of course not applied, because this would have led to erasure of the amorphous mark. However, knowledge of the linear relation between amorphous resistance and threshold voltage allows extrapolation to the known resistance for the RESET state. Therefore it is possible to predict a threshold voltage of 5.8 V for the mark in Fig. 8.3. Using the length of the mark, the more interesting material specific threshold field is therefore 29(±5) V/mm. The accuracy is low because of the extensive extrapolation.

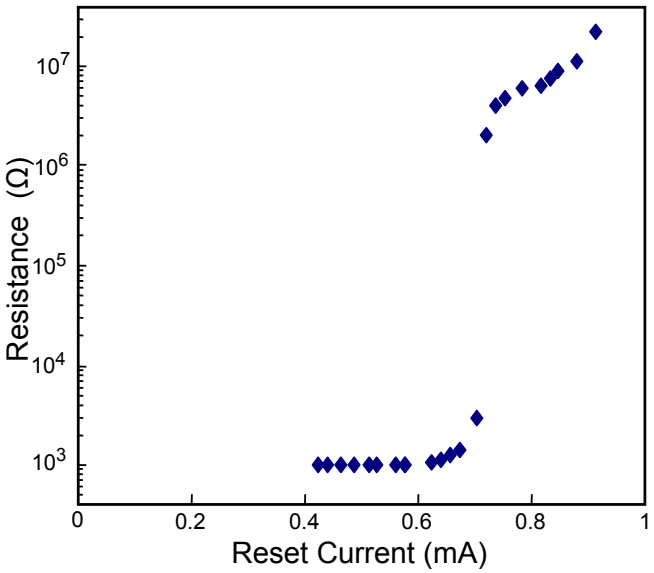

(a)

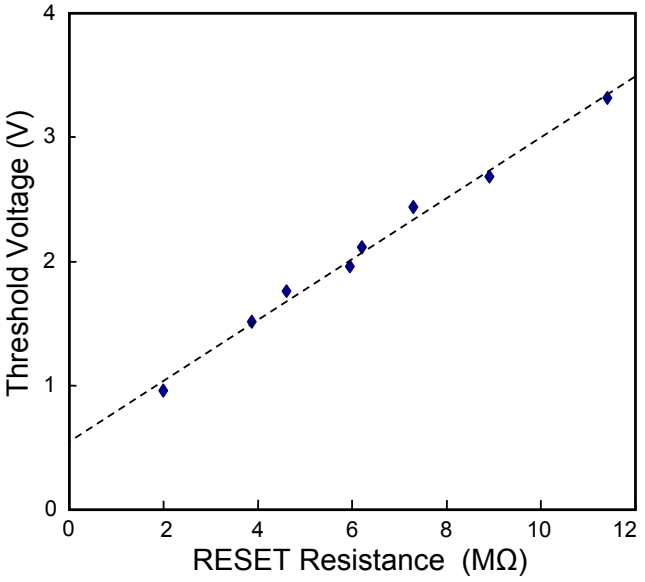

(b)

Figure 8.4: *Results for increasing the amorphous mark size to about whole length of line cell.* ***(a)*** *Resistance versus stepwise increase of current during RESET pulse.* ***(b)*** *Required threshold voltage to switch amorphous mark with stepwise increasing RESET resistances.*

8.4.3 Over-programming

If, compared to the final result of the previous section, still higher RESET currents/voltages are used, interesting behaviour is observed. The amorphous resistance reaches a maximum and is then decreasing; see Fig. 8.5(a). This behaviour we observed earlier for similar cells as presented in Chapter 6. In contrast, the threshold voltage also reaches a maximum, but then remains fairly constant; see Fig. 8.5(b). In our earlier work we even observed a still slightly increasing threshold voltage when the amorphous resistance decreases. Generally it is assumed that a linear relation holds between threshold voltage and the amorphous state resistance [78, 23] (see also Fig. 8.4(b)). Such a relation holds before the maximum in resistance and threshold voltage is reached, but is not maintained for higher RESET currents. Therefore it is interesting to relate this so-called over-programming behaviour at high RESET currents to the structure of the line cell as observed with TEM.

Figure 8.6 shows TEM images of an over-programmed line cell. It is directly evident that the amorphous mark has been shifted outside the line into the phase-change flap. Since the flap does not restrict the width of the amorphous mark as the line is doing, the mark develops a mushroom shape with a dome inside the flap. Note that it is a 2D mushroom and not a 3D mushroom shape that occurs in the Ovonics type phase-change memory [84, 21].

An important question is how deep the 'stem' of the mushroom is still inside the line of the line cell, i.e. what is the location of the crystalline amorphous boundary in the line. For that tilting the sample inside the TEM is very useful, indicating that the amorphous mark hardly extends into the line with the boundary only about 20 nm away from the end of the line. The length of the mark is 125±7 nm. The corresponding threshold voltage for this over-programmed mark is 3.3 V. The more relevant material specific parameter is the threshold field, which is thus 26±2 V/mm, which is actually close to the crude approximation 29±5 V/mm made in the previous section.

An interesting question is why the amorphous mark shifts outside the line into the flap. However, even before the mark shifts outside the line, it will in a line with uniform width (and thickness) not be located in the middle of the length of the line, but shifted towards one side [9]. The reason for this shift is the thermoelectric Thomson(-Seebeck) effect. Depending on the majority charge carrier this asymmetric shift will occur towards the anode for p-type conduction and to the cathode for n-type conduction. For the phase-change cells the Seebeck effect is associated with p-type conduction. Details of the observations and explanation of the asymmetric location of the amorphous mark in line cells are given in [9].

If the power of the electrical pulse is increased beyond the one needed to produce an amorphous mark up to the end of the line, it will also start melting material in the flap. During cooling particularly the region in the line that is surrounded by poorly heat conducting SiO_x can experience too slow cooling rates and can thus recrystallize. This probably explains why the 'stem' of the amorphous mark in the line is so short. A direct relation between threshold voltage and amorphous resistance implies that they are both governed by the length of the amorphous mark. If due to

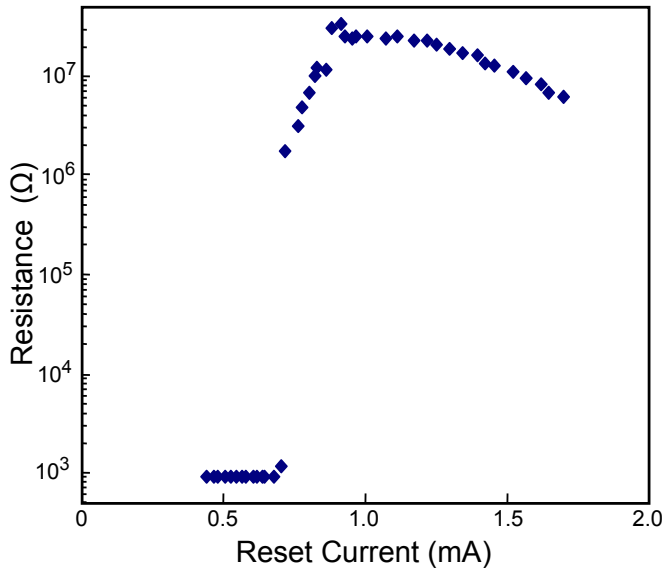

(a)

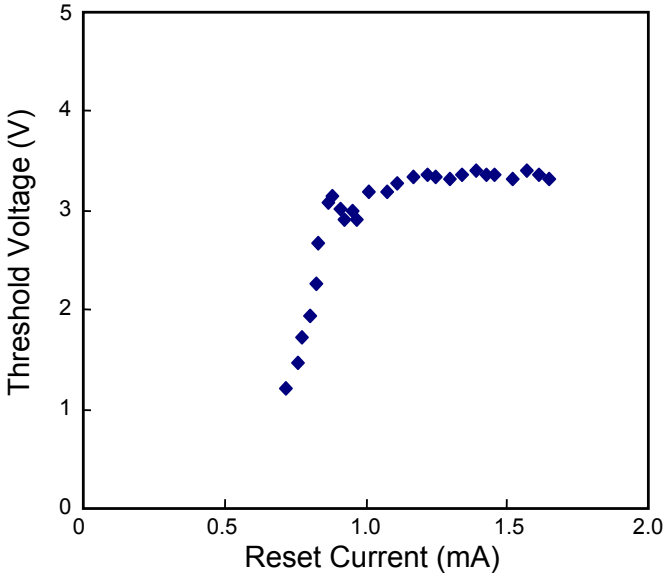

(b)

Figure 8.5: *Over-programming.* ***(a)*** *Resistance versus step wise increasing RESET current.* ***(b)*** *Threshold voltage versus RESET current used to create amorphous mark.*

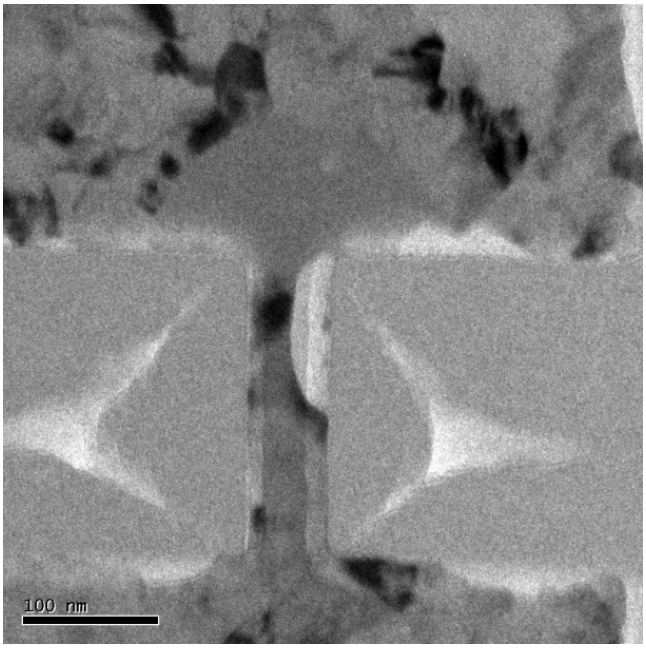

Figure 8.6: *TEM image indicating that the amorphous mark shifted out of the line into the flap.*

over-programming the amorphous mark moves outside the line, the shortest length l across the amorphous mark that bridges the two electrodes still determines the threshold voltage. However, the amorphous resistance R_a decreases, because the width of the current path w increases and therefore considering for the phase-change material a constant film thickness t and resistivity ρ the resistance R_a will decrease, because $R_a = \rho l/wt$. This explains the observed relations between threshold voltage and amorphous resistance before and after over-programming.

For actual operation this over-programming is not desired, because it is associated with unnecessary power consumption. If the polarity of the applied electrical pulses remains the same, always the same side of the line is molten. The repeated melting during cycling will eventually lead to decomposition of the phase-change material. Sufficiently severe decomposition can then be associated with the SET stuck typically observed for line cells after 1 to 100 million cycles (see Chapter 6 and [52]). An interesting point is now that if due to the Thomson-Seebeck effect the amorphous mark is continuously on one side of the line, the SET stuck can be avoided by starting to apply the opposite polarity of the electrical pulses. Then, the amorphous mark is shifted to the other side of the line that did not experience melting and thus decomposition up to that time. Interestingly, this strategy only works for line cells and not for the mushroom type Ovonic cells.

8.4.4 Electromigration

Mass transport can be coupled to charge transport in the presence of a strong electrical field which is known as electromigration. In case of phase change alloys, different elements can move in opposite directions leading to decomposition in the line cell. [103] In particular lines which contain severe constrictions, like depicted in Fig. 8.2(b), will be most prone to decomposition and electromigration. Figure 8.7 shows results of a line cell that is approaching its end of life after a number of switching cycles ($1.4 \cdot 10^5$) that is much lower than average (10^7). The evolution of SET and RESET resistance with the number of switching cycles is shown in Fig. 8.7(a). Again the excellent resistance contrast between the SET-RESET states of four orders of magnitude is shown. Already after about 10^4 switching cycles the amorphous resistance starts to decrease significantly, which is a clear indication that the cell is deteriorating due to decomposition of the phase-change material due to the repeated local melting of the phase-change material in conjunction with large electrical fields present within the molten mark (see Chapter 6). The reason for the strongly reduced cyclability of the line cell can be readily deduced from the TEM image shown in Fig. 8.7(b). Indeed, a severe constriction is present that can be associated with locally very high current densities and thus strongly accelerated decomposition and electromigration. The strong acceleration is obvious, because once a constriction is present, for instance as shown in Fig. 8.2(b), electromigration will locally reduce the width of the constriction and thereby continuously accelerate the electromigration. [65]

Before FIB preparation the line cell was in the RESET state having a resistance of 7.3 MΩ. However, an amorphous mark cannot be detected in TEM images of this line cell taken at various tilts and it is almost certainly absent. Apparently during TEM sample preparation crystallization has occurred. A relatively large single crystal occupies most of the total volume of the line cell up to the constriction that is present at the end of the line. The origin of this large single crystal is probably crystal growth from the melt. Due to the constriction the molten region cannot readily conduct heat along the line and the lower cooling rates then (because the phase-change material is a poor glass former) lead to growth of the large crystal. A similar argument was used to explain why most of the line was crystalline in the example shown in the previous section on over-programming.

During the voltage pulses applied to the line cells a current density of typically 10^8 A/cm^2 holds in our cells; this is also the minimum value required to melt the phase-change material. In Ref. [102] a current density of 10^6 A/cm^2 was sufficient to melt much larger sized $Ge_2Sb_2Te_5$ lines and when this current density was maintained during a few milliseconds until breakage of the line due to electromigration occurred. Typical current density values for electromigration are indeed 10^6 - 10^7 A/cm^2 for Al or Cu metallization lines and can be even as low as 10^4 A/cm^2 for solder joints [86]. Therefore it is remarkable that the line cells can still be switched typically 10^7 times with our high current densities of 10^8 A/cm^2. Crucial for this large number of switching cycles is the short pulses used and in addition probably the low density of grain boundaries present. Indeed, when care is taken to apply short RESET pulses like 10 ns, it is possible to reproducibly achieve for similar cells 10^9 cycles [16].

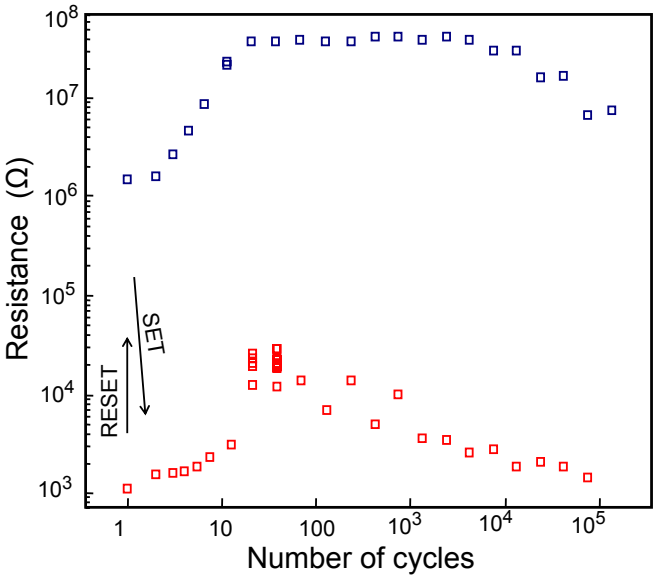

(a)

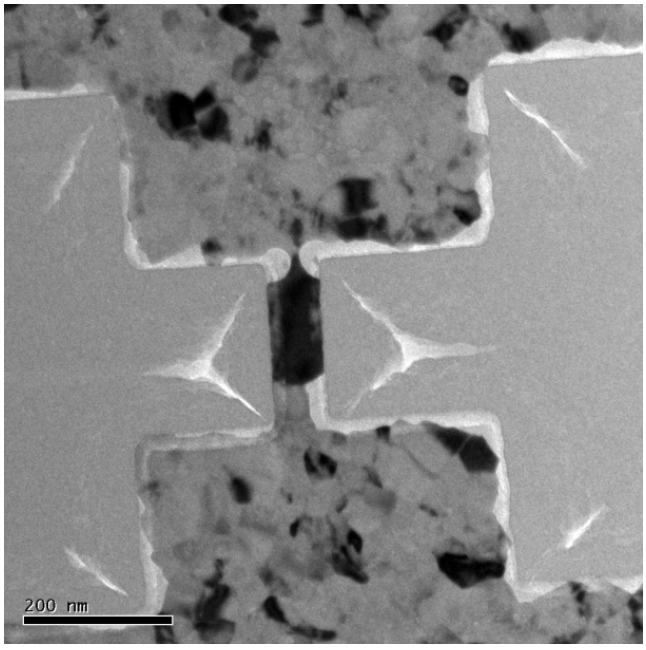

(b)

Figure 8.7: *Unusual line cell with limited number of switching cycles ($1.4{\cdot}10^5$) due to electromigration within a constriction.* ***(a)*** *SET and RESET resistances as a function of switching cycles.* ***(b)*** *TEM image indicating that the line cell is almost broken due to electromigration, which before breakage can lead to insufficient quenching rates and thus to SET stuck.*

8.5 Conclusions

The present work demonstrates the importance of being able to correlate electrical results of phase-change cells with TEM imaging of the actual structure of the cells. Minimum amorphous mark, optimum and over-programmed amorphous marks and cell near to failure by electromigration have been imaged in conjunction with their corresponding electrical behaviour.

Particularly the over-programming effect where the amorphous mark moves due to the Thomson effect outside the line into the phase-change flap has not been presented before and leads to special electrical behaviour where the amorphous resistance is decreasing, but the threshold voltage is remaining constant or even slightly increasing.

An important conclusion from the present work on line cells is that in case the average crystal size of the phase-change material is about equal to the width of the line cell, the edges of the line cell can become rough and can obtain jagged shapes which strongly increase the probability that locally within the line constrictions occur. Constrictions limit the life time of the line cell due to electric field induced and accelerated decomposition and electromigration. Nevertheless with similar type of cells a reproducible endurance of 10^9 cycles can still be achieved.

Chapter 9

Processing PRAM cells for TEM observation

9.1 Introduction

The main objective of this PhD project has been observing PRAM cells in the TEM while these cells are still fully accessible for electrical characterization and switching. This was considered to be an ambitious goal from the start which has been reached as a proof of principle. Extensive electrical characterization of the NXP PRAM cells has been performed (see e.g. also Chapter 4 to 7 of this thesis and [52, 9, 28, 29, 16]) and also to much lesser extent TEM images have been recorded of post-mortem PRAM cells (see Chapter 4, Chapter 8 and [9]). The main motivation to pursue this goal is that correlative studies of TEM imaging and electrical switching and characterization of PRAM line cells are lacking. Still, for answering many open questions concerning PRAM cells, e.g. related to reliability issues, correlative research on switchable PRAM TEM samples is required. The great potential of this approach has been demonstrated recently for phase-change nanowires [66].

To give a few examples of open questions: (1) It is still not fully known how the amorphous mark is erased during the crystallization pulse, i.e. if nanoscale filaments are formed first or that the crystallization front proceeds uniformly or in another manner. (2) Cyclability of the memory is limited by decomposition of the PCM and by electromigration. These processes are not properly observed and understood for nanoscale PCM cells. (Chapter 6, [83, 34, 39, 65, 102, 103]) (3) The transformation from the crystalline to the amorphous phase is associated with a volumetric expansion of ≈6% [75, 98]. Since the phase-change material is completely encapsulated, this volumetric expansion will create large stresses within the PCM. In return, these stresses influence the crystallization process; this is not properly understood. (4) The relations between amorphous mark length and resistance or threshold voltage tend to be proportional, but for detailed studies of these relations correlative research on switchable PRAM TEM samples is needed. (Chapter 6 and Fig. 8.5)

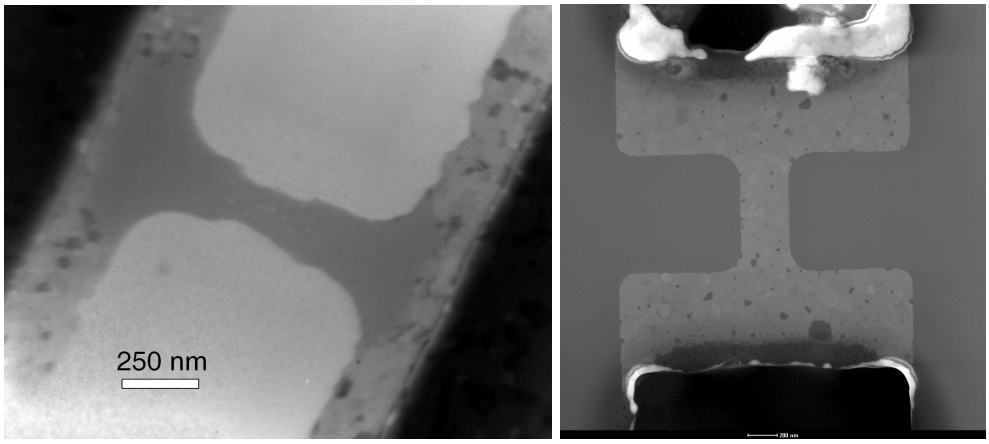

(a) (b)

Figure 9.1: ***(a)*** *TEM image of PRAM cell that was prepared for TEM by NXP and was still switchable. The cell was unintentionally brought to the amorphous phase during the preparation process. This was most likely related to accumulation of electronic charge that causes a discharge spike.* ***(b)*** *Scanning transmission electron microscope (STEM) image of a PRAM cell prepared for TEM observation by NXP (image courtesy of Frans Voogt). A 3 nm thick Pt layer was applied on the cell to avoid forming a large amorphous mark as observed in (a). It was assumed that this layer was too thin to have any effect, however the layer shorted the cell and it could not be switched anymore.*

This chapter gives an extensive overview of the experimental steps that were taken in order to produce switchable PRAM TEM samples. Therefore the experimental section of this chapter is large and is divided into two parts. In Section 9.2.1 the procedure for producing switchable PRAM TEM samples as employed by NXP in Nijmegen is described. In the rest of Section 9.2 the procedure developed and performed completely within the Zernike Institute in Groningen is described; Section 9.2.2 gives a complete overview of the procedure and Section 9.2.3 to Section 9.2.6 gives detailed information on individual steps of this procedure. Although the procedure employed by NXP did not turn out to be a robust method to produce switchable PRAM TEM cells, still interesting results were obtained that are described in Section 9.3. The reader who is not interested in all the details of the preparation procedure can directly move on to this results section which can be read independently, i.e. without requiring knowledge from the experimental section.

9.2 Experimental

9.2.1 Observing switchable PRAM cells in the TEM

As the name *transmission electron microscope* suggests the electrons have to be transmitted through the cell to be observed. Although the resolution of an SEM is adequate to observe the cells it is not possible to directly distinguish between the amorphous and crystalline phase. The TEM however has a much higher resolution and provides immediate contrast between the phases (Fig. 9.1(a)).

The PRAM cells are produced on top of 725 µm thick silicon wafers. The structures of the cells are patterned by lithography on top of silicon dioxide and silicon nitride layers and are covered by several more of these layers. These so-called passivation layers below and on top of the memory cell have a total thickness of about 2.5 µm. To observe the PRAM cells in the TEM with adequate contrast and resolution, the total thickness cannot exceed 200 nm. Removing all the silicon beneath the cell is not enough to observe the cells in the TEM because the total thickness is then still 2.5 µm. To reach the goal of 200 nm, the passivation layers have to be removed to large extent from both top and bottom sides of the cell. The principle of this process is shown in Fig. 9.3.

Figure 9.1(a) illustrates one of the TEM observable PRAM cells that was provided by NXP. This particular cell was still switchable. However, it had unintentionally been switched to the amorphous state during the sample preparation process. This was most likely caused by accumulation of electric charge during the FIB milling process (see Section 9.2.6). A solution to this problem was to apply a 3 nm Pt layer on top of the cell that allows for dissipation of the charge. However, this layer was still too thick and shorts the cell. Figure 9.1(b) shows one of seven PRAM cells that were prepared in this way for TEM by NXP for this project but could not be switched anymore. Although a solution for this problem was found (Section 9.2.6) it was too late for the processing to be performed again at NXP.

The FIB preparation was performed as follows: A 3 mm disc was cut from the wafer containing the PRAM cells in the middle. The 725 µm thick disc was thinned to about 100 µm (see 9.2.3). The remaining silicon was removed from the back by a dedicated FIB in Nijmegen with the aid of a gas injection system. The system at the NXP facilities of Nijmegen is able to selectively remove silicon while the silicon oxide passivation layer containing the cells is kept intact. Figure 9.2(d) shows the back of the sample prepared by NXP. The bond pads are visible from the back where the 100 µm of the silicon wafer was removed completely. Instead of a stack of layers firmly attached to a rigid silicon substrate the layers have now become a very delicate membrane. Normally the bond pads are only visible from above (as in Fig. 2.10(a)) because the silicon wafer is opaque.

The membrane was milled from both sides to about 100 nm above the cell in a FIB setup although without the aid of a gas injection system. This particular FIB step could also be performed later during the project in Groningen (see Section 9.2.6). Figure 9.2(c) is a close up showing the location of the line cell, i.e. in the middle. This image is about the maximum resolution that can be obtained with a normal

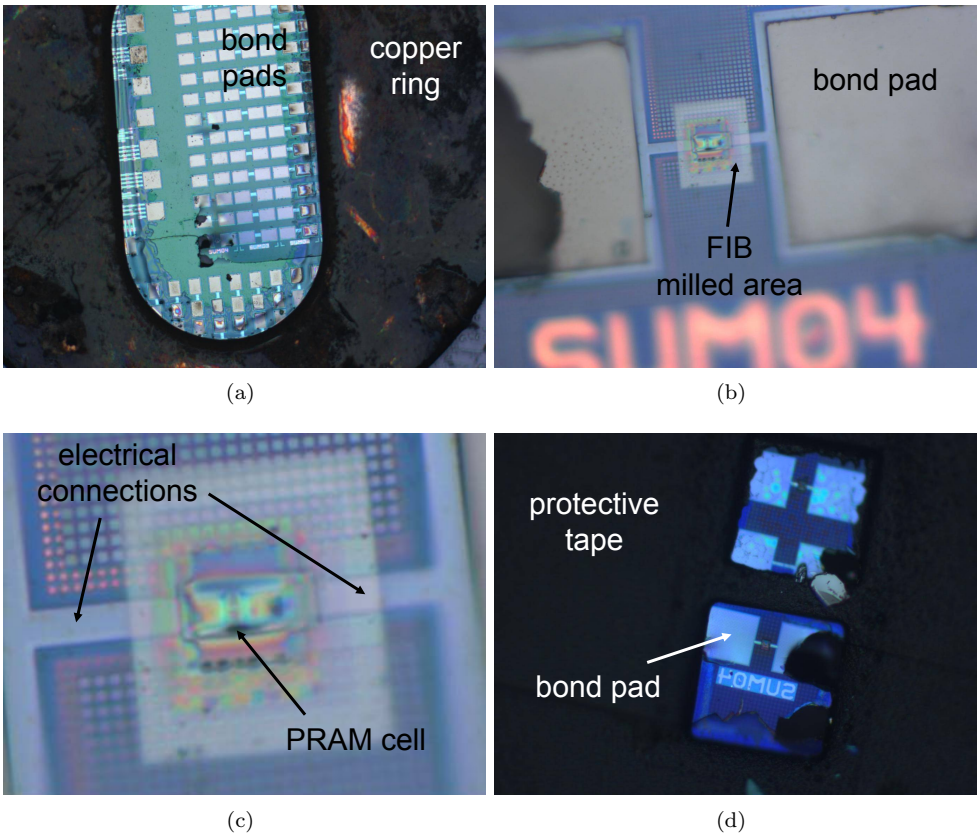

Figure 9.2: *Optical microscope images of the PRAM cell shown in Fig. 9.1(a).* ***(a)*** *Overview image showing the bond pads and a 3 mm diameter disc glued on top op the wafer. This disc was added for mechanical toughness. However, with the disc on top it was no longer possible to apply extended electrodes (see Section 9.2.4)* ***(b)*** *The actual cell with two bond pads and a square area milled by the FIB setup. The jagged black/grey area on the left is where the probe needles punctured the membrane (see main text) which is the reason extended electrodes were required, i.e. for making electrical contact outside the thin membrane region.* ***(c)*** *Close-up of the FIB milled area.* ***(d)*** *A view from the back side of the sample showing the code "SUM04" in reverse. In this image the punctured holes caused by the probe needle are clearly visible.*

optical microscope. Figure 9.1(a) is a TEM image of the same cell (slightly tilted) which shows great contrast between the amorphous phase (dark grey) and crystalline phase (light grey with black spots).

Unfortunately, the membrane was punctured as our probes landed on the bond pads. The puncture holes from probing the cells can be clearly observed from the back (Fig. 9.2(d)). However, a connection was still made that showed that the cell was in the amorphous state. Figure 9.1(a) confirmed that the cell had a very large amorphous mark. This large amorphous mark was probably not created in the probe station at NXP *before* preparation but caused by static discharging *during* the FIB preparation.

The second of two NXP prepared in-situ switchable PRAM cells *was* probed without puncturing the membrane (see Section 9.3). The cell was switched several times and images were taken after various switching events (Fig. 9.18). However after the cell was probed for five times the membrane was finally punctured too. This clearly showed that it does not make sense to probe a delicate glass membrane with metal probe needles. Therefore it was decided that a different approach was needed to connect to the PRAM cells prepared for TEM. The solution was to extend the electrodes to an area outside of the membrane which this is discussed in Section 9.2.4. Although a total of nine TEM observable cells were provided, only two were actually switchable (Fig. 9.1(a) and 9.18). The other seven were electrically shorted (Fig. 9.1(b)). Unfortunately, the TEM processing performed by NXP was very costly. At the time that a solution was found for every problem a change in the company focus made it impossible for NXP to provide more TEM observable cells. However, during this time an FIB setup was acquired by the Zernike Institute for Advanced Materials. This setup was able to perform most FIB tasks that were possible at the facilities of NXP with the exception of removing the silicon wafer. When an alternative route became available, it was decided to perform the process steps in Groningen and use chemical etching (Section 9.2.5)for removing the silicon wafer instead. Then, after chemical etching of silicon the FIB setup located at the Zernike Institute was used to remove the silicon oxide/nitride layers directly above and below the cell.

9.2.2 Processing of PRAM cells for in-situ TEM: overview of the process

Figure 9.3(a) shows the process that was performed in Groningen to prepare PRAM cells for TEM. First, a disk with a diameter of 3 mm or 4 mm that contain the cell in the middle is cut out of a wafer. Unlike the cell production process performed at NXP, the wafer discs are not made thinner in the initial step using FIB. Instead, a 450 µm deep hole is drilled in the back of the disc with a diamond coated drill. This drilled hole was aligned to the structures on the front of the wafer. Mechanically drilling a hole provided an easy method to direct the etching process to the correct position under the cell. Furthermore, the disc retains its mechanical strength while a disc thinned to 100 µm becomes very fragile and difficult to handle. This is exactly why, during the NXP process, a copper ring was glued on top of the disc (Fig. 9.2(a)).

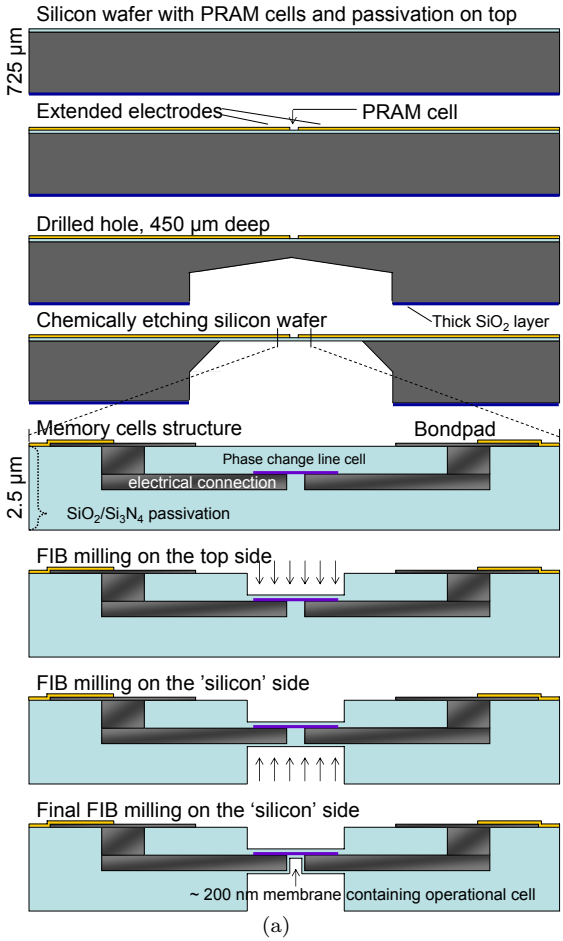

(a)

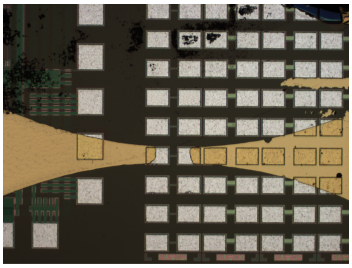

(b)

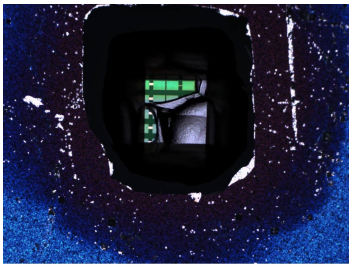

(c)

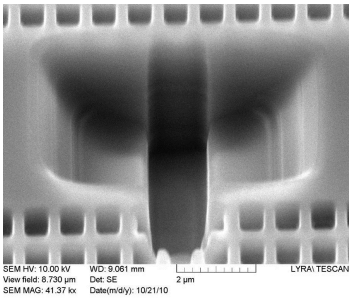

(d)

Figure 9.3: ***(a)*** *Step by step procedure of how a PRAM wafer was processed for TEM observation in Groningen. The steps are described in detail in the following sections.* ***(b)*** *Two extended gold electrodes were produced by optical lithography.* ***(c)*** *Back of a PRAM wafer with a partially etched cavity.* ***(d)*** *SEM image after the final two FIB milling steps (see* ***(a)****) have been performed below the memory cell.*

A solution was found to the problem of creating an electrical connection to the cell without applying mechanical stress to in the membrane: The high conductivity of gold allows for lithography patterned electrodes with a thickness of only 50 nm (see Section 9.2.4). The extended electrodes were produced after the wafer was cut into disks. A connection to these electrodes can then be made on the edge of the disk with conductive epoxy, far away from the very delicate thinned membrane. These electrodes have a resistance in the order of only a few ohms which is negligible compared to the cell resistance.

The remaining silicon was chemically etched using a 20 % KOH solution at 80 °C. A stainless steel holder was constructed by the workshop that protects the front of the cells with synthetic rubber (Viton) o-rings (see Section 9.2.3). The silicon wafers have a silicon oxide layer on the back side of the wafer. This silicon oxide acts as a natural etch stop which means that etching will only occur where the silicon oxide is removed. Figure 9.3(c) shows a wafer disc that was removed from the etch holder before etching was complete. The blue region is the silicon oxide on the back of the wafer disc that was covered by the o-ring. In the center it changed to a purple color where it was exposed to the KOH solution. The bond pads can be observed from the back side along with a large amount of silicon that was not etched. After the silicon is removed under the cells the remaining silicon oxide passivation layer *directly under* the cell is removed with the FIB setup present within the Zernike Institute in Groningen. In three steps Fig. 9.3(a) the silicon oxide is removed to 'as close to the cell' as possible. Figure 9.3(d) is an SEM image of the back of a PRAM cell after the last step of FIB preparation. The cell itself cannot be directly observed in the SEM. In the next four sections experimental details of separate steps in the procedure to produce switchable PRAM TEM samples are given.

9.2.3 Cutting the wafers into 3 mm or 4 mm discs

The silicon wafers with PRAM cells from NXP are cut into 3 mm or 4 mm discs by an ultrasonic disc cutter. The 3 mm discs fit directly into standard TEM holders. However the larger 4 mm discs are more easily etched in the chemical cell (Section 9.2.5) because the chance of leakage is reduced. Even the 3 mm do not fit in the in-situ TEM heating holder because they exceed the maximum thickness. A disposable tip of the single tilt holder (JEOL) was modified to take the 4mm discs.

Discs are cut with a Gatan model 601 ultrasonic disc cutter which has a cylindrical cutter head. A custom drill head for the 4 mm discs was provided by the mechanical workshop. The wafers containing cells are glued with wax to a steel substrate placed on a hot plate. To align the cutter head to be directly over a PRAM cell a brass template was cut in the work shop. The template has holes spaced to the exact distance between the cells on the silicon wafer. The template was also glued to the wafer with wax. When properly aligned it guides the cutter head to the correct location and allows for discs with the PRAM cell completely in the middle. Figure 9.4(b) shows a 4 mm wafer disc that was cut with the ultrasonic cutting tool.

Figure 9.4(b) shows a 3 mm wafer disc after cleaning. An easy method of removing the wafer disc from the steel substrate is to place the substrate on the hot plate again.

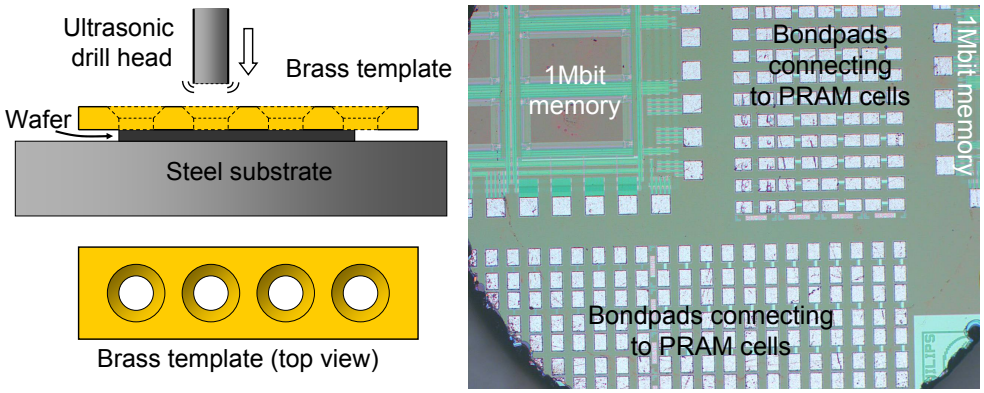

(a) (b)

Figure 9.4: ***(a)*** *A wafer containing PRAM cells was glued on top of a steel substrate. Then, a brass template constructed by the workshop was glued on top of the wafer. Holes in the template aligned to the PRAM cells direct the ultrasonic drill head to the correct location.* ***(b)*** *3 mm disc cut from a PRAM wafer. Observe the similarities between this image and Fig. 9.2(a).*

However this embeds (burns) the grinding powder to the front of the substrate in such a way that it cannot be further cleaned. This leads to a relatively dirty surface of the PRAM cell (see Fig. 9.6(c) in the next section). Therefore it is best to place the substrate in acetone to dissolve the wax.

9.2.4 Preparing extended electrodes to the bondpads

As the name 'bond pad' suggests, connections to outside structures are normally made by a wire bond. But the thinnest bond wires available are still 25 µm thick, i.e. ten times thicker than the membrane. Wire bonding has been successfully performed on the bond pads of unprocessed wafers (Fig. 10.1). However, after the silicon is removed the remaining 2.5 µm membrane is too fragile for wire bonds, even if the bonds are made before etching.

Figure 9.3(b) shows a PRAM cell connected to the extended electrodes. It is easy to see that the extended electrodes are also connected to other structures on the wafer. The presence of the other structures on the wafer limited the options for extended electrodes (see Section 9.2.4). The extended electrodes were processed onto the bondpads of a cell by optical lithography in the NanoLab cleanroom. Normally the lithography works as follows: A layer of resist is spin coated on a complete wafer. An optical contact mask with a desired pattern is aligned on top of the wafer with a microscope in the mask aligner. The wafer with mask on top is then illuminated with a *deep UV* lamp which transfers the pattern of the mask onto the resist. The resist becomes soluble in acetone when it is illuminated. The illuminated resist can be rinsed away leaving the resist on top of wafer that was not illuminated i.e. where

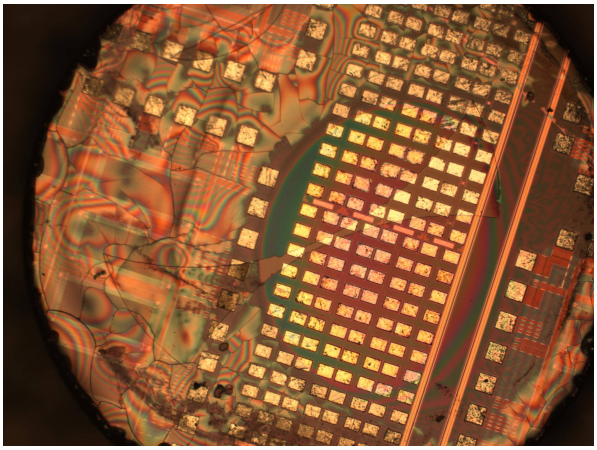

(a)

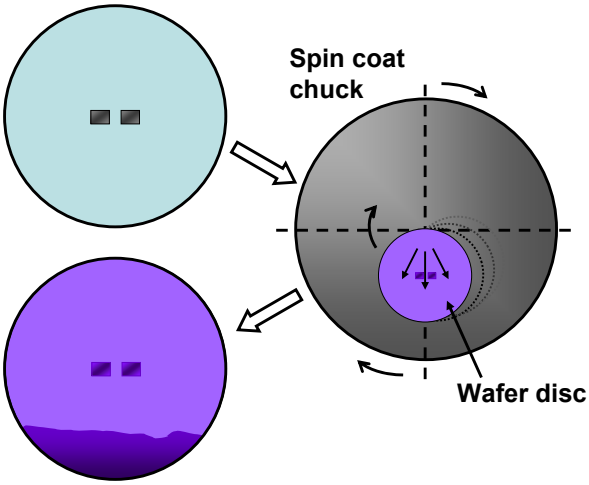

(b)

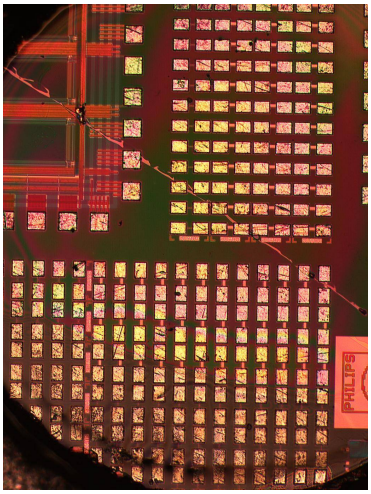

(c)

Figure 9.5: ***(a)*** *A 3 mm disc containing PRAM cells was spin coated after applying photo resist. During spinning the disc was located in the center of rotation. A thick layer of resist was still present as the centrifugal forces were not large enough.* ***(b)*** *A spin coat chuck was designed to spin coat the cell. The cell was placed asymmetrically to the axis of rotation.* ***(c)*** *Wafer disc containing PRAM cells was spin coated with photo resist. Compared to* ***(a)****, a uniform layer of resist is present on top of the disc.*

the contact mask is opaque. A blanket layer of gold with a titanium interlayer is deposited on top of the wafer and patterned resist by means of an electron beam evaporator. Afterwards, the remaining resist with gold on top is dissolved leaving only gold in the shape of the contact mask.

There were several problems with this method. First of all, only smaller wafer pieces were available which created problems with spin coating. Secondly, the design was complicated because a 1 megabit memory array lies on both sides of the single cells (see Fig. 9.4(b)). If more contacts would be made next to each other they would be connected electrically by the memory array. Before a contact mask was designed a test was performed with a commercially available glass contact mask and a 4 mm wafer disc in the mask aligner. Unfortunately this test was unsuccessful and the use of the commercially available masks was abandoned and an alternative route was developed. It was decided that the most versatile method would be to pattern the contacts directly on the 3 mm or 4 mm discs instead of on the wafer before cutting it into discs. Figure 9.5(a) shows a 3 mm disc on which a layer of photo resist was spin coated in the cleanroom. The disc was placed directly on the spin coat chuck which draws air through a hole in the centre, keeping the sample in place. However, due to the surface tension of the liquid photo resist a thick layer was still present on the edge of the disc.

This problem was solved by constructing a special spin coat chuck (Fig. 9.5(b)) that holds the wafer disk off center. Figure 9.5(c) shows a wafer disk with a layer of photo resist. The thickening at the edge still occurs but only at one side. When the wafer discs are inserted properly the thickening will be out of the way of the processed extended bond pad. An attempted was made to construct a contact mask in the mechanical workshop by spark erosion. Unfortunately the dimensions of the required mask were too small. Instead, a mask was produced as follows: Two thin 3 mm diameter copper rings were glued to a larger steel ring (see Fig. 9.6(a)). The copper discs were aligned under a preparation microscope such that the size of the opening between the copper rings was 100 µm. After hardening of the epoxy a 90 µm thick copper-gold alloy wire was placed as a bridge from one copper disc to the other. The wire was soldered to the copper discs by adding a small amount of lead-tin solder paste and heating the wire with a heat gun. It would have been much easier to glue the wire with epoxy but the high intensity deep UV radiation from the mask aligner will damage the epoxy over time.

Figure 9.6(a) shows the process, known as lift-off, of creating the extended electrodes to the wafer disc (i). After spin coating (ii) the cell is placed in an XY-stage (iii). The mask is aligned to the cell under a microscope (Fig. 9.6(b)). The complete XY-stage containing mask and disc are then placed in the deep UV mask aligner and the sample is exposed for 5 minutes. The exposed discs (iv) are placed in isopropanol bath and the illuminated area is dissolved (v). The discs are placed on a large metal substrate containing drops of wax. Each disc is placed on a drop of wax and the metal substrate is placed on a hot plate to glue the discs to the substrate. A 5 nm layer of titanium and a 50 nm thick layer of gold are deposited on the metal substrate containing the discs (vi). The discs are completely covered with the metal layer. After deposition the discs can be taken from the substrate by placing it on the hot plate

again. The standard procedure for removing the resist can now be followed. The resist takes away the gold that was deposited on top but the gold remains on the wafer disc where the resist was removed before deposition (vi). Figure 9.6(c) shows a 3 mm disc with an extended bondpad in place aligned to a PRAM cell.

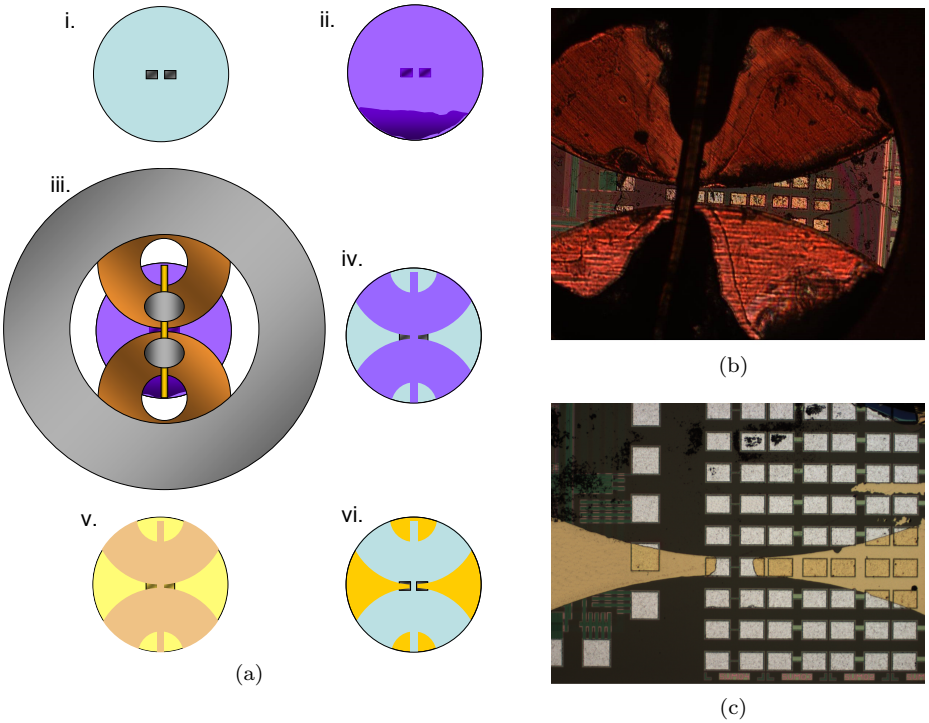

Figure 9.6: ***(a)*** *Process of depositing extended electrodes: i. Wafer disk containing PRAM cells. ii. A layer of photo resist is applied. iii. A shadow mask is aligned to the PRAM cell after which deep UV light is applied. iv. The illuminated resist can be dissolved in isopropanol. v. A gold layer is deposited on top of the disc. vi. The remaining resist is removed leaving the gold directly deposited on top of the disk.* ***(b)*** *Optical microscope image of the shadow mask.* ***(c)*** *Optical microscope image of a disk containing PRAM cells with extended bond pads.*

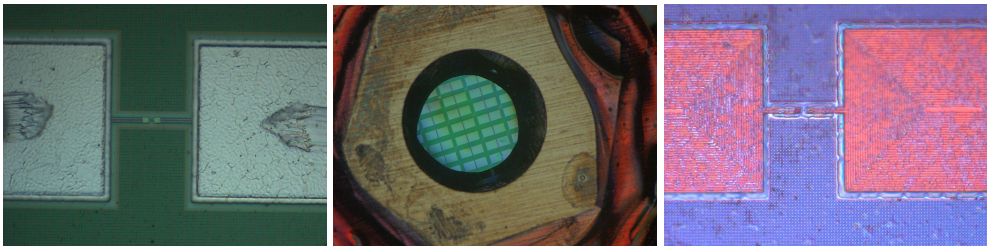

(a) (b) (c)

Figure 9.7: ***(a)*** *Two bond pads connected to a PRAM line cell in the middle.* ***(b)*** *A disk containing PRAM cells was grinded to a thickness of 100 µm and glued upside down on a stainless steel substrate. On the back side a molybdenum ring was glued after which the substrate was placed in a 20% KOH solution at 80° C. The back side of the bond pads are clearly visible.* ***(c)*** *Microscope image of the front of the bond pads after etching. Although the disk was protected with lacquer, this did not protect the front and the bond pads were damaged.*

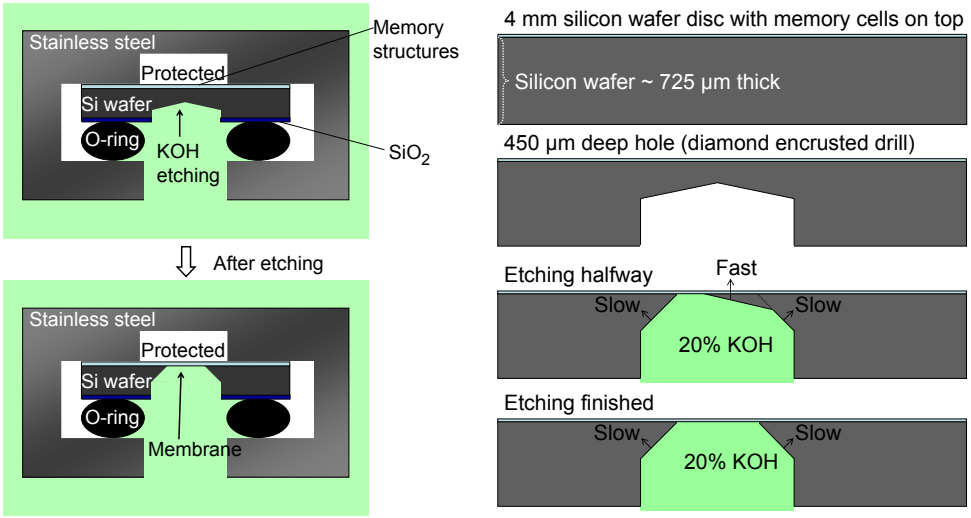

(a) (b)

Figure 9.8: ***(a)*** *Principle of how the etching holder works. An o-ring is placed on the back-side of the wafer disk and protects the front of the wafer disk from the etching fluid.* ***(b)*** *A wafer disk with a hole drilled to depth of 450 µm is placed in the etching holder. Etching stops when a membrane and a pyramid shaped etch pit is left.*

9.2.5 Etching silicon with KOH

The back side of the 4mm silicon wafer discs was etched in a 20% KOH solution at 80 °C [17]. Etching occurs by the following chemical reaction:

$$Si + 2OH^- + 2H_2O \rightarrow SiO_2(OH)_2^{2-} + H_2 \tag{9.1}$$

One of the etch products is hydrogen gas which forms bubbles during the etch process. However silicon can also be etched by first forming silicon dioxide. The silicon dioxide is subsequently etched by a reversible reaction:

$$Si + 2OH^- \rightarrow SiO_2 + H_2 + 2e^- \tag{9.2}$$

$$SiO_2 + 2OH^- \leftrightarrow SiO_2(OH)_2^{2-} \tag{9.3}$$

Figure 9.7(a) shows a PRAM cell and the two connecting bond pads on silicon wafer before etching. A disc cut from the wafer was grinded to a thickness of 100 µm and glued upside down on a stainless steel substrate. On the thinned back side a molybdenum ring was bonded with epoxy. Molybdenum was chosen as it does not react with KOH. The edge and front of the disc were protected by Lacomite, a lacquer solvable in acetone. After etching, the bond pads are visible from the back which is only possible because the silicon was removed (see Fig. 9.7(b)). Although the silicon wafer is completely etched away from the back, the KOH solution also penetrated the protective lacomite layer and was still able to reach the front of the wafer and damaged the structures. Furthermore, the epoxy glue was not stable in the KOH solution.

Figure 9.7(c) shows that both the aluminium on top of the bond pads and the normally not visible patterned copper underneath the aluminium layer have been etched away completely by the KOH. This shows that the wafer disc cannot be placed directly in the KOH solution. Instead, the front side of the disk has to be protected to avoid damage as observed in Fig. 9.7(c). Clearly, only the back side of the wafer disc can be in contact with the KOH solution. Therefore, a stainless steel etching holder was constructed by the mechanical work shop which prevents the KOH solution from entering by a synthetic rubber (*Viton*) o-ring. Figure 9.8 shows the principle of etching.

Figure 9.10(a) is an optical microscope image of a successfully etched window showing bond pads from below. The etch rate depends strongly on the crystal orientation. As the SEM image (Fig. 9.10(b)) shows, this results in a pyramid shaped etch pit and a rectangular membrane. The side walls have a 54.7°angle with respect to the membrane which is the result of the {111} planes acting as an etch stop

A total of three (*Viton*) o-rings are required to prevent the etching fluid from entering the holder (Fig. 9.11(a)). The smallest o-ring is about the size of the 4mm wafer disc and is pressed directly onto the back of the disc. The 4 mm wafer disc size was chosen in favor of the 3 mm side that are standard in the TEM because the large discs have less chance of leaking at the o-ring.

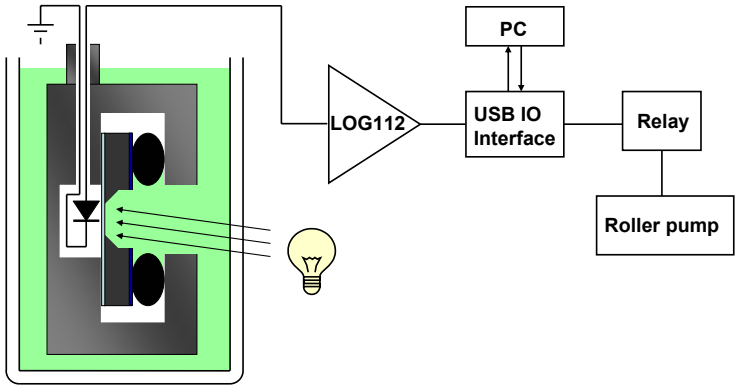

Figure 9.9: *Principle of how etching is controlled. A light source is directed to the back of the wafer disc. Light travels through the beaker glass, the etching solution and reaches the back of the wafer disc through the center of the o-ring. As the wafer disc etches, more light is able to reach the photo diode behind the wafer disc. For simplicity, the two other o-rings and the height adjustment screw between the wafer disc and the photo diode are not shown. Photo current is amplified by a logarithmic amplifier and sampled by a computer program. Etching is finished when a constant photo current is obtained.*

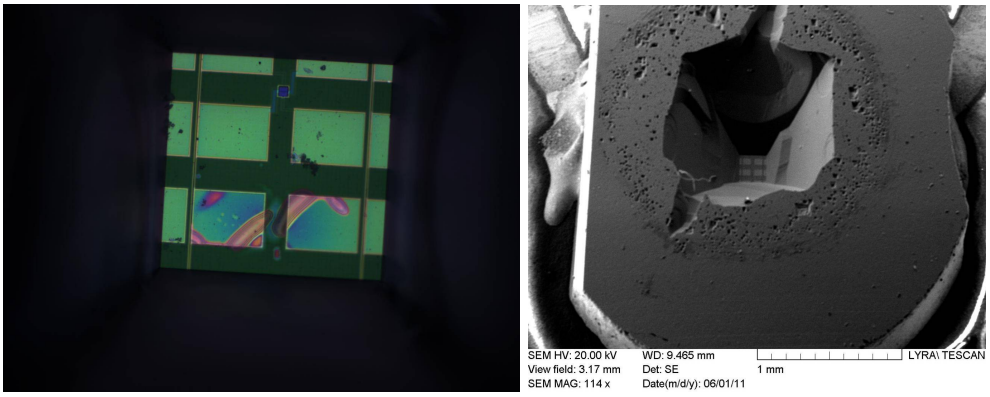

(a) (b)

Figure 9.10: ***(a)*** *Optical micrograph of the back side of PRAM wafer disc where the silicon was etched up to the membrane.* ***(b)*** *SEM image of the same wafer disc showing the pyramid shaped etch pit (see Fig. 9.8(b).*

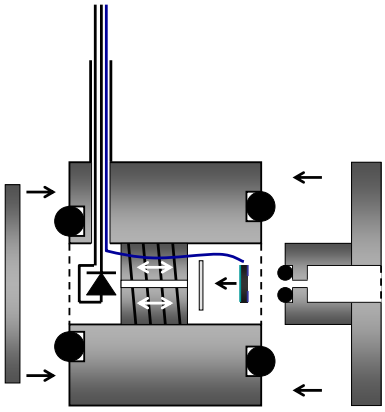

(a)

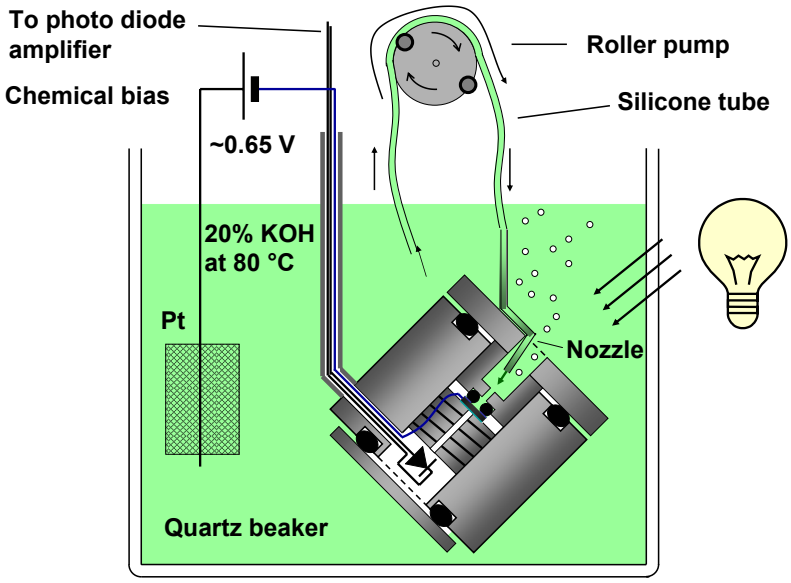

(b)

Figure 9.11: ***(a)*** *Construction of the etch holder used for etching silicon. Three o-rings keep the etch fluid from entering the etching holder. A screw in the etch holder allows for fine tuning the pressure of the o-ring that is pressed directly onto the back of the disc. A photo diode behind the wafer disc is used to monitor the etching process.* ***(b)*** *The etching holder is shown in the etching solution. A lamp is directed to the wafer disc. The light is transmitted solution onto the back of the wafer disc. As etching takes place, more light is able to be transmitted through the wafer disc onto the photo diode (see Fig. 9.9). As etching takes place big bubbles form that block etching fluid from reaching the back side of the wafer disc. A roller pump connected to a nozzle creates a flow of etching fluid that removes the big bubbles.*

Two additional o-rings are required to fully close the holder. A screw inside the holder allows for adjusting to different wafer thicknesses (Fig. 9.11(a)). The wafer disc is electrically isolated from the stainless steel holder by a plastic foil. Electrical contact to the wafer disc is made by a wire (blue in Fig. 9.11(a)) that connects to the disc by a clip. Figure 9.11(b) shows the etching holder lowered into the KOH solution. Before the etch holder is placed in the fluid a drop of hydrofluoric acid (1% solution) is applied to the silicon for one minute to etch away the native silicon oxide that forms on bare silicon.

The etching process was monitored optically. A lamp is directed at the quartz beaker (Fig. 9.11(b)). Light is transmitted through the fluid and directly onto the back of the wafer disc. As the etched wafer disc becomes thinner, more light is able to be transmitted through the dark grey silicon wafer disc. The screw behind the wafer disc has hole in the middle which allows the light to shine on a photo diode directly behind the screw. The light of the photo diode is amplified by a logarithmic amplifier and sampled by a computer through a USB interface (Fig. 9.9). The logarithmic amplifier is able to provide a photo current signal over five orders of magnitude. The photo current signal can be monitored throughout the etch process. The etching of silicon in KOH is a well-established process and was found to be relatively easy when a wafer disc was 'merely' placed in the solution as Fig. 9.7 shows. However, many unforeseen problems were created by the small size of the wafer disc and opening of the etching holder. Hydrogen gas bubbles formed during the etching process block the narrow channel to the silicon disc. The etching fluid is not replenishing even though a magnetic stirrer was always used.

Etching usually stopped after a few hours. This was indicated by the fact that gas bubbles stopped forming and the photo diode current became constant. After the wafer disc was taken out of the etching holder it was discovered that the etched silicon was covered by an electrically insulating layer which led to the following explanation: Gas bubbles blocking the narrow channel leading to the etched region cause the concentration of the etching product ($SiO_2(OH)_2^{2-}$) to increase. Naturally this will force the reversible third chemical reaction (Eq. 9.3) to the left. The (electrically insulating) SiO_2 formed in this chemical reaction is deposited onto the silicon which in the end stops the etching reaction from occurring altogether.

During most of the project the wafer disc was electrically connected to the etching holder due to the construction of the holder. It was found that the etch stop could be avoided when a negative bias with respect to a platinum counter electrode was applied to the holder (and cell). However a relatively high voltage of -1.4 volts was required which led to oxidation of the platinum counter electrode. Furthermore, one of the disadvantages of the bias voltage is that it breaks down the silicon dioxide membrane. Figure 9.12(d) shows an over-etched membrane from the back which was damaged heavily because it was exposed to the KOH for too long.

Figure 9.12(a) shows a wafer disc that was not etched fully and was taken out of the solution because etching stopped (i.e. photo current obtained a stable value). The etched surface appears to be quite rough. The etch holder was placed back in the solution after applying the HF step again to remove the any silicon dioxide. Etching commenced again and the holder was taken out of the solution after the photo

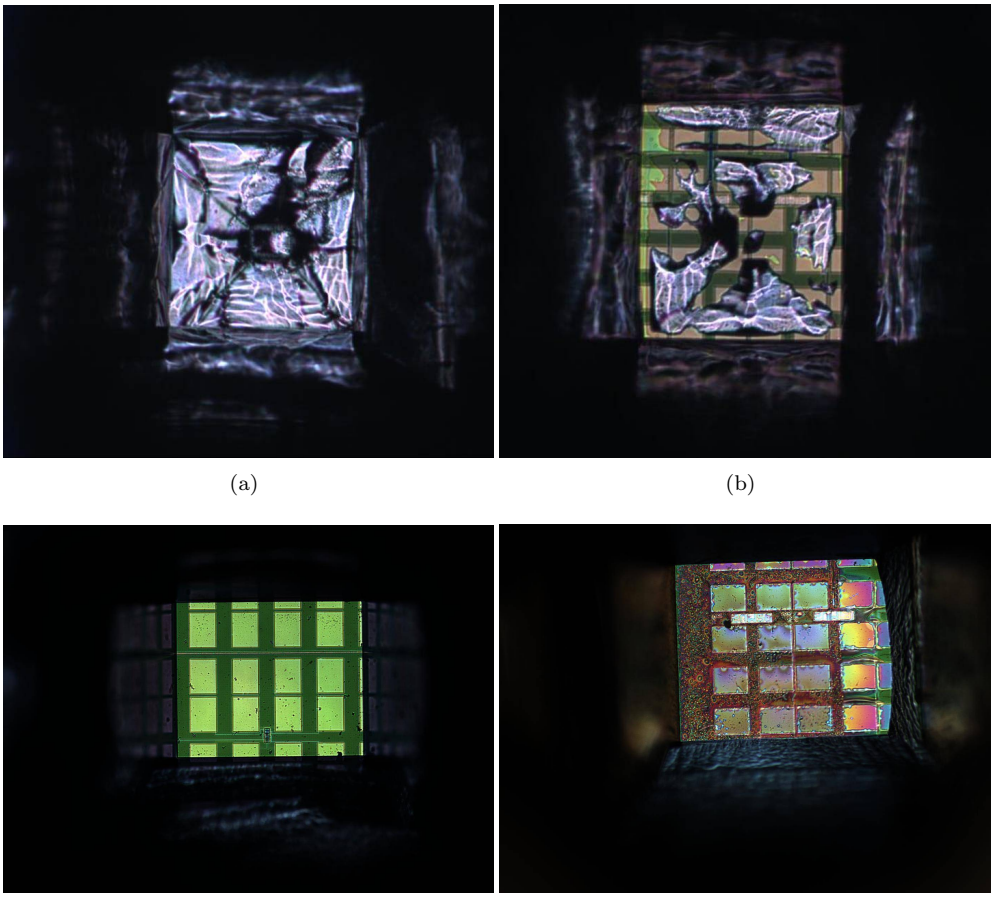

(a) (b)

(c) (d)

Figure 9.12: ***(a)*** *Back side of a wafer disc after etching appeared to be finished. Although a stable photo current was obtained a thin layer of silicon was still present on the back of the membrane. The wafer disc was placed in the etch holder again and a drop of HF solution was applied to remove any SiO_2 that acted as an etch stop.* ***(b)*** *After etching a stable photo current was reached again however, not all the silicon was etched. Small islands still remained that could not be etched further without damage to the membrane.* ***(c)*** *Properly etched membrane showing the bond pads from the back side.* ***(d)*** *When the bias voltage applied to the wafer disc is too high the membrane will be damaged. This can be related by break down of the SiO_2 of the membrane by the etching solution. However, when no bias voltage is applied etching will stop (see* ***b****) because the silicon wafer forms a SiO_2 layer. A bias voltage of -0.65 V was found to keep etching going without damage to the membrane.*

current became stable again. Figure 9.12(b) shows that small regions of silicon were not etched. Interestingly, the remaining silicon patches are islands, not electrically connected to the boundary. This shows that etching was only able to take place where the silicon was electrically connected.

A nozzle was constructed to inject fresh etching fluid directly into the etched region with the use of a roller pump. The injected fluid removes the bubbles although etching still stopped especially with a continuous flow. The best results were obtained by pulsing the pump: The computer program monitoring the etch rate was used to turn on the pump for only six seconds every minute. This 'blows' away big bubbles when the pump is on and allows normal etching to occur in between. Furthermore an attempt was made with an ultrasonic bath to remove the bubbles however this was also not successful and led to leaking.

One of the solutions was to modify the etch holder by the mechanical workshop to accommodate for a separate electrical connection to the wafer disc insulated from the etch holder. This direct connection allows for the monitoring of the electrical current supplied to the wafer disc (instead of the etch holder and the wafer disc). It was found that etching could be performed at a much lower voltage of -0.65 V with respect to the counter electrode.

It is believed that the etch process should be performed in future with an additional reference electrode and a potentiostat. Unfortunately, due to time constraints it was too late to incorporate this as it would have led to better understanding of the etch process. Another possible solution would be to abandon the use of an etch holder with o-rings and focus on protecting the front of the wafer. This would allow a less constrained etching process.

9.2.6 Focused ion beam preparation for in-situ TEM

A set of 4 mm discs were cut from a wafer containing a PRAM cell in the center of the disc. A 450 µm hole was drilled and extended electrodes where prepared in the cleanroom. The remaining silicon was etched by KOH (see previous section). The wafer discs were glued with conductive epoxy to a chip carrier which allows for an easy contact to be made in the probe station. On the back side of the discs a layer of titanium of 4 nm thick was deposited by electron beam evaporation. This layer prevents electric charge from building up in the FIB. Although a conductive layer is necessary for proper observation and milling in the FIB this layer could not be applied to the front of the wafer as it shorts the cells electrically. Instead, a layer of *poly(3,4-ethylenedioxythiophene) poly(styrenesulfonate)* (PEDOT:PSS) was spin coated on the front size of the wafer disc after bonding it to the chip carrier. This is a conductive polymer that is dissolved in water. Although it is conductive, it was found that the parallel resistance it adds is in the order of 10^8 ohm This value was obtained by applying a DC voltage to a cell until it was 'destroyed'. The remaining resistance from the PEDOT:PSS could then be measured. Since the measured parallel resistance of the PEDOT:PSS was about an order of magnitude larger than the maximum cell resistance in the amorphous state it's influence can be neglected.

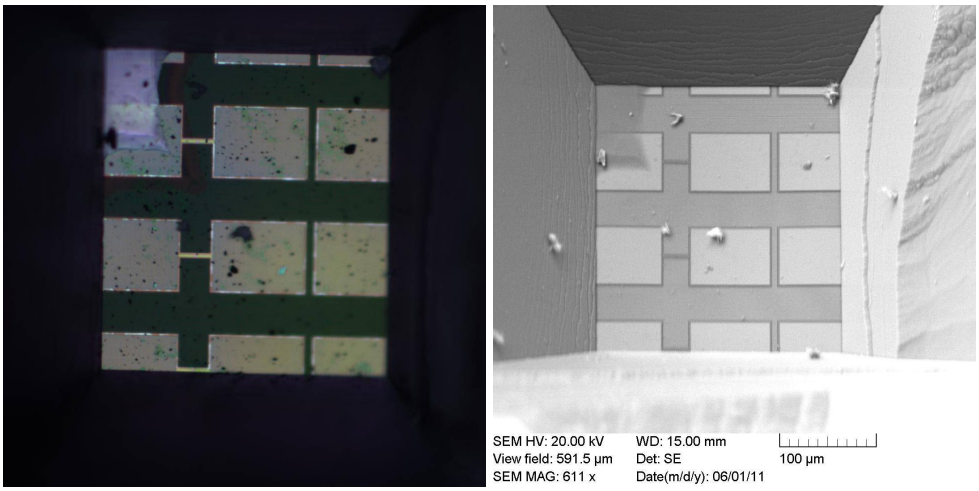

(a) (b)

Figure 9.13: *The back side of a disc containing PRAM cells after etching in KOH.* ***(a)*** *Optical micrograph showing the back side of the membrane.* ***(b)*** *Image recorded in the FIB/SEM after a 4 nm titanium layer was deposited. After this step, the sample can be processed further for TEM observation*

For FIB milling a Ga ion source was used with an acceleration voltage of 30 kV. The proper mill depth setting (i.e. mill time) was determined by visual judgment after adjacent PRAM cells were milled to varying depths. On the front side of the PRAM cell a rectangular hole was milled by FIB which is shown in Fig. 9.14(a). This corresponds to the first FIB milling step described in Fig. 9.3(a). Although a lot of material is removed, the membrane is not thin enough to be observed in the TEM with adequate resolution. After the PRAM cell is reversed, another square hole is milled by FIB up to the electrical contacts (see Fig. 9.14(c)) that connect the bond pads to the PRAM cell corresponding to the second FIB milling step Fig. 9.3(a). A final FIB milling step that removes the material in between the electrical contacts up to the PRAM line cell leaves a thin membrane in the order of 200 nm thick which is thin enough for TEM observations. A PRAM cell, prepared for TEM by the process described earlier in this chapter (Sections 9.2.2 to 9.2.5), is shown in Fig. 9.15(a). The bright regions are thinner as a result of the FIB milling steps shown in Fig. 9.14. The outline of the dog-bone shaped line cell is shown by the blue line. An image with a higher magnification is shown in Fig. 9.15(b). The cell is in the crystalline state which is observed by the light and dark contrast present within the TEM image of the line cell. The image quality shows that the TEM sample was thinned to an excellent thickness. However, the bright circles that can be observed in the SiO_2 surrounding the line cell indicate that voids are present in the SiO_2. These voids must have formed during (one of) the last FIB thinning steps and indicate that the favorable thickness also led to some clearly observable damage to the sample. Although this cell

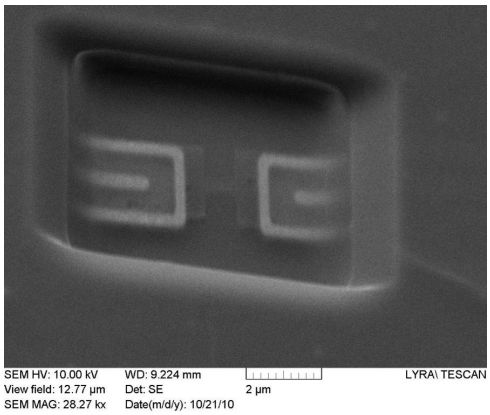

(a)

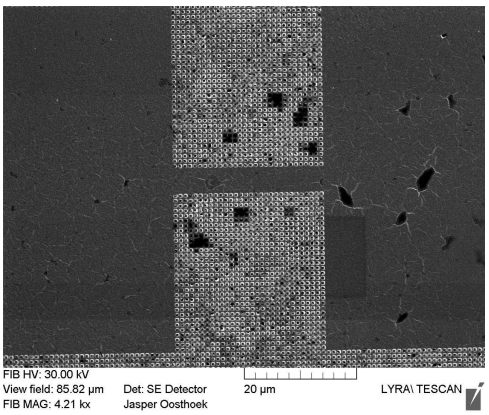

(b)

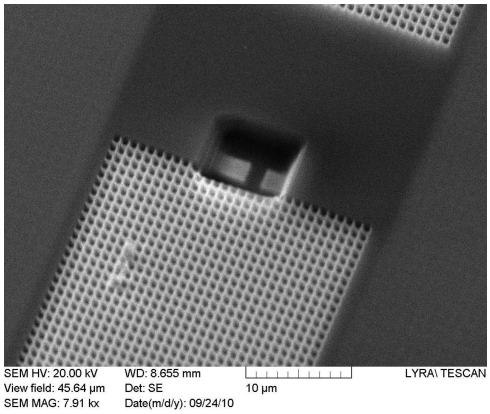

(c)

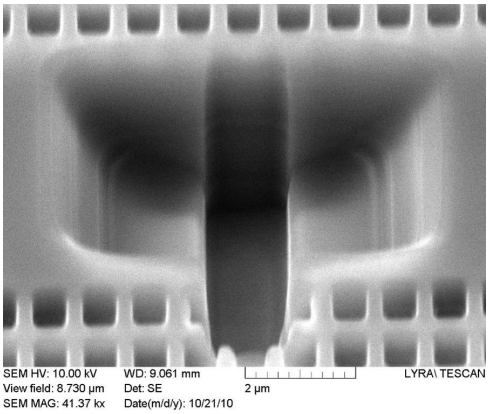

(d)

Figure 9.14: ***(a)*** *FIB/SEM image taken from the front side of a PRAM cell after a hole was drilled as close to the line cell as possible. The outline of the dog-bone shaped line cell can be observed.* ***(b)*** *SEM image of the back side of the membrane. The outline of the bond pads and line cell are clearly visible.* ***(c)*** *SEM image taken after a square hole was etched by FIB to a depth almost reaching the electrical contacts that connect the bond pads to the cell. The electrical contacts are now clearly visible.* ***(d)*** *SEM image taken after a second rectangular hole was etched in between the electrical contacts. The depth of the hole was chosen to be as close to the phase-change line cell as possible.*

could not be switched, because it did not contain the extended contacts, it represents a proof of principle that processing of switchable TEM samples was possible. All required individual steps to achieve such samples could be performed as explained and demonstrated in the last 5 sections (Sections 9.2.2 to 9.2.6).

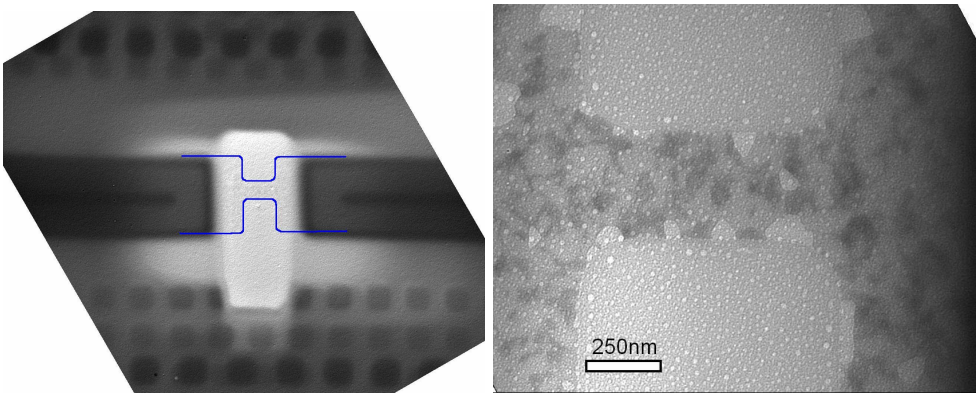

(a) (b)

Figure 9.15: *TEM images of a PRAM cell prepared by the process described earlier in this chapter.* ***(a)*** *Square and rectangular etched holes that were shown in Fig. 9.14(c) 9.14(d) are clearly observable in this overview TEM image.* ***(b)*** *TEM image showing the line cell in more detail, indicating that the TEM sample was thinned to an excellent thickness. Using under- and overfocused TEM images it can be demonstrated that the white spots that can be observed in the SiO_2 surrounding the line cell correspond to voids in the SiO_2. These voids must have formed during (one of) the last FIB thinning steps and indicate that the favorable thickness was accompanied by some damage to the sample.*

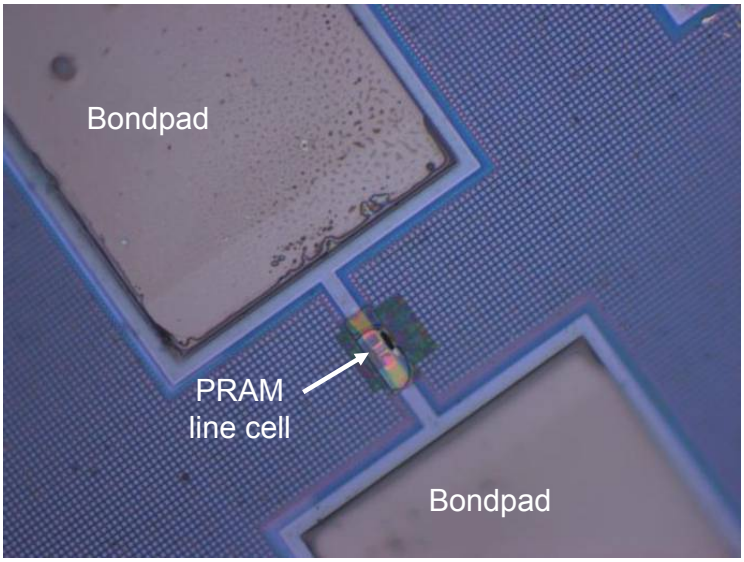

Figure 9.16: *Overview light microscopy image of a PRAM line cell that is prepared by dedicated FIB processes in such a way that it can be observed locally with TEM, but still is fully electrically accessible so that it can be switched and characterized electrically.*

9.3 Results

A PRAM line cell was processed by NXP using FIB (see Section 9.2.1 for the details) in such a way that it could be observed in the TEM without breaking the electrical connections to the cell. Hence, the cell could still be switched and characterized electrically.

An overview light microscopy image is shown in Fig. 9.16, indicating the locally thinned region around the line cell and the two bond pads that were used for making the electrical connection. Note that the FIB preparation was performed in various steps (see Section 9.2.1). In a first step the Si substrate was removed completely over a large area also underneath the bond pads. This made it almost impossible to contact the bond pads with any probe needle system without puncturing the thin membrane. Still, a relevant switching experiment could be performed on this line cell where the electrical properties can be correlated with TEM images. In order to understand the results the overview TEM image shown in Fig. 9.17(a) is required. It shows that the line cell still has proper electrical contacts on both sides, but the rectangular runners that are imaged black in the TEM image show a 90 °turn connections only towards the upper side in the image. The analogous 90 °turn connections which should be observable at the lower side in the image are absent, because apparently the material had been removed during the FIB process only leaving at this location a thin SiO_2 region. This makes the electrical connection to the line cell asymmetric. Another

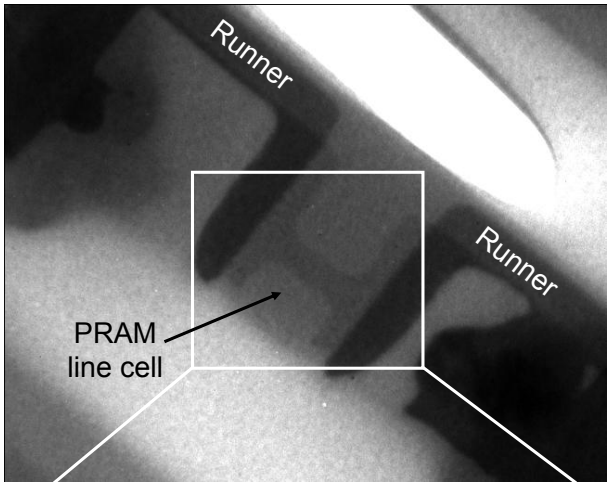

(a)

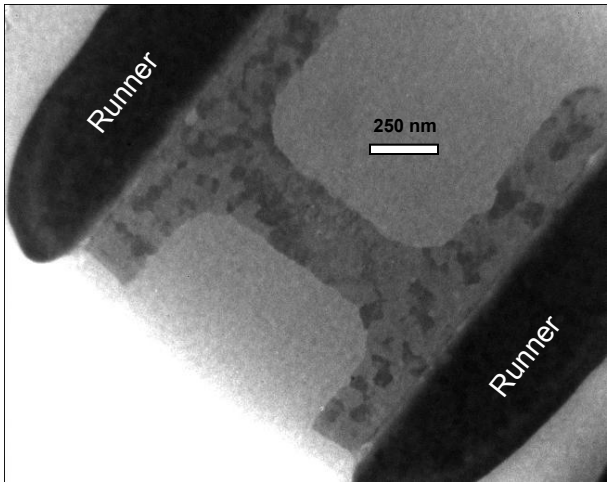

(b)

Figure 9.17: ***(a)****: Overview TEM image showing faintly the dog-bone shaped PRAM line cell in the middle. The cell is still being electrically connected on both sides by the black runners (showing a 90 °turn at the upper side). The brightest area on top indicates a hole made during the FIB process. Also on the lower left side a relatively bright area can be discerned which correspond to a thin region, where the FIB process has actually completely removed the 90 °turns of the runners on the lower side making the electrical connection quite asymmetric.* ***(b)****: More detailed bright-field TEM image of the PRAM line cell showing crystalline contrast in phase-change material throughout the line cell indicating that it is in the SET state. A relatively defocused electron beam with long exposure times of 20 s. was needed to obtain sufficient contrast without damaging the line cell by the incident energetic (200 kV) electrons.*

asymmetry that can be observed in the image is that a hole through the membrane is present only near the top side of the image (most bright region).

Figure 9.18 summarizes the main results of this section, i.e. showing TEM images for a switching experiment allowing a unique direct correlation between TEM images and electrical characterization and switching. Figure 9.18(a) shows the initial state of the cell after preparation indicating that the cell is in the fully crystalline SET state. This is in agreement with the measured resistance of the cell of 2.0 kΩ. This resistance is very similar to the one measured for line cells in the original (thick) memory. Figure 9.18(b) shows the structure in the line cell after a 50 ns RESET pulse was applied. It can be clearly observed that this pulse successfully produced an amorphous mark (outlined blue) in the cell. However, another interesting feature can be observed, because the comparison between Fig. 9.18(a) and 9.18(b) indicates that a much larger part of the line cell was molten during the SET pulse (blue + red regions). The region outlined red must have been recrystallized during (insufficiently fast) cooling. The corresponding resistance of the line cell with the amorphous mark (outlined blue) is 1.0 MΩ. This resistance value, that is 500 times higher than of the initial SET state, indeed proofs that an amorphous mark must be present, but this value is about a factor 5 to 10 lower than the RESET resistance normally measured for the same line cells in a (thick) memory. This demonstrates that the amorphous mark is much smaller than usual and corroborates the observation that a larger part of the line cell was molten but also recrystallized due to insufficiently fast cooling.

The reason that a smaller amorphous mark is obtained than the region molten during the RESET pulse is straightforward. Due to the FIB preparation most of the volume surrounding the line cell has been removed and heat conduction away from the cell to the surrounding material is not as effective as in a normal thick memory. Therefore the heat produced in the line cell due to Joule heating during the RESET pulse cannot be conducted away fast enough and in combination with the extremely high crystal growth rates that are possible in this so-called fast-growth PCM allows for crystallization in a part of the molten region. This process results in a shorter amorphous mark and a lower resistance than observed usually for the cells in a thick memory. Still, an interesting feature is that this recrystallized part has an asymmetric position that is in accordance with the asymmetric configuration of the electrical connection by the runners as was explained above. It is also evident that the hole produced by the FIB (cf. Fig. 9.17(a)) is not relevant, because heat can still be conducted effectively along the hole by the runners. Therefore, it may be concluded that the PRAM line cell operation is not seriously affected when most of the volume surrounding the line cell is removed by FIB as long as the complete electrical connection to the line cell is preserved and not damaged by the FIB process.

The amorphous mark observable in Fig. 9.18(b) could be erased by a 200 ns 2.8 V SET pulse, i.e. the observed threshold voltage was 2.8 V. The result of this operation is shown in Fig. 9.18(c). The corresponding line cell resistance was 2.6 kΩ, somewhat higher than the 2.0 kΩ resistance of the initial SET state shown in Fig. 9.18(a). Indeed, careful inspection of the TEM image shows that the amorphous mark is not completely erased and that still residual amorphous regions (outlined blue) are present.

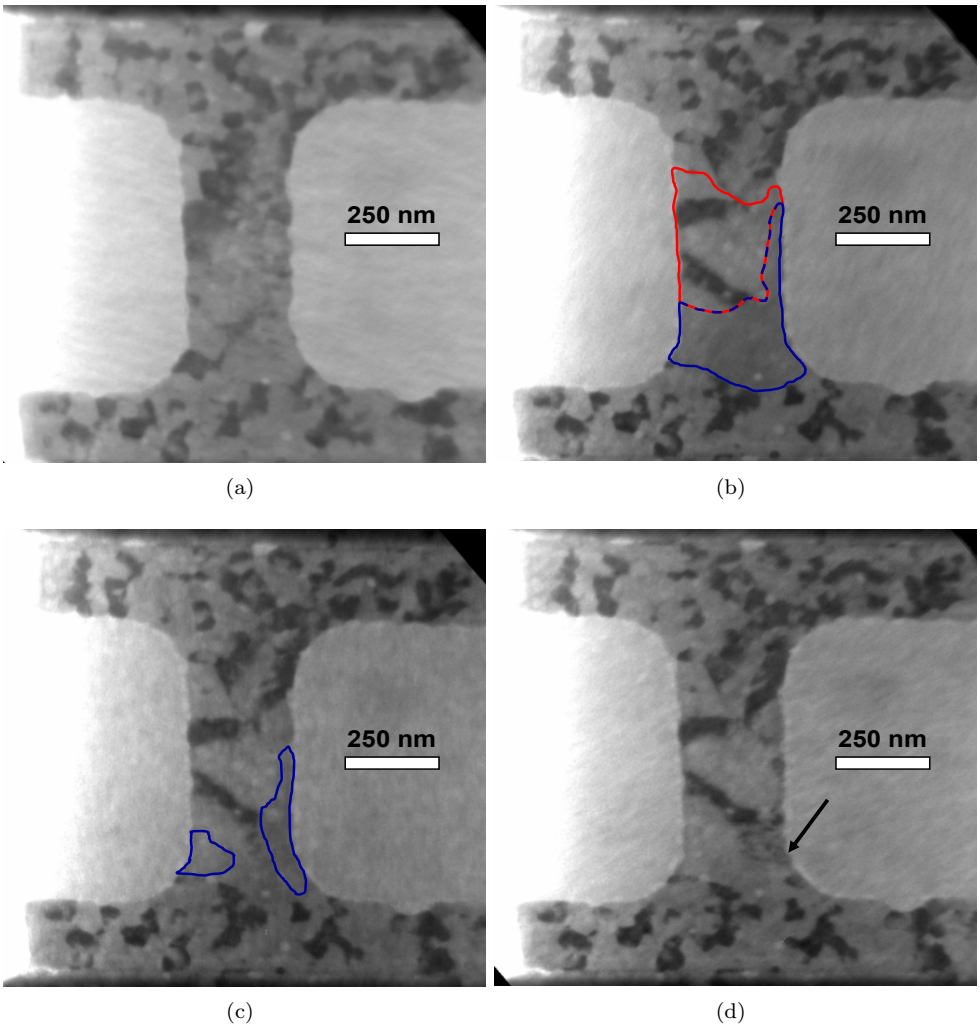

Figure 9.18: *Correlation of TEM images and electrical characterization and switching. The* ***(a)*** *shows the initial SET state (fully crystalline, 2.0 kΩ.). The* ***(b)*** *shows the structure after a 50 ns RESET pulse, indicating the amorphous mark (outlined blue), the region that was molten during the SET pulse (blue + red regions) and the region that recrystallized during cooling (outlined red). The corresponding resistance is 1.0 MΩ.* ***(c)*** *shows again the SET state after a 200 ns 2.8 V pulse resulting in a resistance of 2.6 kΩ, but still residual amorphous regions (outlined blue) are present. The bottom-right image shows the subsequent SET state after a series of 200 ns pulses, with voltages increasing to 4 V as shown in Fig. 9.19, that removed the residual amorphous regions, decreasing the resistance from 2.6 to 2.0 kΩ. The arrow in* ***(d)*** *points at a region that has been crystallized during the series of 200 ns pulses.*

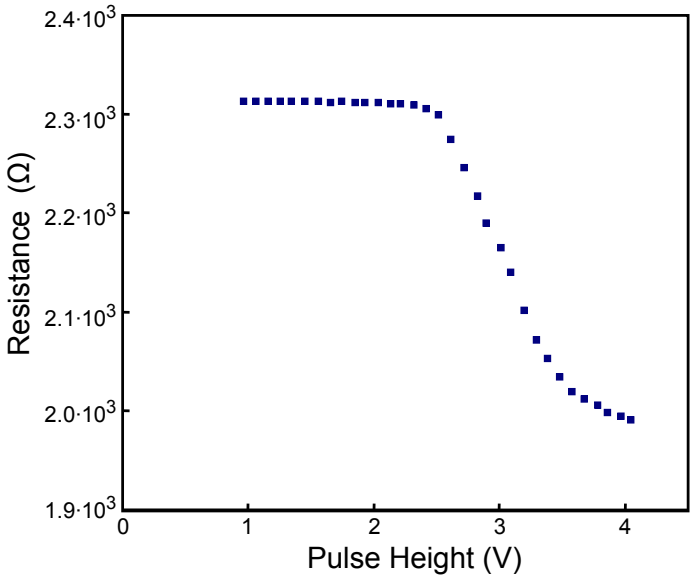

Figure 9.19: *A series of SET pulses (200 ns) with increasing pulse height (1 to 4 V) were applied in between obtaining Fig. 9.18(c) and 9.18(d). It can be observed that the resistance shows a gradual development that can be explained by a step by step growth of the crystalline area.*

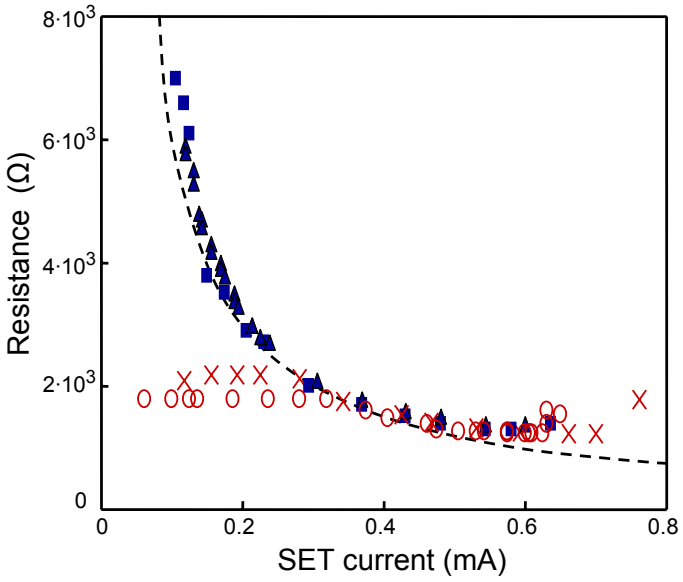

Figure 9.20: *Development of the SET resistance of various line cells as a function of gradually increasing SET current. The filled squares and triangles correspond to normal behavior whereas the crosses and open squares correspond to anomalous behavior which are described in detail in the main text.*

Another interesting result that can only be obtained by correlating TEM images with the observed threshold voltage is that the more relevant material specific threshold field can be determined. In order to do so, the threshold voltage has to be divided by the amorphous mark length, which is generally unknown, but can now be directly measured in the TEM image (top right image in Fig. 9.18). The observed length is 250±20 nm giving a threshold field of 11±1 V/µm . In the previous chapter 8 for the same PCM a threshold field of 26±2 V/µm was determined. In the seminal work by Lankhorst [52] a threshold field for the same PCM of 14 V/µm was derived, but their data show that for short line cells the threshold field seems higher than for long ones (ranging between 20 and 10 V/µm). This indeed also seems to hold in our case, because in the previous chapter the line cells examined had a length of 225 nm and in this chapter the length of the line cells is 800 nm. The threshold field was determined by Krebs et al. [45] for various materials giving the following values (in V/µm): 8.1±0.2 for $Ge_{15}Sb_{85}$, 19±1 for AgInSbTe alloy and 56±2 for $Ge_2Sb_2Te_5$. The present GeInSbTe alloy is most similar to their AgInSbTe alloy merely replacing the same amount of Ag by Ge and indeed the threshold fields determined in this thesis are also close to their value. It might be possible that the threshold field of a PCM is (somewhat) lowered by the defects created in the PCM during the final stages of the FIB process and even by the damage created during TEM imaging by irradiation with 200 kV electrons, where we observed that severe damage to the line cells can be easily created. Unfortunately, we were not able to test this hypothesis of electron irradiation lowering of the threshold field.

Since the SET state shown in Fig. 9.18(c) still contains some residual amorphous regions a series of 200 ns SET pulses was applied with voltages increasing from 1 V to 4 V in steps of 0.1 V. The measured line cell resistances as a function of the voltage of these SET pulses are shown in Fig. 9.19. It can be observed in Fig. 9.19 that for pulses in-between 1.0 and 2.6 V the resistance remains at the initial 2.6 kΩ value. For pulses in-between 2.6 and 3.5 V a decrease of the resistance to 2.0 kΩ can be observed in Fig. 9.19 and starts to stabilize for pulses in-between 3.5 and 4.0 V. Indeed the value of 2.0 kΩ corresponds to the initial fully crystalline SET state shown in Fig. 9.18(b). Figure 9.18(d) shows the TEM image after this complete series of 200 ns pulses (with voltages increasing to 4 V) was applied. Indeed, the residual amorphous regions were removed by the series of pulses. The arrow in Fig. 9.18(d) points at such a region that has been crystallized during the series of 200 ns pulses.

It would be of great interest to repeat the complete switching cycle shown in Fig. 9.18 several times in order to obtain good statistics and to repeat it for various line cells (e.g. with different lengths). Unfortunately this was not possible, because the preparation method with complete removal of the Si substrate also below the bond pads made it nearly impossible to contact these pads by probe needles without destroying the sample. Still, a final interesting comparison between the results obtained in Fig. 9.18 and 9.19 and electrical characterization results, see Fig. 9.20, showing much better statistics can be made. The results of Fig. 9.20 hold for 700 nm long line cells and show the development of the SET resistance when SET pulses with gradually increasing currents are used. Two types of behavior can be observed in Fig. 9.20, which we will call normal and anomalous behavior, respectively: **(1)** Normal

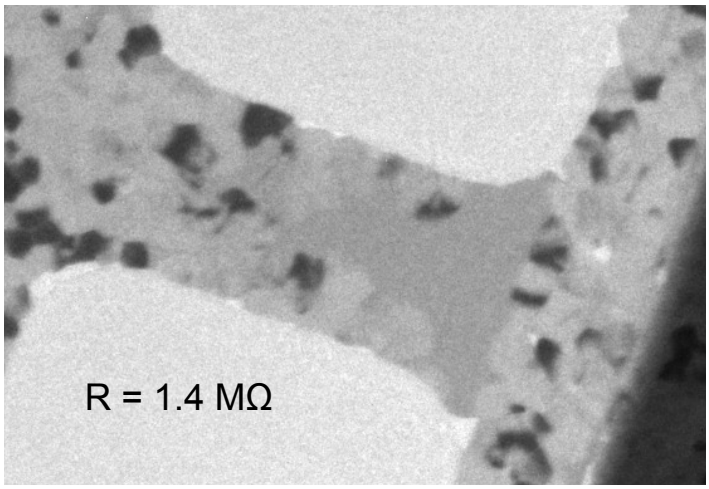

(a)

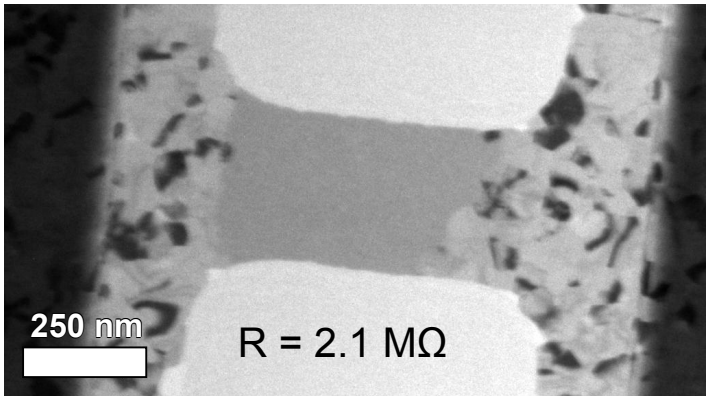

(b)

Figure 9.21: *TEM images of 600 nm long line cells in the RESET state showing on top a line cell with a small amorphous mark with non-uniform shape corresponding to a low resistance of 1.4 MΩ and at the bottom a line cell with a large amorphous mark with uniform filling of the line. Note that these FIB prepared TEM samples were not prepared according to a method that still allows electrical access to the line cells, but were produced according to the method delineated in Chapter 8 of this thesis.*

behavior with a gradual reduction of SET resistance with increasing pulse height (see filled square and triangle symbols in Fig. 9.20). This is typically observed when the initial amorphous RESET resistance was >2 MΩ or when the initial RESET pulse length used was >50 ns. **(2)** Anomalous behaviour with a sudden drop of the resistance to approximately 2 kΩ (see crosses and open circle symbols in Fig. 9.20). This is observed when the initial amorphous RESET resistance was <2 MΩ and the initial RESET pulse length was equal to 50 ns. In both cases the current required for (partial) switching to the SET state is much lower than needed to uniformly heat the full cross section of the line to 600-700 K. This suggests a kind a filament formation in the amorphous mark to explain the results of Fig. 9.20. Representative TEM images of line cells in the initial RESET state that gives rise to the two types of subsequent SET behaviour are presented in Fig. 9.21.

Based on a comparison between the amorphous mark observable in the top left image of Fig. 9.18 with the ones observable in Fig. 9.21 indicates that a similar SET behavior as for the top image in Fig. 9.21 is expected with the anomalous behavior. Indeed, this is observed; also compare Fig. 9.19 with Fig. 9.20. In Fig. 9.19 the sudden drop is to 2.6 kΩ and then a small decrease to 2.0 kΩ. In Fig. 9.20 the sudden drop is to 2.0 kΩ and then a small decrease to about 1.3 kΩ. These results, including the bottom left image in Fig. 9.18, seem to indicate that in case of the anomalous SET behavior a kind of massive crystalline filament is formed that consumes most of the width of the amorphous mark explaining the sudden drop to low resistance values during the SET operation. This only leaves minor residual amorphous regions left which explains the small resistance decrease that is possible with increasing SET currents. The normal SET behavior should then occur with filament(s) having large aspect ratio between length and width. Only in this case a relatively high initial SET resistance of 7 kΩ is expected that can be still reduced gradually and largely to about 1.5 kΩ by a continuously increasing width of the filament(s) until the whole amorphous mark has been crystallized. Unfortunately, formation of these high aspect ratio filament(s) with their gradual lateral growth was not observed in any TEM image. Still, support for this scenario comes from the following simple model.

We start by stating that the power density p_{cryst} required to crystallize a filament of length L and cross-sectional area A should be independent of A and can be written as:

$$p_{cryst} = J^2 \rho \tag{9.4}$$

with J the current density, which can be described by:

$$J = \frac{I}{A} \tag{9.5}$$

with I the total current that is running through the line cell (which in principle only runs through the filament, because the amorphous surrounding has much higher resistance) and ρ the resistivity of the crystalline filament which can be described by:

$$\rho = \frac{RA}{L} \tag{9.6}$$

Now by extracting the cross-sectional area A from Eq. 9.6, substituting it in Eq. 9.5 and then plug the result in Eq. 9.4 gives:

$$p_{cryst} = \frac{I^2 R^2}{\rho L^2} \tag{9.7}$$

Because in our experiment the length of the filament is determined by the amorphous mark length and does not change in a first order approximation when increasing the RESET current pulse and because we also assume that the resistivity of the crystalline filament remains constant, the result in Eq. 9.7 demonstrates that the product of the current I and the resistance R should be constant and thus indicates a hyperbolic behavior. Indeed, the black line in Fig. 9.20 describing a hyperbolic behavior matches the experimental data for the normal SET behavior rather well and thus suggests that the normal SET behavior occurs by formation of filaments which subsequently only grow in the lateral direction until the whole amorphous mark is crystallized.

9.4 Conclusions

Two PRAM cells processed by NXP have been switched and observed in the TEM. However, these cells could not be probed without damage as the silicon was completely removed from the back. The delicate membrane that remained after removal of the silicon was punctured by the probe needles. Still, interesting results have been obtained from one of these cells. The electrical properties could be related to the TEM images: It was found that crystallization initiates from a narrow channel with amorphous marks still present on both sides. The cell could be crystallized completely by applying higher energy SET pulses. Furthermore, it was found that the PRAM cell processed for TEM observation could not be brought to a resistance as high as unprocessed cells. This was related to re-crystallization of the molten region during the melt-quench phase. As a lot of material was removed to allow for TEM observation, the heat dissipation is impacted. Therefore it takes longer for the temperature of the active phase-change material to cool leading to re-crystallization. This was supported by the observation of a single crystal in the center of the line after being brought to the amorphous state. A different crystal structure was observed when the cell was still in the crystalline state. This proves that more material was molten than the region that became amorphous. Although many more PRAM cells were processed for TEM by NXP these experienced problems with a protective platinum layer that acted as an electrical short across the cell. Because it was not possible anymore for NXP to process PRAM cells for TEM this was attempted in Groningen. All the steps to process PRAM cells for TEM observation that could still be switched in-situ have been performed. Furthermore, a solution was found for creating an electrical contact to the cell without probe needles as well as providing a protective layer replacing platinum. However, due to time constraints it was not possible to perform all these steps to a single PRAM cell.

Chapter 10

Charge Collection Microscopy on in-situ switchable PRAM

10.1 Abstract

An imaging method has been developed based on charge collection in a scanning electron microscope (SEM) that allows for discriminating between the amorphous and crystalline states of PRAM line cells. During imaging the cells are electrically connected and can be switched between the states and the resistance can be measured. This allows for electrical characterization of the line cells in situ in the SEM. Details on sample and measurement system requirements are provided which turned out to be crucial for the successful development of this method. Results show that the amorphous or crystalline state of the line cells can be readily discerned, but the spatial resolution is relatively poor. Nevertheless, it is still possible to estimate the length of the amorphous mark and also for the first time we could observe the shift of the amorphous mark from one side of the line cell to the other side when the polarity of the applied (50 ns) RESET pulse is reversed.

10.2 Introduction

Although PRAM has a large potential as future non-volatile solid-state memory. Reliability issues still have to be addressed in order to allow mass-scale production of this memory technology. Improved understanding is required of the relation between nano-structure and properties of actual PRAM cells. A very suitable technique for establishing this relation is Transmission Electron Microscopy (TEM) which was explored in Chapter 8. Electrical characterization was performed on real memory cells that were brought to certain well-defined final states. These cells were then prepared for imaging using a focused ion beam instrument and were analysed by a TEM. To allow for imaging in the TEM, the cells were locally thinned from both sides leaving a $\approx$ 250 nm thick membrane. However, after preparation these particular cells

could not be switched anymore because the electrical contacts had been removed. It would seem ideal that the electrical switching and characterization are combined employing in situ TEM observations. Recent examples of this approach are provided in [61, 54, 62, 32]. However, a disadvantage of this approach is that locally the PRAM cell (i.e. with the layers above and below the active phase-change medium) has to be thin in order to allow for TEM imaging. This reduced thickness clearly alters the thermal properties and thereby also the electrical properties of the PRAM cells (see Section 9.3). Therefore the cells in a memory will not behave the same way as in situ analyzed cells.

In this chapter we explore an alternative imaging technique that can be combined with in situ electric switching and characterization. This alternative technique is *Charge Collection Microscopy* (CCM) that can be performed in a Scanning Electron Microscope (SEM). Particularly for semiconductor samples CCM, often named Electron Beam Induced Current (EBIC), has proven to be a powerful technique [53, 94]. The advantage of CCM for the present PRAM line cells is that in principle it should be possible to image the local conductivity in the PCM in the line cell which is still present on top of the silicon wafer. The passivation layer has to be thinned only from the top side and the electron beam has to only reach the phase-change material below the passivation layer. Therefore, the electrical behavior of the in situ analyzed cell will be more comparable to the cell behavior in the actual memory. Preparing PRAM line cells such that they can be imaged and still can be electrically switched and characterized is much less demanding in case of SEM than TEM (see also Chapter 9). Moreover, an SEM chamber containing the sample generally provides much more space for hosting additional equipment such as a probe station than is available in a TEM holder. These arguments make it highly interesting to explore the potential of applying CCM to in situ switchable PRAM line cells.

10.3 Methods

10.3.1 Connecting to the PRAM cell

In order to establish an electrical connection from the bond pads to the specimen current (SC) detector, a chip carrier device was constructed. Two millimeter size copper contacts were glued on a substrate. Wires could be soldered to the contacts. Aluminum wires with a diameter of 25 µm were ultrasonically bonded from the copper contacts to bond pads of the PRAM cells.

Figure 10.1(a) shows an SEM image of a bonded PRAM cell. The large contrast in the SEM image is a result of static charging of the surface. Due to charging, some bond pads are bright white while others appear black. Figure 10.1(b) shows an image taken with the SC detector. The bond wires in Fig. 10.1(b) are indeed bright white as they are directly connected to the SC. Quite surprisingly; all the other structures not electrically connected to the bond wires can be distinguished. Furthermore, both images appear to be very similar apart from having an inverted brightness.

The amorphous phase has a three orders of magnitude larger resistance than the crystalline phase. The crystalline phase is able to drain charge carriers easily to the

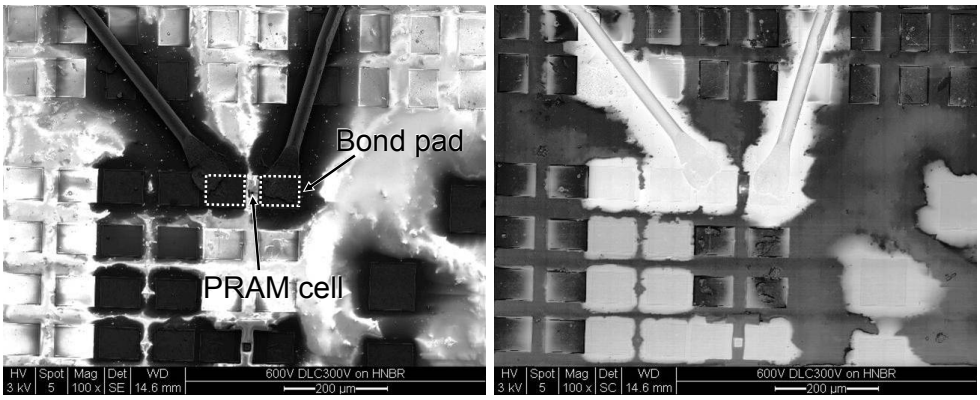

(a) SEM image (b) Specimen current image

Figure 10.1: *The bond pads of a PRAM line cell are connected the specimen current detector by a bond wire. The PRAM cell is located in between the bond wires. Apart from the inverted brightness, the specimen current image appears to be very similar to the SEM image as it shows the same features.*

SC detector. The higher resistance of the amorphous mark should in theory prevent charge carriers from reaching the crystalline phase. Therefore, the amorphous phase should appear dark and the crystalline phase white. This hypothesis was tested by imaging at a higher magnification.

Figure 10.2 show SEM and SC images of the PRAM cell at different magnifications. Because of surface charging that had been built up, the PRAM cell was severely damaged, i.e. showing signs that it actually had 'exploded'. The visible structure shows a hole where the passivation layer on top of the line of PCM has broken off. Figure 10.2(d) shows that the region around the opening is very bright as this is the location connected directly the SC detector. Unfortunately, no images could be taken without charging leading to catastrophic failure as Fig. 10.2 shows. Furthermore, the passivation layer on top of the cell is in the order of 800 nm which was found to be too thick for obtaining a good contrast. A solution to these problems was found that will be described in the next two sections.

10.3.2 Removing passivation

Initial results showed that it is not possible to perform CCM of the PCM line cell with an 800 nm passivation (SiO_2) layer on top. Therefore, a method was required to remove locally a controlled amount of this passivation layer. One of the methods was wet etching of the passivation with a buffered HF solution. However, this will remove the passivation on the whole surface when it would be more desirable to remove it locally, i.e. directly above the PRAM cell. By making use of a **Focused Ion Beam** (FIB) system the passivation could be milled locally in a controlled fashion.

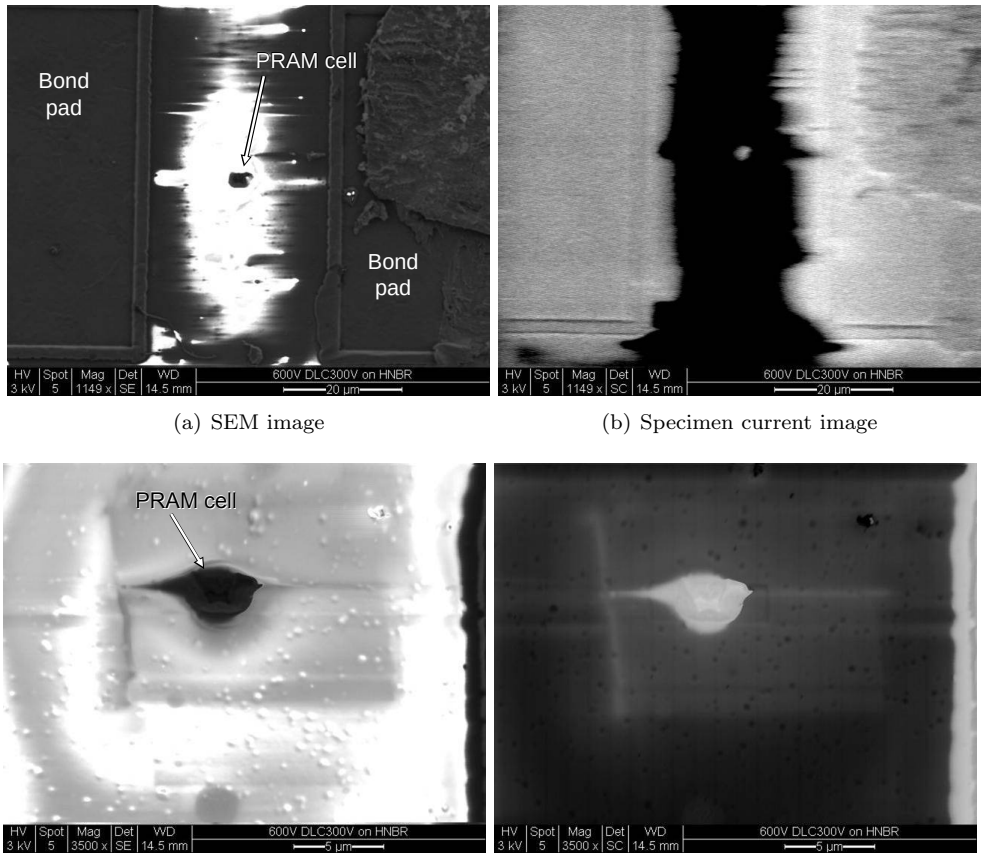

(a) SEM image (b) Specimen current image

(c) SEM image (d) Specimen current image

Figure 10.2: *SEM and specimen current (SC) images of a PRAM cell. On this cell a passivation layer of ± 800 nm was still present. Charging of the SEM beam had resulted in damage to the layer directly above the cell.*

Figure 10.3 is an SC image of a bonded PRAM cell. A circle shaped region had been milled using FIB. The same method described in Section 9.2.6 was applied. Although this method appears earlier in this thesis for readability, it was the work in this chapter that has led to the results in Chapter 9.

10.3.3 Resistive contrast imaging

Resistive contrast imaging (RCI) is a type of CCM that provides a resistance map between two test nodes on a structure [94]. RCI is normally used in the failure analysis of semiconductor devices. This differs from EBIC where a local electric field already present in a structure, for instance a pn-junction, leads to a sample current. However, when a local field is present it will appear in an RCI image as shown in Section 10.4.2. By using RCI, one side of a suspect device is connected to the ground and the other

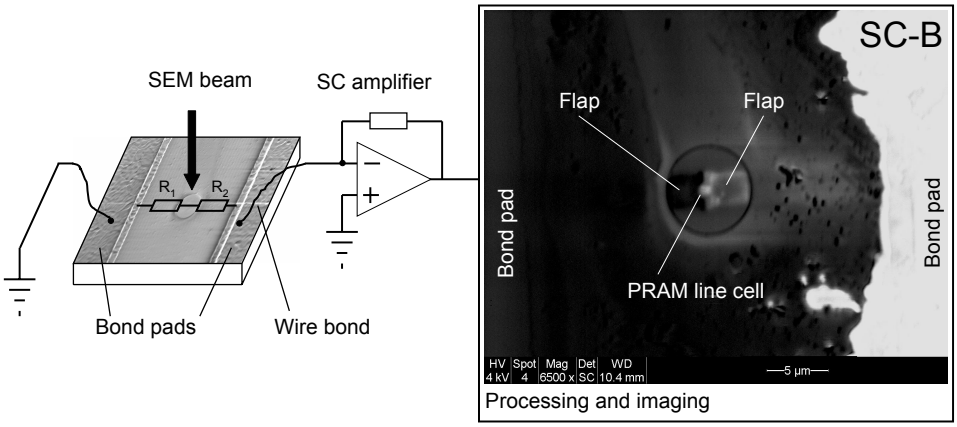

Figure 10.3: *Schematic representation of resistance contrast imaging (RCI), a form of CCM. The RCI/SC image shown is an actual PRAM cell brought to a high resistance state. The left side is connected to the ground and appears dark, where the right side that appears bright is connected to the SC detector.*

side to the SC amplifier. All the structures electrically connected to the SC detector will pick up the beam electrons and appear white.

Figure 10.3 is a schematic representation of RCI performed on a PRAM cell brought to the amorphous state. The left bond pad is connected to the ground by a wire bond while the right bond pad is connected to the SC amplifier which is a virtual ground. Therefore a negligible voltage difference is present across the bond pads. The amorphous mark itself provides the resistance difference necessary for RCI. R_1 and R_2 are the electrical resistances at a *specific location* in the sample leading to each bond pad. The contrast is based on the fact that the difference in resistance acts as a current divider for the injected beam electrons. A circular shaped region had been milled by FIB prior to this experiment. This leaves a passivation layer on top of the cell with a thickness of about a hundred nanometers. The FIB procedure is described in Chapter 9. Furthermore, a conductive polymer was spin coated on top of the wafer piece (Section 9.2.6). This conductive layer avoids the build-up of charge on the surface that leads to catastrophic failure (Fig. 10.2).

Figure 10.3 shows an SC image of a PRAM 700×300 nm^2 line cell programmed to the amorphous state. An SEM image of the same cell is incorporated in Fig. 10.3 as well. The left bond pad is connected to the ground and appears dark in the SC image while the right bond pad is connected to the SC detector and therefore appears very bright. Figure 10.3 shows that the largest amount of contrast appears directly at the location of the cell. Furthermore the phase change line can be distinguished. It appears that an amorphous mark is present at the left side of the line because the line itself appears bright. Although the line cell can be distinguished the contrast is quite poor. The electrical sensitivity of the PRAM cells led to a high chance of failure of the device.

10.3.4 In-situ SEM probe station

Because of the high failure rate of the devices many bonded devices would have been required. Furthermore, many cells are located close together on the same wafer and only one cell can be accessed by bonding. Due to the limited availability of PRAM cells this would have been very inefficient and time consuming. The method of wire bonding to the PRAM cells was abandoned and as an alternative a miniature probe station was constructed that fits inside the SEM (Fig. 10.4). It has similar components as the normal probe needle system (see Section 2.2.7) and is able to perform all switching operations and resistance measurements of the normal probe station. Only temperature measurements could not be performed in-situ in the SEM. Since many cells are present on one wafer piece, the in-situ probe station added a lot of flexibility to the measurements. When a cell is damaged, the next cell on the wafer could be easily accessed.

A vacuum throughput with seven coaxial throughputs was used in order to provide a connection between the electronics outside the SEM and the in-situ probe station (Fig. 10.4). During initial testing of in-situ SEM along with the electrical characterization setup a direct connection between the signal ground and the SEM ground was present. Each time a vacuum pump of another SEM in the same room switched on, the cell was programmed to the RESET state. Although the SEM acts as a Faraday cage this does not completely protect the cell as the pulses still need several nanoseconds to spread out across the system. This is enough time for a voltage difference to occur somewhere across a signal wire and a ground wire that programs the cell to the amorphous state, which is exactly what happened. To avoid this problem a ground switching arrangement was incorporated into the electronics of the probe station.

In *measurement mode*, the grounds are connected as shown in Fig. 10.5. In this mode it is possible to switch the PRAM cells between the amorphous and crystalline state and measure the resistance. The probe station chassis (see Fig. 10.4(a))is connected directly to the ground of the electrical characterization setup to electrically shield the cell. The vacuum throughput is screwed onto the SEM with Teflon screws to electrically insulate the signal ground from the SEM ground. The SEM and signal are indeed electrically connected but only through the ground filters of the electrical characterization setup (Section 2.2) and the connection of the SEM chassis to the same earth ground.

To obtain a stable image the chassis of the in-situ probe station and one side of the cell need to be connected to the SEM ground. Because the probe station is not connected anymore, the Faraday cage of the SEM protects the cell. However, to switch or measure the resistance of the cell, the signal ground and chassis of the in-situ probe station cannot be connected to the SEM ground.

Figure 10.5 shows the probe station in *measurement mode*. The chassis of the in-situ probe station is connected to the signal ground of the electrical characterization setup. The SEM ground is only connected to the signal ground through the ground filters. As in the probe needle system of the normal probe station a reed relay shorts the 330 kΩ series resistor to obtain a 1 kΩ series resistance.

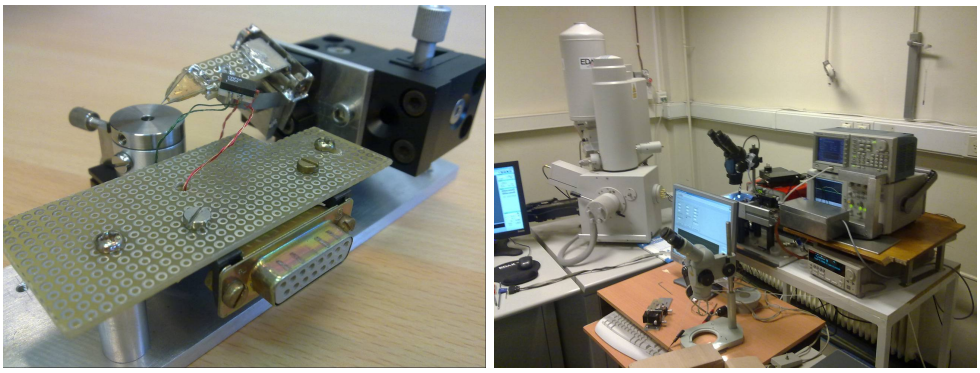

(a) (b)

Figure 10.4: *The probe station for in-situ CCM is shown in* ***(a)****. It is connected to the electrical characterization setup and fits well inside the SEM (see* ***b****).*

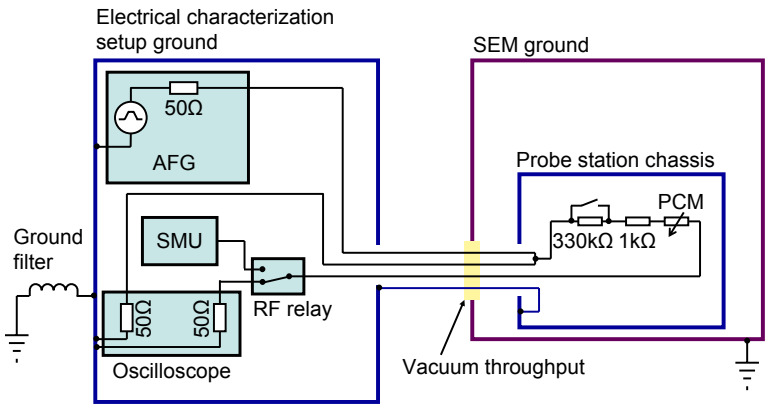

Figure 10.5: *Ground arrangement shown in measurement mode. In this mode it is possible to switch the PRAM cells and measure the resistance, imaging is not possible. The probe station chassis is connected directly to the ground of the electrical characterization setup to electrically shield the cell. There is a connection to the SEM ground, however this connection is indirectly through the earth ground.*

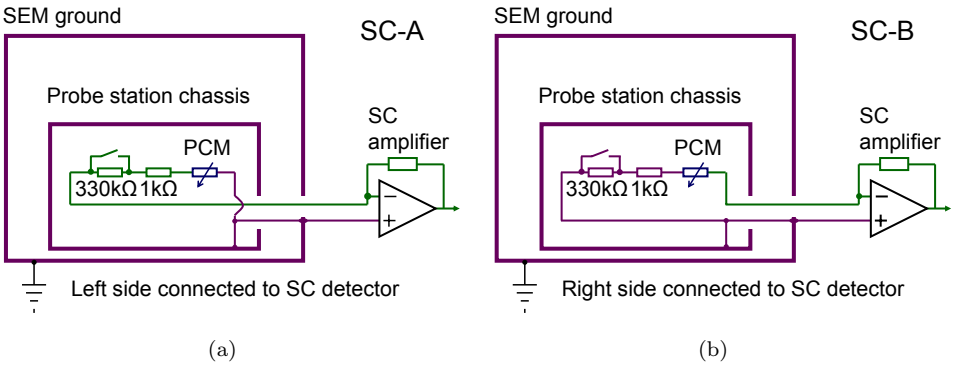

(a) (b)

Figure 10.6: *Ground arrangement showing the probe station in imaging mode.* ***(a)*** *shows left side of the PRAM cell connected to the SC detector and the right side to the ground. In* ***(b)*** *the connections are reversed.*

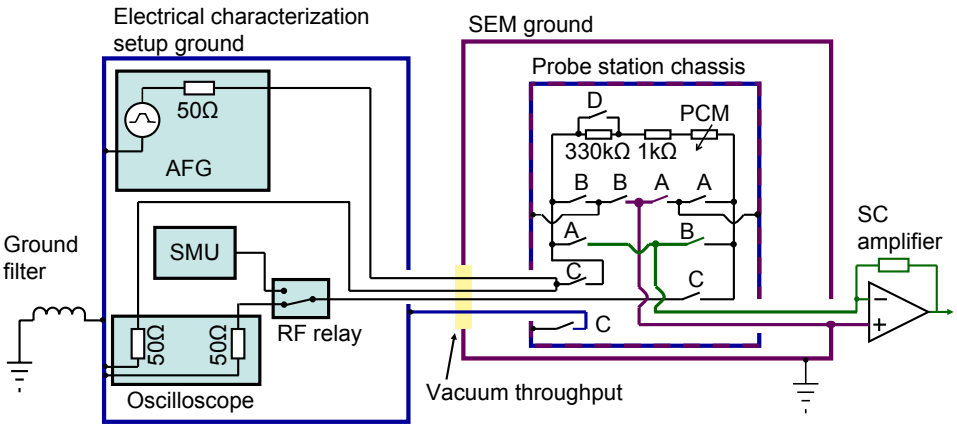

Figure 10.7: *A total of nine reed relays were needed in the in situ probe station to switch between the circuits shown in Fig. 10.5 and 10.6. For clarity, all the relays are open and no connections are made to the cell. However, opening all the relays simultaneously was avoided as this will lead to static charging in the SEM and damage to the cell when the relays are closed (see text).*

Figure 10.6(a) shows the in situ probe station in *imaging mode A*. The electrical characterization setup is completely disconnected from both the in-situ probe station chassis and the PRAM cell. Figure 10.6(a) shows that the left side of the cell is connected to the SC amplifier and the right side of the cell is connected to the (SEM) ground. Figure 10.6(b) shows *imaging mode B* which has the connections to the cell reversed.

To be able to combine connections shown in Fig. 10.6 and 10.5 a quite elaborate switching system containing ten reed relays was required (Fig. 10.7). The commercially available vacuum throughput contained seven electrical connections, three of which are needed for the connection to the electrical characterization setup. The remaining four connectors were used for switching the RF reed relays. The reed relays are identical to the reed relays used in the regular probe needle system (see section). A power supply similar to the one used to switch the relays in the probe needles system was constructed (Fig. 2.10(b)).

Closing all the relays marked either A or B results in the connections shown in Fig. 10.6(a) or Fig. 10.6(b) respectively. These connections provide *imaging mode A* and *B*. Closing the relays marked C will connect the cell and in-situ probe station chassis as shown in Fig. 10.5. To switch between *measurement mode* and *imaging mode*, relays A, B and C are all temporarily closed which was incorporated into the Labview code. Although this temporarily connects the SEM ground to the ground of the electrical characterization setup it also shorts the cell which protects the cell from voltage spikes. The relays A, B and C can never all be opened at the same time as the probe station will be able to become electrically charged by the electron beam. This was found to result in catastrophic failure of the cell.

10.4 Results

Figure 10.8 shows the probe needles of the in-situ probe station in contact with the bond pads of a PRAM cell. A square region directly on top of the PRAM cell was milled and thus removed using the FIB. Figure 10.9 show two low magnification SC images of a PRAM cell connected by the probe needles. The magnification is too low to observe the cell, however these images give an overview of the process. The cell was brought to the amorphous state in situ in the SEM prior to generating the images. In Fig. 10.9(a) the left bond pad is connected to the SC detector and the right bond pad is connected to the SEM ground (image mode *SC-A*). Figure 10.9(b) has the connections to the cell reversed (image mode *SC-B*). Figure 10.9 quite clearly shows that more than just the bond pads and cell are visible. Interestingly, the FIB milled region is only visible in Fig. 10.9(b). Because the cell was brought to the amorphous state a clear separation in brightness is observed. The cell acts as a barrier for charge collection which either drains to the side connected to the SC detector (bright parts) or to the ground (dark parts).

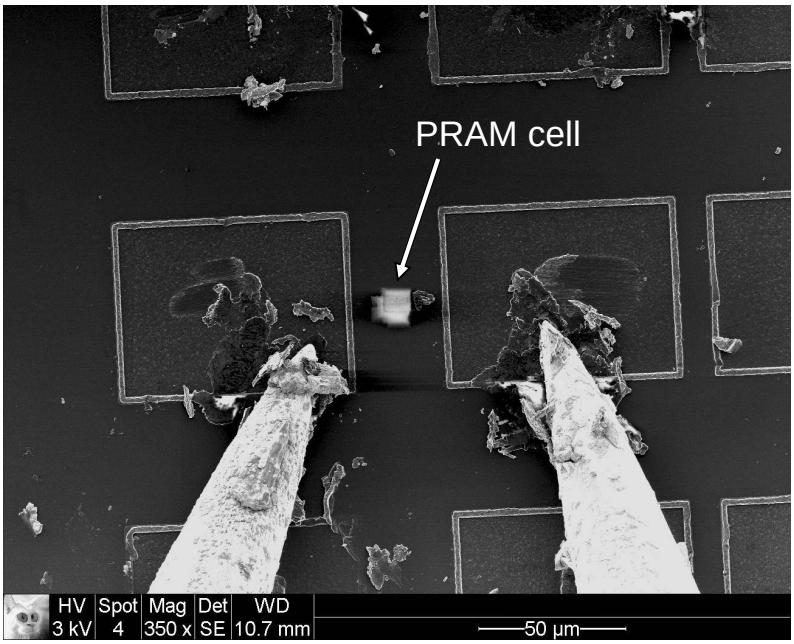

Figure 10.8: *SEM image of a PRAM cell connected by the probe needles. The location of the milled region above the PRAM cell is shown in the image.*

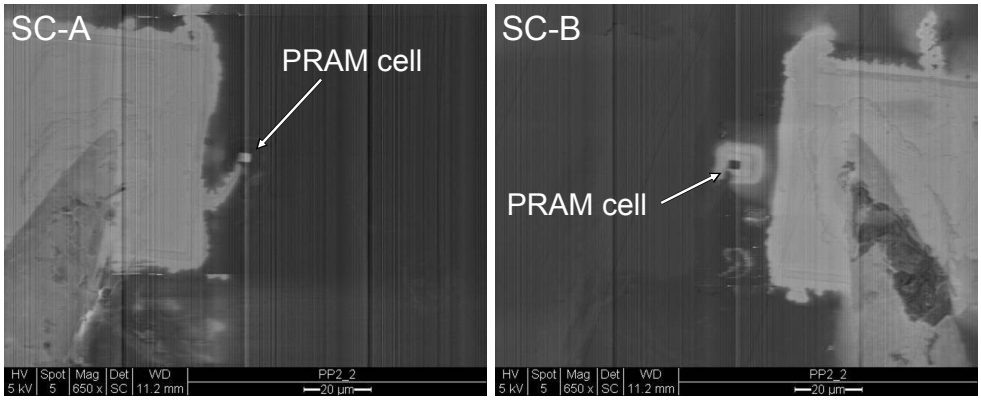

(a) (b)

Figure 10.9: *Two low magnification CCM images are shown where in* ***(a)*** *the left side of the cell is connected to the SC detector and the right side is connected to the ground and in* ***(b)*** *the connections are reversed. Because the cell is in the amorphous state, the cell resistance acts as an electrical barrier and therefore either one of the two probe needles is visible where the other is not.*

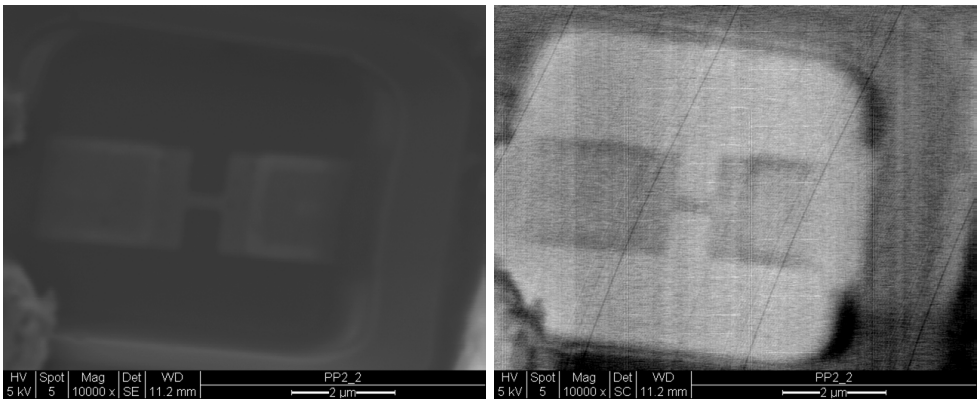

(a) (b)

Figure 10.10: *An SEM image and an SC image is shown of the same PRAM cell as in Fig. 10.9. The dog-bone shaped line cell can be clearly observed in both images. The cell was brought to the crystalline state and therefore the complete cell can be distinguished in* ***(b)****.*

10.4.1 Switching a PRAM line cell in situ in the SEM

Figure 10.10(a) is an SEM image of the same PRAM cell shown in Fig. 10.9 but taken with higher magnification. A square shaped region had been milled in the FIB leaving only a thin layer of passivation on top of the cell not more than about 100 nm thick. Figure 10.10(b) shows an SC image of the same cell in the crystalline state with a cell resistance of 0.62 kΩ.

The cell was connected as shown in Fig. 10.6(a). The right side of the cell is connected directly to the ground. However, the relay parallel to the 330 kΩ was opened as it was found to increase contract. Therefore the left side of the cell is connected to the SC amplifier by a 331 kΩ series resistance in total. This resistance imbalance naturally drains more signal to the ground than to the SC amplifier. Therefore the PRAM line cell appears dark. However, the region around the cell obscures the image and the contrast is quite low compared to images where the cell is programmed to the amorphous state. The contrast mechanism is not as straight forward as Fig. 10.3 might predict as static charging of the passivation layer and gallium implantation by FIB milling also have to be taken into account.

The PRAM cell was programmed to the amorphous state with a 3.9 V, 50 ns RESET pulse. The pulse shape of the RESET pulse shown in Fig. 10.11(a) is slightly distorted because of large number of reed relays in the in situ probe station (see Fig. 6.2(a)). The cell resistance was measured for 10 seconds as a function of time (Fig. 10.11(b)). The resistance increase in time follows the well-established power law [78]. From Fig. 10.11(b) a resistance of R_1=1.20 MΩ was obtained with a power law coefficient $\alpha = 0.083$. These are quite typical values which only shows that the FIB processed cell displayed 'normal' cell behavior.

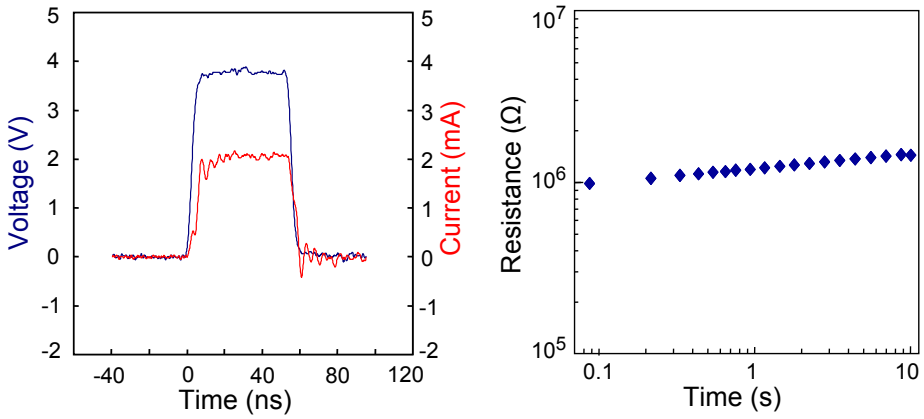

Figure 10.11: *A RESET pulse and resistance measurement as a function of time after RESET that programmed the cell shown in Fig. 10.10 to the amorphous state. The cell resistance measurement displays quite typical behavior (see text).*

Figure 10.12 shows SC images of the same cell in the amorphous state. Unlike Fig. 10.10(b) where the cell is in a crystalline state and the SC image has almost no contrast, the signal to noise ratio in the amorphous state is quite high. This is a natural consequence of the electrical obstruction created by the amorphous mark for charge flowing to the SC detector.

10.4.2 Observation of an electric field at the crystal boundary

Figure 10.13 show SC images of a PRAM cell programmed to the amorphous phase. At the location where the boundary between the crystalline and amorphous phase is expected a very bright and a dark region can be observed. This region has the appearance of a dipole. Such a region can also be observed in Fig. 10.12 however not as striking as in Fig. 10.13. The bright region indicates that more signal is directed to the SC detector while the dark region indicates that charge is directed away from the detector and to the ground. When the connections to the cell are reversed the intensities of the bright and dark regions are also inverted. This indicates that signal is directed in a specific physical direction, either towards the SC detector or away from the SC detector respective of how the cell is connected to the SC detector. This contrast can be explained by the presence of an electric field at the location of the amorphous/crystalline interfaces. Figure 10.14 shows an SEM image of the same region as Fig. 10.13.

The inset of Fig. 10.15 shows the location of the line cell taken from Fig. 10.13, The outline of the cell, as obtained from Fig. 10.14 is also shown in Fig. 10.15(a). Because the image shifts between SEM, *SC-A* and *SC-B* mode, the images cannot be accurately linked. However, Fig. 10.14 shows features that also appear in the SC

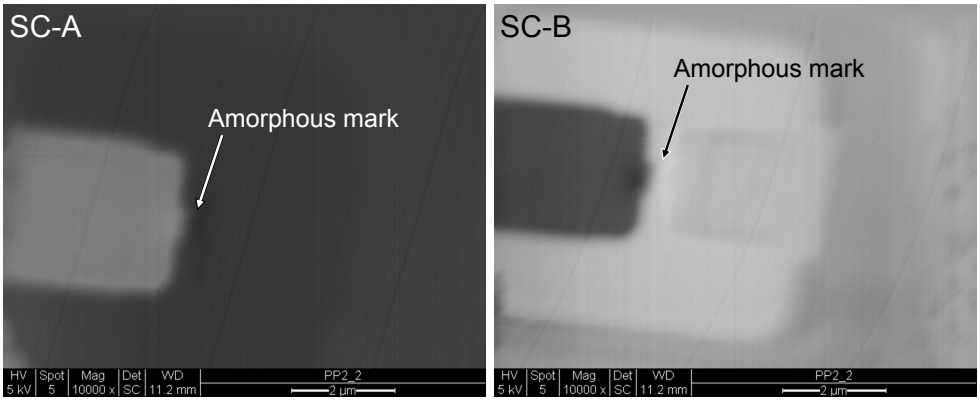

(a) (b)

Figure 10.12: *Two SC images of the cell shown in Fig. 10.10 which was brought to the amorphous state. In* ***(a)*** *the left side of the cell is connected to the SC detector and the right side is connected to the ground. In* ***(b)*** *the connections are reversed. The location of the amorphous mark is shown in the images.*

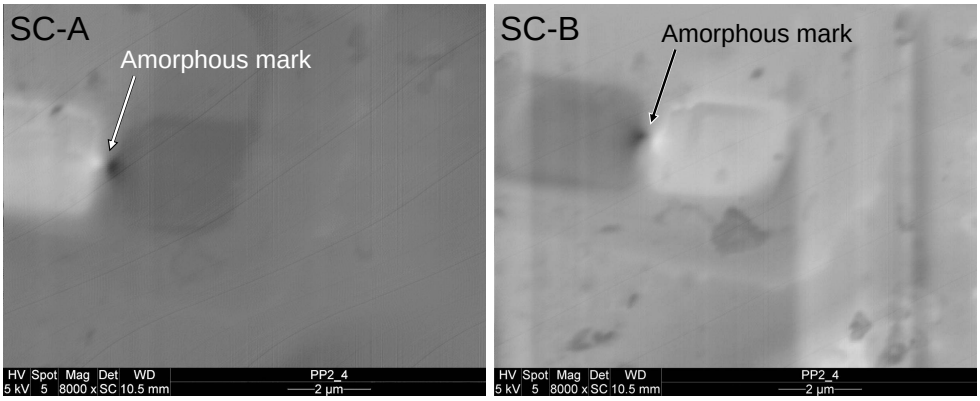

(a) (b)

Figure 10.13: *Two SC images of the cell shown in Fig. 10.10 which was brought to the amorphous state. In* ***(a)*** *the left side of the cell is connected to the SC detector and the right side is connected to the ground. In* ***(b)*** *the connections are reversed. At the location where the amorphous mark is expected a bright and dark region is observed which can be explained by an electric field at the location of the amorphous and crystalline boundaries (see main text).*

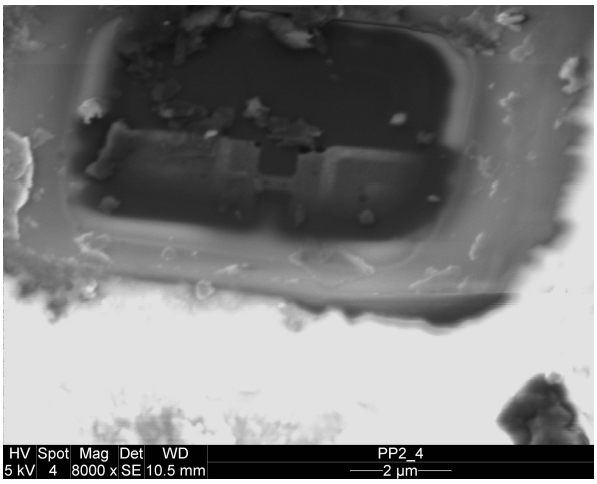

Figure 10.14: *SEM image of the same cell shown in Fig. 10.13. The region milled by using the FIB setup is located slightly to the side of the cell which is a result of misalignment during FIB processing. Still the dog-bone shaped line cell is clearly visible.*

images. These features can be used to make the images overlap. The main images of Fig. 10.15 show the SC signal across the line at the location of the amorphous mark. Although the contrast is not high the lines allow for the determination of the length of the amorphous mark of 480 ± 50 nm. The assumption is made that a field is present at the interface which leads to the highest signal at that location. The question remains whether this is the actual amorphous mark length, because other information of the possible length of the amorphous mark is lacking. Nevertheless, comparing earlier TEM images (Fig. 4.1 and 4.2) indicate that the mark length appears reasonable.

The spatial resolution in the SC images for observing the amorphous mark in the line cells appears quite low (about 100 nm). The main reason for this is that the 5 kV electron beam is severely broadened when it has to be transmitted through the top passivation layer (with a thickness of about a hundred nanometers) before it reaches the phase-change material in the line cell. Furthermore, the SC detector will pick up a signal that is based on the electrons that are injected in the sample. The secondary electrons picked up in the SEM image are drawn from the top layer of the sample only. Based on Monte Carlo simulations, an electron beam of 5 kV is broadened to 47 and 99 nm for Si thicknesses of 50 and 75 nm, respectively ([31]). The beam broadening is defined as the radius within which 90% of the transmitted electrons lie as they exit from the layer. Indeed, the values for this broadening have similar magnitude as the observed resolution in our SC images, also indicating that the remaining passivation layer cannot be more than 100 nm thick. Other factors like charging of the insulating SiO_2 and picking-up of SE electrons directly by the probes of the miniature probe station can deteriorate image quality and resolution, but turn out less relevant for the observed resolution than the beam broadening.

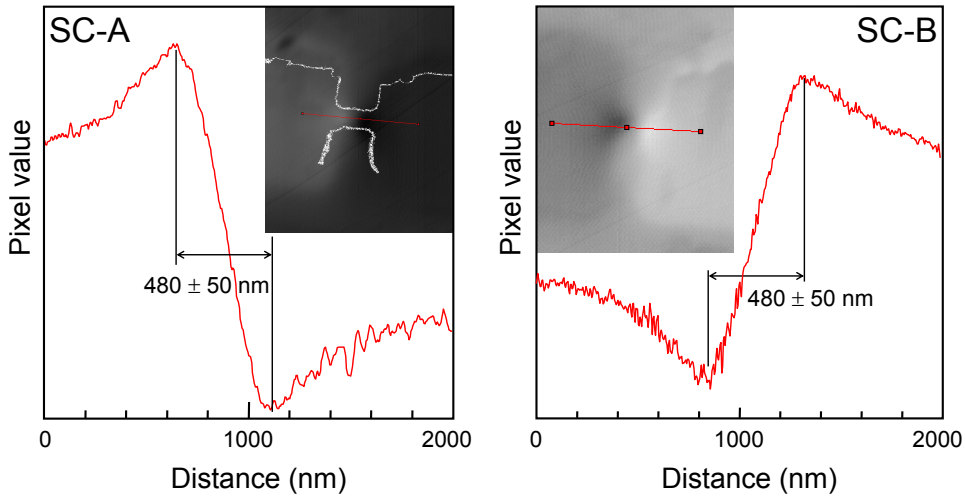

(a) (b)

Figure 10.15: *The insets show location of the amorphous mark taken from Section 10. In* ***(a)*** *the left side of the cell is connected to the SC detector and the right side is connected to the ground. The boundary of the phase change material is shown in the inset which is taken from Fig. 10.14. In* ***(b)*** *the connections are reversed.*
A line is drawn through length of the line cell of which the intensity is shown in the main figure. A length of the amorphous mark of 480 ± 50 nm can be estimated from the distance between the peaks.

10.4.3 Observation of Thomson-Seebeck effect

A 2000×340 nm^2 PRAM line cell was programmed to the amorphous state in situ in the SEM. The two SC images depicted in Fig. 10.16 show that the amorphous mark is located on the left side of the line. The current direction as indicated in Fig. 10.16 is to the right.

The amorphous mark is located at the anode side of the line which confirms the work of Castro et al. [9] performed on similar PRAM line cells. The mark will be in a line with uniform width (and thickness) not be located in the middle of the length of the line, but shifted towards one side [9]. The reason for this shift is the thermoelectric Thomson-Seebeck effect. Depending on the majority charge carrier this asymmetric shift will occur towards the anode for p-type conduction and to the cathode for n-type conduction. For the phase-change cells the Seebeck effect is associated with p-type conduction. The present results therefore agree with this earlier finding and explanation of [9]. The image is slightly distorted. This can be attributed to charging of the surface during the measurement. The PRAM cell was brought back to the

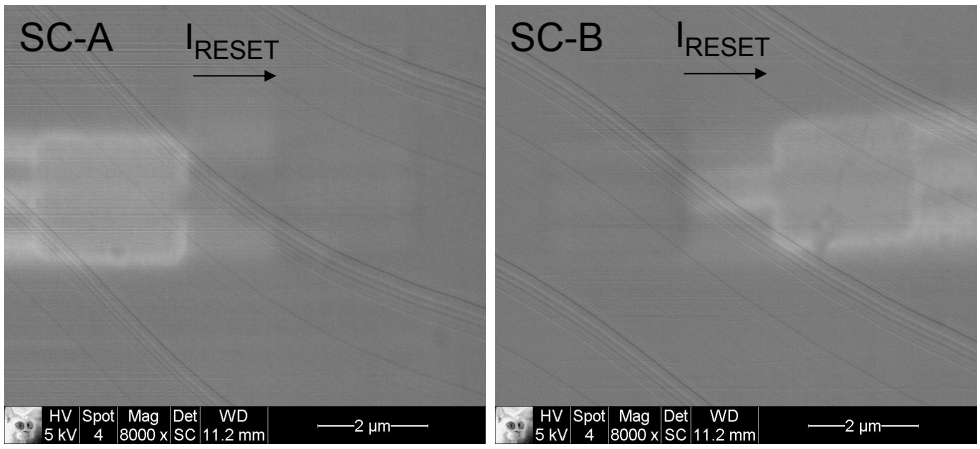

(a) (b)

Figure 10.16: *A 2000×340 nm^2 PRAM line cell was brought to the amorphous state in situ in the SEM. Although the contrast is low, the amorphous mark is located at the left side of the line. This is the anode side with respect to the programming current direction.*

crystalline state by a SET pulse. Subsequently, the cell was programmed again to the RESET state however the pulse polarity was reversed. Two SC images were taken from the cell in this state (Fig. 10.17).

Figure 10.17 shows that the amorphous mark is now located in the middle, with respect to the length of the line cell. The cell was SET and RESET again with the current direction to the left. Quite interestingly, the amorphous mark after programming was located completely to the right, i.e. at the anode side of the cell (Fig. 10.18). These results therefore show for the first time that using in situ switching we were able to observe the shift of the amorphous mark from one side of the line cell to the other when we reverse the polarity of the applied voltage pulse. Interestingly, this shift occurred via one intermediate step where the amorphous mark, after the first pulse with reversed polarity, becomes located more or less in the centre of line cell.

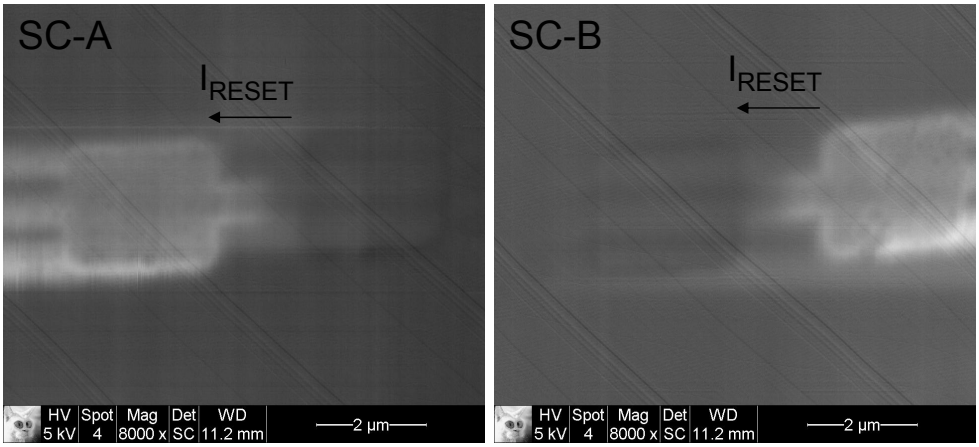

(a) (b)

Figure 10.17: *After crystallization, the cell shown in Fig. 10.16 was brought to the amorphous state again. However the programming current direction was reversed. The amorphous mark was found to be located in the middle of the line.*

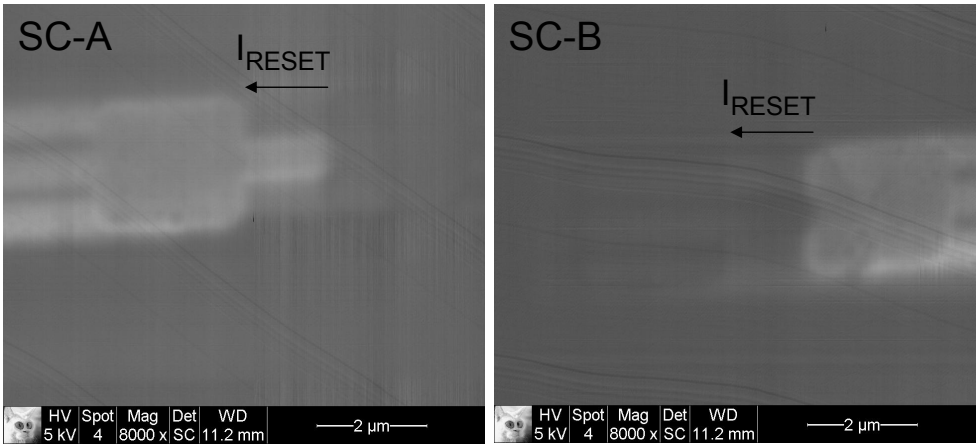

(a) (b)

Figure 10.18: *The cell shown in Fig. 10.17 was crystallized and brought to the amorphous state for the third time. As in Fig. 10.17 the current direction was to the left which resulted in an amorphous mark completely to the rightmost side of the line.*

10.5 Discussion and conclusions

Although the line-cell could not be observed directly with the contrast available in standard SEM mode, still an additional interesting phenomenon was observed. In large geometry cells the location of the amorphous mark could be linked to the current direction of programming. In some cells, as shown in Fig. 10.13, a large contrast at the location of the line is observed. This contrast could be explained by an electric field present at the both the amorphous/crystalline interfaces. Because there is an interface at both sides of the amorphous mark also a bright and a dark region are observed. Conductive atomic force microscope measurements on partly crystallized phase change layers have confirmed that a boundary charge is actually present that can explain the observed contrast [48]. The presence of a local field indicates that the contrast mechanism is based on both RCI [94] and EBIC [53, 94].

A method was developed for observing PRAM line cells using charge-collection microscopy in an SEM while the cells still could be switched (using pulses with a rising and falling edge in the order of nanoseconds) and characterized electrically. In order to achieve this a few hurdles had to be taken:

1. Using FIB the thick (800 nm) passivation layer on top of the phase-change material in the line cell had to be removed locally. A conductive polymer spin coated on top of the wafer piece was required in order to avoid the build-up of charge on the surface that leads to catastrophic failure. This polymer had the advantage of not influencing the measurement because the additional resistance added in parallel could be neglected.
2. A mini-probe station was developed that can be operated inside the SEM chamber. A commercially available vacuum throughput containing seven coaxial connectors was used to connect the in situ probe station to the outside electronics; three connectors were needed for the connection to the electrical characterization setup and four connectors were used for switching ten RF reed relays. This elaborate switching system was required to allow unperturbed (e.g. by spurious pulses) imaging (in SE and SC mode), switching and electrical characterization of the cells.

The developed method showed that a clear difference could be observed between line cells in the crystalline state and containing an amorphous mark. An amorphous mark length of 480 $\pm$ 50 nm could be identified. The resolution, particularly compared to TEM, is relatively poor and is probably mainly caused by spreading of the electron beam when it has to go through the top passivation layer. Still, the advantage of the present CCM in the SEM is that the behavior of the line cell is not affected seriously by removal of material around the cell, which is a serious problem for TEM specimen (cf. Chapter 9). The most interesting result of the present work is related to the asymmetric position of the amorphous mark in the line cell (nearer to the anode) due to the Thomson-Seebeck effect. For the first time we could observe for a single cell how the amorphous mark is moved from one-side to the other side of the line when the voltage polarity is reversed. Interestingly, after reversal of the polarity the first pulse moves the mark to the center of the line and only the second pulse moves it to the opposite side.

Bibliography

[1] D. Adler, H. K. Henisch, and N. Mott, *Rev. Mod. Phys.* **50**, 209 (1978).

[2] R. Bez, E. Camerlenghi, A. Modelli, and A. Visconti *P. IEEE* **91**, 489 (2003).

[3] R. Bez, and A. Pirovano, *Mat. Sci. Semicon. Proc.* **7**, 349 (2004).

[4] R. Bez, *Micro. Engn.* **80**, 249 (2005).

[5] M. Boniardi, A. Redaelli, A. Pirovano, I. Tortorelli, D. Ielmini, and F. Pellizzer, *J. Appl. Phys.* **105**, 084506 (2009).

[6] H.J. Borg, M. van Schijndel, J.C.N. Rijpers, M.H.R. Lankhorst, G.F. Zhou, M.J. Dekker,I.P.D. Ubbens, and M. Kuijper, *Jpn. J. Appl. Phys.* **40**, 1592 (2001).

[7] S. Braga, A. Cabrini, and G. Torelli, *Appl. Phys. Lett.* **94**, 092112 (2009).

[8] G. Bruns, P. Merkelbach, C. Schlockermann, M. Salinga, M. Wuttig, T.D. Happ, J.B. Philipp, and M. Kund, *Appl. Phys. Lett.* **95**, 043108 (2009).

[9] D. Tio Castro, L. Goux, G.A.M. Hurkx, K. Attenborough, R. Delhougne, J. Lisoni, F.J. Jedema, M.A.A. Zandt, R.A.M. Wolters, D.J. Gravesteijn, M. Verheijen, M. Kaiser, R.G.R. Weemaes, and D.J. Wouters, "Evidence of the thermo-electric Thomson effect and influence on the program conditions and cell optimization in phase-change memory cells," *Tech. Dig. - Int. El. Devices. Meet.* 315 (2007).

[10] Y.C. Chen, C.T. Rettner, S. Raoux, G.W. Burr, S.H Chen., R.M. Shelby, M. Salinga, W.P. Risk, T.D. Happ, G.M. Mcclelland, M. Breitwisch, A. Schrott, J.B. Philipp, M.H. Lee, R. Cheek, T. Nirschl, M. Lamorey, C.F. Chen, E. Joseph, S. Zaidi, B. Yee, H.L. Lung, R. Bergmann, and C. Lam, "Ultra-Thin Phase-Change Bridge Memory Device Using GeSb," *Tech. Dig. - Int. El. Devices. Meet.*, 1-4 (2006).

[11] W.Y. Cho, B.-H. Cho, B.-G. Choi, H.-R. Oh, S. Kang, K.-S. Kim, K.-H. Kim, D.-E. Kim, C.-K. Kwak, H.-G. Byun, Y. Hwang, S. Ahn, G.-H. Koh, G. Jeong, H. Jeong, and K. Kim, *IEEE. J. Solid-St. Circ.* **40**, 293 (2005).

[12] Y. Choi, I. Song, M.-H. Park, H. Chung, S. Chang,B. Cho, J. Kim, Y. Oh, D. Kwon, J. Sunwoo, J. Shin, Y. Rho, C. Lee, M.G. Kang, J. Lee, Y. Kwon, S. Kim, J. Kim, Y.-J. Lee, Q. Wang, S.o Cha, S. Ahn, H. Horii, J. Lee, K. Kim,

H. Joo, K. Lee, Y.-T. Lee, J. Yoo, and G. Jeong, "High Bandwidth DRAM & PRAM," *ISSCC* 2.5 p. 46 (2012).

[13] P. Fantini, S. Brazzelli, E. Cazzini, and A. Mani, *Appl. Phys. Lett.* **100**, 013505 (2012).

[14] J. Feinleib, J. deNeufville, S. C. Moss, and S. R. Ovshinsky, *Appl. Phys. Lett.* **18**, 254 (1971).

[15] M. Gill, T. Lowrey, and J. Park, "Ovonic unified memory - a high-performance nonvolatile memory technology for stand-alone memory and embedded applications," *ISSCC*, 12.4 (2002).

[16] L. Goux, D. Tio Castro, G.A.M. Hurkx, J.G. Lisoni, R Delhougne., D.J. Gravesteijn, K. Attenborough, and D.J. Wouters, *IEEE. T. Electron. Dev.* **56**, 354 (2009).

[17] M. Gad-el-Hak, "The MEMS Handbook", CRC Press (2001).

[18] J. Hellmig, A.V. Mijiritskii, H.J. Borg, K. Musialkova, and P. Vromans, *Jpn. J. Appl. Phys.* **42**, 848 (2003).

[19] Y.C. Her, H. Chen, and Y.S. Hsu, *J. Appl. Phys.* **93**, 10097 (2003).

[20] Y.C. Her, and Y.S. Hsu, *Jpn. J. Appl. Phys.* **42**, 804 (2003).

[21] S. Hudgens, and B. Johnson *MRS Bul.* **29**, 829 (2004).

[22] D. Ielmini, D. Mantegazza, A. L. Lacaita, A. Pirovano, and F. Pellizzer, *Solid State Electron.* **49**, 1826 (2005).

[23] D. Ielmini, A. L. Lacaita, and D. Mantegazza, *IEEE. T. Electron. Dev.* **54**, 308 (2007).

[24] D. Ielmini, S. Lavizzari, D. Sharma, and A. L. Lacaita, "Physical interpretation, modeling and impact on phase change memory (PCM) reliability of resistance drift due to chalcogenide structural relaxation," *Tech. Dig. - Int. El. Devices Meet.* p. 939 (2007).

[25] D. Ielmini, and Y. Zhang, *J. Appl. Phys.* **102**, 054517 (2007).

[26] D. Ielmini, S. Lavizzari, D. Sharma, and A. L. Lacaita, *Appl. Phys. Lett.* **92**, 193511 (2008).

[27] D. H. Im, J. I. Lee, S. L. Cho, H. G. An, D. H. Kim, I. S. Kim, H. Park, D. H. Ahn, H. Horii, S. O. Park, U. I. Chung, and J. T. Moon, *Tech. Dig. - Int. El. Devices Meet.*, p. 211 (2008).

[28] F.J. Jedema, M.A.A. in 't Zandt, and W.S.M.M. Ketelaars, *Appl. Phys. Lett.* **91**, 203509 (2007).

[29] F. Jedema, *Nat. Mater.* **6**, 90 (2007).

[30] F. Jedema, M. in 't Zandt, R. Wolters, and D. Gravesteijn, *Jpn. J. Appl. Phys.* **50**, 024102 (2011).

[31] D.C. Joy, "Monte Carlo Modeling for Electron Microscopy and Microanalysis", Oxford University Press (1995).

[32] Y. Jung, S.-W. Nam, and R. Agarwal, *Nano Lett.* **11**, 1364 (2011).

[33] J. Kalb, F. Spaepen, and M. Wuttig, *Appl. Phys. Lett.* **84**, 5240 (2004).

[34] D.M. Kang, D. Lee, H.M. Kim, S.W. Nam, M.H. Kwon, and K.B. Kim, *Appl. Phys. Lett.* **95**, 011904 (2009).

[35] I.V. Karpov, M. Mitra, D. Kau, G. Spadini, Y.A. Kryukov, and V.G. Karpov, *J. Appl. Phys.* **102**, 124503 (2007).

[36] V.G. Karpov, Y.A. Kryukov, S.D. Savransky, and I.V. Karpov, *Appl. Phys. Lett.* **90**, 123504 (2007).

[37] DC. Kau, S. Tang, I.V. Karpov, R. Dodge, B. Klehn, J.A. Kalb, J. Strand, A. Diaz, N. Leung, J. Wu, S. Lee, T. Langtry, K.-W. Chang, C. Papagianni, J. Lee, J. Hirst, S. Erra, E. Flores, N. Righos, H. Castro, and G. Spadini, "A stackable cross point phase change memory" *Tech. Dig. - Int. El. Devices. Meet.* p. 617 (2009).

[38] P.K. Khulbe, T. Hurst, M. Horie, and M. Mansuripur, *Appl. Opt.* **41**, 6220 (2002).

[39] C. Kim, D.M. Kang, T.Y. Lee, K.H.P. Kim, Y.S. Kang, J. Lee, S.W. Nam, K.B. Kim, and Y. Khang, *Appl. Phys. Lett.* 94, 193504 (2009).

[40] H.E. Kissinger, *Anal. Chem.* **29**, 1702 (1957).

[41] V.Y. Kolosov, and A.R. Tholen, *Acta Mater.* **48**, 1829 (2000).

[42] B.J. Kooi, and J.T.M. De Hosson *J. Appl. Phys.* **95**, 4714 (2004).

[43] B.J. Kooi, W.M.G. Groot, and J.T.M. De Hosson, *J. Appl. Phys.* **95**, 924 (2004).

[44] B.J. Kooi, R. Pandian, J.T.M. De Hosson, and A. Pauza, *J. Mater. Res.* **20**, 1825 (2005).

[45] D. Krebs, S. Raoux, C.T. Rettner, G.W. Burr, M. Salinga, and M. Wuttig, *Appl. Phys. Lett.* **95**, 082101 (2009).

[46] D. Krebs, R.M. Schmidt, J. Klomfaβ, J. Luckas, G. Bruns, C. Schlockermann, M. Salinga, R. Carius, and M. Wuttig, *J. Non-Cryst. Solids* **358**, 2412 (2012).

[47] S. Kremers, "Optical properties of phase change materials for novel optical and electrical storage applications," Ph.D. thesis, RWTH Aachen University, 2009.

[48] H.J. Kroezen, G. Eising, G. Ten Brink, G.A. Palasantzas, B.J. Kooi, A. Pauza, *Appl. Phys. Lett.* **100**, 094106 (2012).

[49] A.L. Lacaita, A. Redaelli, D. Ielmini, F. Pellizzer, A. Pirovano, A. Benvenuti, and R. Bez, "Electrothermal And Phase-Change Dynamics In Chalcogenide-Based Memories," *Tech. Dig. - Int. El. Devices Meet.* p. 911 (2004).

[50] A.L. Lacaita, *Solid State Electron.* **50**, 24 (2006).

[51] M.H.R. Lankhorst, L. van Pieterson, M. van Schijndel, B.A.J. Jacobs, and J.C.N. Rijpers, *Jpn. J. Appl. Phys.* **42**, 863 (2003).

[52] M.H.R. Lankhorst, B. Ketelaars, and R.A.M. Wolters, *Nat. Mater.* **4**, 347 (2005).

[53] H.J. Leamy, *J. Appl. Phys.* 53, R51 (1982).

[54] S.-H. Lee, Y. Jung, R. Agarwal, *Nano Lett.* **8**, 3303 (2008).

[55] D. Lencer, M. Salinga, B. Grabowski, T. Hickel, J. Neugebauer, and M. Wuttig, *Nat. Mater.* **7**, 972 (2008).

[56] J. Luckas, S. Kremers, D. Krebs, M. Salinga, M. Wuttig, and C. Longeaud, *J. Appl. Phys.* **110**, 013719 (2011).

[57] J. Luckas, "Electronic transport in amorphous phase-change materials," Ph.D. thesis, RWTH Aachen University, 2012.

[58] S. Maitrejean, G. Ghezzi, E. Gourvest, G. Betti Beneventi, A. Fantini, N. Pashkov, G. Navarro, A. Roule, F. Fillot, P. No , S. Lhostis, O. Cueto, C. Jahan, J.F. Nodin, A. Persico, M. Armand, L. Dussault, C. Vall, Ph. Michallon, R. Morel, A. Brenac, M. Audier, JY Raty, F. Hippert, L. Perniola, V. Sousa, and B. de Salvo, *IEEE Interconnect Tech. Conf.* p. 1 (2012).

[59] T. Matsunaga, J. Akola, S. Kohara, T. Honma, K. Kobayashi, E. Ikenaga, R.O. Jones, N. Yamada, M. Takata, and R. Kojima, *Nat. Mater.* **10**, 129 (2011).

[60] E.R. Meinders, and M.H.R. Lankhorst, *Jpn. J. Appl. Phys.* **42**, 809 (2003).

[61] S. Meister, D.T. Schoen, M.A. Topinka, A.M. Minor, and Y. Cui, *Nano Lett.* **8**, 4562 (2008).

[62] S. Meister, S.-B. Kim, J.J. Cha, H.-S. P. Wong, and Y. Cui, *ACS Nano* **5**, 2742 (2011).

[63] M. Mitra, Y. Jung, D.S. Gianola, and R. Agarwal, *Appl. Phys. Lett.* **96**, 222111 (2010).

[64] M.C. Morilla, C.N. Afonso, A.K. Petfordlong, and R.C. Doole, *Philos. Mag. A-Phys. Condens. Matter Struct. Defect Mech. Prop.* **73**, 1237 (1996).

[65] S.W. Nam, D. Lee, M.H. Kwon, D.M. Kang, C. Kim, T.Y. Lee, S. Heo, Y.W. Park, K. Lim, H.S. Lee, J.S. Wi, K.W. Yi, Y. Khang, and K.B. Kim, *Electrochem Solid St.* **12**, H155 (2009).

[66] S.-W. Nam, R. Agarwal, *Science* **336**, 1561 (2012).

[67] T. Nirschl, J.B. Phipp, T.D. Happ, G.W. Burr, B. Rajendran, M.H. Lee, A. Schrott, M. Yang, M. Breitwisch, C.F. Chen, E. Joseph, M. Lamorey, R. Cheek, S.H. Chen, S. Zaidi, S. Raoux, Y.C. Chen, Y. Zhu, R. Bergmann, H.L. Lung, and C. Lam, "Write strategies for 2 and 4-bit multi-level phase-change memory," *Tech. Dig. - Int. El. Devices Meet.* p. 461. (2007).

[68] T. Ohta, N. Yamada, H. Yamamoto, T. Mitsuyu, T. Kozaki, J. Qiu, and K. Hirao, *Mater. Res. Soc. Symp. Proc.* **674**, V1.1.1 (2001).

[69] J.K. Olson, H. Li, T. Ju, J. M. Viner, and P.C. Taylor, *J. Appl. Phys.* **99**, 103508 (2006).

[70] N. Oomachi, S. Ashida, N. Nakamura, K. Yusu, and K. Ichihara, *Jpn. J. Appl. Phys.* **41**, 1695 (2002).

[71] S.R. Ovshinsky, *Phys. Rev. Lett.* **21**, 1450 (1968).

[72] A.E. Owen and J.M. Robertson, *IEEE. T. Electron. Dev.* **20**, 105 (1973).

[73] A. Padilla, G.W. Burr, K. Virwani, A. Debunne, C.T. Rettner, T. Topuria, P.M. Rice, B. Jackson, D. Dupouy, A.J. Kellock, R.M. Shelby, K. Gopalakrishnan, R.S. Shenoy, and B.N. Kurdi, "Voltage polarity effects in GST-based Phase Change Memory: Physical origins and implications" *Tech. Dig. - Int. El. Devices Meet.*) p. 29.4.1 (2010).

[74] R. Pandian, B.J. Kooi, J.T.M. De Hosson, and A. Pauza, *J. Appl. Phys.* **100**, 123511 (2006).

[75] R. Pandian, B.J. Kooi, G. Palasantzas, J.T.M. De Hosson, and A. Pauza, *Adv. Mater.* **19**, 4431 (2007).

[76] A.K. Petfordlong, R.C. Doole, C.N. Afonso, and J. Solis, *J. Appl. Phys.* **77**, 607 (1995).

[77] L. van Pieterson, M.H. Lankhorst, M. van Schijndel, A.E. Kuiper, and J.H. Roosen, *J. Appl. Phys.* **97**, 083520 (2005).

[78] A. Pirovano, A.L. Lacaita, F. Pellizzer, S.A. Kostylev, A. Benvenuti, and R. Bez, *IEEE. T. Electron. Dev.* **51**, 714 (2004).

[79] A. Pirovano, A.L. Lacaita, A. Benvenuti, F. Pellizzer, and R. Bez, *IEEE. T. Electron. Dev.* **51** 452 (2004).

[80] D.A. Porter, and K.E. Easterling, "Phase Transformations in Metals and Alloys," 2nd Edition, CRC Press (1992).

[81] S. Privitera, C. Bongiorno, E. Rimini , R. Zonca, A. Pirovano, and R. Bez, *Mater. Res. Soc. Symp. Proc.* **803**, HH1.4. (2003).

[82] E. Prokhorov, A. Mendoza-Galvn, J. Gonzlez-Hernndez, and B. Chao, *J. Non-Cryst. Solids* **353**, 1870 (2007).

[83] B. Rajendran, M.H. Lee, M. Breitwisch, G.W. Burr, Y.H. Shih, R. Cheek, A. Schrott, C.F. Chen, M. Lamorey, E. Joseph, Y. Zhu, R. Dasaka, P.L. Flaitz, F.H. Baumann, H.L. Lung, C. Lam, "On the dynamic resistance and reliability of phase change memory," *IEEE Symp. VLSI Tech.* p. 96 (2008).

[84] S. Raoux, *Ann. Rev. Mater. Res.* **39**, 25 (2009).

[85] S. Raoux, W. Wenic, and D. Ielmini, *Chem. Rev.* **110**, 240 (2010).

[86] F. Ren, J.-W. Nah, K.N. Tu, B. Xiong, L. Xu, and J.H.L. Pang, Appl. Phys. Lett. 89, 141914 (2006).

[87] A. Redaelli, A. Pirovano, E. Pellizzer, A. L. Lacaita, D. Ielmini, and R. Bez, *IEEE Electron Devic. Lett.* **25**, 684 (2004).

[88] G. Ruitenberg, A.K. Petford-Long, and R.C. Doole, *J. Appl. Phys.* **92**, 3116 (2002).

[89] I. Satoh, and N. Yamada, *Proc. Spie* 4085, 283 (2001).

[90] M.A. Schulze, and J.A. Pearce, *Proc. Spie* **1902**, 106 (1993).

[91] R.R. Shanks, and C. Davis "A 1024-Bit Nonvolatile 15ns Bipolar Read-Write Memory" *IEEE Int. Solid. St c. Conf.* p. 112 (1978).

[92] K. Shportko, S. Kremers, M. Woda, D. Lencer, J. Robertson, and M. Wuttig, *Nat. Mater.* **7**, 653 (2008).

[93] J. Siegel, A. Schropp, J. Solis, C. N. Afonso, and M. Wuttig, *Appl. Phys. Lett.* **84**, 2250 (2004).

[94] C.A. Smith, C.R. Bagnell, E.I. Cole, F.A. DiBianca, D.G. Johnson, W.V. Oxfort R.H. Propst, *IEEE T. Electron. Dev.* **ED-3**, 282 (1986).

[95] M. Telford, "The case for bulk metallic glass," *Mater. Today*, p. 36 (2004).

[96] A.W. Smith, *Appl. Opt.* **13**, 795 (1974).

[97] Y.P. Varshni, *Physica* **34**, 149 (1967).

[98] V. Weidenhof, I. Friedrich, S. Ziegler, and M. Wuttig, *J. Appl. Phys.* **86**, 5879 (1999).

[99] M. Wuttig, and N. Yamada, *Nat. Mater.* 6, 824 (2007).

[100] M. Wuttig, D. Lsebrink, D. Wamwangi, W. Welnic, M. Gillessen, and R. Dronskowski, *Nat. Mater.* **6**, 122 (2007).

[101] N. Yamada, E. Ohno, N. Akahira, K. Nishiuchi, K. Nagata, and M. Takao, *Jpn. J. Appl. Phys.* **26** Suppl. 26-4, p. 61 (1987).

[102] T.-Y. Yang, I.-M. Park, B.-J. Kim, and Y.-C. Joo, *Appl. Phys. Lett.* **95**, 032104 (2009).

[103] T.-Y. Yang, J.-Y. Cho, Y.-J. Park, and Y.-C. Joo, *Acta Mater.* **60**, 2021 (2012).

[104] Y. Yin, T. Noguchi, H. Ohno, and S. Hosaka, *Appl. Phys. Lett.* **95**, 133503 (2009).

[105] M.S. Youm, Y.T. Kim, Y.H. Kim, and M.Y. Sung, *Phys. Status Solidi A* **205**, 1636 (2008).

[106] G.F. Zhou, *Mater. Sci. Eng.* **A304-306**, 73 (2001).

Summary

The past decade, Flash memory has found widespread consumer usage in e.g. USB sticks and later on in smart phones and tablet computers. Flash memory is based on storing electric charge in an electrode surrounded by an insulator (silicon oxide). It was predicted that Flash memory would not meet the demands of future memory because further miniaturization would lead to very high local electric fields [2, 4]. This apparent future limitation of Flash memory had prompted research on other types of non-volatile memories. Some of these types of *Random Access Memories* (RAMs) that were expected to replace Flash memory are *Magnetoresistive RAM* (MRAM), *Ferroelectric RAM* (FeRAM) and *Phase-change RAM* (PRAM or PCRAM). Phase-change materials (PCMs) had already seen great commercial success in re-writable optical memories (CD-RW, DVD±RW and rewritable Blu-ray disc). In these optical discs laser pulses are used to switch small regions between the amorphous (disordered) and crystalline (ordered) phase. A fully electrical non-volatile memory based on a well studied material made great sense. In PRAM, each individual memory cell is an electrical resistor made from phase-change material which can be switched by electrical instead of optical pulses. PRAM did not have the predicted problems with miniaturization that Flash has.

Within the research field of PRAM, several memory types were proposed. NXP, which at the time was still called Philips Semiconductors, introduced the line-cell geometry aimed for the embedded market. The inability to image the switching of the memory cells prompted the collaboration between NXP and the Zernike Institute for Advanced Materials in Groningen, which has access to a *transmission electron microscope* (TEM) together with funding from the Materials innovation institute (M2i). The aim of this project has been to be able to switch PRAM cells while they are imaged in the TEM. This has been a very ambitious goal which in the end has been reached as a proof of principle. However, many other aspects of PCMs as well as PRAM line-cells produced by NXP have been studied as well.

The phase-change material used in the memories by NXP has been studied in the TEM. This initial study was an introduction to the crystallization aspects of PCMs. For this study an amorphous (blanket) layer of PCM was deposited on 20 nm or 50 nm thick silicon nitride membranes. Another silicon oxide layer was deposited on top of the PCM to protect it from oxidation. To be able to image samples in the 200kV TEM present at the Zernike institute, the total thickness of the membrane cannot exceed 200 nm. By heating these membranes in the TEM, the material begins to

crystallize which is one of the striking property of PCMs. Many images were taken at regular intervals while the crystals grow. An image filter procedure (algorithm) has been developed which allows for the discrimination between the phases. Subsequently, an image processing procedure has been presented that allows the determination of the evolution rate in a series of images. This procedure directly quantified the pure growth rate without being affected by factors like varying growth directions, varying boundary shapes during growth or new nucleation events. The activation energy for pure growth was found to be 3.0 eV (assuming an Arrhenius type dependence of growth rate on temperature). It was found that the samples without any capping layer had an order of magnitude higher nucleation rate than the samples with silicon oxide capping layer. This difference was attributed to the partial oxidation of the phase-change layer in air. However, interestingly the growth rates of the samples with and without capping layers were comparable.

In another study the crystallization properties of the blanket films were compared to the memory retention of the PRAM cells which is the time it takes for a memory cell to crystallize i.e. return to lowest energy state. The retention time of a PRAM line cell was obtained in a probe station for various temperatures in the range of 110 °C to 150 °C. From the data a retention time of 10 years at 80 °C was extrapolated. Assuming an Arrhenius type dependence, an activation energy of 2.7 eV was obtained. An equivalent retention time was calculated from the growth rate of the blanket films in the TEM. This equivalent retention time was much higher than the retention time of PRAM cells measured in the probe station. This difference has to be attributed to the fact that the amorphous layer of the blanket films were as-deposited and the PRAM cell was melt-quenched (created by RESET pulse). This conclusion is corroborated by the observation that the retention time measured for a PRAM cell by in situ heating in a TEM is similar to the ones measured in a probe station.

Another interesting property of PRAM is the ability to be switched many times between the low energy crystalline (SET) state and the higher energy amorphous (RESET) state. Doped SbTe PRAM line cells with dimensions $225\times50\times20$ nm^3 produced by e-beam lithography could be SET/RESET for at least 100 million cycles. The memory retention of the PRAM cell was measured both isothermally and isochronally, which gave the same activation energies for growth, 1.7 eV. The isothermal and isochronal retention measurements were repeated on PRAM cells produced by optical lithography and activation energies of 3.0 eV and 3.3 eV were found, respectively. Although the isothermal and isochronal retention measurements were again very similar, they strongly deviate from what we found for the cells produced by e-beam lithography. This deviation mainly originates from the different ways the cells are produced. Cell cycling and geometry explained for a smaller part the differences that were found.

The previous study was repeated. However, various cell properties (i.e. the amorphous and crystalline resistances, amorphous resistance drift, threshold voltage, threshold-voltage drift, crystallization temperature, and activation energy for crystallization) were measured during cell cycling on the same cells and can therefore be directly related. Cells could be cycled typically 100 million times and show stable properties after an initialization phase of about 100 cycles up to about $5\cdot10^5$ cycles.

Beyond this number of cycles the amorphous resistance, the threshold voltage and the crystallization temperature decrease significantly. This behavior is attributed to electromigration induced decomposition of the active phase-change material in the line cell.

As the crystallization temperature drops, the molten region can partly re-crystallize as it is melt-quenched, i.e. more time is spent above the crystallization temperature leading to smaller amorphous mark, which starts to become apparent after $\approx 3.3{\cdot}10^5$ cycles. Finally the cell becomes stuck in the SET state after typically 10 to 100 million cycles. Although the material is still molten during the application of a RESET pulse this does not load to an amorphous melt-quenched state as the cell fully crystallizes directly after the pulse.

During the previous study the crystallization temperature and memory retention properties were measured by means of a temperature ramp instead of keeping the memory cell at a fixed temperature. An interesting observation has been that when a phase-change memory cell is brought to the amorphous state and the temperature is increased by various fixed rates, the resistance is not a uniquely defined function of temperature. In fact, when a PRAM cell is brought to the amorphous state the resistance will increase as a function of time even when the cell is kept at constant temperature. This resistance drift will also occur during the temperature ramp, which will lead to a dependence of the resistance on the ramp rate. Lower ramp rates will allow more time for drift and lead to a higher resistance (R) at a specific temperature (T). In addition, by raising the cell temperature the effect of drift is accelerated. Therefore, E_A cannot be obtained by increasing the temperature without properly taking resistance drift into account.

For doped SbTe, we showed that a ramp up to 413 K and cooling back to room temperature accelerates drift by a factor of 500 with respect to drift for the same time interval solely at room temperature. The activation energy of conduction and pre-exponential factor were measured as a function of annealing temperature (based on the time-independent slope of log(R) versus 1/kT due the absence of additional drift below the annealing temperature). An increase of both parameters was observed and all the experimental results were reproduced excellently on the basis of a theoretical model that takes the temperature dependence of the optical band gap into account. According to our model the change of the optical band gap with changing temperature does not alter after various annealing temperatures from room temperature up to 418 K, but annealing increases the absolute value of the band gap by 47 meV. Still it has to be emphasized that the temperature dependence of the optical band gap has to be taken into account; neglecting it leads to a significant overestimation of the values derived for the optical band gap and pre-exponential factor.

The previous studies based on PRAM cells have all been focused on the electrical and thermal properties of the cell. Another study demonstrates the importance of being able to correlate electrical results of phase-change cells with TEM imaging of the actual structure of the cells. Minimum amorphous mark, optimum and over-programmed amorphous marks and cell near to failure by electromigration have been imaged in conjunction with their corresponding electrical behaviour. Particularly the over-programming effect where the amorphous mark moves due to the Thomson

effect outside the line into the phase-change flap was observed which leads to special electrical behaviour where the amorphous resistance is decreasing, but the threshold volt-age is remaining constant or even slightly increasing. An important conclusion from this study on line cells is that in case the average crystal size of the phase-change material is about equal to the width of the line cell, the edges of the line cell can become rough and can obtain jagged shapes which strongly increase the probability that locally within the line constrictions occur. Constrictions limit the life time of the line cell due to electric-field induced and accelerated decomposition and electromigration. Nevertheless with similar type of cells a reproducible endurance of 10^9 cycles can still be achieved.

The previous study was based on PRAM cells that could not be switched anymore because the connections to the cells were removed during the preparation process for TEM. However, two PRAM cells that were prepared for TEM that could still be switched were provided by NXP. However, these cells could not be probed without damage as the silicon was completely removed from the back. The delicate membrane that remained after removal of the silicon was punctured by the probe needles. Still, interesting results have been obtained from one of these cells. The electrical properties could be related to the TEM images: It was found that crystallization initiates from a narrow channel with amorphous marks still present on both sides. The cell could be crystallized completely by applying higher energy SET pulses. Furthermore, it was found that the PRAM cell processed for TEM observation could not be brought to a resistance as high as unprocessed cells. This was related to re-crystallization of the molten region during the melt-quench phase. As a lot of material was removed to allow for TEM observation, the heat dissipation is impacted. Therefore it takes longer for the temperature of the active phase-change material to cool leading to re-crystallization. This was supported by the observation of a single crystal in the center of amorphous mark after being brought to the amorphous state. A different crystal structure was observed when the cell was still in the crystalline state. This proves that more material was molten than the region that became amorphous. Although many more PRAM cells were processed for TEM by NXP these experienced problems with a protective platinum layer that acted as an electrical short across the cell. Because it was not possible anymore for NXP to process PRAM cells for TEM this was attempted in Groningen. All the steps to process PRAM cells for TEM observation that could still be switched in-situ have been performed. Furthermore, a solution was found for creating an electrical contact to the cell without probe needles as well as providing a protective layer replacing platinum. However, due to time constraints it was not possible to perform all these steps to a single PRAM cell.

Another study was prompted by the availability of an *scanning electron microscope* (SEM) which has a so-called specimen current detector at the Zernike Institute. A method was developed for observing PRAM line cells using charge-collection microscopy in an SEM while the cells still could be switched (using pulses with a rising and falling edge in the order of nanoseconds) and characterized electrically. The developed method showed that a clear difference could be observed between line cells in the crystalline state and containing an amorphous mark. An amorphous mark length of 480 $\pm$ 50 nm could be identified. The resolution, particularly compared to TEM,

is relatively poor and is probably mainly caused by spreading of the electron beam when it has to go through the top passivation layer. Still, the advantage of the present charge collection microscopy in the SEM is that the behavior of the line cell is not affected seriously by removal of material around the cell, which has been a serious problem in previous studies based on the TEM.

In some cells a large contrast at the location of amorphous/crystalline boundary. This contrast could be explained by an electric field present at the boundary between the phases. Because there is an interface at both sides of the amorphous mark with opposite direction of polarity both a bright and a dark region are observed.

The most interesting result of the present work is related to the asymmetric position of the amorphous mark in the line cell (nearer to the anode) due to the Thomson-Seebeck effect. For the first time we could observe for a single cell how the amorphous mark is moved from one-side to the other side of the line when the voltage polarity is reversed. Interestingly, after reversal of the polarity the first pulse moves the mark to the center of the line and only the second pulse moves it to the opposite side.

Samenvatting

De afgelopen tien jaar is Flash geheugen veel toegepast in o.a. USB sticks en later ook in smartphones en tablets. Het principe van Flash geheugen is gebaseerd op het vasthouden van elektrische lading in een elektrode die is ingepakt in een isolator (siliciumoxide). Er was voorspeld dat Flash geheugen in de toekomst de eisen niet meer aan zou kunnen omdat verdere miniaturizatie zou leiden tot erg hoge locale elektrische velden [2, 4]. Het destijds verwachtte einde van Flashgeheugen in de toekomst heeft geleidt tot wetenschappelijk onderzoek aan andere types permanent computergeheugen. Enkele types geheugen waarvan verwacht werd dat ze Flash zouden vervangen zijn magnetisch geheugen (Magnetoresistive Random Access Memory of MRAM), ferroelektrisch geheugen (Ferroelectric RAM of FeRAM) en phase-change (vertaald met fase veranderings≈) geheugen (Phase-change RAM of PRAM). Phase-change materialen (PCMs) waren al een groot commercieel succes in de vorm van herschrijfbare optische media (CD-RW, DVD±RW en herschrijfbare Blu-ray disc). Bij optische media worden laserpulsen gebruikt om kleine gebiedjes PCM te schakelen tussen de amorfe (ongeordende) en kristallijne (geordende) structuur. Een volledig elektrisch permanent geheugen gebaseerd op deze zeer goed bestudeerde materialen leek een logische keuze. In PRAM, bestaat elke individuele geheugencel uit een elektrische weerstand gemaakt van PCM welke kan worden geschakeld door elektrische in plaats van optische pulsen. PRAM leek niet de verwachte miniaturisatieproblemen te kennen die verwacht werden voor Flash geheugen.

Binnen het onderzoeksgebied van PRAM werden verschillende types geheugens voorgesteld. NXP, dat toendertijd nog bekend stond als Philips Semiconductors, introduceerde het lijncelgeheugen dat bedoeld was voor *embedded* toepassingen, bijvoorbeeld voor chips in paspoorten of chipkaarten. Omdat het erg ingewikkeld is om de verschillende geschakelde toestanden van het geheugen zichtbaar te maken werd contact gezocht met het *Zernike Institute for Advanced Materials* in Groningen, waar een transmissieelektronenmicroscoop aanwezig was, en het *Materials innovation institute* (M2i). Het doel van dit project was om PRAM lijncellen van toestand te schakelen en dit zichtbaar te maken met de TEM. Dit was een erg ambitieus doel waarvan uiteindelijk alleen alle verschillende stappen los werden gerealiseerd maar wat uiteindelijk niet in z'n geheel is gehaald. Maar, veel verschillende aspecten van PCMs en PRAM lijncellen geproduceerd door NXP zijn onderzocht, wat tot nieuwe en verassende resultaten heeft geleid die in dit proefschrift beschreven zijn.

Hetzelfde PCM dat ook werd gebruikt in de geheugens van NXP is als dunne

laag bestudeerd met de TEM. Deze eerste studie was een kennismaking met de kristallisatieaspecten van PCMs. Voor deze studie is een amorfe dunne laag PCM gedeponeerd op een 20 nm of 50 nm dik siliciumnitride membraan. Op deze laag is vervolgens een laag siliciumoxide gelegd. Om deze laag zichtbaar te maken onder de 200 kV TEM mag de totale dikte van het membraan niet dikker zijn dan ≈200 nm. Door de membranen op te warmen in de TEM begint de amorfe PCM-laag te kristalliseren. Er werd een serie opnames gemaakt met regelmatige tijdsintervallen terwijl de kristallen groeien. Een beeldverwerkingsalgoritme werd ontwikkeld welke in staat is om onderscheid te maken tussen de amorfe kristallijne fases. Vervolgens werd een tweede algoritme ontwikkeld dat de groeisnelheid kan bepalen uit een serie opnames. Deze procedure is in staat een kwantitatieve analyse van de groeisnelheid te leveren die niet beïnvloed wordt door factoren als groeirichting, gebogen grensvlakken tussen de fases en kristalnucleatie. De gemeten activatie energie van de pure kristalgroei was 3.0 eV (uitgaande dat de groeisnelheid een Arrhenius type temperatuurafhankelijkheid volgt). Bij enkele membranen waar de siliciumoxide laag niet op was aangebracht werd een orde van grootte hogere nucleatiesnelheid gemeten terwijl de groeisnelheid vergelijkbaar was. Dit verschil was te verklaren met gedeeltelijke oxidatie doordat het PCM direct contact had met lucht.

In een andere studie werden de kristallisatieeigenschappen van de dunne lagen vergeleken met de (geheugen)retentietijd van PRAM lijncellen. De retentietijd is de tijd waarna amorf geschakelde cellen spontaan kristalliseren, ofwel terugkeren tot hun lage energie staat. Deze retentietijd van lijncellen werd gemeten in een meetopstelling die werd ingesteld op verschillende temperaturen binnen het gebied van 110 °C to 150 °C. Vanuit de meetdata kon een retentietijd van 10 jaar op 80 °C worden geëxtrapoleerd. Uitgaande van een Arrhenius temperatuurafhandelijkheid werd een activeringsenergie voor kristallisatie van 2.7 eV gevonden. Een vergelijkbare retentietijd werd uitgerekend vanuit de groeisnelheid van de membranen met dunne laag PCM. Deze equivalente retentietijd was veel hoger die die van de lijncellen. Dit verschil kon worden verklaard met het feit dat de dunne lagen werden gemeten in de gedeponeerde toestand (dus zonder eerst geschakeld te zijn) terwijl de lijncellen meerdere keren werden geschakeld en de amorfe structuur onstond door afschrikken vanuit de vloeistoftoestand (*melt-quenching*). Deze conclusie werd verder onderbouwd met een in de TEM gekristalliseerde amorfe PRAM lijncel die kristallisatiegedrag vertoonde vergelijkbaar met de geheugens in de elekctrische meetopstelling en niet overeen kwam met de dunne laag die ook in de TEM werd gemeten.

Een andere interessante eigenschap van PRAM is de mogelijkheid om vele malen te schakelen tussen de lage energie kristallijne (SET) toestand en de hoge energie amorfe (RESET) toestand. Gedoteerd antimonium/tellurium (SbTe) PRAM lijncellen ter grootte van $225\times50\times20$ nm^3 gemaakt met e-beam lithografie konden tot honderdmiljoen keer worden geschakeld tussen de SET en RESET toestand. De geheugenretentie werd zowel isotherm (op constante temperatuur) als isochroon (constante stijgsnelheid vsn de temperatuur) gemeten welke beiden een activeringsenergie voor groei van 1.7 eV opleverden. De isotherme en isochrone retentiemetinge werden herhaald op PRAM cellen geproduceerd met optische lithografie waarbij een activeringsenergie van respectievelijk 3.0 eV en 3.3 eV werd gevonden. Hoewel de isotherme

en isochrone metingen een vergelijkbaar resultaat opleverden werd er dus een groot verschil gevonden tussen de cellen geproduceerd met e-beam lithografie en met optische lithografie. Dit verschil ontstond vooral uit de verschillen in productieprocessen en in mindere mate door de celgeometrie.

In een nieuwe studie werden verschillende celeigenschappen (amorfe en kristallijne weerstand, verandering van de amorfe weerstand en omschakelspanning (*threshold voltage*) met de tijd (*drift*), kristallisatietemperatuur en activeringsenergie) gemeten terwijl de cel, tussen de metingen door, vele malen werd geschakeld tussen de SET en RESET toestand. Om deze manier werden de verschillende celeigenschappen gerelateerd aan het aantal keer dat de cel geschakeld werd. Lijncellen konden honderdmiljoen keer worden geschakeld en kende, na een initialisatiefase, stabiele eigenschappen tussen ongeveer 100 en $5{\cdot}10^5$ keer schakelen. Als de cel vaker werd geschakeld ontstond er een sterke afname van de amorfe weerstand, omschakelspanning, en kristallisatietemperatuur. Dit gedrag werd verklaard door decompositie van het actieve gedeelte van de lijncel die onstaat door elektromigratie. Wanneer de kristallisatietemperatuur daalt dan kan het door de schakelpulsen gesmolten gebied gedeeltelijk kristalliseren omdat de cel zich langere tijd boven de kristallisatietemperatuur bevindt. Dit leidt tot een kleiner amorf gebied wat duidelijk begint te worden na ongeveer $3.3{\cdot}10^5$ keer schakelen. Uiteindelijk blijft de cel *gevangen* in de SET-toestand na 10 tot 100 miljoen keer schakelen. Hoewel de lijncel bij iedere RESET puls smelt leidt dit niet meer tot een amorfe toestand omdat de cel volledig kristalliseert direct tijdens het afkoelen na de puls.

In de hiervoor beschreven studie werden de kristallisatietemperatuur en geheugenretentie gemeten door middel van een constante opwarmsnelheid (isochroon) in plaats van bij een constante temperatuur (isotherm). Een intressant fenomeen deed zich voor: wanneer de PRAM geheugencel (lijncel) naar de amorfe (RESET) toestand werd gebracht en de temperatuur met een constante snelheid toenam, bleek dat de weerstand niet een uniek gedefinieerde functie van de temperatuur was maar afhing van de opwarmsnelheid. Daarnaast neemt de weerstand toe in de tijd wanneer de geheugencel na het schakelen op constante temperatuur wordt gehouden. Deze weerstandstoename (drift) vindt ook plaats ten tijde van opwarming waardoor er een afhankelijkheid tussen de weerstand en de opwarmsnelheid ontstaat. Lagere opwarmsnelheden laten meer tijd toe voor weerstandstoename die ontstaat door drift en de resulterende weerstand op een specifieke temperatuur is daardoor hoger. Doordat de temperatuur wordt verhoogd wordt de weerstandsdrift ook versneld. Daarom kan de activeringsenergie van geleiding niet gemeten worden tijdens opwarming wanneer er nog drift plaats vindt.

Voor gedoteerde SbTe werd aangetoond dat een temperatuurtoename tot 140 °C en vervolgens weer afkoelen leidt tot toename in weerstand die vergelijkbaar is met een 500 keer zo lange tijd als de geheugencel op kamertemperatuur gehouden was. De activeringsenergie van geleiding en de pre-exponentiële factor werden gemeten als functie van de maximum bereikte temperatuur (gebaseerd op de tijdsonafhankelijke richtingscoëfficient van log(R) versus 1/kT vanwege de afwezigheid van de additionele drift onder de maximum bereikte temperatuur). Er werd een toename van beide beide parameters geobserveerd en de experimentele resultaten konden uitstek-

end worden gereproduceerd op basis van een theoretisch model dat er van uitgaat dat de optische bandgap afhangt van de temperatuur. Volgens ons model blijft de temperatuursafhankelijkheid van de optische bandgap ongewijzigd door drift maar neemt de absolute waarde van de bandgap voor en na drift toe met 47 meV. Echter, er moet worden benadrukt dat de temperatuursafhankelijkheid van de optische bandgap in acht moet worden genomen bij berekening van de bandgap. Wanneer deze buiten beschouwing wordt gelaten, dan leidt dat tot een significante overschatting van de bepaalde waarden van de optische bandgap en de pre-exponentiele factor.

De hievoor beschreven studies aan PRAM cellen focusten allemaal op de elektrische en thermische eigenschappen van de geheugencel. Een andere studie toont het belang aan van het correleren van elektrische resultaten met miscroscoopbeelden van de structuur van dezelfde PRAM geheugencel. Minimumlengte van het amorf geschakelde gebied, optimale lengte en over- (te ver) geprogrammeerde amorfe gebieden en geheugencellen die het bijna begaven werden gecorreleerd met hun corresponderende elektrische gedrag. In het bijzonder werd ontdekt dat bij overgeprogrammeerde lijncellen het amorfe gebied buiten de lijn schuift, wat kon worden verklaard door het Thomson-Seebeck effect. Dit leidt tot eerder onverklaarbaar gedrag dat wanneer de weerstand afneemt de omschakelspanning toch een lichte toename kan vertonen. Een andere observatie was dat wanneer de gemiddelde kristalgrootte van het PCM vergelijkbaar is met de breedte van de lijncel, de randen ruw kunnen worden en gehoekte vormen aan kunnen nemen waardoor de kans toeneemt op locale vernauwingen binnen de lijn. Vernauwingen limiteren de levensduur van de lijncel doordat door elektrisch veld geïnduceerde en geaccelereerde decompositie en elektromigratie plaats kan vinden. Desalniettemin konden vergelijkbare cellen tot wel 10^9 keer worden geschakeld.

De hiervoor beschreven studie was van PRAM cellen die niet meer geschakeld konden worden omdat de elektrische verbindingen naar de cel verwijderd waren tijdens het TEM preparatieproces. Echter, twee PRAM cellen, die door NXP volgens een ander proces waren geprepareerd voor TEM observatie, konden wel geschakeld worden. Maar het bleek niet mogelijk elektrisch contact te maken door middel van probe-naalden zonder schade aan de cellen. De oorzaak lag in het verwijderen van het ondersteunende silicium onder de cellen, nodig voor TEM observatie, wat de cellen tot een mechanisch uiterst kwetsbaar membraan maakte. Daarentegen leverden deze twee cellen interessante resultaten op. De elektrische eigenschappen konden worden gecorreleerd aan de TEM beelden: Er werd ontdekt dat de kristallisatie initieert vanuit een smal kanaal met amorfe gebieden aan weerskanten. De cel kon na deze observatie volledig gekristalliseerd worden doormiddel van SET pulsen. Ook bleek dat de PRAM cel die was geprepareerd voor TEM observatie niet geschakeld kon worden tot een weerstandswaarde zo hoog als de niet geprepareerde cellen. Dit kon worden gerelateerd aan het terugkristalliseren van het gesmolten gebied tijdens de afkoelfase. Omdat relatief veel materiaal verwijderd was, een vereiste voor TEM observatie, werd het afvoeren van warmte negatief beïnvloed. Omdat het afkoelen langer duurt is er daarom meer tijd beschikbaar voor kristallisatie. Deze conclusie werd gestaafd door de observatie van een eenkristal in het midden van het amorfe gebied nadat de cel naar de amorfe toestand werd gebracht. Voordat de cel in de amorfe toestand werd

gebracht was er een andere kristalstructuur aanwezig op de locatie van het eenkristal wat er op duidt dat dat deel van de cel gesmolten geweest was.

Hoewel veel meer PRAM cellen werden geprepareerd voor TEM door NXP bleken deze cellen niet te schakelen omdat er een beschermende platinalaag tegen elektrostatische ontlading aangebracht was die de cellen kortsloot. Omdat het bij NXP niet meer mogelijk was om PRAM cellen te prepareren voor TEM werd dit in Groningen verder uitgevoerd. Alle stappen die daarvoor nodig waren konden worden uitgevoerd. Ook werd er een oplossing gevonden voor het maken van elektrisch contact met de cellen zonder de probe-naalden alsmede werd een beschermende laag gevonden ter vervanging van platina die de cellen niet kortsloot. Echter, door tijdsgebrek konden deze stappen niet allemaal in samenhang met elkaar worden uitgevoerd op een enkele geheugencel.

Een andere studie was gebaseerd op de aanwezigheid van een *scanning electron microscope* (SEM) met een zogenaamde *specimen current* detector die beschikbaar was binnen het Zernike Instituut. Een methode werd ontwikkeld om PRAM lijncellen te observeren met *charge-collection* microscopie in een SEM terwijl de cellen nog steeds geschakeld konden worden (met pulsen die stijgtijden hadden in de orde van nanoseconden) en elektrisch gekarakteriseerd konden worden. Met de ontwikkelde methode kon een duidelijk verschil worden geobserveerd tussen kristallijne cellen en cellen met een amorf gebied. Van een amorf gebied kon een lengte van 480 ± 50 nm worden aangetoond. De resolutie, vooral in vergelijking met TEM, is relatief laag wat zeer waarschijnlijk wordt veroorzaakt door verbreding van de elektronenbundel door de passivatielaag die bovenop de cel ligt. Toch heeft de methode van charge collection microscopie in de SEM als voordeel dat het schakelgedrag van de cellen niet (significant) beïnvloed wordt door het verwijderen van materiaal rond de cel omdat dit maar aan één kant plaats vindt. Dit in tegenstelling tot eerdere studies gebaseerd op TEM. In sommige cellen werd een groot contrast geobserveerd ter plaatse van de grens tussen de amorfe en kristallijne fase. Dit contrast kon worden verklaard door de aanwezigheid van een elektrisch veld aan het grensvlak. Omdat er een grensvlak is aan beide kanten van het amorfe gebied met een tegengestelde polarisatierichting werd er zowel een helderder als een donkerder gebied waargenomen. Het meest interessante resultaat van deze studie was het kunnen detecteren van de asymmetrische positie van het amorfe gebied zoals veroorzaakt door het Thomson-Seebeck effect. Voor de eerste keer kon worden geobserveerd dat voor een enkele cel het amorfe gebied verschoof van een kant van de lijn naar de andere kant wanneer de schakelspanning werd omgekeerd. Wanneer de schakelspanning voor de tweede keer werd omgekeerd verschoof het amorfe gebied weer terug naar de originele positie.

Acknowledgments

Als allereerste mijn promotor Bart, ik wil je bedanken voor het vertrouwen dat je vanaf het begin af aan in me heb gehad. Het was duidelijk dat dit project een hele grote uitdaging zou worden en je hebt me de kans gegeven om me helemaal vast te bijten in het onderwerp. Je gaf me alle vrijheid, misschien wel meer dan goed voor me was, omdat het jouw visie is dat een promovendus moet leren om een project op eigen kracht te leiden. Je was heel erg geïnteresseerd in alle onverwachte richtingen waar m'n nieuwsgierigheid me in verzeild liet raken. Bij één vastomlijnd onderwerp is het dan ook niet gebleven. Tegen het einde was het heel erg moeilijk om te accepteren dat door omstandigheden, zoals de economie, in situ TEM observatie van schakelbare PRAM lijncellen niet meer mogelijk was. Uiteindelijk heb je me gelukkig overtuigd om een punt te zetten achter de lopende projecten; de productie van TEM cellen en het vergaren van drift metingen. Toch koos ik er voor om in m'n eigen tijd de drift metingen nog te verwerken tot een publicatie waarbij je een grote steun bent geweest. Bart, het was heel inspirerend om met je samen te werken en ik ben erg gegroeid onder jouw wetenschappelijke leiding. Daarnaast was het heel motiverend om na een lange dag op een conferentie toch gewoon een biertje met je te kunnen drinken en het over andere dingen te kunnen hebben dan wetenschap.

For correcting my thesis I would like to give a special thanks to the reading committee: Matthias Wuttig, Tamalika Banerjee and in particular Jurriaan Schmitz. The quality and quantity of your suggestions have really improved my work.

Mijn collega's bij NXP, Dirk Gravesteijn, Friso Jedema, Frans Voogt, Rob Wolters, Fred Hurkx en Karen Attenborough, ik wil jullie heel erg bedanken jullie interesse en hulp bij mijn onderzoek en de interessante discussies tijdens meetings. Zonder jullie samples had het onderzoek niet plaats kunnen vinden, veel dank daarvoor. Frans Voogt, in het bijzonder ben ik jou dankbaar voor je enorme inzet en expertise bij de productie van de TEM samples die geweldige microscoopbeelden opleverden.

I greatly acknowledge M2i for their support and being such an outstanding employer. In het bijzonder wil ik Irina Bruckner en Derk Bol bedanken voor jullie hulp en luisterend oor.

Daniel Krebs and Martin Salinga, thanks so much for all the fruitful scientific discussions during several conferences. I am very grateful to your scientific contributions that helped me finish my last publication.

M'n eerste Master's student Rudy, veel dank dat je je juist in mijn onderzoek wou verdiepen. We konden op een ouwe-jongens-krentenbrood manier met elkaar door één

deur wat het werken soms wel te gemakkelijk maakte. En uiteindelijk is het project dat onmogelijk leek *gewoon gelukt* en heeft het tot interessante wetenschappelijke resultaten geleid die nog gepubliceerd gaan worden. Hulde en veel dank daarvoor.

My second Master's student Almendo, you have been one of the hardest workers that I've come across and an inspiring person to work with. You've shown great eagerness to learn and flexibility each time the chemical etching process needed to be changed. Thank you for being such a great help in making me accomplish the proof of principle of the main goal of this project.

Ramanathaswamy, thank you very much for the spicy Indian food you cooked for me and for genuinely embodying what it means to be a Swamy.

George, thank you for all the fruitful discussions we had and for allowing me to fulfill my teaching duties during your electronics course.

Gert, ik ben je dankbaar voor je hulp en SEM expertise en dat je het levende bewijs bent dat het meest vals klinkende muziekdoosje toch een gouden raderwerkje kan hebben en dat bij iemands intentie goede daden belangrijker zijn dan grote woorden.

Peter, goeie vriend, collega en zeer gerespecteerd luidsprekeroloog. Ik ben je erg dankbaar en denk met veel plezier terug aan de tijd dat je zonder uitzondering iedere ochtend het hele lab weer een lach op het gezicht toverde met je opgewekte stemming.

Arjan, heel erg bedankt voor je vertrouwen in m'n Labview skills waar ik m'n eerste baan aan heb overgehouden.

And of course, I would like to thank all the other members of the *NMI-group*: Orcun *Mr T.* Ergincan, Gopi, Klaas Bernd, Robin, Arno, Anna, Jan-Wîîllem, Tobias, Jamo, Hans, Oleksander.

Ook zal ik de mooie tijd binnen de *MK-groep* niet vergeten. Jeff, ik wil je heel erg bedanken voor je vertrouwen in me en voor de vliegende start van het project. Dankzij je motivatie ben ik buitengewoon snel afgestudeerd en kon ik direct door met mijn onderzoek waar alles van het begin af aan perfect geregeld was. Heel erg veel dank voor de volledige toegang die je bood aan je omvangrijke arsenaal aan wetenschappelijke apparatuur, optische en elektronenmicroscopen en productietools. Ik heb er dankbaar gebruik van gemaakt.

Willem-Pier, ik ben je dankbaar voor elke keer dat je met zeer goede ideeën kwam maar vooral ook je eerlijkheid wanneer je me niet kon helpen. Dit leidde tot een buitengewoon hoge toepasbaarheid van je suggesties.

Paul, heel erg bedankt voor je oneindige interesse in mijn onderzoek en dat je altijd direct bereid was om elk willekeurig apparaat of onderdeel te vinden en ieder niet radioactief metaal uit het periodiek systeem voorhanden had.

David, thanks for being a great help with building my electrical setup and being able to solve any technical problem.

Pim, heel erg bedankt voor je hulp bij het *efficiënt* programmeren in Labview.

Detsmeister, ik wil je bedanken voor alle zeer goeie gesprekken, je grote interesse in m'n onderzoek en de mooie tijd bij de buitenlandse reis.

Asselio Mozzarelli, thank you for finally embracing your true name and for all the beautifully sounding Italian words you taught me although I won't be using them in Italy.

YuTao, thank you for your interesting ideas and help and expertise with the focused ion beam setup.
Elly, ik kon altijd bij je binnenlopen al was het maar om even een praatje te maken. Dank je voor de gezelligheid en het piekfijn regelen van de administratieve taken.
And of course, I would like to thank all the other members of the *MK group*: Sriram, Kalpak, Ismael, Enne, Lam, Mikhail, Zhenguo, Vasek, Willem, Dave, Emiel and Tony.

Johan Holstein, Frank Bakker en Jasper van den Berg, bedankt voor jullie hulp bij het produceren van de verlengde elektrodes in de NanoLab cleanroom. Johan, in het bijzonder wil ik je bedanken voor je flexibiliteit bij het gebruik van de *deep-UV* lithografiemachine.
Siemon Bakker†, veel dank voor het uitlenen van de probe-station aan het begin van m'n project waardoor ik heel snel met metingen kon beginnen.

Veel dank gaat uit naar de mooie gekken van T.F.V. 'Professor Francken' waar het altijd gezellig is in de Frankenkamer en ik de nodige ontspanning kon vinden tijdens de lunchpauze, bij de vele borrels, BBQs en natuurlijk de buitenlandse reis *aka* SLEF. Met veel plezier denk ik terug aan de mooie tijd met Onur, Bijl, KB, Bas, Bosch, Blokmeister, Remko, Rudy, Detsi, Jakko, Jabs, Compaijen, Ernst, Cora, Patman, Henk-Jan, Chairman, Pijnacker, Thijs, Olger, Tobias, Boerma, Paul, Mannold, Susan, Reeuwerd, Marten, Sjoerd, Tamminga, Carlitos, Jorn, Maurits, Jacobse, Laurens en vele anderen.

Veel dank gaat uit naar m'n paranimfen Gert en Rudy. Gert, ik heb veel met je kunnen lachen en met plezier denk ik terug aan de mooie tijd op de uni en tijdens alle reisjes die we gemaakt hebben. Je hebt de gave om problemen die groot lijken te relativeren tot overzienbare ongemakken. Je relaxte instelling heeft me tijdens stressvolle momenten erg geholpen waar ik je dankbaar voor ben.
Rudy, heel erg bedankt voor de vele avondjes discussiëren over muziek en het goede gezelschap bij de vele concerten waar we naartoe zijn geweest. En natuurlijk bedankt voor de vele keren dat je bereid was m'n publicaties en ander geschreven werk te screenen op taalkundige correctheid. Hoewel de inhoud soms langs je heen ging wist je altijd weer genoeg net niet perfect lopende zinnen te vinden.

En tot slot wil ik mijn lieve familie bedanken en natuurlijk eerst m'n ouders. Bob en Trudi, jullie hebben een geweldige veilige maar vrije omgeving gecreeërd om in op te groeien. Op het eiland kon ik helemaal ongedwongen op het wad spelen en hutten bouwen in het bos. Ook gaven jullie alle ruimte om m'n technische interesse te ontwikkelen wat jaren later uiteindelijk tot m'n proefschrift heeft geleid. Erg dankbaar ben ik voor het vertrouwen dat jullie altijd in me hebben gehad en jullie zijn een hele grote steun voor me.
En last but not least, m'n grotere broer Jelmer. Broer, omdat we maar weinig schelen ben je altijd een bijna vanzelfsprekende aanwezigheid in m'n leven geweest. Steeds vaker realiseer ik me hoeveel steun ik aan je heb gehad waar ik je heel erg voor wil bedanken.

List of publications

1. *Crystallization studies of doped SbTe phase-change thin films and PRAM line cells: Growth rate determination by automated TEM image analysis*,
J.L.M. Oosthoek, B.J. Kooi, J.T.M. De Hosson, D. Gravesteijn, K. Attenborough, R. Wolters, and M. Verheijen *Proc. E/PCOS Symp.* p. 140 (2009).

2. *Memory retention of doped SbTe phase change line cells measured isothermally and isochronally*,
J.L.M. Oosthoek, B.J. Kooi, K. Attenborough, F.A.M. Hurkx, and D.J. Gravesteijn, *Mater. Res. Soc. Symp. Proc.* G14-04-H07-04 (2010).

3. *Growth Rate Determination through Automated TEM Image Analysis: Crystallization Studies of Doped SbTe Phase-Change Thin Films*,
J.L.M. Oosthoek, B.J. Kooi, J.T.M. De Hosson, R.A.M. Wolters, D.J.Gravesteijn, and K. Attenborough, *Microsc. Microanal.* **16**, 291 (2010).

4. *Evolution of cell resistance, threshold voltage and crystallization temperature during cycling of line-cell phase-change random access memory*,
J.L.M. Oosthoek, K. Attenborough, G.A.M. Hurkx, F.J. Jedema, D.J. Gravesteijn, and B.J. Kooi, *J. Appl. Phys.* **110**, 024505 (2011).

5. *The influence of resistance drift on measurements of the activation energy of conduction for phase-change material in random access memory line cells*,
J.L.M. Oosthoek, D. Krebs, M. Salinga, D.J. Gravesteijn, G.A.M. Hurkx, and B.J. Kooi *J. Appl. Phys.* **112**, 084506 (2012).

6. *Nanostructure-property relations for phase-change random access memory (PRAM) line cells*,
B.J. Kooi, J.L.M. Oosthoek, M.A. Verheijen, M. Kaiser, F.J. Jedema, D.J. Gravesteijn, *Phys. Status Solidi* **249**, 1972 (2012).

7. *Correlative TEM and electrical properties study of switchable phase-change random access memory line cells*,
J.L.M. Oosthoek, F.C. Voogt, M.A. Verheijen, G.A.M. Hurkx, D.J. Gravesteijn, B.J. Kooi, *in preparation.*

8. *Charge Collection Microscopy of in-situ switchable PRAM line cells in an SEM: method development and unique observations*
J.L.M. Oosthoek, R.W. Schuitema, G.H. ten Brink, D.J. Gravesteijn, B.J. Kooi, *in preparation.*